THE UNIVERSITY OF CHICAGO

EXPLORING NONEQUILIBRIUM PHYSICS OF POLYELECTROLYTE COMPLEXES VIA X-RAY, NEUTRON, IMAGING, AND MODELING

A DISSERTATION SUBMITTED TO
THE FACULTY OF THE PRITZKER SCHOOL OF MOLECULAR ENGINEERING
IN CANDIDACY FOR THE DEGREE OF
DOCTOR OF PHILOSOPHY

BY
HAO WU

CHICAGO, ILLINOIS
AUGUST 2019

To my Father and Mother

TABLE OF CONTENTS

LIST OF FIGURES

LIST OF TABLES

ACKNOWLEDGMENTS

I would like to start by thanking my advisor, Dr. Matthew Tirrell, for his guidance, support, and encouragement. I have always admired Matt's attitude and perspicacity in science and research and appreciated him for giving me the opportunity to working with him. I have learned many important things from him, which will continue to benefit me in the future. I would also like to thank my committee members, Drs. Paul Nealey and Jeffrey Hubbell. Their scientific knowledge and suggestions provided important insights into my research.

I would like to say thank you to the members at Tirrell group. Surrounded by them in the past few years, I have learned a lot from them by osmosis. They have not only been great colleagues and collaborators but also amazing friends. I would like to thank Drs. John Colson, Samanvaya Srivastava, Lorraine Leon, Eun Ji Chung, Blair Brettman, Handan Acar, Jeffrey Vieregg, and Amanda Marciel for their advice and suggestions when I started my graduate research. I would like to thank Lu Li, Michael Lueckheide, Michael Mellas, Mat Schnorenberg, Whitney Fowler, Yu Tian, Ge Zhang, Harrison Paul, Kedan Stevens, Angelika Neitzel, and Dean Mastropietro for their help and support. I would especially like to thank Jun Mao, Jeffrey M. Ting, Olivia Werba, Siqi Meng, Alexander Marras, and Artem Rumyantsev at the de Pablo group who directly worked with me on many projects.

I owe a great debt of gratitude to a number of scientists at national laboratories who provided tremendous help for my research. I thank Drs. Thomas M. Weiss, Ivan Rajkovia, and Tsutomu Matsui at the Stanford National Accelerator Laboratory for their assistance in X-ray scattering experiments and insightful discussions. I thank Drs. Xiaobing Zuo, Mrinal Bera, Yuzhi Liu, Wei Chen, and Jan Ilavsky in the Advanced Photo Source at the Argonne National Laboratory, who helped me on beamline and electron microscopy experiments and data analysis. I thank Drs. Elizabeth G. Kelly, Steven Kline, Paul Butler, Boualem Hammouda, and Yimin Mao at the National Institute of Standands and Technology, for their great help on SANS experiments. I thank Drs. William Heller, Kunlun Hong, Sai Venkatesh Pingali, Carrie Gao, and Mr. Tianyu Li at Oak Ridge National Laboratory, for

their assistance on neutron scattering experiments and polymer synthesis. I also thank Dr. Chenhui Zhu at Lawrence Berkeley National Laboratory for his help on X-ray scattering experiments. Additionally, I would like to thank Dr. Junyou Wang at the Eastern China University of Science and Technology, who provided raw materials to me.

Also, I would like to thank scientists at facilities at the University of Chicago for their help on my experiments including Drs. Tera Lavoie and Yimei Chen for help with electron microscopy and Dr. Philip Griffin for help with spectroscopy and rheometer.

More importantly, I would like to thank family and friends who supported me in the past five years. I would especially like to thank my wife for always believing in me and my dreams. Finally, I would like to thank my parents. They taught me how to be a man with honesty, decency, and integrity. I would not be who I am today without their unwavering support and encouragement.

ABSTRACT

Polyelectrolyte complexes are a condensed phase that forms when oppositely charged units mix together in an aqueous environment. Despite its ubiquity in natural and technological settings, it is still challenging to have an in-depth understanding of the origin of its structural complexity in general and kinetic pathways of nonequilibrium phenomena in particular.

The first goal of this dissertation is to investigate the nonequilibrium phenomena, kinetic pathways, and long-term stability of these electrostatic self-assemblies. Emphasis is placed on their morphological complexities and time-dependent structural evolution under a variety of parameters including preparation protocol, salt type, and solution salt concentration. By employing a combination of X-ray scattering and electron imaging, sharp distinctions between thermodynamically stable products and kinetically trapped metastable structures are revealed and their structural heterogeneities are identified. Notably, the kinetic pathway of the morphological transformation between the thermodynamic products and kinetic products is determined to be a two-step process.

Then, the next goal is to dive into the interparticle interactions of the thermodynamically stable nanoscale assemblies, i.e. polyelectrolyte complex micelles. A variety of experimental techniques and modeling methods, such as synchrotron small-angle X-ray scattering and pair distribution function analysis, are employed to provide a comprehensive characterization of their physical properties, including morphology, core and corona size, and radius of gyration. The growing prominence of a repulsive interaction in these micelles is observed in dilute solutions within a concentration range where micelle-micelle interaction has been ignored. The origin of the repulsive intermicellar correlation among these nanoscale electrostatic self-assemblies is further identified to be from the coronal responses via a quasi-hard-sphere interaction.

Next, this dissertation concentrates on the nonequilibrium kinetics of polyelectrolyte complex micelles, including formation, molecular exchange, and dissociation, via a combination of a series of experiments and physical modeling.

First, the superfast self-assembly kinetics is investigated by time-resolved small-angle X-ray scattering equipped with a stopped-flow device that enables a temporal resolution of a few milliseconds. It is found that the initial aggregation of the oppositely charged polyelectrolytes is completed within 80 ms, and the following micelle growth continues to proceed up to a few minutes. Experimental data and thermodynamic analysis show that, contrary to their uncharged counterparts, polyelectrolyte complex micelles do not go through a micelle fusion process during formation. A two-step formation mechanism is proposed to explain the experimental observation, which involves an ultrafast polyelectrolyte pairing step and a prolonged cluster aggregation step.

Second, the molecular exchange in polyelectrolyte complex micelles at near-equilibrium states is further explored using time-resolved small-angle neutron scattering and deuterium labeling. The aim is to investigate the dependency of the molecular exchange rate on polymer block length, system temperature, and solution salinity. During the experimented time period, no clear evidence is observed to show the chain exchange between the deuterium-rich micelles and hydrogen-rich micelles when they are mixed. Neither the elevation of system temperature nor increase of solution salinity, two common ways to weakening the strength of electrostatic interactions, seem to unlock the molecular exchange at the experimented time scale. The underlying reason is attributed to the failure of overcoming the large activation energy barrier caused by the breakup of the ionic bonds between oppositely charged groups.

Last, the kinetic pathway of dissociation kinetics in polyelectrolyte complex micelles is found to be a process that involves three distinct steps: micelle swelling, fragmentation, and separation. Furthermore, the dependencies of micelle dissociation rate on different parameters, i.e. salt concentration, solution temperature, and polyelectrolyte block length, are examined both by experimental data and physical predictions, which are in a good agreement. An analytical expression is further derived to illustrate the relationship between the micelle dissociation rate and a variety of parameters, such as interfacial tension, micelle size, charge block length, and salinity, which can direct the rational design of polyelectrolyte-

based particles in demand.

Together, the efforts in this dissertation contribute to the fundamental understanding of the structures and kinetics in polyelectrolyte complexes, pave the way for researchers to dig into the nonequilibrium phenomena in electrostatic-driven self-assemblies, and provide new paradigms for the rational design of novel materials for a myriad of practical applications.

CHAPTER 1

INTRODUCTION

1.1 Polyelectrolytes and polyelectrolyte solutions

Polyelectrolytes are polymers whose repeat units bear electrolyte groups. Polymers with positively charged groups are called polycations and polymers with negatively charged groups are referred to polyanions. These electrolyte groups can dissociate in polar solvents such as water, releasing counterions into solutions and thus rendering the polymer chains charged. Polyelectrolytes are ubiquitous in nature and have been existing on the Earth even before the birth of life billions of years ago.[1] The advances in synthesis methods have facilitated the research on synthetic polyelectrolytes. A list of important natural polyelectrolyte and synthetic polyelectrolytes can be seen in Table 1.1. Depending on their abilities of releasing counterions, polyelectrolytes can be categorized into weak polyelectrolytes or strong polyelectroltyes. A strong polyelectrolyte is capable of dissociating almost all counterions into solutions with reasonable pH values; a weak polyelectrolyte, by contrast, has a dissociation constant (pK_a) and could only be fully charged in a pH range of 2 to 10.

Understanding the conformation and behaviors of polyelectrolytes in solutions has been a challenging task. Quantitative and theoretical description of the electrostatic mechanism in polyelectrolytes is far from complete, owing to the many variables existing in simple system and the complicated interplay they correlate with each other. Polyelectrolyte solution is a cocktail with various molecular interactions intermingling in one system. For example, consider a single natural polyelectrolyte chain RNA in salty water, as schematized in Figure 1.1.[2] Possible molecular interactions include: (1) long-range electrostatic forces between phosphate groups, counterions, and salt ions; (2) hydrogen binding between the amine groups and water molecules; (3) short-range Van Der Waals interaction among different atoms and molecules; (4) chain connectivity; (5) counterion absorption between the salt ions and the charged groups (6) π-π stacking among aromatic rings; and (7) cation-π interaction between an electron-rich π system and an adjacent cation.[3]

The balance among these interaction forces, synergistically or antagonistically, results in unique characteristics of polyelectrolyte solutions that are unseen in solutions of their

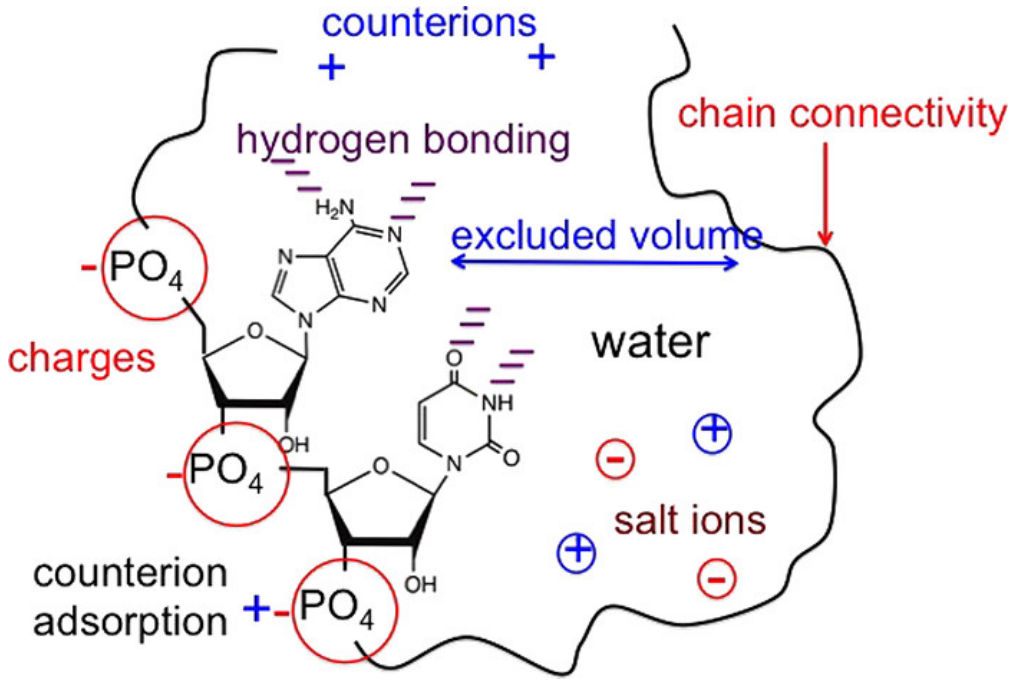

Figure 1.1: Structural complexities in a single RNA molecule. Reprinted (adapted) with permission (Reference 1). Copyright (2017) American Chemical Society

neutral counterparts. For example, the viscosity of polyelectrolyte solutions is proportional to the square root of polymer concentration as $\eta \sim c^{1/2}$,[4] while for solutions of neutral polymers the viscosity is proportional to polymer concentration. X-ray or neutron scattering experiments present a well-pronounced peak in polyelectrolyte solutions, whereas no such peak is observed in solutions of neutral polymers.

1.1.1 Bjerrum length and Debye screening length

There are two fundamental parameters that have significant consequences on the physics of polyelectrolyte solutions: the Bjerrum length, l_B, and the Debye screening length, κ^{-1}. The Bejerrum length is the separation at which the electrostatic interaction energy between two charged monomers are comparable to the thermal energy k_BT, where k_B is the Boltzmann constant and T is the temperature in Kelvin. Consider two charged monomers z_ie and z_je are dispersed in a medium with a dielectric constant ϵ with a distance of r_{ij}, their electrostatic interaction energy, U_{ij} can be written as:

Table 1.1: A list of some important natural and synthetic polyelectrolytes.

Natural polyelectrolyte	**Category**	**Abbreviation**
Nucleic acids	Polyanion	-
Poly (L-lysine)	Polycation	PLL
Poly (L-glutamic acid)	Polyanion	PLGA
Alginates	Polyanion	-
Chitosan	Polycation	-
Cellulose-based	Polyanion or polycation	-
Starch-based	polyanion or polycation	-
Dextran-based	polyanion or polycation	-
Synthetic polyelectrolyte	**Category**	**Abbreviation**
Poly (acrylic acid)	Polyanion	PAA
Poly (allylamine)	Polycation	PAH
Poly (styrene sulphonate)	Polyanion	PSS
Poly (N, N-dimethylaminoethyl methacrylate)	Polycation	PDMAEMA
Poly (diallyldimethyl ammonium chloride)	Polycation	PDADMAC
Poly (vinylbenzyl trimethylammonium)	Polycation	PVBTMA
Poly (N-methyl-2-vinylpyridinium)	Polycation	PM2VP
Poly (ethylene imine)	Polycation	PEI

$$\frac{U_{ij}}{k_{\mathrm{B}}T} = z_i z_j \frac{e^2}{4\pi\epsilon_0\epsilon k_{\mathrm{B}}T}\frac{1}{r_{ij}} \tag{1.1}$$

where e is the electronic charge, z_i is the valency of the ith ion, and ϵ_0 is the permittivity of a vacuum. The Bjerrum length is defined as:

$$l_{\mathrm{B}} \equiv \frac{e^2}{4\pi\epsilon_0\epsilon k_{\mathrm{B}}T} \tag{1.2}$$

It is seen that when the distance between two charges, r_{ij} is close to the Bjerrum length, and thus U_{ij} is on the same magnitude of the thermal energy k_BT. According to the mean-field Poisson-Boltzmann electrostatics, the Debey screening length is the range of electrostatic forces, which is given by:

$$\kappa^{-1} = \left(\frac{e^2}{\epsilon_0\epsilon k_{\mathrm{B}}T}\sum_i z_i^2 n_{i0}\right)^{-1/2} \tag{1.3}$$

where n_{i0} is the average number concentration of the ith ion. The strength of electrostatic

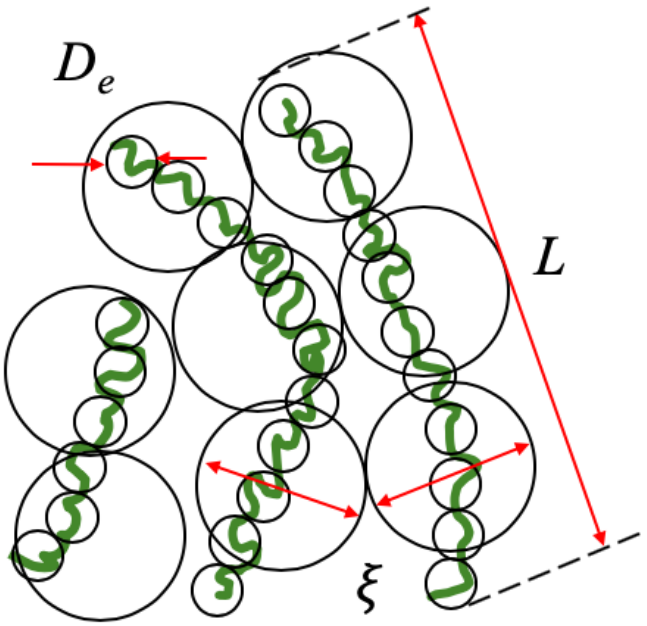

Figure 1.2: Different length scales in a semidilute polyelectrolyte solution.

interations, l_B, its range, κ^{-1}, and the counterion concentration, I, are related by:

$$\kappa^{-1} = \frac{1}{\sqrt{8\pi l_B N_A I}} \tag{1.4}$$

1.1.2 Electrostatic length scales and scaling theory

In 1976, de Gennes et al. generalized the scaling concepts in polyelectrolyte solutions in their seminal work.[5] In dilute polyelectrolyte solutions, where the polyelectrolyte concentration, c, is below the overlap concentration, $c^\star$, the chain conformation is a result of the balance of electronic and entropic parts of free energy of individual chains.[4] An electrostatic blob is an imaginary domain within which the electrostatic interaction does not perturb the chain conformation. The polyelectrolyte chain (a few monomers) behaves just like a neutral polymer in a good solvent. At length scales larger than the electrostatic blob, the polyelectrolyte chains have to adopt a stretched conformation due to the long-range electrostatic repulsion between like-charged monomers. Consider a polyelectrolyte chain with N monomers, f fraction of charged monomers, and a Kuhn length b, some important parameters in the scaling

Table 1.2: Important parameters about the scaling theory of polyelectrolyte solutions.

Lengths	Expression	Physical meaning
g_e	$g_e \approx \left(uf^2\right)^{-2/3}$	number of monomers in an electrostatic blob
D_e	$D_e \approx b g_e^{1/2}$	size of an electrostatic blob with g_e monomers
L	$L \approx D_e \frac{N}{g_e} \approx bN\left(uf^2\right)^{1/3}$	the end-to-end distance of a chain
$c^\star$	$c^\star \approx b^{-3}u^{-1}f^{-2}N^{-2}$	overlap concentration

theory are presented in Table 1.2, including the size of the electrostatic blob D_e, the number of monomers in an electrostatic blob g_e, the size of the chain L, and the overlap concentration $c^\star$.[6, 7, 8]

In semidilute polyelectrolyte solutions where the polyelectrolyte concentration is beyond the overlap concentration, the polyelectrolyte chains start to interact with each other and chain conformation is affected by the spatial filling constraints. The correlation length θ is defined as the distance that two neighboring polyelectrolyte chains can reach at the highest probability, and can be estimated as:

$$\xi \sim b^{-1/3}\left(l_{\mathrm{B}}f^2\right)^{-1/6}c^{-1/2} \tag{1.5}$$

At this length scale, the charges on the polyelectrolyte chains are compensated by surrounding counterions. In average, the net charge of each correlation volume equals to zero, and the polyelectrolyte chain is a random walk of correlation blobs.

1.2 Polyelectrolyte complexes

Polyelectrolyte complexes (PECs) are a major class of macromolecular self-assembled materials based on electrostatic interactions. These materials are usually formed from mixing aqueous solutions of oppositely charged polymeric macroions, where the process is believed to be initiated by electrostatic interactions and facilitated by the entropic gain from the release of counterions. When aqueous solutions of oppositely charged polyelectrolytes mixed, they tend to undergo an associate liquid-liquid phase separation, leading to a polyelectrolyte-rich

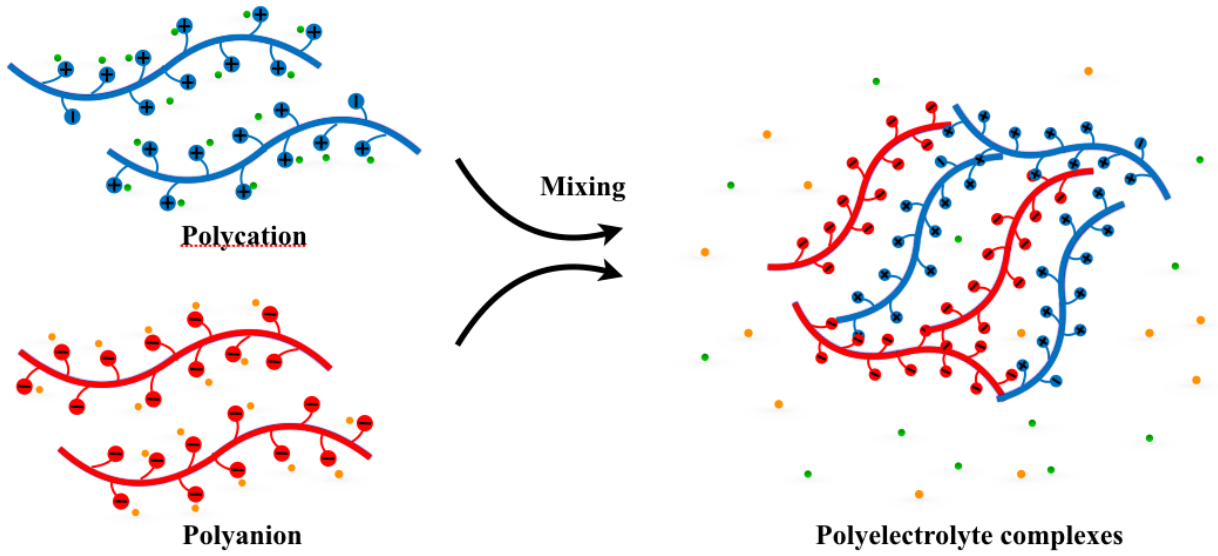

Figure 1.3: Schematic description of polyelectrolyte complexation between oppositely charged polyelectrolytes.

phase called coacervate and a polyelectrolyte-deficit phase called supernatant. Experimentalists have observed the liquid-liquid phase separation in polyelectrolyte-containing systems over eight decades, initially in natural macromolecules. For example, as early as in 1929, Bungenberg-de Jong and Kruyt reported the complexation between a disorder polypeptides, gelatin, and a biologically derived polyelctrolyte, gum arabic.[9] Since then, coacervates and coacervation have been found in a myrid of biological senarios such as intracellular organelles, nucleotide transportation, and RNA condensation.[10, 3, 11, 12] Yet, systematic study on the structure-property relationship of polyelectrolyte complexes have been done using mainly synthetic polyelectrolytes.[13, 14, 15, 16] A common pair is poly (acrylic acid) (PAA) and poly (allylamine) (PAH).

1.2.1 Physics of polyelectrolyte complexation: equilibrium and nonequilibrium

Theorists and simulators have been seeking fine theories and sophisticated algorithms to describe the physics of polyelectrolyte complexation. The first theoretical framework is the

Voorn-Overbeek (VO) theory proposed in the 1960s, which is based on a combination of a Flory-Huggins approximation for the mixing entropy and a Debye-Hückel approximation for the free energy of mixing.[17] Recently, considerable efforts have been taken to consider some important factors that are absent in the VO theory but present in the real world, including phase approximation (RPA),[18, 19, 20, 21, 22, 23] field theoretic simulations,[24, 25] and liquid state theory.[26, 27] For example, RPA considers the finite size and charge connectivity in the description of the electrostatic free energy. Vast disparities from the predictions of the VO theory are revealed by including the excluded volume interactions and non-zero size of the ions. By employing the polymer reference interaction site model (PRISM), Perry and Sing could incorporate the chain connectivity into a modified liquid state theory.[27]

Here, we provide a brief description of the VO theory as a starting point, and continue to introduce some new insights from our group. There are many comprehensive reviews on the advances of theories of polyelectrolyte complexation. Consider a system that comprises of a mixture of polycations and polyanions in a salt-free solution. The free energy, F, can be written as:

$$\frac{l^3 F}{V k_{\mathrm{B}} T} = -\frac{\sqrt{4\pi}}{3}\left(\frac{\ell_{\mathrm{B}}}{l}\right)^{3/2}\left(\sum_i \alpha_i \phi_i\right)^{3/2} + \sum_i \frac{\phi_i}{N_i}\ln\phi_i + \sum_i \sum_{j<i} \chi_{ij}\phi_i\phi_j \qquad (1.6)$$

where l is the lattice size, V is the total volume, l_B is the Bjerrum length, and α_i, ϕ_i, and N_i are the charge density, volume fraction, and chain length of component i, respectively. The first term corresponds to the electrostatic effects described under the Debye-Hückel approximation; the second term is the mean-field entropy of mixing per lattice site; and the last term denotes the nonionic interactions between two or more components. In a situation in which the polcations and polyanions have the same block length N and volume fraction ϕ, and assume the solvent-polymer interactions are negligible compared to electrostatic interaction ($\chi = 0$), the free energy of the VO theory, f_{VO}, is simplified to:

$$f_{\mathrm{VO}} = \frac{\phi}{N}\ln\phi + (1-\phi)\ln(1-\phi) - \frac{(4\pi l_{\mathrm{B}}/l)^{3/2}\,(\sigma\phi)^{3/2}}{12\pi} \tag{1.7}$$

In Equation 1.7, the first term is positive but very small for large N, the second term is always negative, and the third term is positive. When the term $\sigma^3 N$ exceeds a threshold, the mixture of polyions will undergo liquid-liquid phase separation, leading to a polymer-rich coacervate phase and a polymer-deficient supernatant phase.

Despite its simplicity, the VO theory has been found in line with many synthetic polymeric systems.[28, 29, 30] Recently, with a combination of experiments and simulation, Li and coworkers reported new features about the phase behaviors in polyelectrolyte complexes.[31] First, salt counterions are presumably believed to be distributed evenly in the coacervate and supernatant phase; however, they found that salt ions have preferential partitioning into the supernatant phase. Moreover, they demonstrated an interesting self-suppression phenomenon in complexation when the total polymer concentration increases. These new features call for new paradigms to elucidate polyelectrolyte complexation, e.g. more comprehensive theories and advanced computer simulations.

Recently, nonequilibrium physics of polyelectrolyte-based complexes have attracted considerable attention. In fact, nonequilibrium physics is quite common in biological soft matters[32] and is related to the origin of complex behaviors in many biological systems, such as cytoskeletal networks,[33] protein folding,[34] hemostasis,[35], and ribosome assembly.[36] Due to the complexities of the interacting forces and molecular architectures existing in polyelectrolytes, it is not unusual to find that polyelectrolyte complexes are kinetically trapped in nonequilibrium states, leading to unique features that are not accessible in traditional equilibrium states. The study of nonequilibrium physics of soft matter and the employment of kinetic trap to obtaining far-from-equilibrium analogs of polymer gels, liquid crystals and emulsions have made strides.[37, 38, 39, 40, 41, 42, 43] These new characteristics present challenges to bringing in new paradigms and developing a theoretical framework for systematic engineering of desired far-from-equilibrium properties.

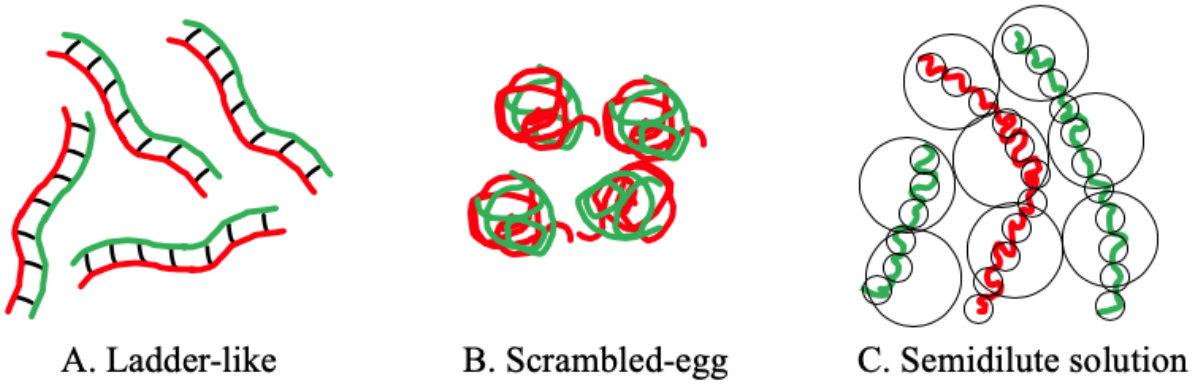

Figure 1.4: Schematic description of three structure models of polyelectrolyte complexes: (A) ladder-like, (B) scrambled-egg, and (c) semidilute solution.

1.2.2 Structure and thermodynamics of polyelectrolyte complexes

Like many other disorder soft matter systems, polyelectrolyte complexes are quite inhomogeneous and their internal structures vary over a spectrum, depending on the characteristics of the components and the external conditions of the reaction. Generally, a borderline can be drawn between three distinct models: (see Figure 1.4) (i) the ladder-like structure resulted from the ionic group pairing on a molecular level, (ii) the scrambled-egg model where globules are formed within the complex phase, and (iii) the semidilute solution where the complexed polyelectrolytes behave like polyelectrolytes in semidilute solutions.[13, 44, 45, 46, 47, 48] So far, there is no definite theory to predict what exact structures form when two polyelectrolytes are mixed. A general rule is that strong polyelectrolytes with high chain rigidity tend to form ladder-like structures, while weak polyelectrolytes are more likely to form structures that are comparable to semidilute polyelectrolyte solutions.[49]

Thermodynamics of the polyelectrolyte complexation phenomenon is represented by the lowering of Gibbs free energy, which is attributed to mainly two aspects: (i) the entropic gain from the release of condensed counterions from the backbones of individual polyelectrolytes, and (iii) the enthalpic change due to the Coulombic attraction between oppositely charged. Isothermal calorimetry (ITC) experiments have revealed that the enthalpic change can be positive or negative, depending on the chemical details of the constituent polymers as well

as external factors like mixing order, solution salinity, and pH value. The entropic gain from counterion release is usually a bigger driver of the complexation process. Its strength is orders of magnitude larger than the loss of freedom caused by the confinement of polyelectrolyte chains in the coacervate domain. Other factors, such as chain hydrophobicity and hydrogen bonding, also play nontrivial roles, and in some cases, their contribution can even surpass that of the correlated electrostatic interactions and lead to rare behaviors. For example, Kim and coworkers reported a like-charged complex coacervate formed by two cationic polyelectrolytes, the electrostatic repulsion between which is overcome by the strong short-range cation-π interactions.[50]

1.3 Surfactant micelles

1.3.1 Background

Surfactant molecules usually contain a hydrophilic head and a hydrophobic tail. In aqueous phases, surfactants form aggregates with cores having the hydrophobic tails and the hydrophilic heads in contact with the surrounding liquids. These amphiphilic surfactant aggregates are named as micelles, a term that is borrowed from biology and widespread by Hartley in his classic book *Paraffin Chain Salts: A Study in Micelle Formation.*[51] Although surfactant micelles are ubiquitous in nature and industry for centuries without noticing, the first report of surfactant micelles in scientific literature could only date back to the 1910s, where speculations of the existence of *colloidal ions* are made to explain the good conductivity in sodium palmitate solutions.[52]

1.3.2 Kinetics of surfactant micelles

One important feature of surfactant micelles is their molecular kinetics in dynamic equilibrium states. Upon formation, the constituent amphiphilic molecules do not stay in the aggregates, but rather escape from and re-enter into the micelles on a time scale of nanosec-

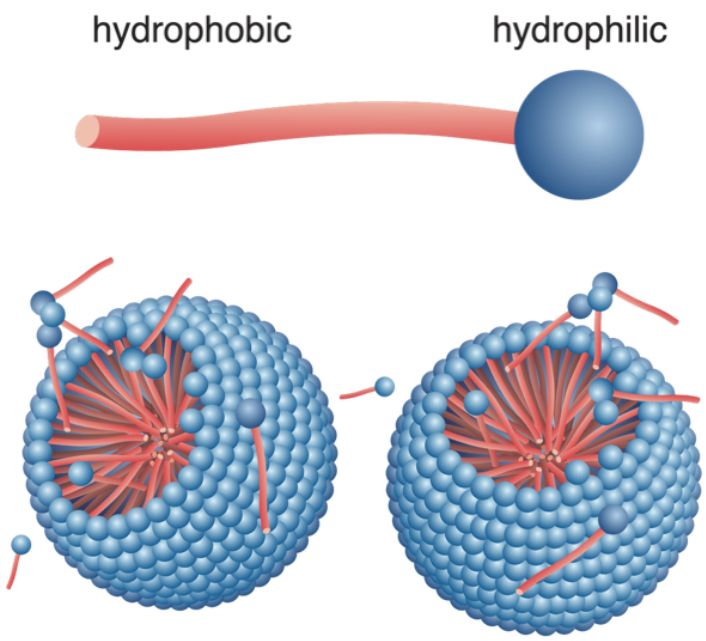

Figure 1.5: Schematic picture of the components of a surfactant amphiphilic molecule and the morphology of a spherical surfactant micelle.

onds to microseconds. Theoretical description of the kinetic pathways is first proposed by Aniansson and Wall in the 1970s, where two primary mechanisms are considered: (1) a stepwise chain expulsion/insertion mechanism and (2) a collective micelle fusion/fission mechanism.[53, 54, 55] Light scattering studies have revealed that the molecular exchange kinetics in surfactant micelles are basically governed by these two mechanisms: a fast mode of unimer expulsion/insertion and a slow mode of micelle fission/fusion.[56, 57, 58, 59, 60, 61] These traits play important roles in practical applications such as detergents, emulsion, and surface coating.

1.4 Amphiphilic block copolymer micelles

Amphiphilic block copolymers are macromolecules made of two or more chemically distinct polymer chains that have various affinities for different solution environments. These materials tend to spontaneously self-assemble into nanostructures when dispersed in a selective solvent that favors selective solvation of one block and/or selective aggregation of one block.

Duo to the interplay among many attributes, a broad range of morphologies have been reported, including spheres, rods, cylinders, double-layered sheets. Spherical core-corona nanostructures is the most common and most studied one, where the solvophobic blocks aggregate and form the core while the other block constitutes the corona. Block copolymer micelles are revealed to be kinetically frozen or the exchange is too slow to measure in most cases, especially in polar solvents like water.[62, 63, 64, 65, 66, 67, 68] This stark contrast has attracted great interest because the chain exchange is highly relevant to the micelle formation and dissociation, the dynamics that determine micelle size, morphology, stability, and their drug encapsulation and delivery effectiveness. The kinetic frozen state of the micelle also partially explains the existence of various micellar morphologies, as many of them are not in equilibrium states. This self-assembly phenomenon is quite common in biological systems and has been extensively employed to build polymeric nanocapsules for a myriad of biomedical applications due to their favorable properties, including enhanced biocompatibility and prolonged circulation time in vitro and in vivo.[69, 70, 71, 72] Thus, revealing the fundamental mechanism of the chain exchange process will be essential to not only facilitate the fundamental understanding of the self-assembling phenomenon, but also provide essential directions for advancing technological applications in nanomedicine and its allied fields. For example, in drug delivery, Alexis and co-workers have identified how the clearance and biodistribution of polymeric nanoparticles are highly related to size and structural properties.[73]

1.4.1 Kinetics in amphiphilic block copolymer micelles

Inspired by Aniansson and Wall, in the late 1980s, Halperin and Alexander developed a theory to describe the chain exchange kinetics in synthetic polymeric micelles.[74] They claimed that the single chain expulsion/insertion mechanism is dominant, and the micelle fission/fusion is energetically unfavorable due to the osmotic repulsion between macromolecular micelle coronas. In the 1990s, Halperin, Tirrell, and Lodge further discussed the residence

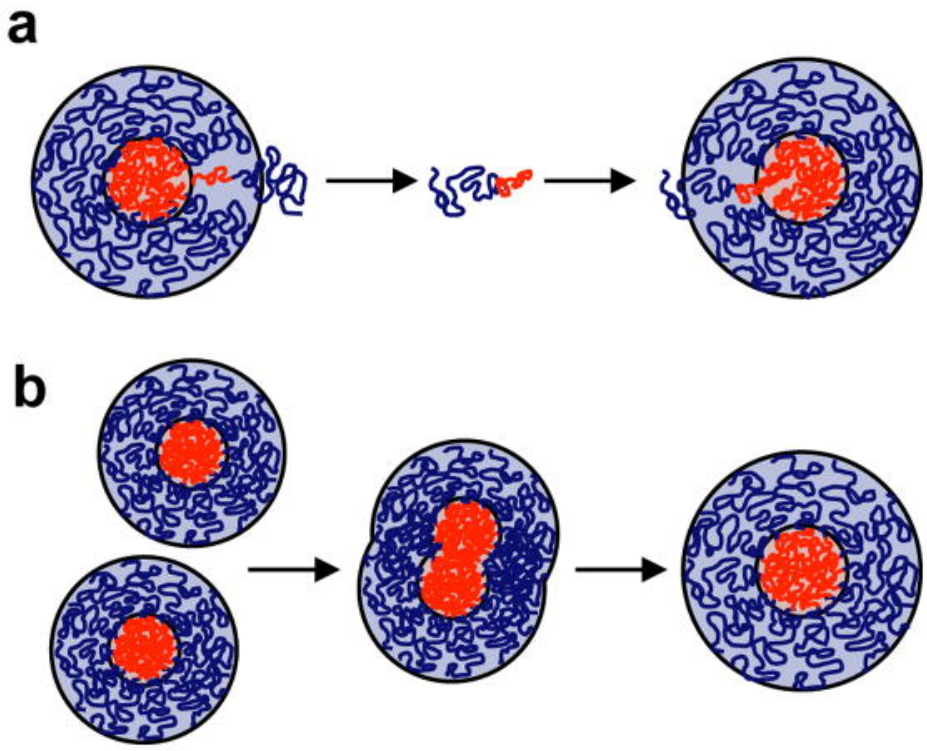

Figure 1.6: Two kinetic pathways of molecular exchange in amphiphilic block copolymer micelles.

time of the single chain expulsion and its strong molecular weight dependence, and extended the theory into tethered polymer chains, including highly branched polymers and end-grafted chains on surfaces.[75] Later, Dormidontova theoretically predicted that micelle fission is a slow process at equilibrium states but plays a major role when micelles re-equilibrate from a disturbed perturbation (such as during T-jump experiments).[76] Despite the abundance of insights from theoretical works, experimental investigation of the chain exchange kinetics has remained scarce due to the lack of appropriate methods and various limitations of different techniques.

1.5 Polyelectrolyte complex micelles

Polyelectrolyte complex micelles form when oppositely charged block polymers are mixed together in aqueous media. The charged blocks electrostatically associate and phase separate,

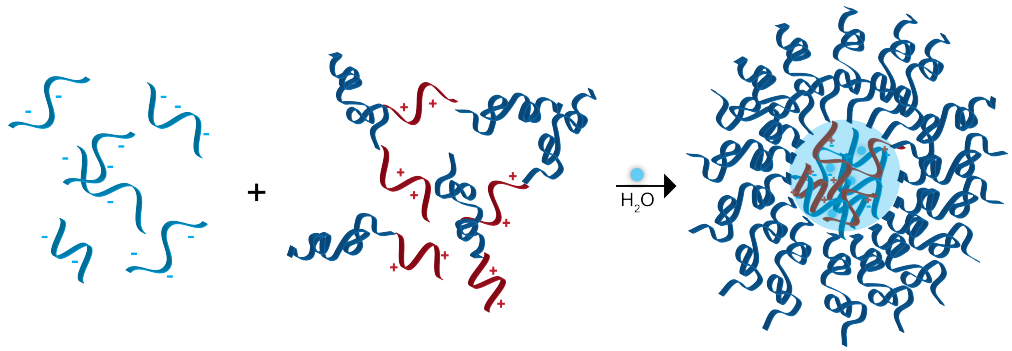

Figure 1.7: Schematic representation of the Formation of a polyelectrolyte complex micelle by negatively charged homopolymers and positively charged diblock copolymers.

leading to a dense, polymer-rich core stabilized by a neutral block corona. Often, these electrostatic self-assemblies are termed polyelectrolyte complex (PEC) micelles, coacervate complex core micelles (C3Ms),[77] or polyion complex micelles (PIC).[78] The comparatively strong ionic interactions between the oppositely charged blocks, the conservation of a large amount of water in complex domains (ca. 30-90 wt %), and the responsiveness to external stimuli (e.g., pH or ionic gradients) confer this type of material versatility for a range of biomedical applications, including tissue growth scaffolds, therapeutics encapsulation and delivery, and bio-adhesives.

Despite the sharp contrast between the driving forces, PEC micelles have been understood in an analogous way with ABC micelles. The structural evolution of PEC micelles over a range of polymer concentration is proceed in a similar way with their counterparts formed by neutral polymers. That is, increasing the polymer concentration of the PEC micelle solutions from moderate to high (ca. 5-40 wt %) led to the structural evolution of the phase-separated complex domains transitioning from disorder arrays to body center cubic lattice and further to hexagonally packed cylindrical morphologies.[79]

1.5.1 Emerging applications of PEC micelles: nucleic acid delivery

Cationic polymers constitute a major class of non-viral gene delivery vectors that hold potential for enabling site-specific delivery of novel therapeutics to intracellular targets. These

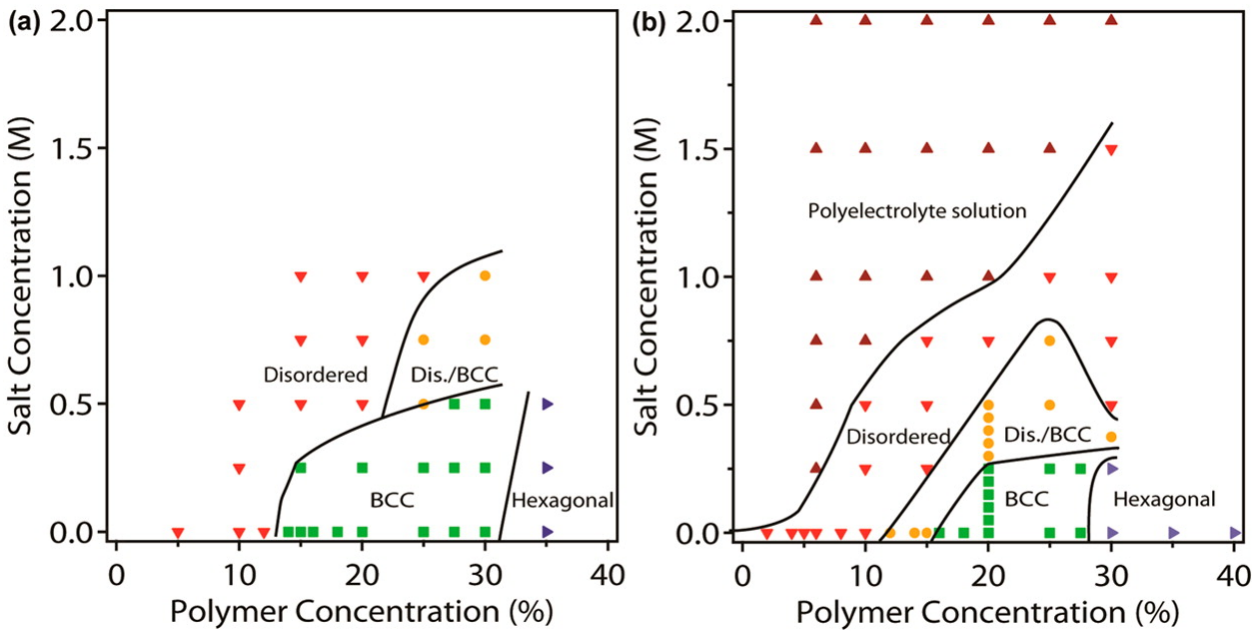

Figure 1.8: Phase diagrams showing the structural evolution of the polyelectrolyte complex micelles formed by two symmetric diblock copolymers (a) and two triblock copolymers (b), when varying the polymer concentration and salt concentration. Reprinted (adapted) with permission (Reference 14). Copyright (2016) American Chemical Society

positively-charged macromolecules can condense large nucleic acids into small nanostructures and neutralize the negatively-charged moieties on the nucleic acid chains, protecting them from potential enzymatic degradation and promoting successful transfection into various cell types. The resulting endocytosed polyplex micelles are sensitive to biologicallypertinent environmental settings, such as ionic strength, temperature, pH, etc., which influence the structure and stability of the compartmentalized nucleic acid. This can even be exploited to disrupt the micelles on-demand in a controlled manner.

The concept of nanomedicine has been coined for over decades. The biggest hurdle of its prevalence may lie on the discovery of constituent materials with effectiveness and safety.[80] In order to reach its full function, a nanocarrier has to circumvent a chain of obstacles and accomplish a series of tasks, which include (i) entering circulation or target tissue, (ii) avoiding excretion, (iii) avoidance of nuclease degradation, (iv) escape of immune recognition, (v) extravasation, (vi) cellular uptake, and (vii) endosomal release. These complexities combined present a very daunting challenge for nanoparticle

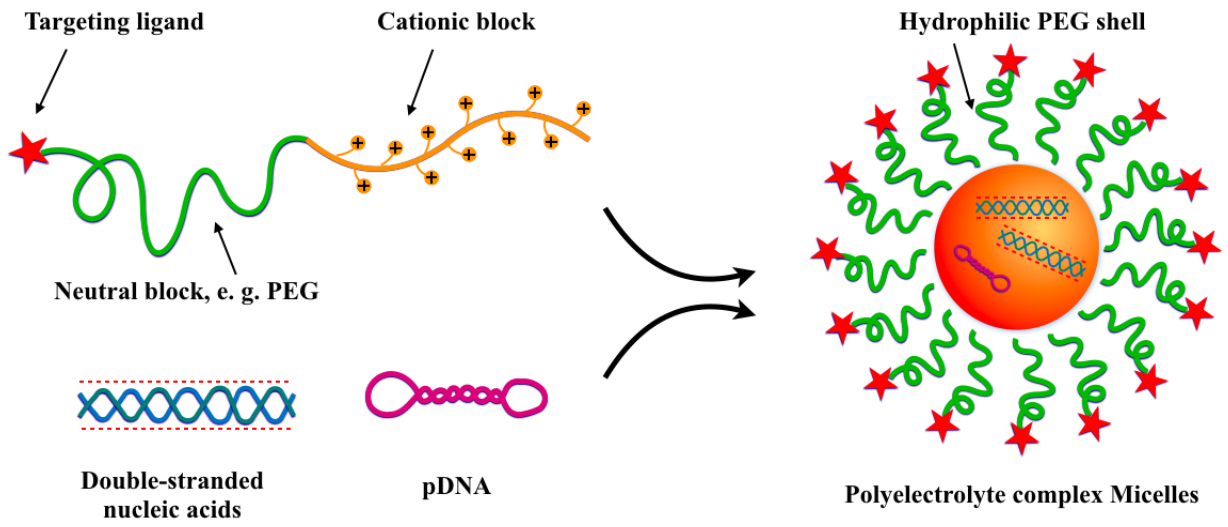

Figure 1.9: Schematic representation of the design strategies for polyelectrolyte complex micelles as nucleic acid delivery vehicles.

formation.[81, 82, 83, 84, 85, 86, 87, 88, 89] A variety of nanoscale materials have been developed, including virus, brush polymers, dendrimers, polymeric micelles, stable nucleic acid-lipid particles, liposomes, and metal/inorganic particles.[90] Among them, polyelectrolyte complex micelles based on complexation between biocompatible cationic polymers and negatively charged nucleic acids are a promising candidate and have shown excellent results both *in vitro* and *in vivo* experiments.[80, 91, 92] PEC micelles can overcome most of the challenges by incorporating versatile functionalities. For example, PEG blocks are commonly used to form the shell of the PEC micelles, preventing the nuclease degradation and immunological responses and prolonging the circulation time. The periphery of PEC micelles is often covalently linked to cell or tissue targeting ligands to increase transfection efficacy. However, challenges still remain. When nanoparticles are internalized by endocytosis, they are encapsulated in endosomes. Efficient gene transfer entails nanoparticle escape from endosomes, the so-called endosomal escape. However, Researchers still do not understand its exact mechanism.[93, 94, 95, 96]

Table 1.3: A list of light scattering techniques.

Source	Light	X-ray	Neutron
Dynamic	DLS	XPCS	NSE
Static	SLS	SAXS	SANS

1.6 Experimental techniques

When it comes to the characterization of matters, a variety of experimental techniques have been commonly employed in chemical laboratories all across the globe. Like the way living creatures explore the world, the very basic idea is to extract the desired information out of noise, i.e. the *contrast*. Variations in electron density of matters are employed by many experimental techniques, including light scattering and electron microscopy. Light scattering and electron microscopy are two complementary techniques to get structural information about materials. Light scattering techniques provide convoluted information in reciprocal space, while electron microscopy usually provides information for individuals in real space. Generally, it is relatively easy to prepare samples for light scattering experiments but hard to interpret data. In contrast, for electron microscopy experiments, sample preparation is hard but data interpretation is not too difficult. Light scattering techniques include static light scattering (SLS), dynamic light scattering (DLS), X-ray scattering, and neutron scattering, and electron microscopy includes surface electron microscopy (SEM), transmission electron microscopy (TEM), cryogenic transmission microscopy (cryo-TEM), and flow-cell electron microscopy. For light scattering techniques, depending on the ways they collect information, they can be divided into subgroups of dynamic or static. The dynamic subgroup includes DLS, X-ray photon correlation spectroscopy (XPCS), and neutron spin echo (NSE). The static subgroup includes SLS, SAXS, and SANS. Here, we briefly introduce DLS, SAXS, and SANS, the three experimental techniques that are frequently employed in this research.

1.6.1 Dynamic light scattering

Fundamentals of DLS. Small Objects change the direction of light when they are hit by photons. This phenomenon is called light scattering in optics. Dynamic light scattering (DLS) employs measurement of the light scattering intensity at very short time intervals (e.g. 200 ns). DLS is a crucial technique to get a quick determination of the size and size distribution, morphology, and scattering intensity on nanoparticle samples in the range of 1 to 100 nm. It is accessible to most chemical laboratories and can provide first insights on the structures of the scattering objects. These quantitative information are useful to decide if further in-depth characterizations are needed. In the domain of micelle study, DLS is widely employed to determine their size, size distribution, and diffusion coefficients.

The following summarizes DLS analysis based on scattering theory outlined in Hiemenz and Lodge. The scattering wave vector (q) is defined by:

$$q = \frac{4\pi n}{\lambda} \sin\left(\frac{\theta}{2}\right) \tag{1.8}$$

where λ is the wavelength of the incident light, n is the refractive index of the solution, and *theta* is the angle between the incident and scattering laser. The fluctuation of electric filed generated by the ensemble collection of solution particles under Brownian diffusion can be expressed using a field autocorrelation function:

$$G_1 = \int_0^\infty E(t)E(t+\tau)d\tau = exp^{-\mathrm{D}q^2\tau} \tag{1.9}$$

where E is the electric field, τ is the delay time, and D is the diffusion coefficient. The experimentally measured intensity correlation function (G_2) is equivalent to the actual electric field autocorrelation (G_1) through the Seigert relationship:

$$G_2(\tau) = 1 + \gamma G_1(\tau) \tag{1.10}$$

where γ is a coherence factor indicating the efficiency of the photo collection system.

The hydrodynamic radii of scatters under Brownian diffusion can be calculated via Stokes-Einstein relationship given by:

$$R_{\mathrm{h}} = \frac{k_{\mathrm{B}}T}{6\pi\eta D} \tag{1.11}$$

where k_B is the Boltzmann constant, T is the absolute temperature, and η is the viscosity of the solution (here as taken that of water). The diffusion coefficient D and polydispersity index were extracted by fitting intensity correlation functions to a 2^{nd} order-expanded single exponential in:

$$G_2 = A\left[1 + B\exp\left(-2\Gamma\tau + \mu_2\tau^2\right)\right] \tag{1.12}$$

where A is the amplitude or intercept of the correlation function, B is the baseline, Γ is the decay rate, and μ_2 is proportional to the distribution width. The diffusion coefficient and polydispersity index (PDI) are respectively expressed as:

$$D = \frac{\Gamma}{q^2} \tag{1.13}$$

$$PDI = \frac{\mu_2}{\Gamma^2} \tag{1.14}$$

where σ is the standard deviation of a hypothetical Gaussian distribution centered on $\mathrm{R_h}$.

Requirements and limitations. There are a few requirements and limitations about dynamic light scattering. Before conducting an experiment, one should, first, make sure that the sample solution is completely transparent (Turbidity will cause errors by multiple scattering); second, make sure the sample does not absorb light of the wavelength used; third, the concentration of the sample should be high enough; forth, the sample in solution should be thermodynamically stable, and last but not least, the molecules in solution should

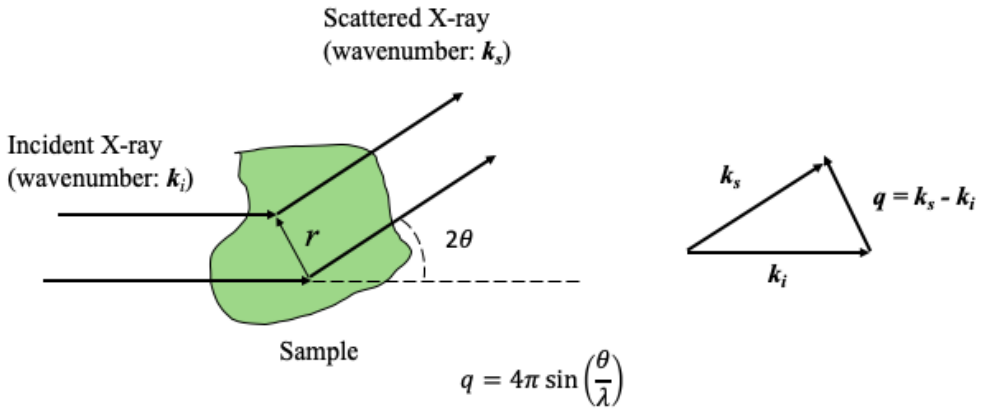

Figure 1.10: Schematic picture showing a incident X-ray scattered by a piece of material and the definition of the scattering vector.

have a different refractive index from that of the solvent.

1.6.2 Small-angle X-ray scattering

Basics of SAXS. X-ray scattering probes structural information at nanometer length scales by generating contrast from variation of electron density in matters. SAXS have been widely used to study size, shape, and interactions of matters with the spatial resolution of 10 to 1000 Å. Unlike electron microscopy, which provides real space information, x-ray scattering creates reciprocal space data. When a X-ray beam radiate a piece of matter, X-ray photons interact with the outer part of the electronic cloud of an atom, and the interaction of radiations is characterized by a scattering length b_i, and its density $\rho(r)$ as $\rho(r) = \sum \rho_i(r) b_i$ with $\rho_i(r)$ being the local density of scatterers of type i. The spatial information is converted into the scattering vector $\mathbf{q}$ with a modulus of $q = 4\pi \sin(\theta)/\lambda$.

An archetypal X-ray beamline setup can be represented by Figure 1.11.[97] A sample is placed between a beam source and a 2-dimensional area beamstop. The beam source is calibrated by slits before it heats the sample. At least two monitors, m_1 and m_2, are installed. The upstream beam monitor, m_1, calibrates the variations from the incident flux, and the downstream beam monitor, m_2, normalizes the transmittance of the sample. The

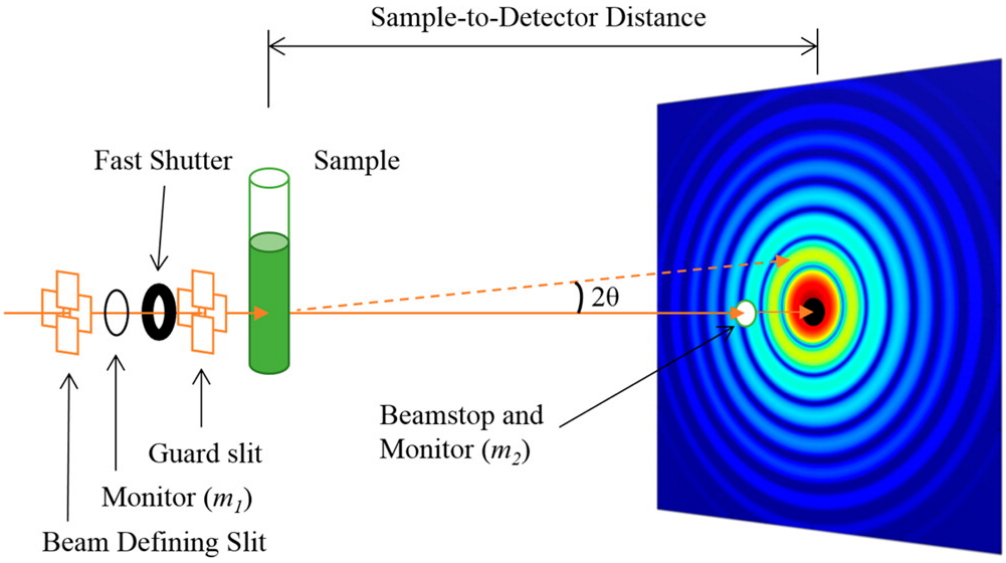

Figure 1.11: A sketch of the optical components of a SAXS beamline. Reprinted (adapted) with permission (Reference 26). Copyright (2016) American Chemical Society

2D area detector is used to collect the elastically-scattered photons. The photon count value on each pixel of the 2D detector after the normalization by the downstream monitor, m_2, is defined as the total scattering intensity I as $I \equiv \frac{J}{m_2}$. The pure scattering intensity of the sample can be further calculated by subtracting the photons scattered by the sample container and solvent from the total scattering intensity.

Data analysis. Typically, SAXS can provides two aspects of structural information: (1) the mean morphological properties of individual particles, which is represented by a form factor $P(q)$, and (2) the positional correlation of the particle that contains in the term of $S(q)$. For N identical particles dispersed in an radiated volume V, the scattering intensity if given by:

$$I(q) = \frac{N}{V} \left[\rho(r) - \rho_0\right]^2 V_p^2 P(q) S(q) \tag{1.15}$$

where V_p is the volume of each particle, and $\rho(r)$ and ρ_0 are the scattering length densities of the particles and medium, respectively. The form factor $P(q)$ is defined as:

$$P(q) = |A(q)|^2 = \left| \frac{1}{V_P} \int \rho(r) e^{-iqr} dr \right|^2 \tag{1.16}$$

where $A(q)$ is the amplitude of scattering X-ray and is the Fourier transform of a particle's electron density. For the simplest case where the particles are perfectly spheres whose center of mass is at the origin with radius R, the form factor is written as:

$$P(q) = [\rho(r) - \rho_0]\, V_{\mathrm{P}} \frac{3(\sin(qR) - qR\cos(qR))}{(qR)^3} \tag{1.17}$$

For dilute solutions, the interparticle correlation, $S(q)$, is usually neglected as the relative positions of the particles are random. Yet, when particles come close, their relative positions are no longer random due to some forces between them, like electrostatic interactions, and the $S(q)$ is defined as:

$$S(\boldsymbol{q}) = \frac{1}{N_{\mathrm{p}}} \left| \sum_{l=1}^{N_{\mathrm{p}}} \mathrm{e}^{-\mathrm{iqr}_l} \right|^2 \tag{1.18}$$

where r_l is the position of particle r.

There may be three ways to calculate $S(q)$. The first one is using the equation of definition above. Yet, it is obviously seen that the positions of particles in solutions are not practically identifiable. The second and third method are applied for isotropic spheres with proper approximations. The second way is to extract $S(q)$ from I(q) using the relatioship $S(q) = \frac{I(q)}{P(q)}$. It is based on a few assumptions: (i) all particles are identical, (ii) the particles intrinsic properties, such as size and shape, are independent with their positions and number density in solutions, and (iii) no extra interparticle interactions emerge when the particle concentration increases. The third way is to find out the type of interparticle force using radial density function, $g(r)$, and Ornstein-Zernike approach. For N identical spherical particles, $S(q)$ is expressed as:

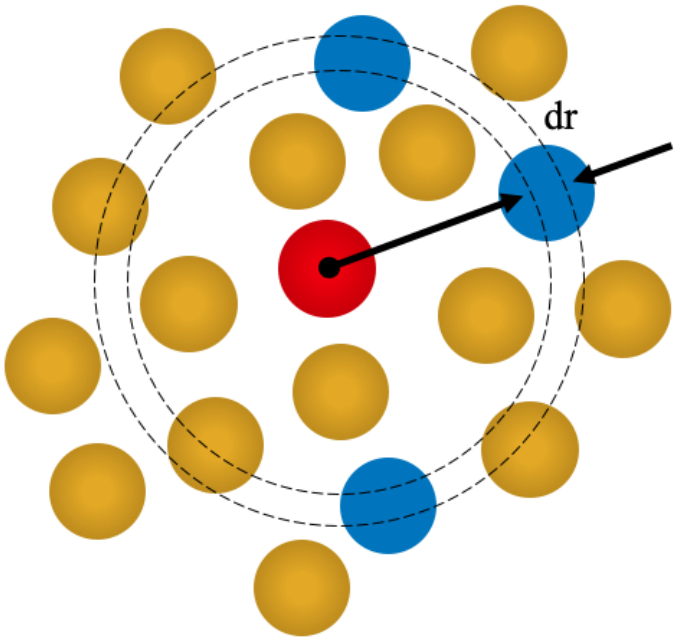

Figure 1.12: Schematic representation of the radial density function g(r).

$$S(q) = 1 + N \int (g(r) - 1) \left(4\pi r^2\right) \frac{\sin(qr)}{qr} \mathrm{d}r \tag{1.19}$$

where $g(r)$ denotes the probability of finding a particle at a distance of r away from a reference particle. As depicted in Figure 1.12, the blue particles are those which are within the circular shell as dotted in orange. $g(r)$ is related to the interparticle interaction potential $U(r)$ as follows:

$$g(r) = \frac{U(r)}{k_B T} \tag{1.20}$$

where k_B is the Boltzmann constant and $U(r)$ represents the many-body contributions. In Ornstein-Zernike approach, the $S(q)$ is written as:

$$S(q) = \frac{1}{1 - N/V c(q)} \tag{1.21}$$

where $c(q)$ is the direct correlation function denoting the direct interactions between the

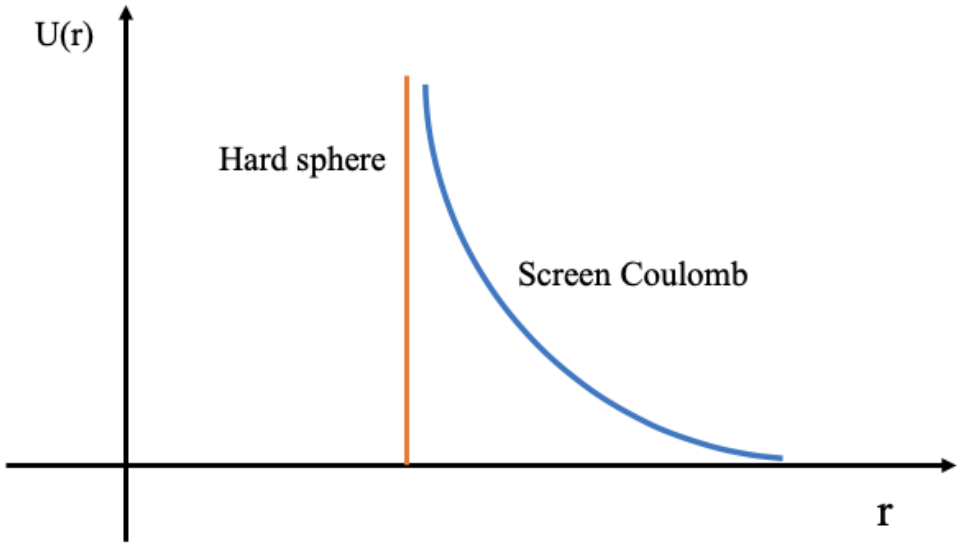

Figure 1.13: Representation of two interparticle interaction potentials.

pair of interacting particles. The Ornstein-Zernike equation can be solved using closure relations, which describes the relationship between $U(r)$ and $c(r)$. For examples, the hard sphere potential is used with the Percus-Yevick closure relation and the screened Coulomb potential is used with the Mean Spherical Approximation. The profiles of the hard sphere potential and screened Coulomb potential are depicted in Figure 1.13.

In many cases, scatterers are not spheres. It is difficult to split the form factor and structure factor; however, the power laws of the different regions on the I(q) versus q curve can provide important information. For example, consider a scattering curve shown in Figure 1.14, the whole curve can be divided into four regions: interparticle region at low q range, Guinier region, Porod region, surface fractal region, and high q region of inter-atomic structures. The very low q region contains the information about interparticle interactions among scatterers. The Guinier region is where the radius of gyration, R_g, can be extracted using:

$$I(q) = I_0 \exp\left(-\frac{q^2 R_g^2}{3}\right) \tag{1.22}$$

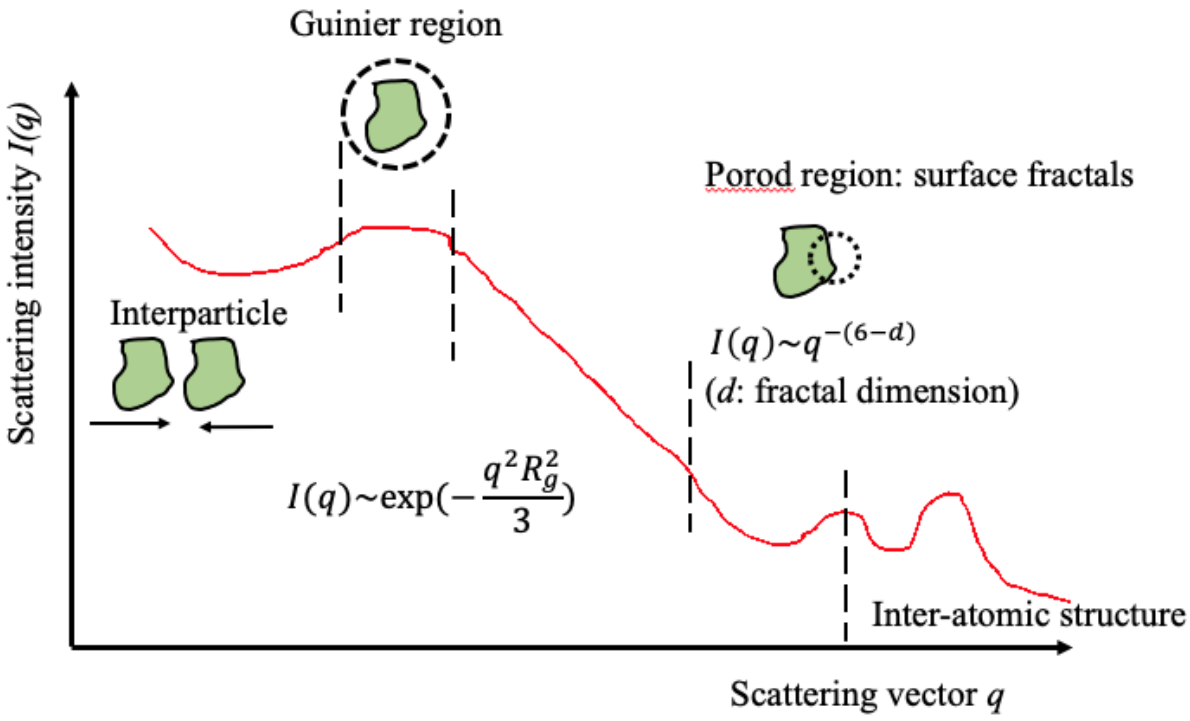

Figure 1.14: Representation of two interparticle interaction potentials.

where I_0 is the absolute intensity obtained by extrapolating q to zero. At the Porod region, the dimension of the surface fractals can be determined from the Porod exponent, n, by:

$$I(q) \propto q^{(-n)} \tag{1.23}$$

The Porod law describes the relationship between the slope of the plot (ln[I(q)] versus ln[q]) and fractal dimension of the scattering objects. For 1-dimensional objects like rods and cylinders, the exponent is 1. For 3-D objects such spheres with smooth surfaces, n equals to 4. A slope of -2 represents a signature of Gaussian chains in a dilute solution.

1.6.3 Small-angle neutron scattering

In many ways, neutron scattering operates in a very similar way as X-ray scattering, except for the incident light source. SANS also represents a powerful technique to study structural

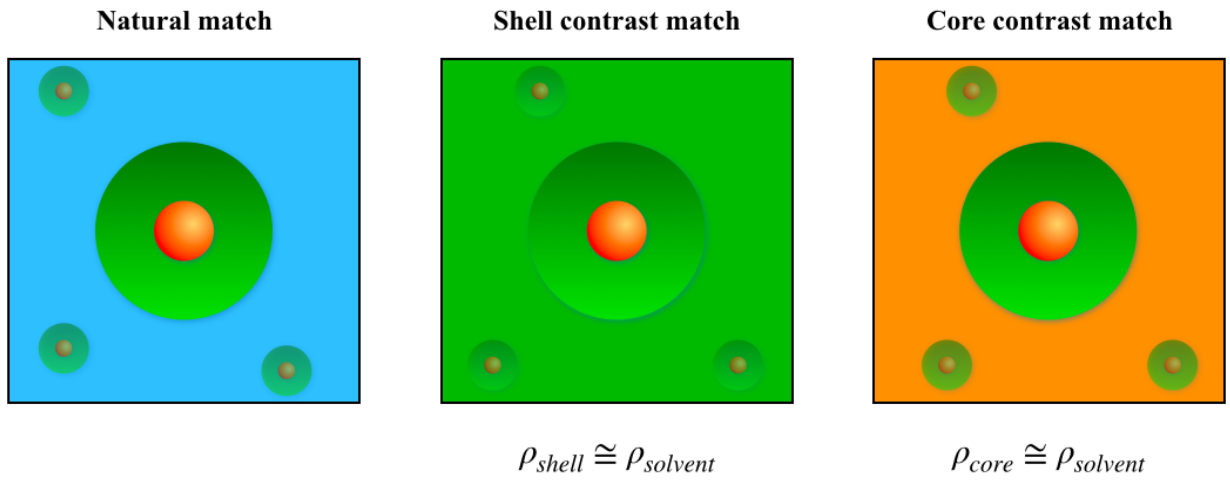

Figure 1.15: Three contrast matching strategies employed in neutron scattering.

information with a nanometer resolution. However, SANS possesses many advantages over SAXS. First, due to the low flux and low affinity, SANS is non-invasive and is unlikely to cause beam damage to samples. Second, the neutron contrast for most soft matters is large, whereas the electron density variation is usually small. Third, hydrogen and deuterium have very different neutron scattering length densities, which can be used to selectively match out certain components by hydrogen/deuterium substitution chemistry. For the study of polymeric micelles, SANS is a powerful tool to investigating the size of micelle core and the thickness of micelle shell by constrat matching.[98] As shown in Figure 1.15, if the scattering length density of the solvent matches either that of the shell or core ($\rho_{shell} \cong \rho_{solvent}$ or $\rho_{core} \cong \rho_{solvent}$), the scattering from the pure shell or core can be measured without any interference terms. In Reality, there are many other considerations should be taken into account, such as the density gradient. Pedersen and Schurtenberger have developed versatile expressions based on off-lattice Monte Carlo simulations for various geometries. Details can be found in these references.[99, 100]

1.7 Aim of this research

So far, most research has focused on the static structure-property relationship of polyelectrolyte complexes. Issues about the kinetics and dynamics in polyelectrolyte-based bulk or nanoscale self-assemblies at nonequilibrium states have been rarely investigated. Thus, there is a long list of unanswered questions regarding the kinetics of polyelectrolyte complexes and PEC micelles, which are crucial to understand the origin of complexities of ionic systems. What are the deterministic factors in the polyelectrolyte complex formation? What are the kinetic pathways? What intermediate structures exist at nonequilibrium states? What the effect of mixing protocols on the formation of the polyelectrolyte complexes? For PEC micelles, how does electrostatic force affect the spatial fillings of PEC micelles in solutions? To what extent the micelles can compress when they collide? What is the mechanism of formation kinetics of PEC micelles? What is the morphological transformation during micelle formation or dissociation? At near equilibrium states, do PEC micelles exchange polymer chains with their surroundings? If yes, in which kinetic pathway? How fast is the process? And what are the affecting parameters?

This thesis attempts to answer the above questions about the structure evolution and kinetic pathways in polyelectrolyte complexes and polyelectrolyte complex micelles.

1.8 Outline of this thesis

The main body of this thesis contains 6 chapters. Each chapter focuses on a different aspect of polyelectrolyte-based self-assemblies. We start from the design of polyelectrolytes, proceed to the creation of polyelectrolyte self-assemblies from these polyelectrolytes, and end with the dissociation of polyelectrolyte self-assemblies back to individual polyelectrolyte. Through this order, the physics of the birth, evolution, and death of non-equilibrium polyelectrolyte complexes are studied.

In **Chapter 2**, we explore the non-equilibrium phenomena and kinetic pathways in poly-

electrolyte complexes. First, we design and synthesize a model polyelectrolyte system that can form either kinetically trapped aggregates or near-equilibrium nanoscale self-assemblies. The origin of morphological complexities formed by self-assemblied polyelectroltye complexes are further discussed. Second, we design two experimental protocols to access and study the intermediate metastable structures during the morphological transformation, by a combination of techniques including small-angle X-ray scattering, light scattering, and cryo-TEM. A distinct two steps are observed in the structural evolution: a fast one corresponding to the breakdown of interconnected transient networks and a slow one characterizing the redistribution of the individual self-assemblies.

In **Chapter 3**, we consider the interparticle interaction among polyelectrolyte complex micelles at a low polymer concentration range, in which intra-particle interactions are rarely determined. We rise to question the accuracy of Guinier approximation in the determination of the radius of gyration for nanoparticles, a way that is widely used in and borrowed indiscriminately from micelles formed by neutral polymers. Then, by employing SAXS and modeling, we attempt to reveal the response of micelle coronas when two micelles come to close.

In **Chapter 4**, we present the first work on the study of nonequilibrium self-assembly kinetics of polyelectrolyte complexes at a temporal resolution of milliseconds. We first design and build experiments that are suitable for multi-component mixtures on synchrotron X-ray beamline with stopped-flow setups for the *in situ* observation of superfast dynamic processes in soft matter systems. Structural evolution of the polyelectrolyte aggregates is monitored

In **Chapter 5**, we explore the molecular exchange in polyelectrolyte complex micelles, which is crucial to understanding many kinetic behaviors in ionic systems. we present the employment of time-resolved small-angle neutron scattering (TR-SANS) technique to assess the chain exchange rate in polyelectrolyte complex micelles in aqueous solutions. The aim is to explore the dependency of the molecular exchange rate on polymer block length, system temperature, and solution salinity. We anticipate these findings would provide fundamen-

tal insights on the origin of morphological complexities and nonequilibrium phenomena in polyelectrolyte-based self-assemblies.

In **Chapter 6**, the dissociation kinetics of PEC micelles triggered by salt jump is investigated by time-resolved static light scattering. Unlike formation kinetics, the time scale of PEC micelle dissociation ranges from minutes to hours. We monitor the temporal evolution of light scattering after a sudden elevation of solution concentration, which is translated to the decrease of the micelle aggregation number using a compressed exponential model. Moreover, we develop a theoretical framework that can describe the micelle dissociation as a three-staged process. Our experimental data is in good agreement with the model's predictions. We also derive an analytical expression to demonstrate the dissociation rate as a function of the polymer block length, solvent temperature, and solution salt concentration.

In the final chapter, we discuss how our findings in the previous chapters have contributed to the fundamental understanding of the structures and kinetics of electrostatic driven self-assemblies. We will discuss open questions and new paradigms discovered by our research.

References

[1] C. P. Brangwynne and A. A. Hymann. *Nature*, pages 524–525.

[2] M. Muthukumar. 50th Anniversary Perspective: A Perspective on Polyelectrolyte Solutions. *Macromolecules*, 50(24):9528–9560, 2017.

[3] Clifford P. Brangwynne, Peter Tompa, and Rohit V. Pappu. Polymer physics of intracellular phase transitions. *Nat. Phys.*, 11:899–904, 2015.

[4] Andrey V. Dobrynin and Michael Rubinstein. Theory of polyelectrolytes in solutions and at surfaces. *Prog. Polym. Sci.*, 30(11):1049–1118, 2005.

[5] P. G. de Gennes, P. Pincus, R. M. Velasco, and F. Brochard. *J. Phys. (Paris)*, pages 1461–1473.

[6] Pierre-Gilles de Gennes. Cornell University Press, 1979.

[7] H. Schiessel and P. Pincus. Counterion-condensation-induced collapse of highly charged polyelectrolytes. *Macromolecules*, 31(22):7953–7959, 1998.

[8] H. Schiessel. Counterion condensation on flexible polyelectrolytes: dependence on ionic strength and chain concentration. *Macromolecules*, 32(17):5673–5680, 1999.

[9] Kruyt H. R. de Jong, Bungenberg. *Proc. Acad. Sci. Amsterdam*, 32:849–855, 1929.

[10] Anthony A. Hyman, Christoph A. Weber, and Frank Jülicher. Liquid-Liquid Phase Separation in Biology. *Annu. Rev. Cell Dev. Biol.*, 30(1):39–58, 2014.

[11] Jarrett Smith, Deepika Calidas, Helen Schmidt, Tu Lu, Dominique Rasoloson, and Geraldine Seydoux. Spatial patterning of P granules by RNA-induced phase separation of the intrinsically-disordered protein MEG-3. *Elife*, 5:1–18, 2016.

[12] Jeffrey R. Vieregg, Michael Lueckheide, Amanda B. Marciel, Lorraine Leon, Alex J. Bologna, Josean Reyes Rivera, and Matthew V. Tirrell. Oligonucleotide-peptide complexes: Phase control by hybridization. *J. Am. Chem. Soc.*, 140:1632–1638, 2018.

[13] Burkart Philipp, Herbert Dautzenberg, Karl-Joachim Linow, Joachim Kötz, and Wladimir Dawydoff. Polyelectrolyte complexes recent developments and open problems. *Prog. Polym. Sci.*, 14:91–172, 1989.

[14] Jasper van der Gucht, Evan Spruijt, Marc Lemmers, and Martien A. Cohen Stuart. Polyelectrolyte complexes: Bulk phases and colloidal systems. *J. Colloid and Interface Sci.*, 361:407–422, 2011.

[15] Jasper van der Gucht, Evan Spruijt, Marc Lemmers, and Martien A. Cohen Stuart. Polyelectrolyte complexes: Bulk phases and colloidal systems. *J. Colloid Interface Sci.*, 361:407–422, 2011.

[16] V. S. Meka, M. K. G. Sing, M. R. Pichika, S. R. Nali, V. R.M. Kolapalli, and P. Kesharwani. A comprehensive review on polyelectrolyte complexes. *Drug Discov. Today*, 22:1697–1706, 2017.

[17] J T Overbeek and M J Voorn. Phase separation in polyelectrolyte solutions; theory of complex coacervation. *J. Cell. Physiol.*, 49:7–22, 1957.

[18] V. Y. Boryu and I. Y. Erukhimovich. A Statistical Theory of Weakly Charged Polyelectrolytes: Fluctuations, Equation of State, and Microphase Separation. *Macromolecules*, 21:3240–3249, 1988.

[19] V. Y. Boryu and I. Y. Erukhimovich. A Statistical Theory of Globular Polyelectrolyte Complexes. *Macromolecules*, 23:3625–3632, 1990.

[20] M. Castelnovo and J. F. Joanny. Complexation between oppositely charged polyelectrolytes: Beyond the Random Phase Approximation. *Eur. Phys. J. E*, 6:377–386, 2001.

[21] M. Castelnovo and J. F. Joanny. Phase diagram of diblock polyampholyte solutions. *Macromolecules*, 35:4531–4538, 2002.

[22] A. V. Ermoshkin and M. Olvera De La Cruz. A modified random phase approximation of polyelectrolyte solutions. *Macromolecules*, 36:7824–7832, 2003.

[23] A. V. Ermoshkin, A. N. Kudlay, and M. Olvera De La Cruz. Thermoreversible crosslinking of polyelectrolyte chains. *J. Chem. Phys.*, 120:11930–11940, 2004.

[24] R. A. Riggleman, R. Kumar, and G. H. Fredrickson. Investigation of the interfacial tension of complex coacervates using field-theoretic simulations. *J. Chem. Phys.*, 136, 2012.

[25] D. J. Audus, J. D. Gopez, D. V. Krogstad, N. A. Lynd, E. J. Kramer, C. J. Hawker,

and G. H. Fredrickson. Phase behavior of electrostatically complexed polyelectrolyte gels using an embedded fluctuation model. *Soft Matter*, 11:1214–1225, 2015.

[26] P. H. Gaskell, A. Saeed, P. Chieux, and D. R. McKenzie. Physical review letters. *Phys. Rev. Lett.*, 67:1286–1289, 1991.

[27] Sarah L. Perry and Charles E. Sing. PRISM-Based Theory of Complex Coacervation: Excluded Volume versus Chain Correlation. *Macromolecules*, 48:5040–5053, 2015.

[28] Chiu Fan Lee, Clifford P. Brangwynne, Jöbin Gharakhani, Anthony A. Hyman, and Frank Jülicher. Spatial organization of the cell cytoplasm by position-dependent phase separation. *Phys. Rev. Lett.*, 111:088101, 2013.

[29] Joel Berry, Stephanie C. Weber, Nilesh Vaidya, Mikko Haataja, and Clifford P. Brangwynne. RNA transcription modulates phase transition-driven nuclear body assembly. *Proc. Natl. Acad. Sci.*, 112:5237–5245, 2015.

[30] Timothy J. Nott, Evangelia Petsalaki, Patrick Farber, Dylan Jervis, Eden Fussner, Anne Plochowietz, Timothy D. Craggs, David P. Bazett-Jones, Tony Pawson, Julie D. Forman-Kay, and Andrew J. Baldwin. Phase Transition of a Disordered Nuage Protein Generates Environmentally Responsive Membraneless Organelles. *Mol. Cell*, 57:936–947, 2015.

[31] Lu Li, Samanvaya Srivastava, Marat Andreev, Amanda B. Marciel, Juan J. de Pablo, and Matthew V. Tirrell. Phase Behavior and Salt Partitioning in Polyelectrolyte Complex Coacervates. *Macromolecules*, 51:2988–2995, 2018.

[32] Shigeyuki Komura and Takao Ohta, editors. pages 213–240. World Scientific Publishing Co. Pte. Ltd., 2012.

[33] Daisuke Mizuno, Catherine Tardin, C F Schmidt, and F C MacKintosh. Nonequilibrium Mechanics of Active Cytoskeletal Networks. *Science*, 315:370–373, 2007.

[34] Evan T. Powers and David L. Powersy. Mechanisms of protein fibril formation: Nucleated polymerization with competing off-pathway aggregation. *Biophys. J.*, 94:379–391, 2008.

[35] Gunther Hollopeter, Hans Michael Jantzen, Diana Vincent, Georgia Li, Laura England, Vanitha Ramakrishnan, Ruey Bing Yang, Paquita Nurden, Alan Nurden, David Julius, and Pamela B. Conley. Identification of the platelet ADP receptor targeted by antithrombotic drugs. *Nature*, 409:202–207, 2001.

[36] H Baier, M Laufer, J Amat, N A Schellart, E Robles, E K Scott, T Hamaoka, H Aizawa, T Hosoya, H Okamoto, T Roeser, W Staub, M R Taylor, P Tanger, F Engert, D H Hubel, S J Smith, C Levinthal, B Reiter, A Muto, M M Poo, M Matsuzaki, H Kasai, K Imoto, and J Nakai. Visualizing Ribosome Biogenesis :. *Science*, 330(October):673–677, 2010.

[37] Tim Sanchez, Daniel T.N. Chen, Stephen J. Decamp, Michael Heymann, and Zvonimir Dogic. Spontaneous motion in hierarchically assembled active matter. *Nature*, 491:431–434, 2012.

[38] Stephan Block and Christiane A. Helm. Equilibrium and nonequilibrium features in the morphology and structure of physisorbed polyelectrolyte layers. *J. Phys. Chem. B*, 115:7301–7313, 2011.

[39] Maelenn Chevreuil, Didier Law-Hine, Jingzhi Chen, Stéphane Bressanelli, Sophie Combet, Doru Constantin, Jéril Degrouard, Johannes Möller, Mehdi Zeghal, and Guillaume Tresset. Nonequilibrium self-assembly dynamics of icosahedral viral capsids packaging genome or polyelectrolyte. *Nat. Commun.*, 9(1):3071, 2018.

[40] Stephen Mann. Self-assembly and transformation of hybrid nano-objects and nanostructures under equilibrium and non-equilibrium conditions. *Nat. Mater.*, 8:781–792, 2009.

[41] Emanuela Zaccarelli. Colloidal gels: Equilibrium and non-equilibrium routes. *J. Phys. Condens. Matter*, 19, 2007.

[42] D. J. Pochan, K. L. Wooley, H. Cui, S. Zhong, and Z. Chen. Block Copolymer Assembly via Kinetic Control. *Science*, 317(5838):647–650, 2007.

[43] Limin Xu, Lingxiang Jiang, Markus Drechsler, Yu Sun, Zhirong Liu, Jianbin Huang, Ben Zhong Tang, Zhibo Li, Martien A. Cohen Stuart, and Yun Yan. Self-assembly of ultralong polyion nanoladders facilitated by ionic recognition and molecular stiffness. *J. Am. Chem. Soc.*, 136:1942–1947, 2014.

[44] Andreas F Thünemann, Martin Müller, Herbert Dautzenberg, and Jean-françois Joanny Hartmut Löwen. Polyelectrolyte Complexes. *Adv. Comput. Simul. Approaches Soft Matter Sci. I*, 166:113–171, 2004.

[45] Jad A. Jaber and Joseph B. Schlenoff. Mechanical properties of reversibly cross-linked ultrathin polyelectrolyte complexes. *J. Am. Chem. Soc.*, 128:2940–2947, 2006.

[46] Linda Gärdlund, Lars Wågberg, and Magnus Norgren. New insights into the structure of polyelectrolyte complexes. *J. Colloid Interface Sci.*, 312(2):237–246, 2007.

[47] Alexei A. Lazutin, Alexander N. Semenov, and Valentina V. Vasilevskaya. Polyelectrolyte complexes consisting of macromolecules with varied stiffness: Computer simulation. *Macromol. Theory Simulations*, 21:328–339, 2012.

[48] Dmitry V. Pergushov, Axel H. E. Müller, and Felix H. Schacher. Micellar interpolyelectrolyte complexes. *Chem. Soc. Rev.*, 41:6888, 2012.

[49] Yaming Jiang, Theresa M. Reineke, and Timothy P. Lodge. Complexation of DNA with Cationic Copolymer Micelles: Effects of DNA Length and Topology. *Macromolecules*, 51(3):1150–1160, 2018.

[50] Sangsik Kim, Jun Huang, Yongjin Lee, Sandipan Dutta, Hee Young Yoo, Young Mee Jung, YongSeok Jho, Hongbo Zeng, and Dong Soo Hwang. Complexation and coacervation of like-charged polyelectrolytes inspired by mussels. *Proc. Natl. Acad. Sci.*, 113:847–853, 2016.

[51] G. S. Hartley. Hermann et Cie, Paris, 1936.

[52] J. W. McBain. Mobility of highly-charged micelles. *Trans. Farady Soc.*, 9:6888, 1913.

[53] E. A. G. Aniansson and S. N. Wall. Kinetics of step-wise micelle association. Correction and improvement. *J. Phys. Chem.*, 79(8):857–858, 1975.

[54] E. A. G. Aniansson and S. N. Wall. Kinetics of step-wise micelle association. *J. Phys. Chem.*, 78:1024–1030, 1974.

[55] E. A. G. Aniansson, S. N. Wall, M. Almgren, H. Hoffmann, I. Kielmann, W. Ulbricht, R. Zana, J. Lang, and C. Tondre. Theory of the kinetics of micellar equilibria and quantitative interpretation of chemical relaxation studies of micellar solutions of ionic surfactants. *J. Phys. Chem.*, 80:905–922, 1976.

[56] L. Cantú, M. Corti, and P. Salina. Direct measurement of the formation time of mixed micelles. *J. Phys. Chem.*, 95(15):5981–5983, 1991.

[57] Bernard Michels, Gilles Waton, and Raoul Zana. Dynamics of Micelles of Poly(ethylene oxide)-Poly(propylene oxide)-Poly(ethylene oxide) Block Copolymers in Aqueous Solutions. *Langmuir*, 13:3111–3118, 1997.

[58] Isabella Goldmints, Josef F. Holzwarth, Kenneth A. Smith, and T. Alan Hatton. Micellar Dynamics in Aqueous Solutions of PEO-PPO-PEO Block Copolymers. *Langmuir*, 13:6130–6134, 1997.

[59] K. Procházka, B. Bedná, E. Mukhtar, P. Svoboda, J. Trněná, and M. Almgren. Non-radiative energy transfer in block copolymer micelles. *J. Phys. Chem.*, 95:4563–4568, 1991.

[60] K. Prochazka, P. Munk, S. E. Webber, Z. Tuzar, D. Kiserow, and C. Ramireddy. Time-resolved fluorescence studies of the chain dynamics of naphthalene-labeled polystyrene-block-poly(methacrylic acid) micelles in aqueous media. *Macromolecules*, 25(1):454–460, 2005.

[61] K. Prochazka, D. Kiserow, C. Ramireddy, Z. Tuzar, P. Munk, and S. E. Webber. Time-Resolved Fluorescence Studies of the Chain Dynamics of Naphthalene-Labeled Polystyrene-*block*-poly(methacrylic acid) Micelles in Aqueous Media. Technical report, 1992.

[62] Jan van Stam, Serge Creutz, Frans C. De Schryver, and Robert Jérôme. Tuning of the Exchange Dynamics of Unimers between Block Copolymer Micelles with Temperature, Cosolvents, and Cosurfactants. *Macromolecules*, 33(17):6388–6395, 2000.

[63] Yongmei Wang, R. Balaji, Roderic P. Quirk, and Wayne L. Mattice. Detection of the rate of exchange of chains between micelles formed by diblock copolymers in aqueous solution. *Polym. Bull.*, 28(3):333–338, 1992.

[64] Timo Rager, Wolfgang H. Meyer, and Gerhard Wegner. Micelle formation of poly(acrylic acid)-block-poly(methyl methacrylate) block copolymers in mixtures of water with organic solvents. *Macromol. Chem. Phys.*, 200(7):1672–1680, 1999.

[65] Guy Hurtrez, Philippe Dumas, and Gérard Riess. Polystyrene-Poly(ethylene oxide) diblock copolymers micelles in water. *Polym. Bull.*, 40(2-3):203–210, 1998.

[66] You Yeon Won, H. Ted Davis, and Frank S. Bates. Molecular exchange in PEO-PB micelles in water. *Macromolecules*, 36(3):953–955, 2003.

[67] L Willner, A Poppe, J Allgaier, M Monkenbusch, and D Richter. Time-resolved SANS for the determination of unimer exchange kinetics in block copolymer micelles. *Europhys. Lett.*, 55(5):667–673, 2001.

[68] M. Jacquin, P. Muller, R. Talingting-Pabalan, H. Cottet, J. F. Berret, T. Futterer, and O. Théodoly. Chemical analysis and aqueous solution properties of charged amphiphilic block copolymers PBA-b-PAA synthesized by MADIX®. *J. Colloid Interface Sci.*, 316(2):897–911, 2007.

[69] Shuguang Zhang. Fabrication of novel biomaterials through molecular self-assembly. *Nat. Biotechnol.*, 21(10):1171–1178, 2003.

[70] Dan Peer, Jeffrey M. Karp, Seungpyo Hong, Omid C. Farokhzad, Rimona Margalit, and Robert Langer. Nanocarriers as an emerging platform for cancer therapy. *Nat. Nanotechnol.*, 2(12):751–760, 2007.

[71] Uttam Kedar, Prasanna Phutane, Supriya Shidhaye, and Vilasrao Kadam. Advances in polymeric micelles for drug delivery and tumor targeting. *Nanomedicine: NBM*, 6:714–729, 2010.

[72] Annette Rösler, Guido W M Vandermeulen, and Harm Anton Klok. Advanced drug delivery devices via self-assembly of amphiphilic block copolymers. *Adv. Drug Deliv. Rev.*, 64:270–279, 2012.

[73] Frank Alexis, Eric Pridgen, and Linda K Molnar. reviews Factors Affecting the Clearance and Biodistribution of. *Mol. Pharm.*, 5(4):505–515, 2008.

[74] A. Halperin and S. Alexander. Polymeric Micelles: Their relaxation kinetics. *Macromolecules*, 22:2403–2412, 1989.

[75] A. Halperin, M. Tirrell, and T. P. Lodge. Tethered chains in polymer microstructures. *Macromol. Synth. Order Adv. Prop.*, 100:31–71, 1992.

[76] Elena E. Dormidontova. Micellization kinetics in block copolymer solutions: scaling model. *Macromolecules*, 32:7630–7644, 1999.

[77] Ilja K Voets, Arie De Keizer, and Martien A Cohen Stuart. Complex coacervate core micelles. *Adv. Colloid Interface Sci.*, 147-148:300–318, 2009.

[78] Atsushi Harada and Kazunori Kataoka. Supramolecular assemblies of block copolymers in aqueous media as nanocontainers relevant to biological applications. *Prog. Polym. Sci.*, 31:949–982, 2006.

[79] Daniel V. Krogstad, Soo-hyung Choi, Nathaniel A Lynd, Debra J. Audus, Sarah L. Perry, D Gopez, Craig J. Hawker, Edward J. Kramer, and Matthew V Tirrell. Small Angle Neutron Scattering Study of Complex Coacervate Micelles and Hydrogels Formed from Ionic Diblock and Triblock Copolymers. *J. Phys. Chem. B*, 118:13011–13018, 2014.

[80] Horacio Cabral, Kanjiro Miyata, Kensuke Osada, and Kazunori Kataoka. Block Copolymer Micelles in Nanomedicine Applications. *Chem. Rev.*, 118:6844–6892, 2018.

[81] Gaurav Tiwari, Ruchi Tiwari, Birendra Sriwastawa, L Bhati, S Pandey, P Pandey, and Saurabh K Bannerjee. Drug delivery systems : An updated review. *Int. J. Pharm. Investig.*, 2:2–11, 2012.

[82] Prashant Kesharwani, Virendra Gajbhiye, and Narendra Kumar Jain. A review of nanocarriers for the delivery of small interfering RNA. *Biomaterials*, 33:7138–7150, 2012.

[83] Muhammad Wahab, Prashant Kesharwani, Mohd Cairul, Iqbal Mohd, and Arun K Iyer. Progress in Polymer Science Recent advances in the design , development , and targeting mechanisms of polymeric micelles for delivery of siRNA in cancer therapy. *Prog. Polym. Sci.*, 64:154–181, 2017.

[84] Kenneth Alan Howard. Delivery of RNA interference therapeutics using polycation-based nanoparticles . *Adv. Drug Deliv. Rev.*, 61(9):710–720, 2009.

[85] Vaibhav Mundra and Ram I. Mahato. Design of nanocarriers for efficient cellular uptake and endosomal release of small molecule and nucleic acid drugs : learning from virus. *Front. Chem. Sci. Eng.*, 8:387–404, 2014.

[86] Rosemary Kanasty, Joseph Robert Dorkin, Arturo Vegas, and Daniel Anderson. Delivery materials for siRNA therapeutics. *Nature Materials*, 12:967–977, 2013.

[87] Judy Lieberman. Tapping the RNA world for therapeutics. *Nat. Struct. Mol. Biol.*, 25:357–364, 2018.

[88] Steven F Dowdy. Overcoming cellular barriers for RNA therapeutics. *Nat. Biotechnol.*, 35:222–229, 2017.

[89] Cynthia E Dunbar, Katherine A High, J Keith Joung, Donald B Kohn, Keiya Ozawa, and Michel Sadelain. *Science*, page 4672.

[90] Leo Y T Chou, Kevin Ming, and Warren C W Chan. Strategies for the intracellular delivery of nanoparticles. *Chem. Soc. Rev.*, 40(1):233–245, 2011.

[91] Pavel S. Chelushkin, Evgeny A. Lysenko, Tatiana K. Bronich, Adi Eisenberg, Victor A. Kabanov, and Alexander V. Kabanov. Polyion complex nanomaterials from block polyelectrolyte micelles and linear polyelectrolytes of opposite charge. 2. Dynamic properties. *J. Phys. Chem. B*, 112:7732–7738, 2008.

[92] Saskia Lindhoud, Willem Norde, and Martien A.Cohen Stuart. Reversibility and relaxation behavior of polyelectrolyte complex micelle formation. *J. Phys. Chem. B*, 113(16):5431–5439, 2009.

[93] James C Kaczmarek, Piotr S Kowalski, and Daniel G Anderson. Advances in the

delivery of RNA therapeutics: from concept to clinical reality. *Genome Med.*, 9:60, 2017.

[94] Martien a Cohen Stuart, Wilhelm T S Huck, Jan Genzer, Marcus Müller, Christopher Ober, Manfred Stamm, Gleb B Sukhorukov, Igal Szleifer, Vladimir V Tsukruk, Marek Urban, Françoise Winnik, Stefan Zauscher, Igor Luzinov, and Sergiy Minko. Emerging applications of stimuli-responsive polymer materials. *Nat. Mater.*, 9(2):101–113, 2010.

[95] Peter Lönn, Apollo D Kacsinta, Xian-shu Cui, Alexander S Hamil, Manuel Kaulich, Khirud Gogoi, and Steven F Dowdy. Enhancing Endosomal Escape for Intracellular Delivery of Macromolecular Biologic Therapeutics. *Sci. Rep.*, 6:32301, 2016.

[96] Tamaki Endoh and Takashi Ohtsuki. Cellular siRNA delivery using cell-penetrating peptides modified for endosomal escape. *Adv. Drug Deliv. Rev.*, 61(9):704–709, 2009.

[97] Tao Li, Andrew J. Senesi, and Byeongdu Lee. Small Angle X-ray Scattering for Nanoparticle Research. *Chem. Rev.*, 116(18):11128–11180, 2016.

[98] Björn Jung and Patrick Theato. Kinetics of block copolymer micelles studied by SAS methods. *Adv. Polym. Sci.*, 259:51–158, 2012.

[99] Jan Skov Pedersen and Carsten Svaneborg. Scattering from block copolymer micelles. *Curr. Opin. Colloid Interface Sci.*, 7:158–166, 2002.

[100] Jan Skov Pedersen. Structure factors effects in small-angle scattering from block copolymer micelles and star polymers. *J. Phys. Chem.*, 114:2839–2846, 2001.

CHAPTER 2

NON-EQUILIBRIUM PHENOMENA AND KINETIC PATHWAYS IN POLYELECTROLYTE COMPLEXES

⋆ This chapter has been published as H. Wu, J. M. Ting, O. Werba, S. Meng and M. V. Tirrell, *J. Phys. Chem.* **149**, 163330 (2018), and J. M. Ting, H. Wu, A. Herzog-Arbeitman, S. Srivastava and M. V. Tirrell, *ACS Macro Lett.* **7**, 727 (2018).

2.1 Introduction

The formation of hierarchical self-assembled structures is often driven by non-covalent interactions, such as hydrogen bonding, hydrophobic effects, and electrostatic interactions.[1, 2, 3, 4, 5] On the energy landscape, these physical interactions are much weaker than chemical covalent bonds.[6] Thus, for complex systems that comprise many modes of non-covalent interactions, the molecular assemblies resulting from specific formation pathways can be kinetically trapped in non-dissipative (i.e., metastable non-equilibrium) states rather than reaching equilibrium states.[7, 8, 9] The transitions between kinetic traps and thermodynamically stable states lead to a non-equilibrium assembly,[10] which may be useful in itself and has been employed to build transient structures that are inaccessible for conventional equilibrium approaches.[11, 12, 13, 14, 15] For example, Korevaar et al.[14] reported that the supramolecular assemblies that were polymerized from -conjugated oligomers formed a short-lived kinetically favored metastable assembly before reaching the thermodynamically favored configuration. Using a chiral tartaric acid as an auxiliary to change the thermodynamic preference, they were able to obtain the metastable assemblies exclusively. Xu and coworkers[16] demonstrated the construction of kinetically trapped ultralong ordered polyion nanoladders by ionic self-assembly. They designed a coordination complex of a stiff bisligand that can self-assemble slowly into cocoon-like structures. These structures immediately transformed into uniform nanoladder morphology upon the addition of an oppositely charged polymer.

Polyelectrolyte complexes (PECs) are a major class of macromolecular self-assembled materials based on electrostatic interaction. These materials are usually formed from combining solutions of oppositely charged polymeric macroions, where the process is believed

to be initiated by electrostatic interactions and facilitated by the entropic gain from the release of counterions.[17, 18, 19, 20, 21] However, polyelectrolyte complexation is often frustrated by many factors such as conformational constraints, chain immobility, a lack of charge complementarity, and the competition between short-range attraction and long-range repulsion.[6, 22, 23] As a consequence, PECs are usually intrinsic out-of-equilibrium structures.[24] The static and dynamic properties of non-equilibrium PEC are determined by not only the chemical nature of constituting polymers and environmental elements, e.g., solution ionic strength, but also by physical processing pathways. The important roles of these factors have been undervalued in the experimental details of many complex coacervation reports to date. Consequently, challenges in the structural reproducibility of complex materials may arise upon scale-up or extension to end-use applications. Recently, Vitorazi and coworkers stressed the importance of the mixing order in coacervation by investigating the thermodynamics of poly(diallydimethylammonium chloride) (PDAD-MAC)/poly(sodium acrylate) (PAA) complexation.[25] Using isothermal titration calorimetry (ITC), they found a two-step coacervation process by adding PDADMAC to PAA or vice-versa and revealed that the phase separation exhibited an exothermic profile upon addition of PDADMAC to PAA but an endothermic profile for the reverse in terms of titration calorimetry response.

Furthermore, the morphological evolution of nonequilibrium PEC assemblies over a wide range of time and length scales is not well understood. The majority of effort has been devoted to finding conditions that circumvent non-equilibrium states in the assembly of coacervate core micelles in a reproducible manner.[26, 27, 28, 29, 30, 31] As a consequence, little effort has been expended to understand the underlying factors governing the morphological transformation and complex internal structures in polyelectrolyte aggregates. Laaser et al. investigated the structural stability and temporal evolution of micelleplexes, comprising poly(dimethylaminoethyl methacrylate)-*block*-poly(styrene) and poly(styrenesulfonate) homopolymers and emphasized the roles of charge imbalance and ionic strength in the interplay between kinetic and thermodynamic products in these systems.[32] Wang et al. proposed

an effective method to stabilize the structures and fluorescent performance of reversible coordination polymers by kinetically trapping their local concentrations in polymeric complex micelle cores.[33] Using a kinetic Monte Carlo simulation, Zhang and co-workers investigated the structure and evolution kinetics of non-equilibrium ionic assemblies of oppositely charged nanoparticles and elucidated the determinative roles of ion correlations in non-equilibrium cluster formation.[34] Overall, contemporary research on accessing non-equilibrium states of soft matter via an ionic self-assembly is scarce and case dependent. Advancements in such areas may create new avenues from a molecular engineering viewpoint to achieve novel functionalities and ultimately to mimic non-covalent macromolecular self-assembly motifs that are omnipresent in nature.

In this chaper, We intend to investigate the formation pathways and non-equilibrium phenomena in electrostatic aggregates that were formed by two oppositely charged styrenic diblock polyelectrolytes, namely, poly(ethylene oxide)-*block*-poly(vinyl benzyl trimethylammonium chloride) (PEO-*b*-PVBTMA) and poly(ethylene oxide)-*block*-poly(styrene sulfonate sodium) (PEO-*b*-PSS). The PVBTMA block is a strong cationic polyelectrolyte and has been demonstrated to be effective in DNA encapsulation,[35] while the PSS block is a strong anionic polyelectrolyte and has been widely used as a proxy for DNA molecules.[36, 37, 38, 39] In order to elucidate the role of processing pathways, two distinct approaches were designed to probe the metastable morphologies of the resulting electrostatic assemblies. The temporal dependence of the structural evolution and the prolonged salt annealing kinetics was revealed by time-dependent light-scattering experiments, and the intermediate morphologies were visualized by cryogenic transmission electron microscopy (Cryo-TEM). Furthermore, the nuanced transformations of the internal structures in the non-equilibrium assemblies were investigated by small-angle X-ray scattering. Our results elaborate the internal structures and the morphological transition of PEC assemblies from kinetic traps to equilibrium states in a spatiotemporal manner.

2.2 Experimental Details

2.2.1 Materials

The following chemicals were reagent grade and used as received, unless stated otherwise: poly(ethylene oxide) methyl ether (2-methyl-2-propionic acid dodecyl trithiocar-bonate) (PEO, Sigma, Reported M_n = 5000 or 10 000), sodium trimethylammonium chloride (VBTMA, Sigma, 99%), 2, 4-vinylbenzenesulfonate (SS, Sigma, 90%), (vinylbenzyl) 2-azobis[2-(2-imidazolin-2-yl)propane]dihydrochloride(VA- 044, Wako Chemicals, USA), acetic acid (glacial, Sigma, SnakeSkin? dialysis tubing (MWCO 3.5K, 22 mm, Thermo 99.85%), and sodium acetate trihydrate (Sigma, $\leq$ 99%). Scientific) was used to purify crude products. The acetate buffer solution was prepared with 0.1M acetic acid and 0.1M sodium acetate trihydrate (0.1M) (42/158, *v/v*) at pH 5.2 for all reactions. All water was filtered through a Milli-Q water purification system at a resistivity of 18.2 MΩ cm at 25 ^{o}C.

2.2.2 Polymer synthesis and characterization

In a typical reaction, to a dried 25 ml round bottom flask, the styrene sulfonate monomer (6.7 mmol at 1.0M monomer concentration), RAFT PEO macromolecular chain transfer agent (0.067 mmol), and VA-044 (0.0067 mmol) were added to an aqueous acetate buffer solution (pH 5.2, 6.7 ml). The reactorwas then sealed, degassed via three cycles of freeze-pump-thaw, and heated at 50 ^{o}C under nitrogen and constant stirring for at least 21 h. Afterward, the reaction was quenched by cooling to room temperature and opening to air. Crude yellow mixtures were dialyzed against Milli-Q water for 3 cycles of 8 h each, followed by lyophilization to yield ca. 2 g free-flowing yellow powder. The synthesis route is shown in Figure 2.1.

For determining the absolute number-average molecular weight (M_n) and dispersity, size-exclusion chromatography (SEC) experiments were conducted on a Waters liquid chromatogram apparatus (consisting of a well-stirred mobile phase reservoir, Waters In-Line

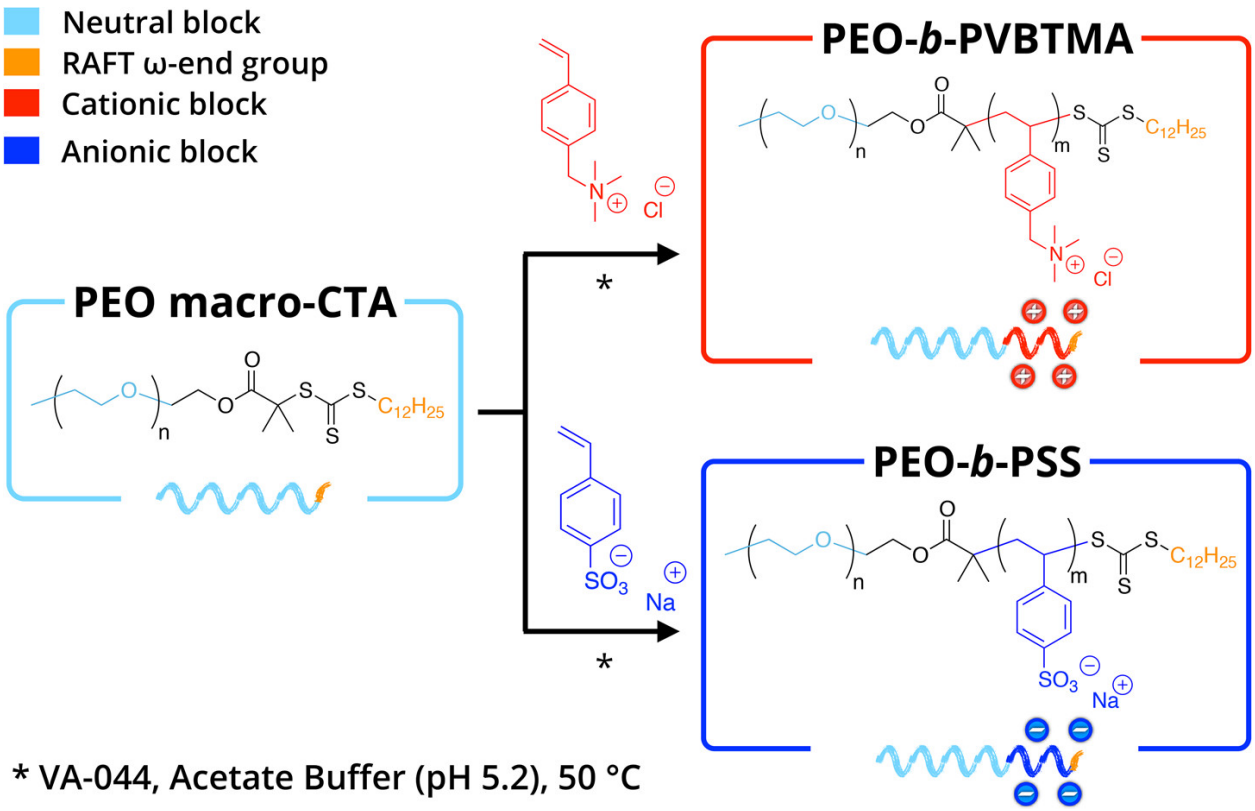

Figure 2.1: RAFT polymerizations were conducted at a PEO macro-CTA to water-soluble azo initiator VA-044 molar equivalence of 10 to 1.

Degasser AF, Waters 1515 Isocratic HPLC pump, and Waters 2707 Autosampler), equipped with three Waters columns (Ultrahydrogel Column 500, Ultrahydrogel Column 120, and Ultrahydrogel Column 250) set at 35 ^{o}C with pore sizes suitable for materials with effective molecular weights from 1 to 400,000 g/mol. The SEC includes a Waters 2998 photodiode array detector, a miniDAWN TREOS II multi-angle laser light scattering (MALS, 3 angles) detector at a laser wavelength of 658 nm, and a Wyatt Optilab T-rEX refractive index detector. Empower 3 Software controlled the setup of the experiments, and ASTRA 6 software was used to analyze the collected refractive index and light scattering data. For PEO-*b*-PVBTMA, a mixture of acetonitrile and water (40/60, %, v/v) with 0.1% trifluoroacetic acid was chosen as the mobile phase at 1.0 mL/min. For PEO-*b*-PSS, a mixture of methanol, acetonitrile, and 0.1 M $NaNO_3$ + 0.02 wt % NaN_3 water (15/15/70, %, *v/v*) was chosen as the mobile phase at 1.0 mL/min. The dn/dc values were calculated using an Abbe refractometer with a red light-emitting diode in the respective SEC mobile phase at 25 ^{o}C; refractive index measurements at five polymer concentrations were collected in triplicate and checked for linearity. 1H NMR experiments were performed on a Bruker AVANCE III HD 400 Mhz NanoBay spectrometer with 16 transients to minimize signal-to-noise. 1H NMR spectra were analyzed using iNMR (Version 5.5.7).

2.2.3 Micelle preparation

Polycation and polyanion stock solutions were prepared in Milli-Q water at the concentration of 5.0 mg/ml and were filtered through 220nm Polyvinylidene fluoride (PVDF) filters before use. All samples were prepared following the direct dissolution protocol or the salt annealing protocol. Electrostatic assemblies were made by mixing the stock solutions under stoichiometric conditions, with the presence of various salt types and salt concentrations. Each charged monomer had a concentration of 2.45 mmol/L. All micelle solutions were made at room temperature. In the protocol of direct dissolution, a certain amount of salt solution was added into pure water, and then polycation stock solution and polyanion stock solution were

added corresponding to the equimolar concentration of the cationic and anionic monomer units. The resulting micelle solution was set aside for at least 1 h before any measurement. Meanwhile, in the protocol of salt annealing, polycation and polyanion stock solutions were mixed prior to the addition of salt. Three salt types (NaCl, NaBr, and NaI) and a wide range of salt concentrations were selectively investigated.

2.2.4 Time-resolved dynamic light scattering

Experiments were carried out on an in-house Brookhaven Instruments BI-200SM Research Goniometer System with a $\lambda = 637$ nm incident laser at 23 ^{o}C. A dust-free decalin bath was used to match the refractive index of glass.

Time-resolved dynamic light scattering experiments were conducted using a script that is written by Cmm scripting language. Time delay and time duration were tailored for different samples and the time resolution. Intensity and correlation functions were recorded right after salt addition. The dead time was ca. 1 s. All of the DLS experiments were conducted at the angle of 90 ^{o}C.

Multi-angle measurements were conducted using a Cmm script. Correlation functions were collected at 14 scattering angles from 20^{o} to 150^{o} at 10^{o} increments, and running duration of each angle was at least 1 min. The angular dependence of D was acquired by plotting q^2 versus decay rate . A linearity over a range of scattering angles is a good indication of isotropic scatters, i.e., spheres when the radius is larger than $\lambda/20$ nm. The correlation function at each angle was fitted to a first-order single exponential using a MATLAB code.

2.2.5 Small-angle X-ray scattering

Small-angle X-ray scattering (SAXS) experiments were carried out on beamline 12-ID-B at Advanced Photon Source, Argonne National Laboratory. The sample-to-detector distance was about 4 m, and the q range covered from 0.002 to 0.5 Å^{-1}. Samples were loaded in thin-walled quartz capillaries or flow cells; 1 wt.% of glycerol was added to each sample to prevent

potential beam damage. Using the SAXSLeepackage at Sector 12-ID-B, the experimentally generated 2D SAXS image was converted into the scattering vector defined as:

$$q = \frac{4\pi}{\lambda} \sin\left(\frac{\theta}{2}\right) \tag{2.1}$$

where λ is the incident X-ray wavelength and θ is the scattering angle. Then the 2D image was azimuthally averaged into a one-dimensional scattering curve. The absolute scattering intensity was calibrated with glassy carbon. The SAXS data were analyzed using the Irena package and fitted by the two-level Beaucage model.

2.2.6 SAXS Modeling

Two models were used to fit the SAXS curves. For micellar particles formed by PEO-*b*-PVBTMA and PAA polyelectrolytes were fitted using a polydisperse core-shell sphere model developed by Kline et al. The form factor can be expressed as:

$$P(q) = \frac{\text{scale factor}}{V_{sph}} \left[\frac{3V_C\left(\rho_C - \rho_S\right) j_1\left(qr_C\right)}{qr_C} + \frac{3V_S\left(\rho_S - \rho_{\text{ solvent }}\right) j_1\left(qr_S\right)}{qr_S}\right]^2 + \text{ bkg} \tag{2.2}$$

$$j_1(x) = \frac{\sin x - x\cos x}{x^2} \tag{2.3}$$

where $j_1(x)$ is the Bessel function; $P(q)$ is the form factor; V_{sph}, V_C, and V_S are the volumes of a single micelle, the micelle core, and the micelle shell, respectively; ρ_C, ρ_C, and ρ_{solv} are the scattering length densities of the micelle shell, micelle core, and solvent, respectively; r_{sph} of the micelle shell and r_C is the radius of the micelle core. The scale is a factor that equals to the volume fraction when the scattering data is on an absolute scale. The *bkg* denotes the background level.

For the polyelectrolyte complexes, a two-level Beaucage model was used to fit the SAXS

curves. This model is developed by Greg Beaucage and is used to fit SAXS data with levels composed of a Guinier part and a power law tail.[40] It can handle SAXS features for which an exact scatter model is difficult or impossible. The model ischaracterized by three parameters: a Guinier scaling factor G, a radius of gyration R_g, a Porod exponent P, and a constant B. The scattering intensity is given by:

$$I(q) = \sum_{i=1}^{2} \left[G_i \exp\left(-\frac{q^2 R_{g,i}^2}{3} \right) + \frac{B_i \left[\operatorname{erf}\left(qR_{g,i}//\sqrt{6} \right) \right]^{3P_i}}{q^{P_i}} \right] \tag{2.4}$$

where erf(x) is the *error function* encountered in integrating the normalized form of the Gaussian distribution and is defined by:

$$\operatorname{erf}(x) \equiv \frac{2}{\sqrt{\pi}} \int_0^x e^{-t^2} dt \tag{2.5}$$

2.2.7 Cryogenic transmission electron microscopy

Cryogenic transmission electron microscopy (Cryo-TEM) was used to image particles. A Field Electron and Ion (FEI) Tecnai^{TM} G2 Spirit BioTWIN TEM was used to image samples set at an accelerating voltage of 120 kV onto a LaB6 emitter at 178 ^{o}C. A droplet of about 3 μL samples containing electrostatic assemblies was pipetted onto a carbon/Formvar grid that is cleaned by a PELCO easiGlow glow discharge instrument. The grid was blotted for 3 s and was quenched rapidly in liquid ethane and subsequently transferred to a single-tilt cryo holder. Imageswere taken using an EagleTM2k CCD camera (up to 4 megapixels) and analyzed with the FEI TEM Imaging and Analysis (TIA) software. Phase contrast was enhanced by imaging at 8-12 μm under focus. Self-assembled aggregates size distributions were reported with ImageJ 1.47v.

2.3 Results and Discussions

2.3.1 Self-assembled polyelectrolyte complexes formation

To demonstrate this idea, we investigated the complexcore assemblies of PEO_{10K} -*b*- $PVBTMA_{100}$ with (1) poly-acrylic acid sodium salt) (PAA158, a weak polyanion, DP = 158) or (2) PEO_{10K}-*b*-$PVBTMA_{100}$ (a strong polyanion). PECs of the PVBTMA and PAA homopolyelectrolytes have reportedly formed liquid-like coacervates with high water content, while pairing PVBTMA with PSS resulted in more kinetically trapped structures.45 Due to space limitations, we only discuss these two cases because the pairings represent the most different types of assemblies we observed. The balance between neutral to charged block length (i.e., DP of 2:1 or 1:1) was important to stability across systems in terms of assembly formation, as observed in literature examples.

In the PEO_{10K}-*b*-$PVBTMA_{100}$/PAA158 system, cryo-TEM imaging illustrated the sphere-like morphology of the micelle cores (Figure 2.2A), with a mean particle diameter of 25 ± 7 nm (95% CI = 24.2, 26.0) and an interquartile range of 9.26 nm. For visualizing native soft matter, little contrast is expected between the hydrated PEO corona and the surrounding vitrified water. Complementary scattering studies to study the PEC corona confirmed this hypothesis. By multiangle DLS, the micelles exhibited an apparent mean hydrodynamic radius (Rh) of 30 nm by a cumulant fitting that did not evolve over time. This unimodal size distribution is shown in Figure 2B with REPES analysis.[41] Furthermore, the observed linear angular dependence of the relaxation rate Γ as a function of the squared scattering wave vector q^2 from θ = 40 to 140° is a characteristic signature of the diffusive mode of spherical scatters. Finally, the intensity profile in the SAXS pattern exhibits a clear plateau up to q ≈ 0.02 nm^{-1}, followed by a I(q) ≈ q^4 dependency, which indicates that the micelle core has a spherical geometry with an approximate diameter of 28 nm when fitted with a polydisperse coreshell model. This is in excellent agreement with the particles observed through cryo-imaging.

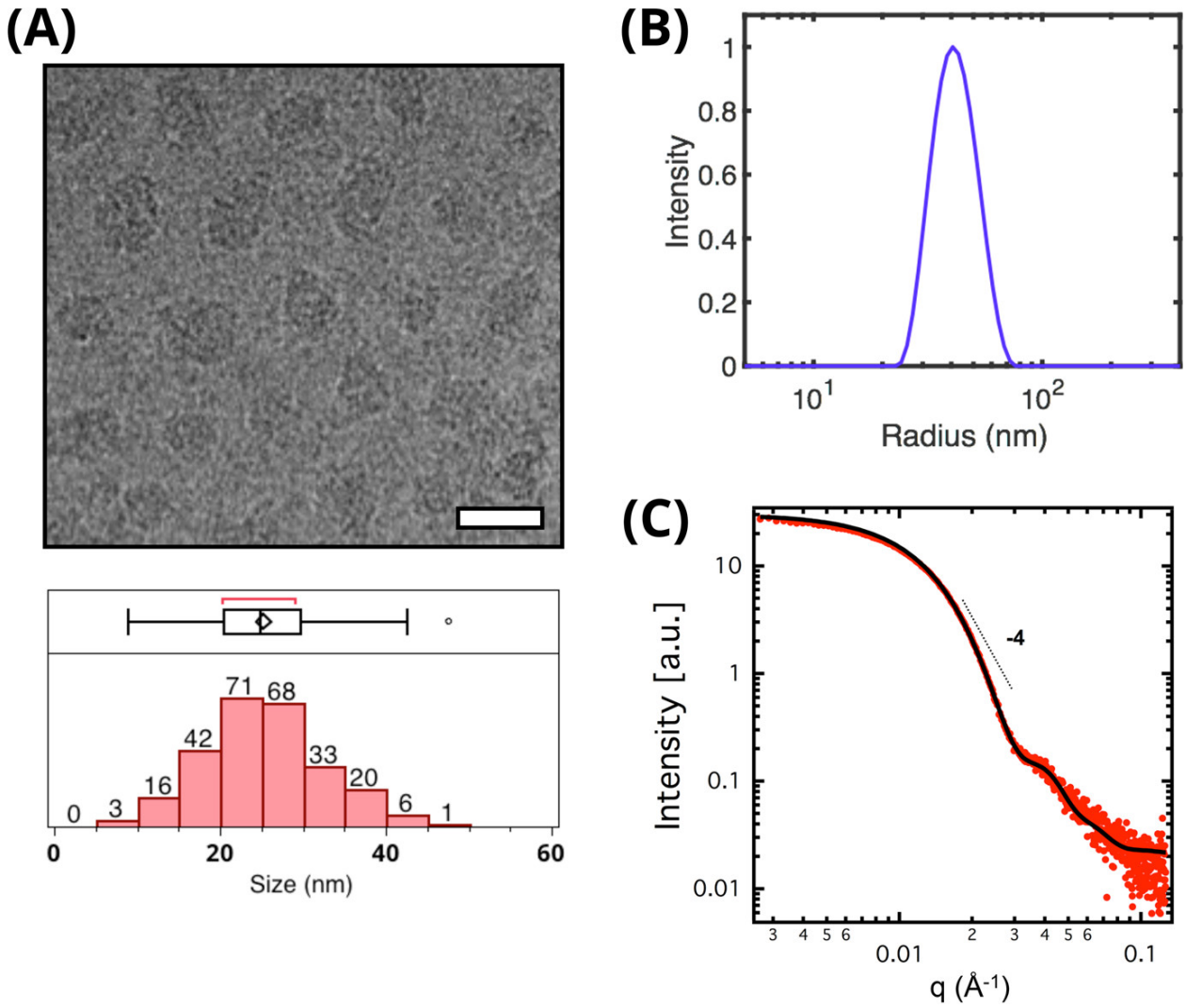

Figure 2.2: Solution assemblies of PEO_{10K}-*b*-$PVBTMA_{100}/PAA_{158}$ at 1 mg/mL, characterized by (A) representative cryo-TEM imaging to visualize particles (scale bar represents 40 nm), (B) DLS to determine the apparent hydrodynamic radius (analyzed with REPES at θ = 90°), and (C) SAXS to quantify morphology/size (red circles denote experimental data; black line represents a fitting to a polydisperse coreshell model).

In contrast, when PEO_{10K}-*b*-$PVBTMA_{100}$ combines with PEO_{10K}-*b*-PSS_{100}, large and interconnected nanoaggregates with high particle polydispersity were observed from cryo-TEM imaging (Figure 2.3A). DLS analysis revealed a broad distribution of large structures that persisted for several weeks. A powerlaw slope of 1.6 in the q-range of 0.003 $Å^{-1}$ < q < 0.2 $Å^{-1}$ suggested the existence of swollen coil-like structures (Figure 2.3B).[42] It is reasonable to infer that these aggregates are kinetically trapped electrostatic assemblies. For uncharged amphiphilic diblock polymer systems, Lund and co-workers have demonstrated that micelle formation is subject to constant intermicellar chain exchange.[43] The incomplete PEC micellization to uniform nanostructures may be attributed to the strong ionic nature of the PVBTMA and PSS blocks, whose ion pairing is known to associate strongly, thereby hindering polymer chains in electrostatic assemblies to escape and equilibrate over time.[44] Nevertheless, these model materials can be used to explore the formation pathways and processing effects between kinetic and thermodynamic products, which has recently been of interest to the advancement of micelleplex delivery vehicles.

In these assemblies, the role of polymer architecture and hydrophobicity can be compared. The choice of using a charged homopolymer/diblock or a diblock/diblock to build a solution assembly typically depends on the intended application. Hofs et al. demonstrated an elegant comparison of such combinations of complex core micelles.[45] They report that the micelles from two diblock polyelectrolytes were less stable than those formed from diblocks and homopolymers, attributing the difference to unfavorable interactions between the two neutral blocks and the entropic penalty incurred by the junction placement at the interface between the core and corona. This may have contributed to the nanoaggregates we observed in the diblock styrenic assemblies in Figure 2.3. Meanwhile, decoupling the competing roles of electrostatics from hydrophobic effects has been a longstanding, difficult problem. Recently, Sadman and co-workers identified that in their series of homopolyelectrolytes more hydrophobic complexes were more resistant to salt.[46] This observation supports the hypothesis of hydrophobic chains impeding mobility inside a complex domain.[47] The chemical moieties

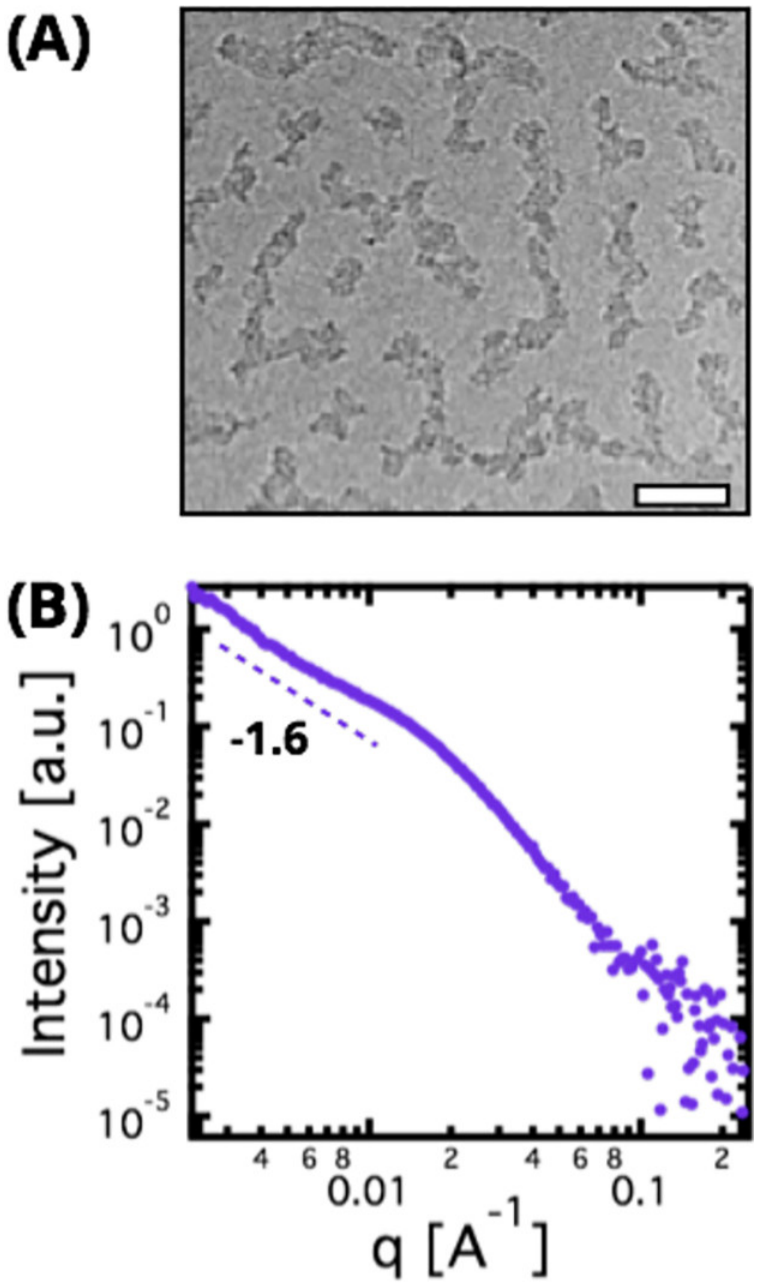

Figure 2.3: Solution assemblies of PEO_{10K}-*b*-$PVBTMA_{100}$/ PEO_{10K}-*b*-PSS_{100} at 1 mg/mL, characterized by (A) cryo-TEM imaging to visualize particles (scale bar represents 40 nm) and (B) SAXS to quantify morphology and size.

in PSS exhibit greater hydrophobicity than PAA, which may account for the difference in solution structures in Figures 2.2 and 2.3.

In the following sections, we report the detailed studies on the internal structures and the kinetics of formation and dissociation in these self-assembled polyelectrolyte complexes in nonequilibrium states..

2.3.2 Effect of salt types

According to the theories in polyelectrolyte complexes, salt ions can condense on the backbonds of the charged polymers, so that electrostatic interactions between oppositely charged polymer chains are strongly weakened. It is well known that the addition of external salts can break up polyelectrolyte complexes. Here, the effect of salt types on the size evolution of the electrostatic assemblies was investigated by using three types of salts, i.e. sodium chloride, sodium bromide, and sodium iodide. The salt concentrations ranged from 0 to 2.5 M. All the samples were prepared by the *Direct Dissolution* process. The critical salt concentration was defined as the concentration where no aggregates were formed and the light scattering intensity was below 10 counts per second. It is shown that, in Figures 2.4 and 2.5 for sample PEO_{10K}-*b*-$PVBTMA_{100}$/PEO_{10K}-*b*-PSS_{100} and sample PEO_{5K}-*b*-$PVBTMA_{50}$/PEO_{5K}-*b*-PSS_{50} both the scattering intensity and hydrodynamic radius decrease significantly with the increase of the salt concentration. It should be noted that all of the measurements were done within 24 hour after the samples were prepared.

The observation suggests that the heavier anions (i.e., $I^- > Br^- > Cl^-$) have stronger effect on the screening of the electrostatic interactions in the polyelectrolyte complex assemblies. Similar phenomena has been reported in bulk coacervate complexes formed by two homopolyelectrolytes. This trend follows the Holfmeister series, which views Cl^- as a moderately inert anion and I^- as a chaotrope that increases polymer solubility.

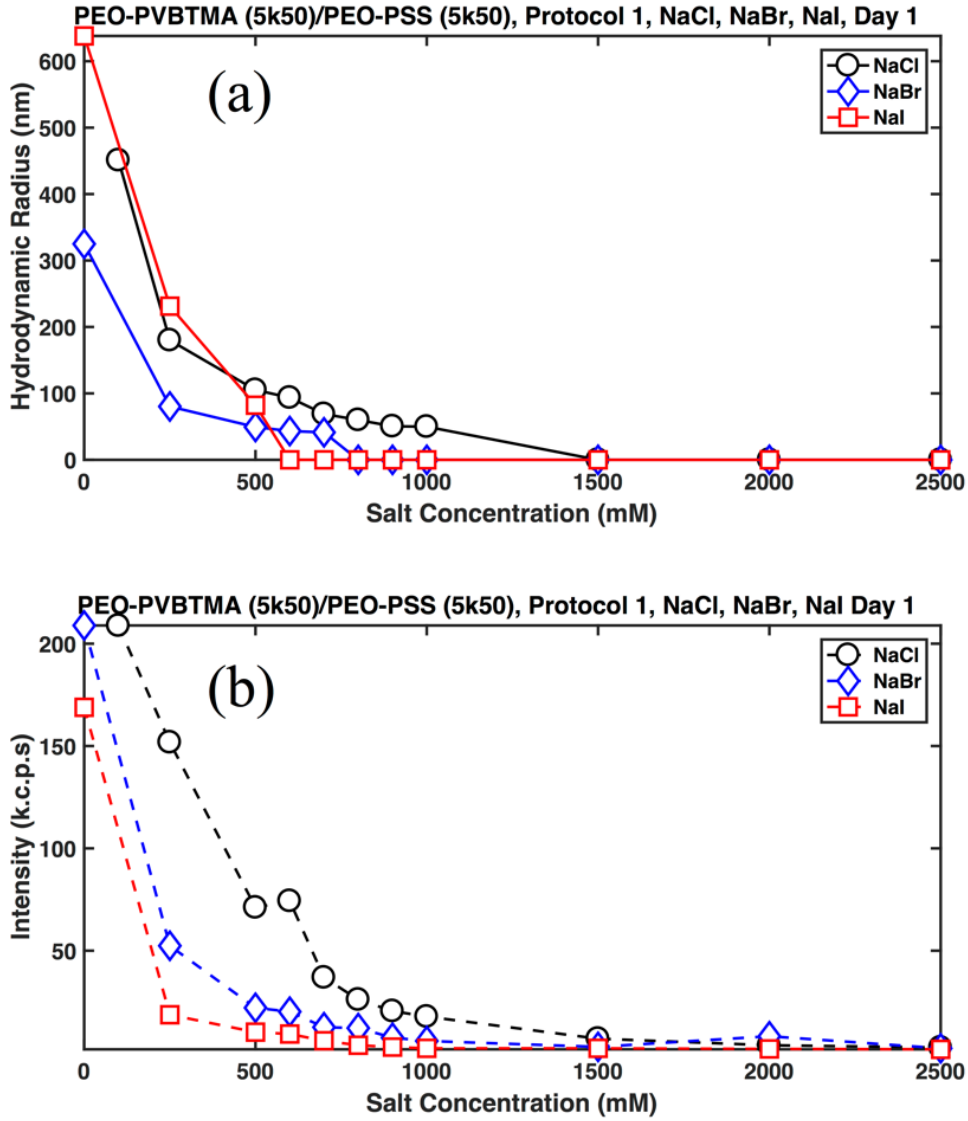

Figure 2.4: The reduction of the average hydrodynamic radii (a) and scattering intensity (b) of the kinetically trapped aggregates under various concentrations of NaCl (black), NaBr (blue), and NaI (red). The sample was PEO_{5K}-*b*-$PVBTMA_{50}$/ PEO_{5K}-*b*-PSS_{50} with a total polymer concentration of 1.0 mg/ml.

Table 2.1: The critical salt concentrations of the polyelectrolyte complexes

Temp (K)	τ (min)	β
T = 293	61.54	2.0
T = 330	51.77	1.84
T = 350	38.57	1.66

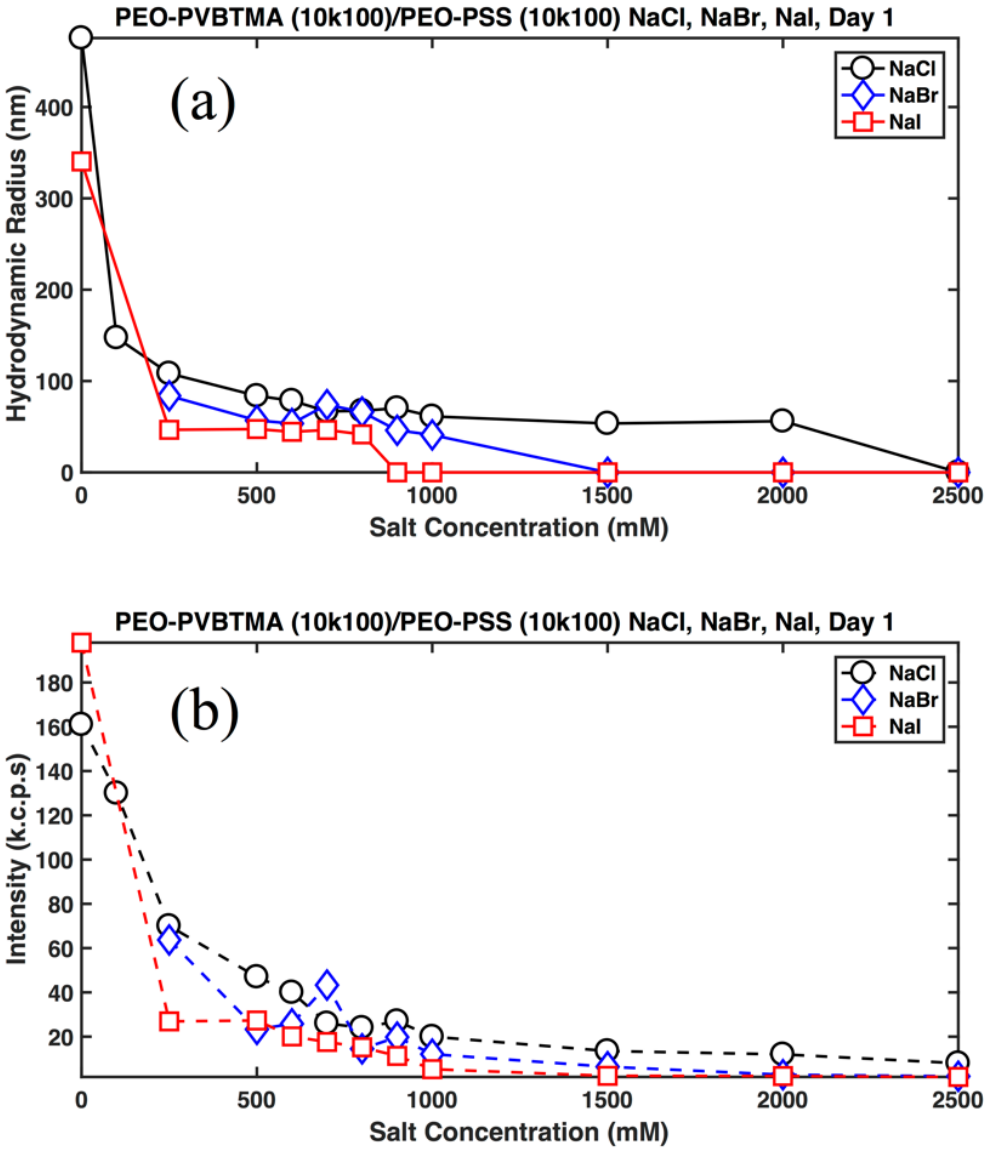

Figure 2.5: The reduction of the average hydrodynamic radii (a) and scattering intensity (b) of the kinetically trapped aggregates under various concentrations of NaCl (black), NaBr (blue), and NaI (red). The sample was PEO_{10K}-*b*-$PVBTMA_{100}$/ PEO_{10K}-*b*-PSS_{100} with a total polymer concentration of 1.0 mg/ml.

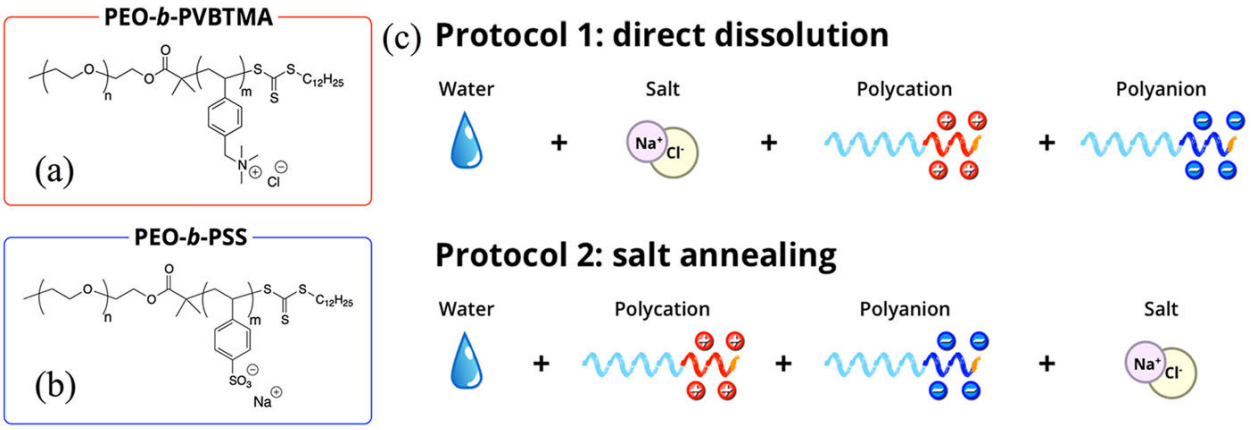

Figure 2.6: The chemical structures of PEO_{10K} -*b*- $PVBTMA_{100}$/ PEO_{10K} -*b*- PSS_{100} (or PEO_{5K} -*b*- $PVBTMA_{50}$/PEO5K -*b*- PSS_{50}) (a) andPEO_{10K} -*b*- $PVBTMA_{100}$/ PEO_{10K} -*b*- PSS_{100} (or PEO_{5K}-*b*-$PVBTMA_{50}$/PEO5K -*b*- PSS_{50}) (b), where 10K or 5K is the molecular weight of the PEO block and 100 or 50 is the degree of polymerization of the PVBTMA or PSS block. (c) Schematic representation of the two processing protocols for polyelectrolyte complexation

2.3.3 Pathway dependency

It is well studied that for amphiphilic polymers, the physical preparation protocols in solution have a marked effect on the dynamics of self-assemblies.[48, 49, 50, 51] For electrostatically driven assemblies, in addition to the hydrophobic-hydrophilic balance and the chemical properties of the constituent monomers, the ionic character of charged segments and the presence of counterions and water throughout the assembly influence the kinetics and thermodynamics of coacervation. As a first approach to clarifying the mechanism of ionic self-assembly in a simple manner, we investigated the assembly of PEO-*b*-PVBTMA and PEO-*b*-PSS using two protocols shown in Figure 2.6. In Protocol 1, the *direct dissolution* method, we prepared samples by sequentially combining the predetermined quantities of water, salt solution, polycation solution, and polyanion solution in this order. In Protocol 2, the *salt annealing* method, assemblies were first made by adding the predetermined quantities of water, polycation solution, and polyanion solution in this order, followed by salt solution. In other words, salt was distinctly added before the complex formation in the former protocol, while salt was added after complexation in the latter protocol.

Following these procedures, electrostatic assemblies of two polymer pairs of different chain lengths (PEO_{5K}-*b*-$PVBTMA_{50}$/PEO5K-*b*-PSS_{50} and PEO_{10K}-*b*-$PVBTMA_{100}$/ PEO_{10K}-*b*-PSS_{100}) were prepared with 500 mM NaBr; the size and size distribution were compared by DLS over two months, shown in Figure 2.7. It was observed that, for the direct dissolution method, both samples formed PEC-core micelles with relatively low colloidal polydispersities (< 0.20 by cumulant fitting) and mean hydrodynamic radius (R_h) of ca. 25 nm (Figure 2.7(a) and 2.7(b)). The size distribution broadened over the course of 70 days with sealed quiescent samples at room temperature. For the salt annealing method, however, the resulting electrostatic assemblies have a mean Rh of 100 nm with broad distributions (Figure 2.7(c) and 2.7(d)), which apparently exceeded the polymers contour length ($L_c \simeq 0.40N_{\mathrm{PEO}} + 0.26N_{\mathrm{PVBTMA}}$). Surprisingly, after 70 days, the sizes and polydispersity metrics of these assemblies evolved into smaller narrower values, which largely matched the micellar products created by the direct dissolution method. As a result, we speculate that these assemblies were likely kinetically trapped aggregates, facilitated by the interplay between strongly charged PVBTMA and PSS blocks.

This convergence can be understood in light of our conceptual understanding of the steps of complex formation. Polyelectrolyte complexation is probably driven by the electrostatic attraction between oppositely charged groups and promoted by the entropy gain from the release of counterions. In the *direct dissolution* method, salt was added to the stock solutions of polycation and polyanion before the complex formation step. The presence of salt may have suppressed the release of counterions upon complexation, which hindered the initial formation of the kinetically trapped aggregates. In comparison, in the salt annealing process, the PEC assemblies were preemptively formed before the addition of salt. The oppositely charged polyelectrolyte chains interconnected with each other rapidly due to the large entropy gain from the counterion release. These chains may have not reached their optimal configurations, and thus some PEO chains may be buried in interconnected complex domains. In other words, we posit that the rearrangement of the hydrophilic chains was

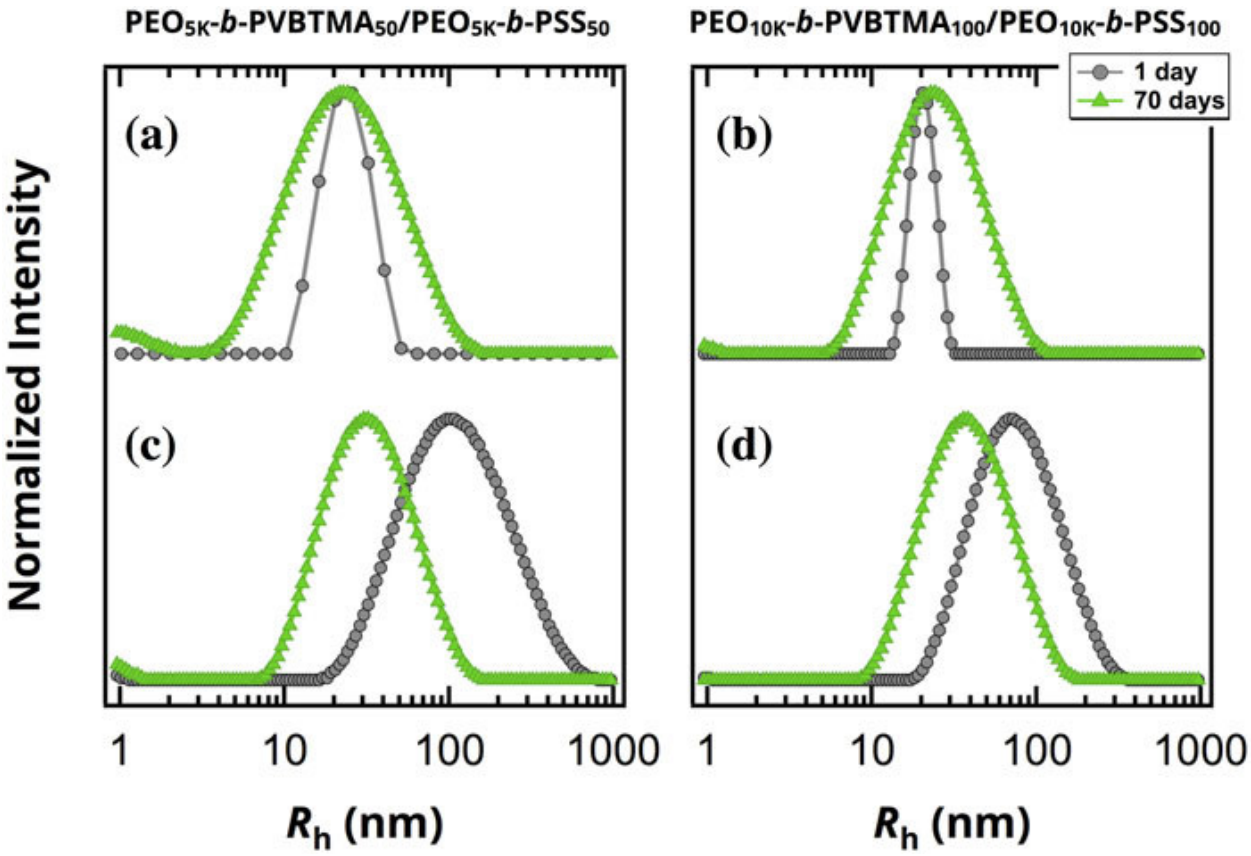

Figure 2.7: Evolution of hydrodynamic radius and radius distribution of polyelectrolyte complexes formed from PEO_{5K}-*b*-$PVBTMA_{50}$/PEO5K-*b*-PSS_{50} [(a) and (c)] and PEO_{10K}-*b*-$PVBTMA_{100}$/ PEO_{10K}-*b*-PSS_{100} with 500 mM NaBr prepared by the direct dissolution [(a) and (b)] and salt annealing protocols [(c) and (d)]

retarded by the large Debye screening length and the large entropic penalty associated with it. This results in the failure of forming uniform micelles with a hydrophilic corona and complexed core. After the salt was added, the interconnected complexes gradually equilibrated, and at over sufficient time, these electrostatic assemblies made from the two methods reached the similar micellar products because they were technically the same thermodynamic process. These observations motivated us to explore the underlying mechanism of structural evolution with additional complementary techniques.

It should be noted that the salt concentration and salt type were chosen based on our findings about the anions abilities to affecting the formation and stability of the polyelectrolyte complex assemblies. Our observation suggests that the heavier anions (i.e., $I^- > Br^- > Cl^-$) have stronger effect on the screening of the electrostatic interactions in the polyelectrolyte complex assemblies. A similar phenomenon has been reported in bulk complexes forming from two homo-polyelectrolytes.[3] This trend follows the Holfmeister series, which views Cl as a moderately inert anion and I as a chaotrope that increases polymer solubility.

2.3.4 Time-dependent structural evolution

Time-resolved DLS. The time dependence of the structural evolution of the electrostatic assemblies is shown in Figure 2.8. The sizes and size distributions were interpreted from the correlation functions in DLS and represented by intensity-averaged values using the NNLS algorithm. Compared with REPES, the NNLS algorithm used here is more sensitive with respect to multi-modal distributions; results analyzed with REPES are available in Figure 2.9. It was observed that both of the two samples PEO_{5K}-*b*-$PVBTMA_{50}$/PEO_{5K}-*b*-PSS_{50} and PEO_{10K}-*b*-$PVBTMA_{100}$/ PEO_{10K}-*b*-PSS_{100} showed two-population distributions within a short time after salt addition. As time elapsed, the sizes of the two polyelectrolyte assemblies became smaller and reduced to a single peak after 25 min or 130 min for the PEO_{5K}-*b*-$PVBTMA_{50}$/PEO_{5K}-*b*-PSS_{50} or PEO_{10K}-*b*-$PVBTMA_{100}$/ PEO_{10K}-*b*-PSS_{100}, respectively. The PEO_{5K}-*b*-$PVBTMA_{50}$/PEO_{5K}-*b*-PSS_{50} sample evolved into a

narrow single-peak distribution with an average diameter of 38 nm after 50 min, and the PEO_{10K}-*b*-$PVBTMA_{100}$/ PEO_{10K}-*b*-PSS_{100} sample showed a single population with an diameter of 75 nm with low polydispersity after 400 min. It should be noted that at 400 min, the PEO_{10K}-*b*-$PVBTMA_{100}$/ PEO_{10K}-*b*-PSS_{100} sample had not reached its equilibrium state since the mean size continued to decrease to 50 nm after 21 hours.

Based on the phenomena we observe, we hypothesize that the overall structural evolution can be described into two stages: (1) disassembly of interconnected aggregates, followed by (2) redistribution of the incipient individual assemblies. In the initial state, polyelectrolyte chains are kinetically trapped due to the interplay between electrostatic interaction, hydrophilic-hydrophobic balance, and entropic penalty association with counterion relocation. Upon salt addition, the electrostatic interactions are weakened because the charged sites on the polymer chains are screened by the abundant counterions. Consequently, the irregularly shaped aggregate complexes broke apart, which was evidenced by the size reduction detected by DLS. The time scale of the structural evolution of this step was relatively fast and dependent on the molecular weight of the polyelectrolytesthe PEO_{5K}-*b*-$PVBTMA_{50}$/PEO_{5K}-*b*-PSS_{50} evolved into a single distribution after 25 min (Figure 2.8(a) to (e)) and the PEO_{10K}-*b*-$PVBTMA_{100}$/ PEO_{10K}-*b*-PSS_{100} transformed to a sole peak after 220 min (Figure 2.8 (g) to (k)). At the second stage, the nascent individual PEC assemblies redistributed to smaller sizes and narrower distribution over a wide range of time, as the data shown in Figure 2.8 (e) to (f) for PEO_{5K}-*b*-$PVBTMA_{50}$/PEO_{5K}-*b*-PSS_{50} and Figure 2.8 (k) to (l) for PEO_{10K}-*b*-$PVBTMA_{100}$/PEO_{10K}-*b*-PSS_{100}. This process was time consuming compared to the disintegration of interconnected aggregates in the first stage. The prolonged redistribution kinetics may probably be attributed to the entropic penalty to breaking down the paired charged sites in the complex cores as well as the additional energetic penalty resulting from the steric repulsion provided by the hydrophilic corona blocks. This size redistribution may be directly associated with the chain exchange process in self-assembled polymeric nanoparticles, which are subject to micelle collision and fragmentation

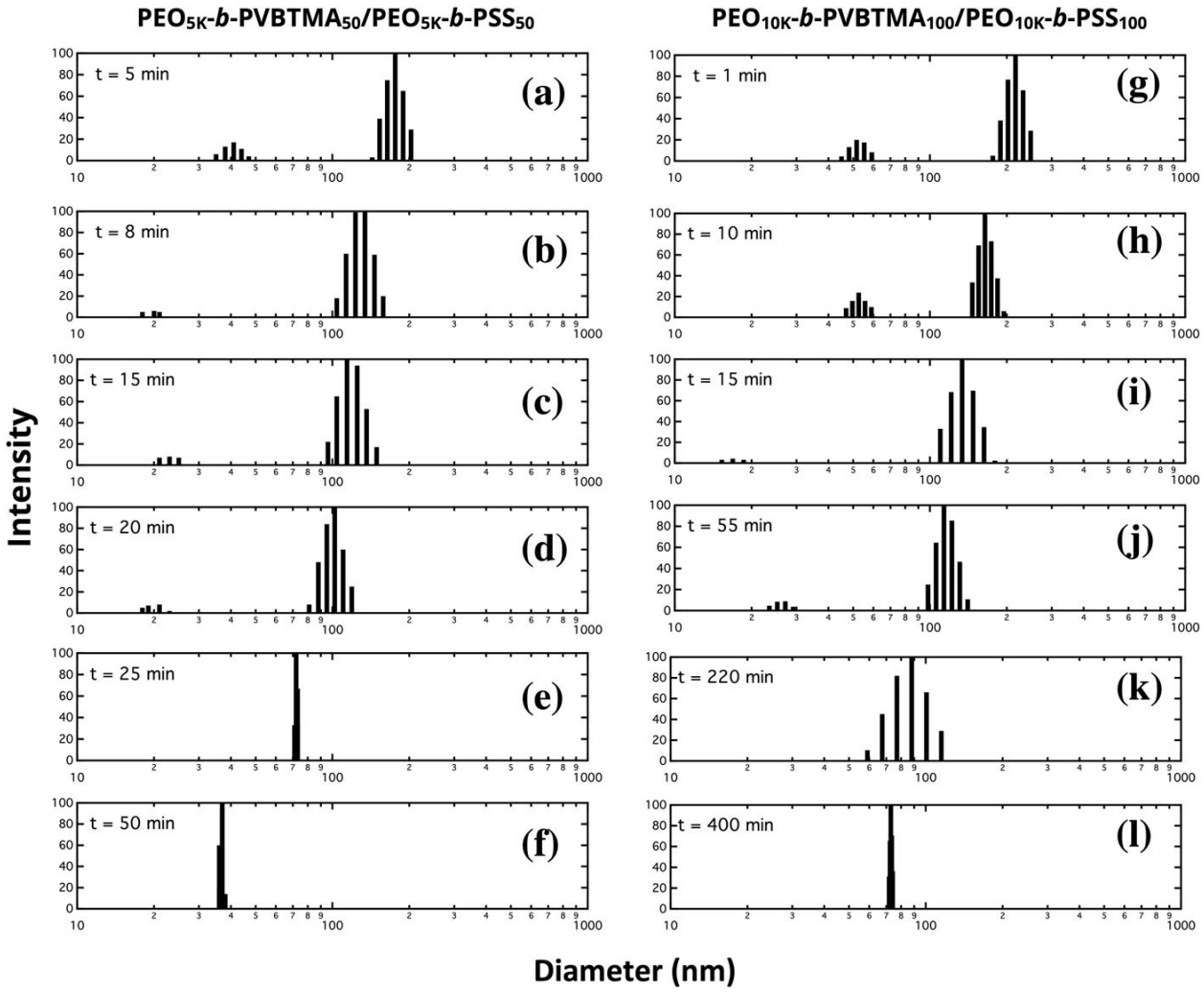

Figure 2.8: The time-dependent structural evolution of sample PEO_{5K}-*b*-$PVBTMA_{50}$/PEO_{5K}-*b*-PSS_{50} at 500 mM NaBr at time moments of 5 min (a), 8 min (b), 15 min (c), 20 min (d), 25 min (e), and 50 min (f). The size evolution of the sample PEO_{10K}-*b*-$PVBTMA_{100}$/ PEO_{10K}-*b*-PSS_{100} at 500 mM NaBr at time moments of 1 min (g), 10 min (h), 15 min (i), 55 min (j), 220 min (k), and 400 min (l). The correlation functions were deconvoluted with the NNLS algorithm.

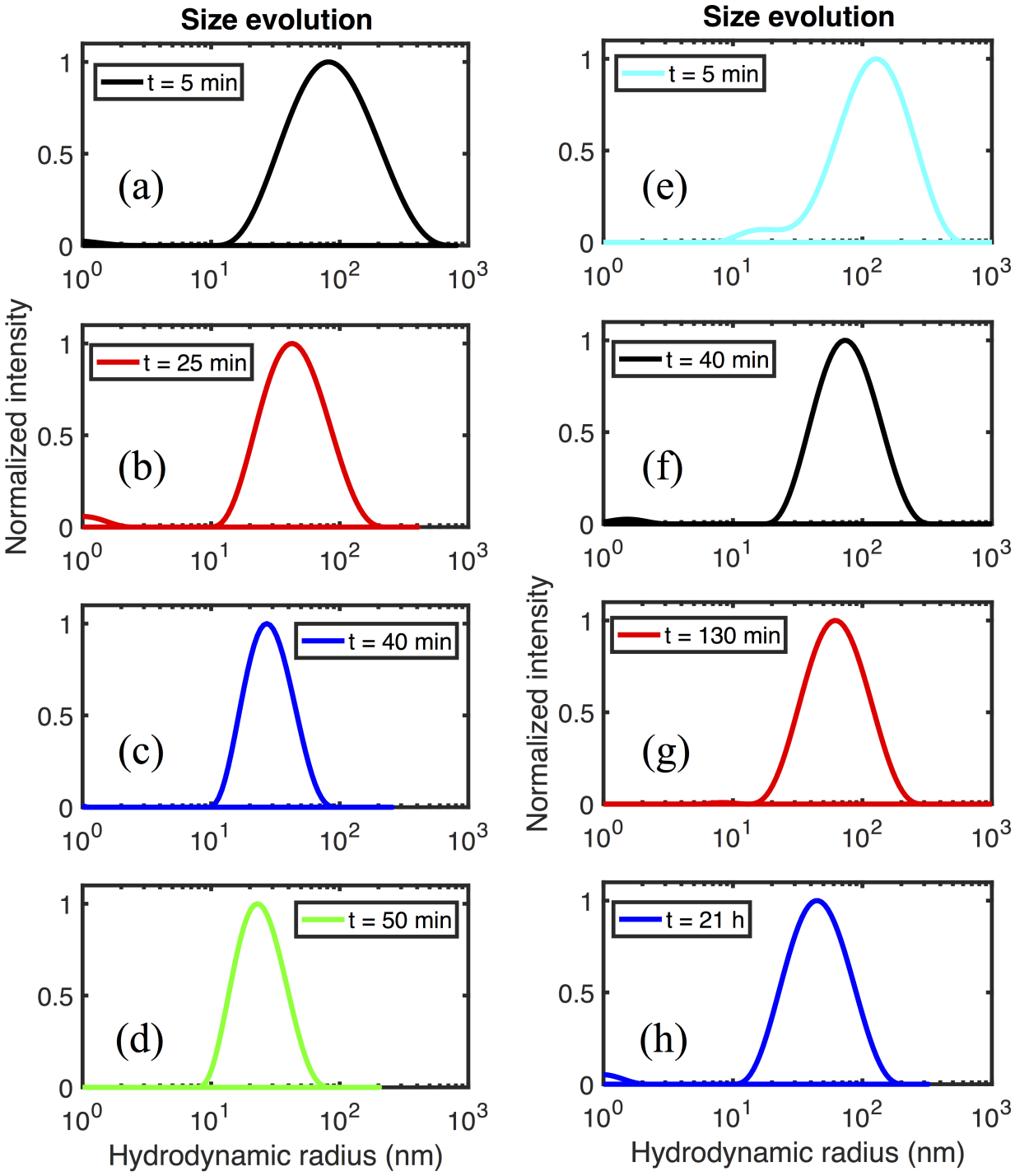

Figure 2.9: The size evolution of the sample PEO_{5K}-*b*-$PVBTMA_{50}$/PEO_{5K}-*b*-PSS_{50} at 500 mM NaBr at time moments of 5 minutes (a), 25 minutes (b), 40 minutes (c), and 50 minutes (d). The size evolution of the sample PEO_{10K}-*b*-$PVBTMA_{100}$/ PEO_{10K}-*b*-PSS_{100} at 500 mM NaBr at time moments of 5 minutes (e), 40 minutes (f), 130 minutes (g), and 21 hours (h). The correlation functions were deconvoluted by the REPES algorithm.

Table 2.2: The R_gs of equilibrium structures.

Sample (with 500 mM NaBr)	R_g
PEO_{5K}-*b*-$PVBTMA_{50}$/ PEO_{5K}-*b*-PSS_{50}	9.3 ± 0.21
PEO_{10K}-*b*-$PVBTMA_{100}$/ PEO_{10K}-*b*-PSS_{100}	9.8 ± 0.35

over long periods of time. Similar observations have been reported in the amphiphilic block copolymer and cationic polyelectrolyte micelles,[52, 53, 43, 54] although the exact mechanism of chain exchange kinetics may be somewhat different for polyelectrolyte complex micelles in the present work.

SAXS on the equilibrium structures. The physical properties of the samples PEO_{5K}-*b*-$PVBTMA_{50}$/PEO_{5K}-*b*-PSS_{50} and PEO_{10K}-*b*-$PVBTMA_{100}$/ PEO_{10K}-*b*-PSS_{100} with 500 mM of NaBr were first characterized by saxs. Both the two samples were prepared via the *Direct Dissolution* mehtod. As we stated above, samples prepared through direct dissolution tend to reach their equilibrium states in a short time period. As shown in Figure 2.10 and Figure 2.11, first, the intensities of these two self-assembled polyelectrolyte complexes with 500 mM NaBr are low, and the noises are high. It is probably because at this salt concentration, the charges of the polyelectrolytes are substantially screened, leading to weak ionic interactions between oppositely charged polyemr chains. Second, no aggregates with large sizes are seen, which indicates that these structures are probably in their equilibrium states. Their R_gs are extracted by the Guinier approxiamtion, and the results are shown in Table 2.2.

Furthermore, multi-angle DLS is employed to dive into the structural information at the lower-q range which is beyond the scope of SAXS measurements. The curves of intensity versus q value of the two samples are are shown in The studied q range is 0.0034 $Å^{-1}$ < q < 0.0256 $Å^{-1}$, the minimum of which (0.0034 $Å^{-1}$) is slightly than that of the SAXS measurement (0.005 $Å^{-1}$). Results shown in Figure 2.12 shows linearities of the intensity over the q range. The measured angle ranges from 15 to 155 ^{o}C.

Two-level Beaucage model fitting. SAXS was employed to further investigate the

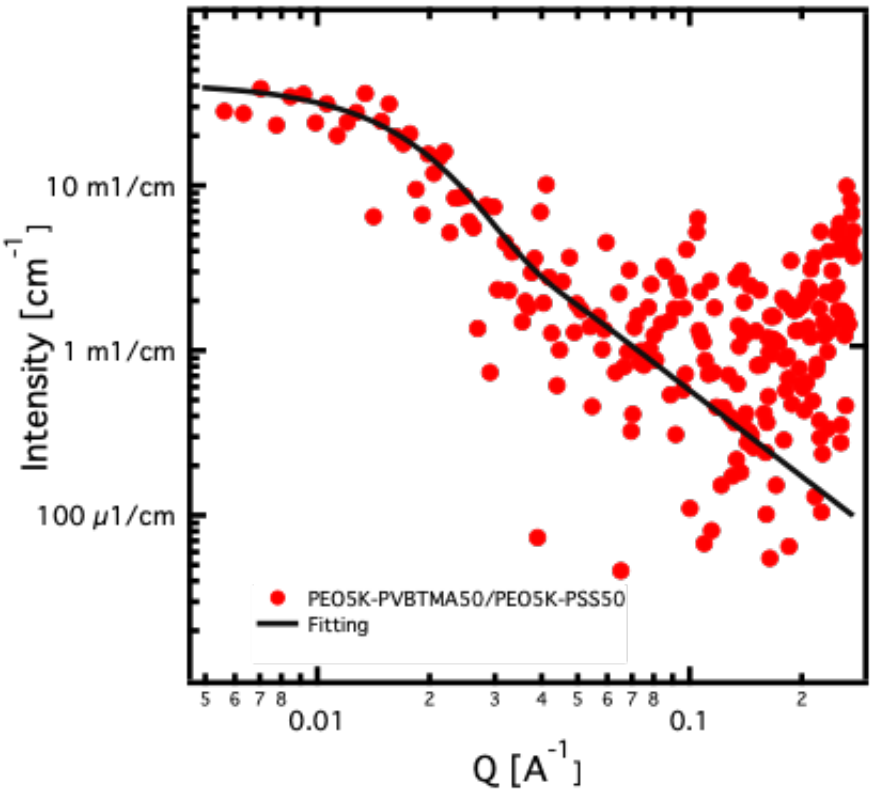

Figure 2.10: The fitting results of the SAXS data of sample PEO_{5K}-*b*-$PVBTMA_{50}$/PEO_{5K}-*b*-PSS_{50} at the concentration of 500 mM of NaBr prepared via the Direct Dissolution method.

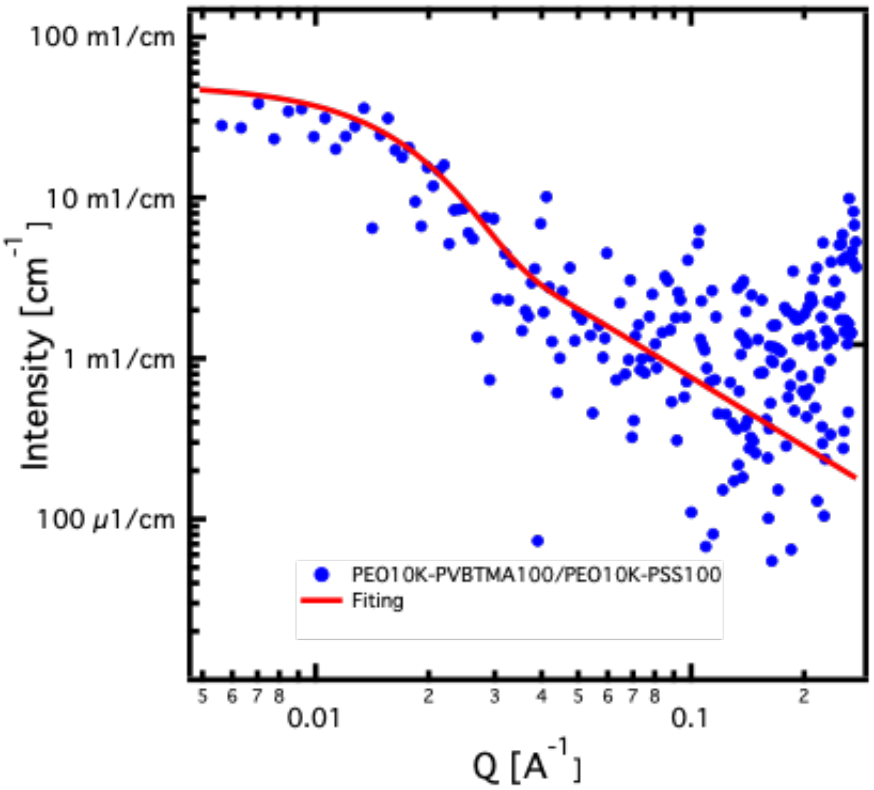

Figure 2.11: The fitting results of the SAXS data of sample PEO_{10K}-*b*-$PVBTMA_{100}$/ PEO_{10K}-*b*-PSS_{100} (b) at the concentration of 500 mM of NaBr prepared via the Direct Dissolution method.

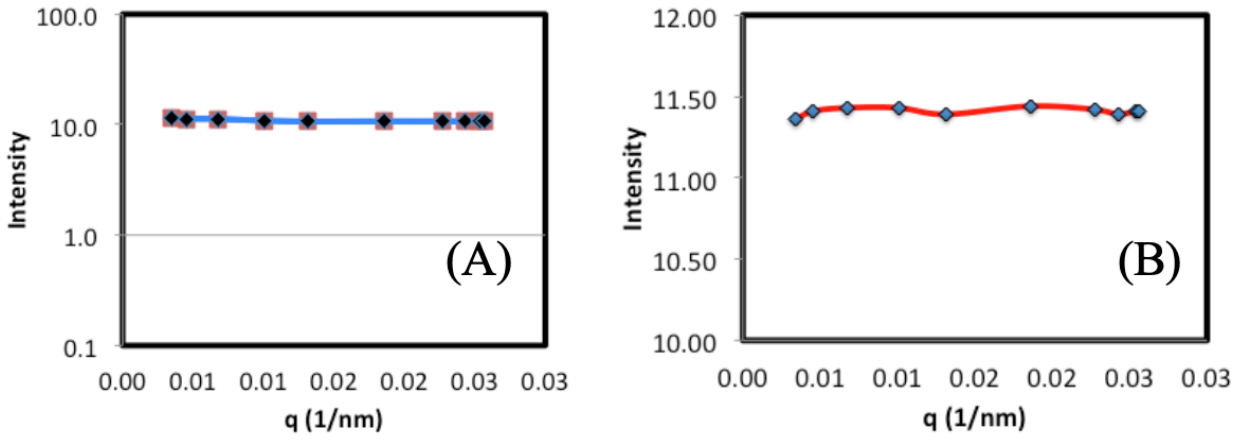

Figure 2.12: Results of multi-angle static light scattering on micelles PEO_{5K}-*b*-$PVBTMA_{50}$/ PEO_{5K}-*b*-PSS_{50} (A) and PEO_{10K}-*b*-$PVBTMA_{100}$/ PEO_{10K}-*b*-PSS_{100} (B).

structural evolution of the non-equilibrated electrostatic assemblies as a function of NaCl from 100 mM to 1000 mM concentration. All curves exhibited an upturn at the low q regime ($q < 0.01$ Å^{-1}), which suggested the presence of large aggregates with $R_g > 200$ nm ($R_g = 2\pi/q_{min}$) (see Figure 2.13). More information was obtained by fitting the SAXS data using the two-level Beaucage model, as described in the experimental details.[55, 40]

This Beaucage model is used to fit SAXS data with levels composed of a Guinier part and a power law tail. It can handle SAXS features for which an exact scatter model is difficult or impossible. Here, the two levels were divided at the $q = 0.01$ Å^{-1}, and each length level was represented by an R_g and a power law slope. The fitting parameters were shown in Tables I and II. The R_g values of the $q < 0.01$ Å^{-1} regimes were not given because of the absence of the corresponding Guinier regions.

We divide a SAXS curve into two levels by making $q = 0.01$ Å^{-1} as a watershed. By doing that, we speculate that: (1) the $q > 0.01$ Å^{-1} level has a Guinier part and a power law tail, while the $q < 0.01$ Å^{-1} level has a power law tail only (its Guinier region is out of the probed minimum q range), and (2) the power law tail of $q < 0.01$ Å^{-1} plummets dramatically in the $q > 0.01$ Å^{-1} level, which makes trivial contribution to the Guinier part and power law tail in the $q > 0.01$ Å^{-1} region. The fits of the SAXS curves are shown in Figures 2.14 and 2.15.

Table 2.3: Mass fractals of the sample PEO_{10K}-*b*-$PVBTMA_{100}$/PEO_{10K}-*b*-PSS_{100} in the range of q >0.01Å^{-1}.

Salt (mM)	q >0.01 Å^{-1}	
	Mass fractal	B2 (cm^{-1} sr^{-1})
100	2.05 ± 0.0050	$0.78 \times 10^{-5} \pm 1.6 \times 10^{-7}$
250	1.92 ± 0.0058	$1.29 \times 10^{-5} \pm 2.8 \times 10^{-7}$
500	1.92 ± 0.0057	$1.30 \times 10^{-5} \pm 2.0 \times 10^{-7}$
600	1.94 ± 0.0077	$1.11 \times 10^{-5} \pm 5.3 \times 10^{-7}$
1000	1.63 ± 0.0055	$5.65 \times 10^{-5} \pm 1.3 \times 10^{-6}$

The second columns of Tables 2.3 and 2.5 contain the Porod exponents that correspond to mass fractals of the large electrostatic assemblies. At the low to intermediate salt concentration of 100-600 mM, the Porod exponents were close to 2.0, which indicates the existence

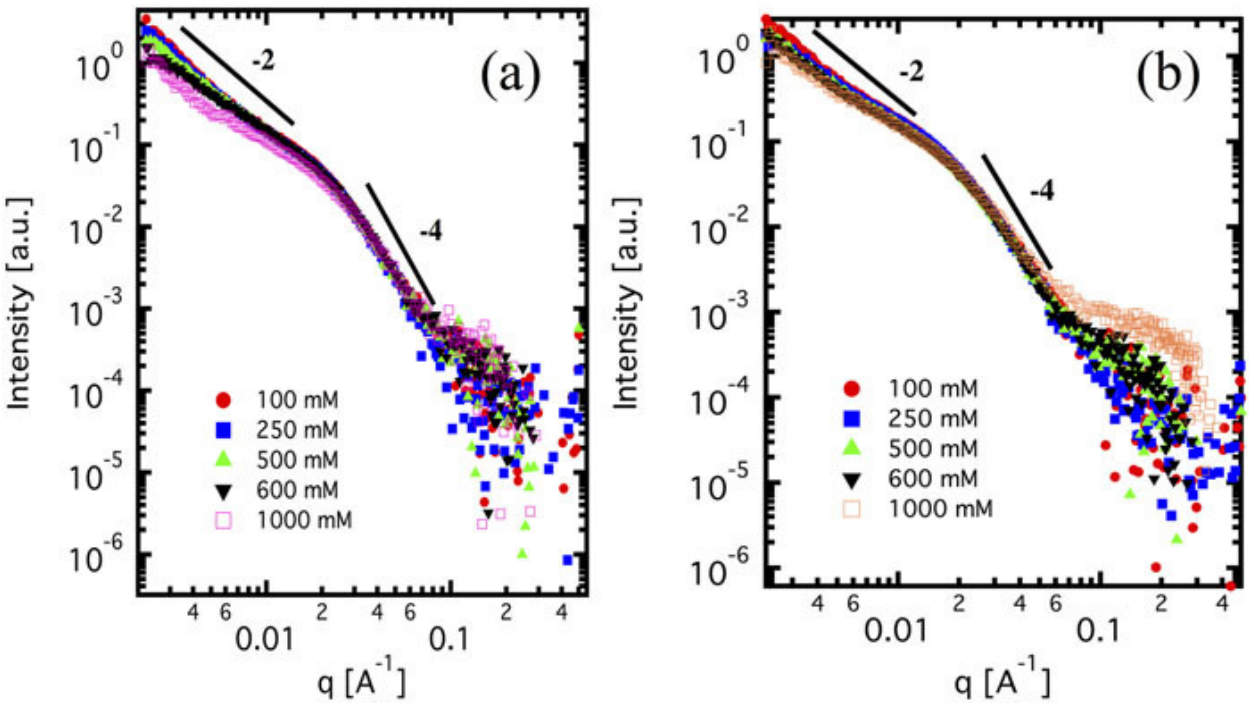

Figure 2.13: SAXS curves for samples PEO_{5K}-*b*-$PVBTMA_{50}$/PEO_{5K}-*b*-PSS_{50} and PEO_{10K}-*b*-$PVBTMA_{100}$/ PEO_{10K}-*b*-PSS_{100} (b) at different concentrations of NaCl. The slopes of 2 and 4 are shown as references that correspond to Gaussian polymer coils and smooth spherical surfaces, respectively.

of mass fractals of 3-dimensional networks with branching and connecting points.[42] We attribute this to the breakup of kinetically trapped aggregates at high ionic strength. This transition is in line with the discussion of chain rearrangements in the DLS experiments. Column 2 in Tables 2.4 and 2.6 shows the evolution of the radius of gyration of the internal structures, and it decreases from 11.1 nm to 9.0 nm over the salt concentration range. The Porod exponents corresponding to surface fractals in column 2 in Table 2.4 between 3.5 and 3.9 (and these in Table 2.6 between 3.1 and 3.9) represent the internal structures and indicate the existence of rough spherical surfaces. Taking the above information into consideration, it is reasonable to infer that the electrostatic assemblies are constructed by local fuzzy globular complexes and interconnected segments between them. The similar results have been founded in the PEO_{5K}-*b*-$PVBTMA_{50}$/PEO_{5K}-*b*-PSS_{50} sample. It should be noted that, in the high q region of the PEO_{10K}-*b*-$PVBTMA_{100}$/PEO_{10K}-*b*-PSS_{100} sample with 1.0 M salt,

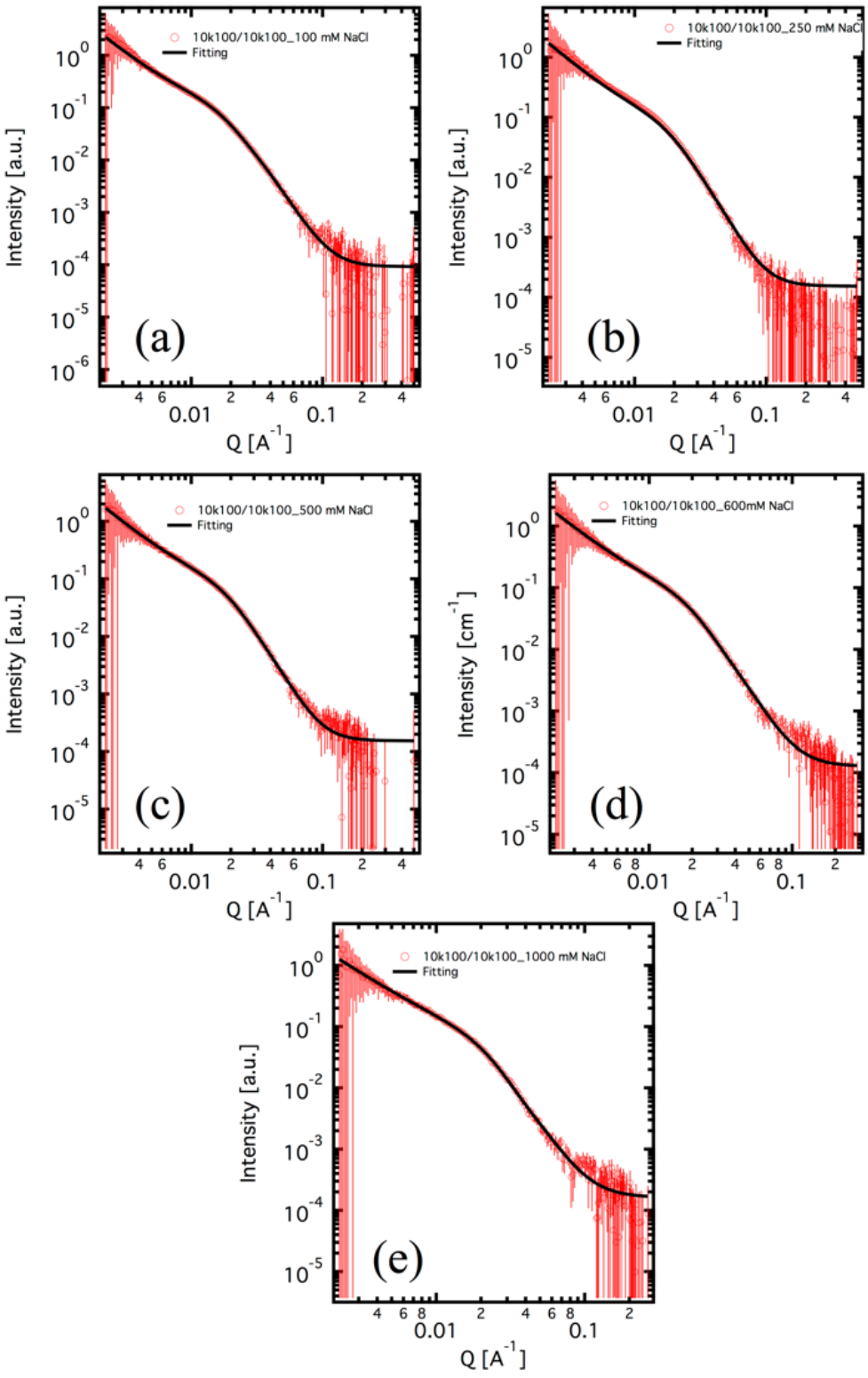

Figure 2.14: The fitting results of the SAXS data of sample PEO_{5K}-*b*-$PVBTMA_{50}$/PEO_{5K}-*b*-PSS_{50} at NaCl of 100 mM (a), 250 mM (b), 500 mM (c), 600 mM (d), and 1000 mM (e). The curves were fitted by the two-level Beaucage model.

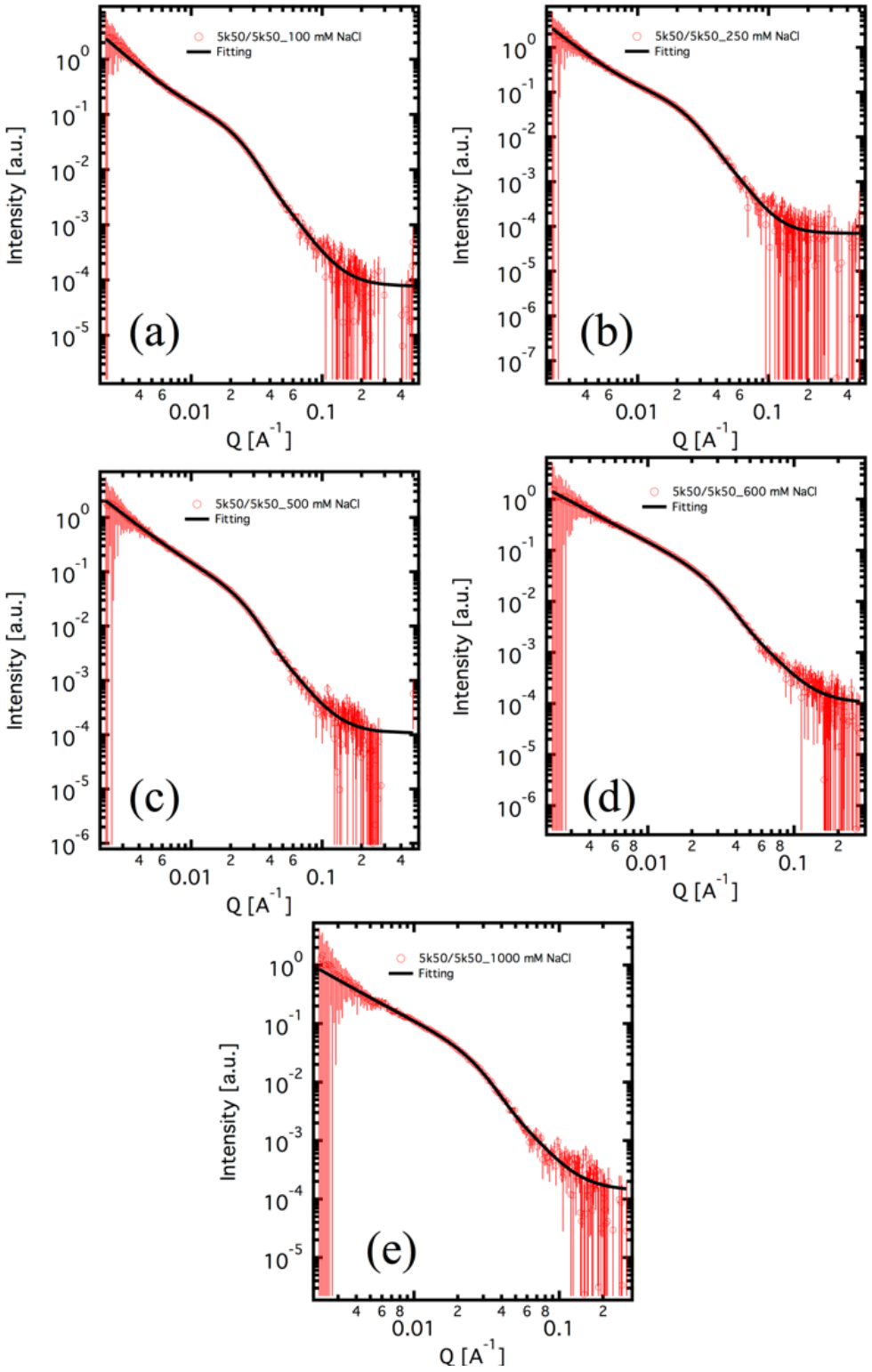

Figure 2.15: The fitting results of the SAXS data of sample PEO_{10K}-*b*-$PVBTMA_{100}$/PEO_{10K}-*b*-PSS_{100} at NaCl of 100 mM (a), 250 mM (b), 500 mM (c), 600 mM (d), and 1000 mM (e). The curves were fitted by the two-level Beaucage model.

Table 2.4: The surface fractal and R_g of the sample PEO_{10K}-*b*-$PVBTMA_{100}$/PEO_{10K}-*b*-PSS_{100} in the range of q <0.01Å^{-1}.

Salt (mM)	q <0.01Å^{-1}			
	R_g (nm)	Surface fractal	B1 (cm^{-1} sr^{-1})	G1c (cm^{-1} sr^{-1})
100	11.1 ± 0.12	3.83 ± 0.003	$2.46 \times 10^{-8} \pm 2.1 \times 10^{-10}$	$0.1826 \pm 5.8 \times 10^{-4}$
250	9.97 ± 0.24	3.93 ± 0.025	$1.72 \times 10^{-8} \pm 1.4 \times 10^{-9}$	$0.1263 \pm 4.0 \times 10^{-4}$
500	9.97 ± 0.12	3.93 ± 0.011	$1.64 \times 10^{-8} \pm 4.2 \times 10^{-10}$	$0.1263 \pm 3.9 \times 10^{-4}$
600	10.0 ± 0.19	3.81 ± 0.013	$2.40 \times 10^{-8} \pm 9.5 \times 10^{-10}$	$0.1257 \pm 6.9 \times 10^{-4}$
1000	9.02 ± 0.21	3.57 ± 0.018	$5.73 \times 10^{-8} \pm 3.2 \times 10^{-9}$	$0.0921 \pm 7.0 \times 10^{-4}$

Table 2.5: Mass fractals of the sample PEO_{5K}-*b*-$PVBTMA_{50}$/PEO_{5K}-*b*-PSS_{50} in the range of q >0.01Å^{-1}.

Salt (mM)	q >0.01 Å^{-1}	
	Mass fractal	B2 (cm^{-1} sr^{-1})
100	2.11 ± 0.0038	$5.68 \times 10^{-6} \pm 7.6 \times 10^{-8}$
250	2.13 ± 0.0041	$2.03 \times 10^{-6} \pm 5.1 \times 10^{-8}$
500	1.92 ± 0.0021	$1.63 \times 10^{-5} \pm 1.6 \times 10^{-7}$
600	1.54 ± 0.0022	$1.00 \times 10^{-4} \pm 9.8 \times 10^{-7}$
1000	1.46 ± 0.0040	$1.08 \times 10^{-4} \pm 2.7 \times 10^{-7}$

there was an approximate Guinier plateau, which might be caused by the smaller structures in the system.

Cryo-TEM. Cryo-TEM is also employed to visualize the intermediate metastable morphologies of the electrostatic assemblies (see Figure 2.16). As expected, without salt, the non-equilibrium assemblies adopted the morphology of polydispersed interconnected aggregates; at high ionic strength, the aggregates were broke apart. For instance, the mean geometric diameter of the PEO_{10K}-*b*-$PVBTMA_{100}$/PEO_{10K}-*b*-PSS_{100} assemblies decreases from 83 ± 44 nm (95% CI = 67, 98) at no salt to 34 ± 17nm (95 %CI= 31, 38) with 1.0 M NaCl, a near 2.5 ticle distribution was affected by salt. The interquartile range (IQR) and corresponding outliers are calculated. In the same PEO_{10K}-*b*-$PVBTMA_{100}$/PEO_{10K}-*b*-PSS_{100} example, the IQR of each respective sample is 56 nm and 21 nm, with remaining larger particles at 1.0 M NaCl identified as outliers. At 1.0 M NaCl, the IQR of PEO_{5K}-*b*-$PVBTMA_{50}$/PEO_{5K}-*b*-PSS_{50} is similarly 14 nm. Overall, these results are consistent with the aforementioned SAXS data. One can observe that, even at high salt concentration where

Table 2.6: The surface fractal and R_g of the sample PEO_{5K}-*b*-$PVBTMA_{50}$/PEO_{5K}-*b*-PSS_{50} in the range of q <0.01Å^{-1}.

Salt (mM)	q <0.01Å^{-1}			
	R_g (nm)	Surface fractal	B1 (cm^{-1} sr^{-1})	G1c (cm^{-1} sr^{-1})
100	8.62 ± 0.07	3.37 ± 0.011	$1.08 \times 10^{-7} \pm 4.9 \times 10^{-9}$	$0.1059 \pm 3.2 \times 10^{-4}$
250	8.73 ± 0.10	3.94 ± 0.015	$1.72 \times 10^{-7} \pm 7.4 \times 10^{-10}$	$0.1041 \pm 3.5 \times 10^{-4}$
500	7.94 ± 0.10	3.22 ± 0.018	$1.58 \times 10^{-7} \pm 8.7 \times 10^{-9}$	$0.0701 \pm 1.6 \times 10^{-4}$
600	7.06 ± 0.20	3.36 ± 0.024	$1.13 \times 10^{-7} \pm 7.6 \times 10^{-9}$	$0.0391 \pm 2.1 \times 10^{-4}$
1000	7.12 ± 0.26	3.13 ± 0.033	$2.26 \times 10^{-7} \pm 2.1 \times 10^{-8}$	$0.0391 \pm 1.3 \times 10^{-4}$

NaCl > 1.0 M, the shape of the electrostatic assemblies is non-spherical. This may be attributed to the chemical nature of the strongly charged PVBTMA and PSS blocks, as they form precipitate bulk complexes, and due to the low contrast between the PEO and the background, the observed objects are primarily polyelectrolyte complexes. A similar morphology has been found in metal containing complex coacervate core micelles.[56] The shape of the complexes may become more globular at higher ionic strength where PVBTMA and PSS blocks form soluble coacervates. The results of PVBTMA/PSS bulk complexes are given in Figure 2.17.

2.3.5 Salt annealing kinetics

The kinetics of the salt annealing process was investigated by time-resolved dynamic light scattering, where the average intensity was collected as a function of time immediately after salt was added. The relaxation functions are shown in Figure 2.18 and are best fitted using the Kohlrausch-Williams-Watts (KWW)[57] equation that can be expressed as

$$\mathrm{I} = \mathrm{A}\exp\left[-\left(\frac{\mathrm{t}}{\tau}\right)^{\beta}\right] + \mathrm{B} \tag{2.6}$$

where I is the intensity, τ is the characteristic relaxation time, and β is the KWW exponent ranging from 0 to 1 and is used to describe a distribution centered about the mean relaxation

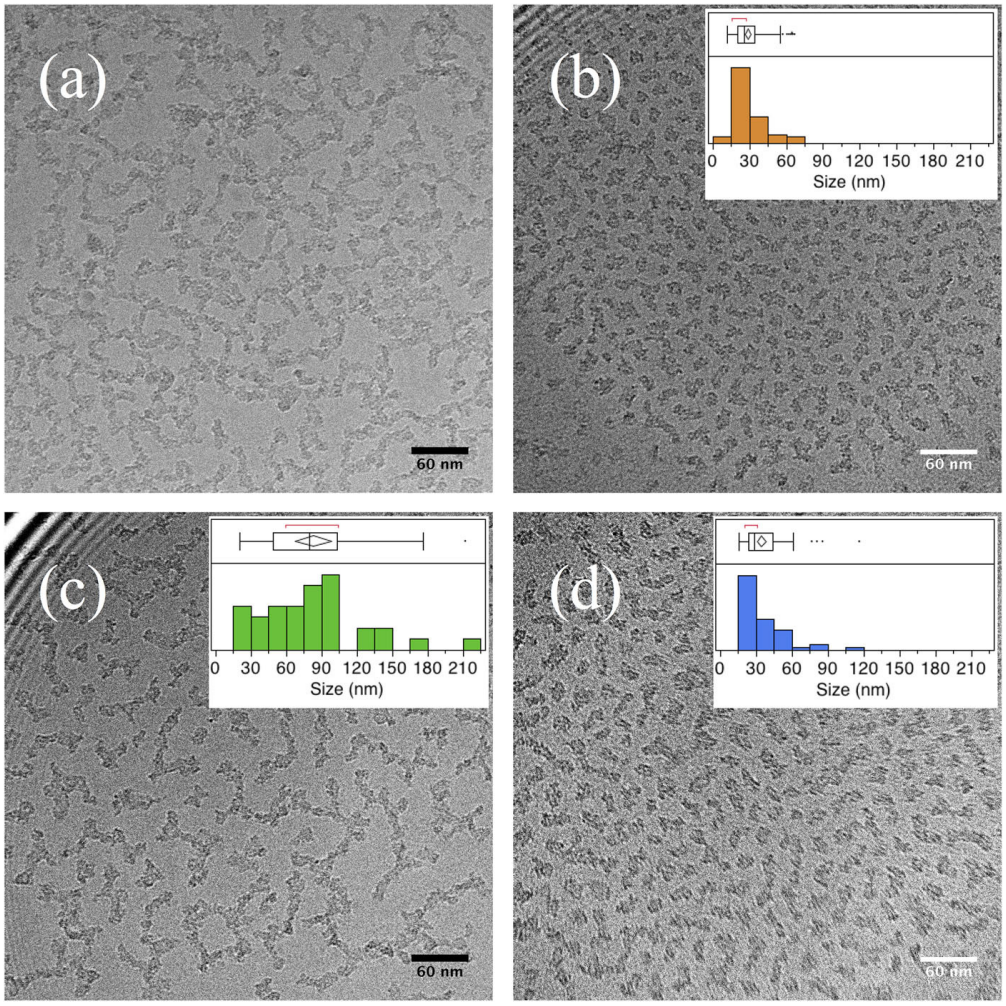

Figure 2.16: Cryo-TEM images of polyelectrolyte complex assemblies: PEO_{5K} -*b*- $PVBTMA_{50}$ / PEO_{5K} -*b*- PSS_{50} without salt (a) and with 1.0M NaCl (b), PEO_{10K} -*b*- $PVBTMA_{100}$ / PEO_{10K} -*b*- PSS_{100} without salt (c) and with 1.0M NaCl (d). The insets are the size distribution based on the corresponding images.

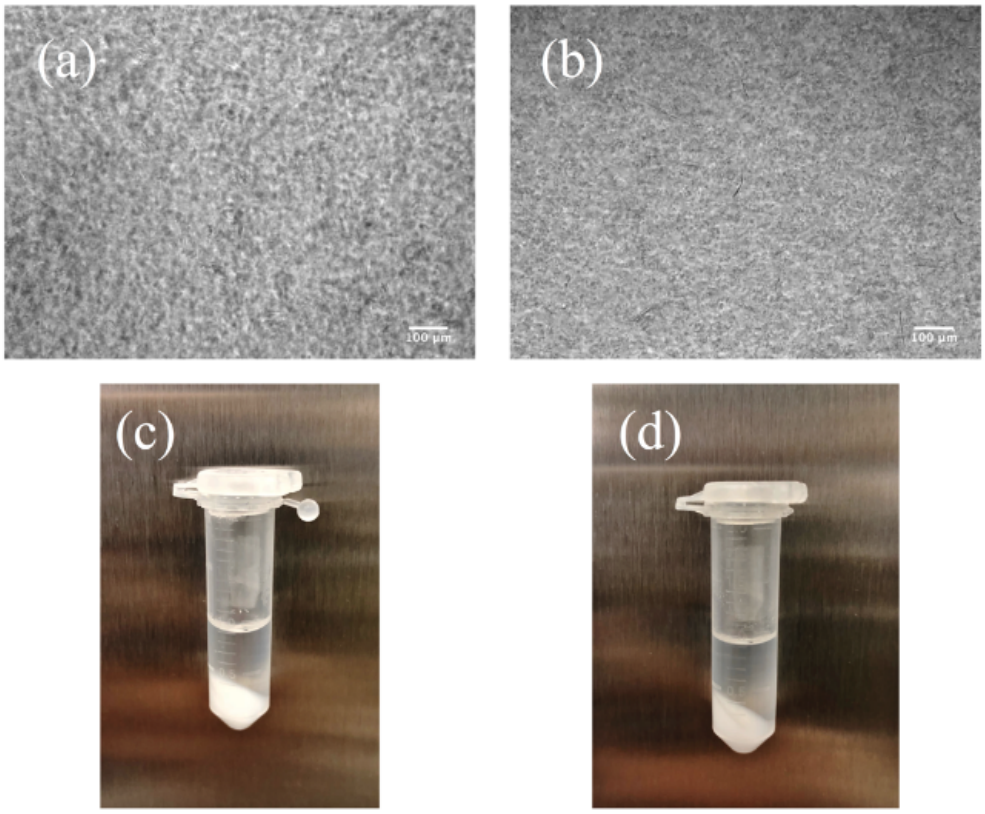

Figure 2.17: Microscopic images of bulk complexes formed by $PVBTMA_{100}$ and PSS_{80} at the ionic strength of 0 mM of NaCl (a) and 1000 mM of NaCl (b). The contrast was enhanced using ImageJ. Image (c) and (d) were snapshots of the sample at 0 mM and 1000 mM of NaCl, respectively.

Table 2.7: Relaxation time, KWW exponents, and mean relaxation time of the decay of the polyelectrolyte complexes.

Temp (K)	τ (min)	β
T = 293	61.54	2.0
T = 330	51.77	1.84
T = 350	38.57	1.66

time, which is calculated as the first moment of the stretched exponential by

$$\langle \tau \rangle = \frac{\tau_{\mathrm{KWW}}}{\beta} \Gamma \left(\frac{1}{\beta} \right) \tag{2.7}$$

where is Γ the gamma function. The KWW stretched exponential function is often used as a phenomenological description of relaxation in disordered systems, such as glasses,[58] polymer melts,[59, 60, 61] and protein gels.[62] For instance, Tang et al. used the KWW model to discriminate the broad rheological relaxation behaviors in associative protein hydrogels.[62] Because the interesting parallels between temperature and salt have been previously demonstrated for PEC assemblies (e.g., time-salt superposition of rheological properties),[63] we attempted to use the KWW model to elucidate the relaxation behaviors of the PEO-*b*-PVBTMA/PEO-*b*-PSS assemblies prepared with the salt annealing method.

The KWW fitting parameters are shown in Table III. It is apparent that the decay rate is strongly dependent on the molecular weight of the polyelectrolytes, with the PEO_{5K}-*b*-$PVBTMA_{50}$/PEO_{5K}-*b*-PSS_{50} micelles (τ = 8.90 min) decaying much faster than the PEO_{10K}-*b*-$PVBTMA_{100}$/PEO_{10K}-*b*-PSS_{100} micelles (τ = 56.6 min). This matched well to the time scales of the size evolution of the assemblies in the aforementioned DLS results. Moreover, two stretched exponents β of 0.82 and 0.30 are obtained, which suggests the presence of wide spectrum relaxation behaviors in the salt annealing process. This broadly distributed relaxation is, to a large extent, originated from the heterogeneous kinetically trapped electrostatic assemblies such as the non-uniform distribution of charged sites and chain entanglement, which was supported by the observation that the PEO_{10K}-*b*-$PVBTMA_{100}$/PEO_{10K}-*b*-PSS_{100} sample (containing more charged sites and longer chain

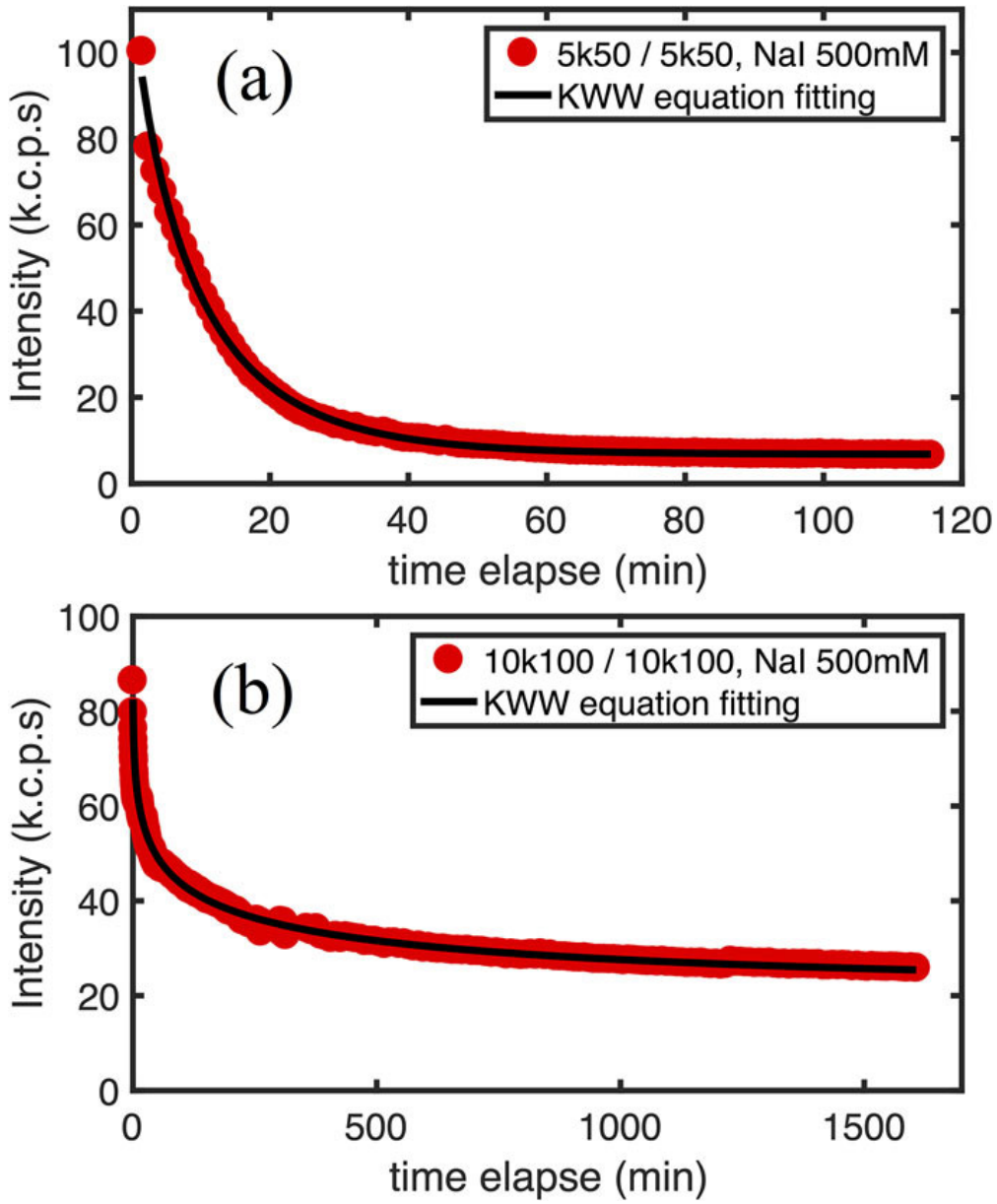

Figure 2.18: The decay of the intensity over time (red dots) fit to a stretched exponential function (block line) for the sample PEO_{5K}-*b*-$PVBTMA_{50}$/PEO_{5K}-*b*-PSS_{50} at 500 mM NaI (a) and PEO_{10K}-*b*-$PVBTMA_{100}$/PEO_{10K}-*b*-PSS_{100} at 500 mM NaI (b).

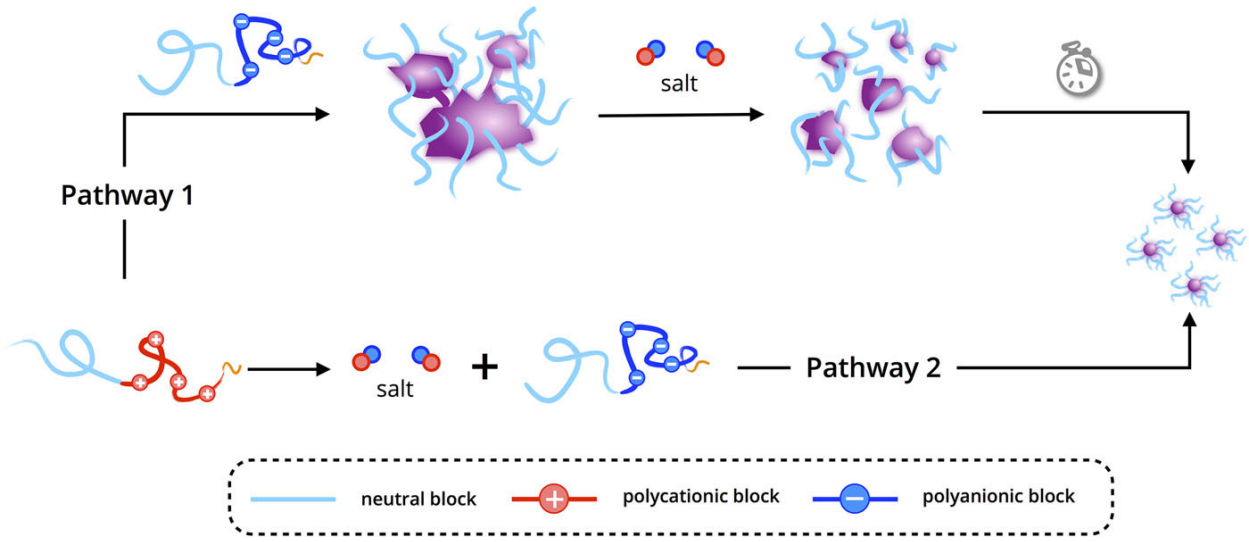

Figure 2.19: Schematic representation of the time-resolved morphological evolution of polyelectrolyte complexes formed from the non-equilibrium assembly (Pathway 1, the *salt annealing* protocol) and equilibrium approach (Pathway 2, the *direct dissolution* protocol).

blocks) exhibited a much longer and broader relaxation kinetics than those of the PEO_{5K}-*b*-$PVBTMA_{50}$/PEO_{5K}-*b*-PSS_{50} sample. To the best of our knowledge, this is the first demonstration of how the KWW model might describe the relaxation kinetics of self-assembled polyelectrolyte complexes that are subjected to salt.

2.4 Concluding Remarks

In this chapter, we show that self-assembled polyelectrolyte complexes with metastable morphologies are formed from strongly charged polyelectrolytes. The morphological transformation and relaxation behaviors of the resulting non-equilibrium aggregates are examined upon the addition of salt. These non-equilibrium assemblies has a significant structural inhomogeneity and consisted of moderately salt-resistant internal complexes and salt-susceptible interconnected components. The irregularly shaped interconnected electrostatic aggregates start to disintegrate in the presence of strong salts and high ionic strengths.

The temporal disintegration of the kinetically trapped assemblies can be discriminated as a two-step process: a fast mode of the breakdown of the interconnected parts and a slow mode

of the redistribution of the nascent individual assemblies. The whole process is schematically represented in Figure 2.19. This feature of generating nano-scale soluble polyelectrolyte micelles from kinetically trapped microscopic assemblies over time can be potentially exploited for the controlled release of therapeutics. Future work will be emphasized on the chain conformational transition in polyelectrolyte precipitates and soluble complexes, the role of chain exchange in the electrostatic assembly redistribution, and the production of polyelectrolyte complex micelles from non-equilibrium polyelectrolyte complexes in a controlled manner. A relevant study about kinetic trapping reversible coordination supramolecules in polyelectrolyte assemblies will also be investigated. We anticipate that the results presented here will attract attention and encourage effort to the non-equilibrium phenomena of polyelectrolyte complexes and will bring new insights into design ideal charged macromolecule-based systems for various application.[61]

References

[1] David C. Sherrington and Kirsti A. Taskinen. Self-assembly in synthetic macromolecular systems via multiple hydrogen bonding interactions. *Chem. Soc. Rev.*, 30:83–93, 2001.

[2] O Ikkala and G.-J. ten Brink. Functional Materials Bades on Self-Assembly of Polymeric Supramolecules. *Science*, 295:2407, 2002.

[3] Sarah L Perry, Lorraine Leon, Kyle Q Hoffmann, Matthew J Kade, Dimitrios Priftis, Katie A Black, Derek Wong, Ryan A Klein, Charles F Pierceiii, Khatcher O Margossian, Jonathan K Whitmer, Jian Qin, Juan J De Pablo, and Matthew Tirrell. *Nat. Commun.*

[4] Frank Biedermann and Hans Jörg Schneider. Experimental Binding Energies in Supramolecular Complexes. *Chem. Rev.*, 116(9):5216–5300, 2016.

[5] Hans Jörg Schneider and Robert M. Strongin. Supramolecular interactions in chemomechanical polymers. *Acc. Chem. Res.*, 42(10):1489–1500, 2009.

[6] Zhijie Zhang, Quan Chen, and Ralph H. Colby. Dynamics of associative polymers. *Soft Matter*, 14:2961–2977, 2018.

[7] Javier Martí-Rujas and Masaki Kawano. Kinetic products in coordination networks: Ab initio X-ray powder diffraction analysis. *Acc. Chem. Res.*, 46:493–505, 2013.

[8] Ursula Mazur and K. W. Hipps. Kinetic and thermodynamic processes of organic species at the solutionsolid interface: the view through an STM. *Chem. Commun.*, 51:4737–4749, 2015.

[9] Lei Wang and Samuel Sánchez. Self-assembly via microfluidics. *Lab Chip*, 15(23):4383–4386, 2015.

[10] Stephen Mann. Self-assembly and transformation of hybrid nano-objects and nanostructures under equilibrium and non-equilibrium conditions. *Nat. Mater.*, 8:781–792, 2009.

[11] Soichiro Ogi, Tomoya Fukui, Melinda L. Jue, Masayuki Takeuchi, and Kazunori Sugiyasu. Kinetic control over pathway complexity in supramolecular polymerization through modulating the energy landscape by rational molecular design. *Angew. Chemie - Int. Ed.*, 53:14363–14367, 2014.

[12] Soichiro Ogi, Kazunori Sugiyasu, Swarup Manna, Sadaki Samitsu, and Masayuki Takeuchi. Living supramolecular polymerization realized through a biomimetic approach. *Nat. Chem.*, 6:188–195, 2014.

[13] Seong-Ho Shin, Sungwook Chung, Babak Sanii, Luis R Comolli, Carolyn R Bertozzi, and James J De Yoreo. Direct observation of kinetic traps associated with structural transformations leading to multiple pathways of S-layer assembly. *Proc. Natl. Acad. Sci.*, 109:12968–73, 2012.

[14] Peter A. Korevaar, Subi J. George, Albert J. Markvoort, Maarten M.J. Smulders, Peter A.J. Hilbers, Albert P.H.J. Schenning, Tom F.A. De Greef, and E. W. Meijer. Pathway complexity in supramolecular polymerization. *Nature*, 481:492–496, 2012.

[15] Yun Yan, Jianbin Huang, and Ben Zhong Tang. Kinetic trapping-a strategy for directing the self-assembly of unique functional nanostructures. *Chem. Commun.*, 52(80):11870–11884, 2016.

[16] Limin Xu, Mengqi Xie, Jianbin Huang, and Yun Yan. Understanding the Structure of Reversible Coordination Polymers Based on Europium in Electrostatic Assemblies Using Time-Resolved Luminescence. *Langmuir*, 32:5830–5837, 2016.

[17] J T Overbeek and M J Voorn. Phase separation in polyelectrolyte solutions; theory of complex coacervation. *J. Cell. Physiol.*, 49:7–22, 1957.

[18] Dimitrios Priftis, Nicolas Laugel, and Matthew Tirrell. Thermodynamic characterization of polypeptide complex coacervation. *Langmuir*, 28:15947–15957, 2012.

[19] Samanvaya Srivastava, Marat Andreev, Adam E. Levi, David J. Goldfeld, Jun Mao, William T. Heller, Vivek M. Prabhu, Juan J. De Pablo, and Matthew V. Tirrell. Gel phase formation in dilute triblock copolyelectrolyte complexes. *Nat. Commun.*, 8:14131, 2017.

[20] Charles E. Sing. Development of the Modern Theory of Polymeric Complex Coacervation. *Adv. Colloid Interface Sci.*, 239:2–16, 2016.

[21] Lu Li, Samanvaya Srivastava, Marat Andreev, Amanda B. Marciel, Juan J. de Pablo, and Matthew V. Tirrell. Phase Behavior and Salt Partitioning in Polyelectrolyte Complex Coacervates. *Macromolecules*, 51:2988–2995, 2018.

[22] M. Muthukumar. 50th Anniversary Perspective: A Perspective on Polyelectrolyte Solutions. *Macromolecules*, 50(24):9528–9560, 2017.

[23] Rajeev Kumar and M. Muthukumar. Origin of translocation barriers for polyelectrolyte chains. *J. Chem. Phys.*, 131, 2009.

[24] NSF. Frontiers in Polymer Science and Engineering. *NSF Workshop*, 2016.

[25] L. Vitorazi, N. Ould-Moussa, S. Sekar, J. Fresnais, W. Loh, J.-P. Chapel, and J.-F. Berret. Evidence of a two-step process and pathway dependency in the thermodynamics of poly(diallyldimethylammonium chloride)/poly(sodium acrylate) complexation. *Soft Matter*, 10:9496–9505, 2014.

[26] Ilja K Voets, Arie De Keizer, and Martien A Cohen Stuart. Complex coacervate core micelles. *Adv. Colloid Interface Sci.*, 147-148:300–318, 2009.

[27] Saskia Lindhoud, Willem Norde, and Martien A.Cohen Stuart. Reversibility and relaxation behavior of polyelectrolyte complex micelle formation. *J. Phys. Chem. B*, 113(16):5431–5439, 2009.

[28] Stefan Van Der Burgh, Remco Fokkink, Arie De Keizer, and Martien A.Cohen Stuart. Complex coacervation core micelles as anti-fouling agents on silica and polystyrene surfaces. *Colloids Surfaces A Physicochem. Eng. Asp.*, 242:167–174, 2004.

[29] Hanne M. Van Der Kooij, Evan Spruijt, Ilja K. Voets, Remco Fokkink, Martien A. Cohen Stuart, and Jasper Van Der Gucht. On the stability and morphology of complex coacervate core micelles: From spherical to wormlike micelles. *Langmuir*, 28(40):14180–14191, 2012.

[30] Marc Lemmers, Ilja K. Voets, Martien a. Cohen Stuart, and Jasper Van der Gucht. Transient network topology of interconnected polyelectrolyte complex micelles. *Soft Matter*, 7:1378, 2011.

[31] Saskia Lindhoud, Willem Norde, and Martien A.Cohen Stuart. Reversibility and re-

laxation behavior of polyelectrolyte complex micelle formation. *J. Phys. Chem. B*, 113(16):5431–5439, 2009.

[32] Jennifer E. Laaser, Yaming Jiang, Shannon R. Petersen, Theresa M. Reineke, and Timothy P. Lodge. Interpolyelectrolyte Complexes of Polycationic Micelles and Linear Polyanions: Structural Stability and Temporal Evolution. *J. Phys. Chem. B*, 119(52), 2015.

[33] Junyou Wang, Aldrik H. Velders, Eliana Gianolio, Silvio Aime, Frank J. Vergeldt, Henk Van As, Yun Yan, Markus Drechsler, Arie de Keizer, Martien A. Cohen Stuart, and Jasper van der Gucht. Controlled mixing of lanthanide(iii) ions in coacervate core micelles. *Chem. Commun.*, 49:3736, 2013.

[34] Rui Zhang, Prateek K. Jha, and Monica Olvera de la Cruz. Non-equilibrium ionic assemblies of oppositely charged nanoparticles. *Soft Matter*, 9:5042, 2013.

[35] Emi Haladjova, Grigoris Mountrichas, Stergios Pispas, and Stanislav Rangelov. Poly(vinyl benzyl trimethylammonium chloride) Homo and Block Copolymers Complexation with DNA. *J. Phys. Chem. B*, 120(9):2586–2595, 2016.

[36] Lixiao Wang and Hyuk Yu. Chain conformation of linear polyelectrolyte in salt solutions: sodium poly (styrenesulfonate) in potassium chloride and sodium chloride. *Macromolecules*, pages 3498–3501, 1988.

[37] K. Kassapidou, W. Jesse, M. E. Kuil, A. Lapp, S. Egelhaaf, and J. R.C. Van Der Maarel. Structure and charge distribution in DNA and poly(styrenesulfonate) aqueous solutions. *Macromolecules*, 30(9):2671–2684, 1997.

[38] Ryan J. Murphy and M. Muthukumar. Threading synthetic polyelectrolytes through protein pores. *J. Chem. Phys.*, 126, 2007.

[39] Yaming Jiang, Theresa M. Reineke, and Timothy P. Lodge. Complexation of DNA with Cationic Copolymer Micelles: Effects of DNA Length and Topology. *Macromolecules*, 51(3):1150–1160, 2018.

[40] G. Beaucage. Small-angle scattering from polymeric mass fractals of arbitrary mass-fractal dimension. *J. Appl. Crystallogr.*, 29:134–146, 1996.

[41] Jaromir Jakes. Regularized Positive Exponential Sum (REPES) Program: A Way of Inverting Laplace Transform Data Obtained by Dynamic Light Scattering. *Collect. Czechoslov. Chem. Commun.*, 60:1781–1787, 1995.

[42] Boualem Hammouda. SANS from polymers: review of the recent literature. *Polym. Rev.*, 50(1):14–39, 2010.

[43] Reidar Lund, Lutz Willner, Michael Monkenbusch, Pierre Panine, Theyencheri Narayanan, Juan Colmenero, and Dieter Richter. Structural observation and kinetic pathway in the formation of polymeric micelles. *Phys. Rev. Lett.*, 102(18):1–4, 2009.

[44] Jingcheng Fu, Hadi M. Fares, and Joseph B. Schlenoff. Ion-Pairing Strength in Polyelectrolyte Complexes. *Macromolecules*, 50(3):1066–1074, 2017.

[45] Bas Hofs, Ilja K. Voets, Arie de Keizer, and Martien A. Cohen Stuart. Comparison of complex coacervate core micelles from two diblock copolymers or a single diblock copolymer with a polyelectrolyte. *Phys. Chem. Chem. Phys.*, 8(36):4242–4251, 2006.

[46] Kazi Sadman, Qifeng Wang, Yaoyao Chen, Bavand Keshavarz, Zhang Jiang, and Kenneth R. Shull. Influence of Hydrophobicity on Polyelectrolyte Complexation. *Macromolecules*, 50(23):9417–9426, 2017.

[47] Evan Spruijt, Joris Sprakel, Marc Lemmers, Martien A Cohen Stuart, and Jasper Van Der Gucht. Relaxation dynamics at different time scales in electrostatic complexes: Time-salt superposition. *Phys. Rev. Lett.*, 105(20):1–4, 2010.

[48] Jean-François Gohy. Block Copolymer Micelles. *Adv. Polym. Sci.*, 190:65–136, 2005.

[49] Yiyong He, Zhibo Li, Peter Simone, and Timothy P. Lodge. Self-assembly of block copolymer micelles in an ionic liquid. *J. Am. Chem. Soc.*, 128(8):2745–2750, 2006.

[50] Adriana M. Mihut, Arnaud Chiche, Markus Drechsler, Holger Schmalz, Emanuela Di Cola, Georg Krausch, and Matthias Ballauff. Crystallization-induced switching of the morphology of poly(ethylene oxide)-block-polybutadiene micelles. *Soft Matter*, 5(1):208–213, 2009.

[51] Dustin Sprouse, Yaming Jiang, Jennifer E. Laaser, Timothy P. Lodge, and Theresa M. Reineke. Tuning Cationic Block Copolymer Micelle Size by pH and Ionic Strength. *Biomacromolecules*, 17(9):2849–2859, 2016.

[52] F. J. Esselink, E. Dormidontova, and G. Hadziioannou. Evolution of block copolymer micellar size and structure evidenced with cryo electron microscopy. *Macromolecules*, 31:2925–2932, 1998.

[53] Pavel S. Chelushkin, Evgeny A. Lysenko, Tatiana K. Bronich, Adi Eisenberg, Victor A. Kabanov, and Alexander V. Kabanov. Polyion complex nanomaterials from block polyelectrolyte micelles and linear polyelectrolytes of opposite charge. 2. Dynamic properties. *J. Phys. Chem. B*, 112:7732–7738, 2008.

[54] Elizabeth G. Kelley, Ryan P. Murphy, Jonathan E. Seppala, Thomas P. Smart, Sarah D. Hann, Millicent O. Sullivan, and Thomas H. Epps. Size evolution of highly amphiphilic macromolecular solution assemblies via a distinct bimodal pathway. *Nat. Commun.*, 5:3599, 2014.

[55] G. Beaucage, S. Rane, S. Sukumaran, M. M. Satkowski, L. A. Schechtman, and Y. Doi. Persistence length of isotactic poly(hydroxy butyrate). *Macromolecules*, 30:4158–4162, 1997.

[56] Yun Yan, Arie De Keizer, Martien A Cohen Stuart, Markus Drechsler, and Nicolaas A M Besseling. Stability of Complex Coacervate Core Micelles Containing Metal Coordination Polymer. *J. Phys. Chem. B*, 112:10908–10914, 2008.

[57] M. Cardona, R. V. Chamberlin, and W. Marx. The history of the stretched exponential function. *Ann. der Phys.*, 16(12):842–845, 2007.

[58] Roger C. Welch, John R. Smith, Marcel Potuzak, Xiaoju Guo, Bradley F. Bowden, T. J. Kiczenski, Douglas C. Allan, Ellyn A. King, Adam J. Ellison, and John C. Mauro. Dynamics of glass relaxation at room temperature. *Phys. Rev. Lett.*, 110:1–4, 2013.

[59] A. Arbe, J. Colmenero, M. Monkenbusch, and D. Richter. Dynamics of glass-forming polymers: Homogeneous versus heterogeneous scenario. *Phys. Rev. Lett.*, 81:590–593, 1998.

[60] Qi Ge, Kai Yu, Yifu Ding, and H. Jerry Qi. Prediction of temperature-dependent free recovery behaviors of amorphous shape memory polymers. *Soft Matter*, 8(43):11098, 2012.

[61] J Colmenero, A Arbe, A Alegría, M Monkenbusch, and D Richter. On the origin of the non-exponential behaviour of the -relaxation in glass-forming polymers: incoherent neutron scattering and dielectric relaxation results. *J. Phys. Condens. Matter*, 11:A363–A370, 1999.

[62] Shengchang Tang, Muzhou Wang, and Bradley D. Olsen. Anomalous Self-Diffusion and Sticky Rouse Dynamics in Associative Protein Hydrogels. *J. Am. Chem. Soc.*, 137:3946–3957, 2015.

[63] Amanda B. Marciel, Samanvaya Srivastava, and Matthew V. Tirrell. Structure and rheology of polyelectrolyte complex coacervates. *Soft Matter*, pages 18–22, 2018.

CHAPTER 3

INTERPARTICLE INTERACTION IN DILUTE SOLUTIONS OF POLYELECTROLYTE COMPLEX MICELLES

⋆ This chapter has been published as H. Wu, J. M. Ting, T. Weiss and M. V. Tirrell, *ACS Macro Lett.* **8**, 819 (2019).

3.1 Introduction

Despite the stark distinctions in the underlying driving forces, the polymer-concentration dependence of the structural evolution in self-assemblies driven by electrostatic interactions, it has been attempted to understand PEC micelles by analogy to the micelles formed by the neutral and amphiphilic block copolymers. It is not obvious that this is warranted. The corresponding characterization techniques, such as the determination of radius of gyration (R_g) via Guinier approximation, are usually indiscriminately borrowed and implemented in PEC micelles. The polymer concentration dependent phase diagram of PEC micelle has been reported by our group, and the phenomena to some extent parallel the uncharged, amphiphilic block copolymer micelles. For example, increasing the polymer concentration of the PEC micelle solutions from moderate to high (ca. 5-40 wt %) led to the structural evolution of the phase-separated complex domains transitioning from disorder arrays to body center cubic lattice and further to hexagonally packed cylindrical morphologies.[1, 2] However, a recent work from our group found that, at lower concentrations (0.5-2.0 wt %), the phenomenological consistency departs, exemplified by the contrast between the formation of interconnected micellar networks in complexation-driven self-assemblies and the individual micelles driven by the solvophobicity-solvophilicity balance.[3] Similar results have been reported by others as well.[4]

In the Chapter, we aim to have a detailed investigation on PEC micelles in dilute solutions (polymer concentration < 0.5 wt %), including their internal structures and determination of the effective interparticle interactions. Dilute solutions of PEC micelles have attracted enormous interest over the past two decades resulting in a burst of publications, the majority of which focused on the co-micellization with various biological molecules, stimuli-responsiveness, and applications.[5, 6, 7] However, detailed examination of their physical

properties has not been widely reported, and some important behaviors are largely unknown. For example, (i) not much is known about how the coronal layers respond when micelles interact and how the electrostatic interaction exhibits influence; and (ii) whether electrostatic force of the core extends beyond the coronas is understood in less details. The micelle-micelle interaction reveals the spatial filling constraints the PEC micelles encounter in dilute solutions, which would be further related to the long-term micelle stability, diffusivity, and reproducibility. From a standpoint of advancing biomedical applications, expanding the fundamental understanding the behaviors of polymeric nanocarriers in dilute solutions is of great significance due to their implications on dosage optimization and stability under physiological conditions.

In the present work, we report the determination of the repulsive intermicellar interactions in PEC micelles at very dilute polymer concentrations (< 0.5 wt %), where we expect that two-body interactions are the dominant, if not the exclusive mode of interaction. Structural details of PEC micelles under dilute concentrations were multi-parameterically investigated using synchrotron small-angle X-ray scattering (SAXS), including the size of the core, corona, R_g, aggregation number, volume fraction, and pair distribution correlations. All the SAXS experiments were carried out on the Biological Small Angle Scattering Beam Line BL4-2 at the Stanford Synchrotron Radiation Light-house (SSRL), SLAC National Accelerator Laboratory.[8] A combinatorial form factor comprising a polydisperse core-shell sphere model that accounts for the micelle morphology and a Gaussian coil function that accounts for the blob scattering from the coronal polymer chains was used to fit SAXS curves. A growing deviation in the low-q range be-tween the form factor and experimental data indicates the appearance of structure factor contributions. We modeled the electrostatic repulsive interaction using the both the hard sphere potential and the Debye-Hückel screened Coulomb potential. The effective interparticle repulsive interaction is further supported by the increasing difference between the apparent R_g of the micelle obtained through a Guinier approximation to the low q data and the real space R_g that is derived from the

pair distribution functions calculated by omitting the low q region.

3.2 Experimental Details

3.2.1 SAXS experiment and modeling

All SAXS experiments were carried out on the Biological Small Angle Scattering Beam Line BL4-2 at the Stanford Synchrotron Radiation Lighthouse (SSRL), SLAC National Accelerator Laboratory. The sample-to-detector distance was set to 3.5 m and X-rays with the wavelength of $\lambda = 1.38$ Å^{-1} (9 keV) were utilized for the measurements. Using a Pilatus3 X 1M detector (Dectris Ltd, Switzerland) the setup covered a range of momentum transfer q $\approx$ 0.0025 - 0.17 Å^{-1} where q is the magnitude of the scattering vector. Aliquots of 30 μL of the polyelectrolyte micellar suspension were loaded onto the automated fluid sample loader at the beamline. Series of sixteen consecutive 1s exposures were collected first from the buffer blank (pure water) and followed by the micelle samples of different concentrations. Solutions were oscillated in a stationary quartz capillary cell during data collection to maximize the exposed sample volume and reduce the radiation dose per unit volume of sample. The collected data were radially integrated, analyzed for radiation damage, and buffer subtracted using the automated data reduction pipeline at the beam line. Only data that did not show any signs of the effects of radiation damage were included in the final average for each sample concentration. More details on the SAXS data collection are available in the literature.[9, 8]

For identical particles with spherical symmetry, the intensity can be expressed as: P(q) is the form factor denoting the size and shape of scatterers, and S(q) is the structure factor that characterizes the interparticulate interactions and approaches to unity at dilute enough concentrations. For micellar particles formed by PEO_{225}-*b*-$PVBTMA_{100}$ and PAA_{158} polyelectrolytes were fitted using a combination of a polydisperse core-shell sphere model, $P(q)_{sh}$, and a polydisperse Gaussian coil function, $P(q)_{coil}$. The equation of the form factor can be expressed as:

$$P(q) = P(q)_{sh} + P(q)_{coil} \tag{3.1}$$

$$P(q)_{sh} = \frac{\phi_{\text{mic}}}{V_S}\left[\frac{3V_C\left(\rho_C - \rho_S\right) j\left(qr_C\right)}{qr_C} + \frac{3V_S\left(\rho_S - \rho_{\text{solv}}\right) j\left(qr_s\right)}{qr_S}\right]^2 + bkg_{sh} \tag{3.2}$$

$$P(q)_{coil} = \phi_{blob}\frac{2\left[(1+U\Xi)^{-1/U} + \Xi - 1\right]}{(1+U)\Xi^2} + bkg_{coil} \tag{3.3}$$

$$j(x) = \frac{\sin x - x\cos x}{x^2} \tag{3.4}$$

$$\Xi = \frac{\left(qR_{g,blob}\right)^2}{1+2U} \tag{3.5}$$

$$U = \frac{M_w}{M_n} - 1 \tag{3.6}$$

where $j(x)$ is the Bessel function; $P(q)$ is the form factor; V_{sph}, V_C, and V_S are the volumes of a single micelle, the micelle core, and the micelle shell, respectively; ρ_C, ρ_C, and ρ_{solv} are the scattering length densities of the micelle shell, micelle core, and solvent, respectively; r_{sph} of the micelle shell and r_C is the radius of the micelle core. The scale is a factor that equals to the volume fraction when the scattering data is on an absolute scale. The *bkg* denotes the background level.

The second term represents the blob scattering from the coronal polymer chains, i.e., PEO, which is calculated by an empirical functional form of scattering from a polydisperse chain in a good solvent. The dispersity of the molecular weight distribution, U, is described by a Schulz-Zimm distribution. As we reported before, the M_w/M_n the PEO we used is 1.02, with which the form of the polydisperse Gaussian coil is reduced to the Debye function. The

R_g of the coronal chain can be extracted from the model but are not discussed. Because of the low polymer volume fraction, these values are expected to have minimal impact on the micelle shape and, consequentially, on the amplitude impact on the SAXS curves. It should be noted that we refrained from using more sophisticated models than the polydisperse core-shell sphere model to avoid data overfitting, a situation that might be encountered when introducing more fitting parameters, e.g., models that consider a thick corona-core interface.

3.2.2 Pair distribution function

The real space R_g is defined as:

$$R_g^2 = \frac{\int_0^{D_{\max}} r^2 P(r) dr}{2 \int_0^{D\,\max} P(r) dr} \tag{3.7}$$

where D_{max} is the maximum intraparticle distance, assumed to be the diameter of the scatterers, depending on the composition and electron distribution of the sample. The I(q) and P(r) are closely related. It is straightforward to calculate the intensity profile from the Debye function, shown in Equation 3.8. Taking the inverse Fourier transformation results in P(r), as seen in Equation 3.9

$$I(q) = \int_0^{D_{\max}} P(r) \frac{\sin(qr)}{qr} dr \tag{3.8}$$

$$P(r) = \frac{r}{2\pi} \int_0^{\infty} qI(q) \sin(qr) dq \tag{3.9}$$

3.2.3 Structure factor modeling

S(q) is the Fourier transform of the particle correlation function g(r), which is a direct measurement of the correlation of particle positions shown as:

$$S(q) = 1 + \left(\frac{\phi}{V}\right)\int_0^\infty 4\pi r^2[1 - g(r)]\frac{\sin qr}{qr}dr \tag{3.10}$$

where ϕ is the micelle volume fraction and V is the volume of a individual micelle, and the height of the first peak of the structure factor is a direct experimental measure of the degree of the nearest neighbor correlations among the scatterers. We have analyzed the data with a hard-sphere potential and the Percus-Yevick approximation for the closure relation.[10] The solution structure factor is written as:

$$S_{HS}^{-1}(q) - 1 = 24\phi\left[\alpha f_1\left(D_{HS}q\right) + \beta f_2\left(D_{HS}q\right) + \phi\alpha f_3\left(D_{HS}q\right)/2\right] \tag{3.11}$$

with

$$\begin{aligned}\alpha &= \frac{(1+2\phi)^2}{(1-\phi)^4}\\ \beta &= \frac{3(2+\phi)^2}{2(1-\phi)^4}\end{aligned} \tag{3.12}$$

and

$$\begin{aligned}f_1(x) &= \tfrac{\sin(x) - x\cos(x)}{x^3}\\ f_2(x) &= \tfrac{2\,\mathrm{sen}\,in(x) - \left(x^2-2\right)\cos(x) - 2}{x^4}\\ f_3(x) &= \tfrac{\left(4x^3-24x\right)\sin(x) - \left(x^4-12x^2+24\right)\cos(x) + 24}{x^6}\end{aligned} \tag{3.13}$$

where D_{HS} denotes the effective hard-sphere distance and ϕ is the volume fraction. The ill-fitted screened repulsive Coulomb potential is not shown here.

3.2.4 Zeta potential measurement

The ζ-potential values were determined using a Wyatt mobiuζ, Dynamic/Electrophoretic Light Scattering instrument using Dynamics (Version 7.4.072) software. Each micelle sample was transferred to a cleaned 45 μL quartz micro-cuvettes for ζ-potential measurements. Electrophoretic mobilities were collected at a voltage amplitude of 2 V (PALS collection period of 15 s) and converted to ζ-potential via the Smoluckohowski equation. The reported values were taken from the average of five measurements. Samples typically have conductivities around 0.4 mS/cm.

3.3 Results and Discussions

3.3.1 SAXS data fitting

As shown in Figure 3.1, the SAXS patterns of the dilute solutions of PEC micelles appear to exhibit a characteristic pattern of isolated spheres without significant interactions. The quasi-plateau region at low q values ($0.003\ \text{Å}^{-1} < q < 0.006\ \text{Å}^{-1}$), which suggests an absence of intermicellar correlation, transitions to a decaying intermediate q range ($0.01\ \text{Å}^{-1} < q < 0.03\ \text{Å}^{-1}$) with a power law of -4, a signature of smooth spherical surfaces, and is then followed by a power law of -2.5 at the high q values ($0.03\ \text{Å}^{-1} < q < 0.1\ \text{Å}^{-1}$) that is indicatively stemming primarily from the scattering of individual polymer chains.

The SAXS curves were fitted using the combinatorial form factor of a polydisperse core-corona sphere model and form factor of a polydisperse Gaussian coil. The former is responsible for the scattering from the core-shell shaped spherical micelles, and the latter account for the scattering from the individual polymer chains. The details of the model for core-shell spheres can be found in the Supporting Information. The fitting parameters are shown in Table 3.1, including the radius of the core, the thickness of the corona, the scattering length densities of the core and corona, and the micelle volume fraction. We observed that the radii of the micelle cores and the thicknesses of the coronas remained constant while the total

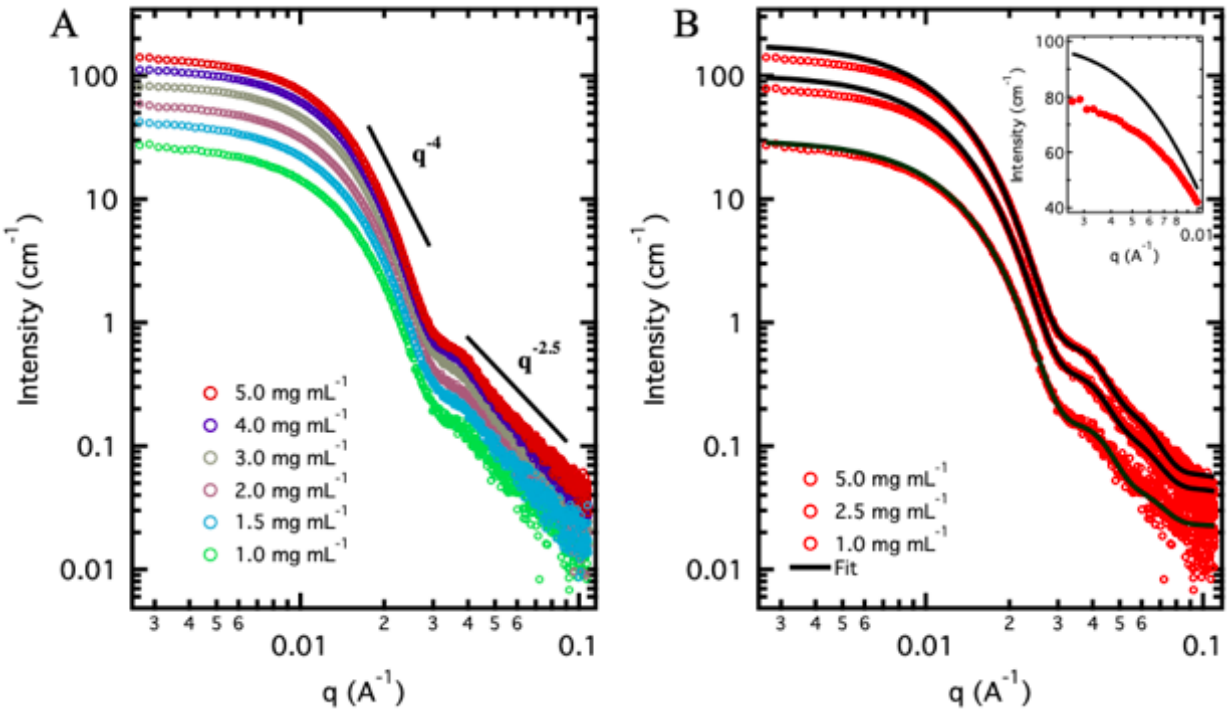

Figure 3.1: (A) SAXS profiles of micelle samples composed of equimolar charged monomers from PEO_{225}-*b*-$PVBTMA_{100}$ and PAA_{158} at total polymer concentration from 1.0 to 5.0 mg mL^{-1}. (B) The fits of a polydisperse corona-core spherical model (black lines) at micelle samples with 1.0, 2.5, and 5.0 mg mL^{-1}, respectively. The inset shows the discrepancy between the scattering profile and the model at 2.5 mg mL^{-1}.

polymer concentration increased from 1.0 to 5.0 mg mL^{-1}. This confirms that the size of micelles does not change over the examined polymer concentration range.

However, in the low q range from 0.003 to 0.01 Å^{-1}, i.e. the Guinier region where the apparent R_g is often extracted via the Guinier approximation, we observed nuanced but nonnegligible disparities between the experimental data and the model at the low q values, indicating the presence of a structure factor. By definition, the SAXS scattering intensity is a product of a form factor and a structure factor. The former describes the geometry of the individual scatterers, while the latter represents the interparticle interactions. The discrepancy grew more pronounced with increasing polymer concentration through 0.5 wt.%, which is illustrated by the inset plot in Figure 3.1B. At low concentrations, e.g., 1.0 mg mL^{-1}, the pure form factor matched the measured SAXS curve fairly well, which indicates an absence

Table 3.1: Fitting parameters of the SAXS curves shown in Figure 3.1.

c (mg mL^{-1})	R_{core} (Å)	Th_{corona} (Å)	SLD_{core} (10^{-6} Å^{-2})	SLD_{corona} (10^{-6} Å^{-2})	SLD_{sol} (10^{-6} Å^{-2})	Volume fraction
5.0	81.66 ± 0.27	106.55 ± 0.16	10.80 ± 0.002	9.85 ± 0.001	9.61 ± 0.002	0.01777
4.0	80.92 ± 0.24	106.85 ± 0.15	10.86 ± 0.002	9.85 ± 0.002	9.61 ± 0.002	0.01360
3.0	80.65 ± 0.23	106.20 ± 0.11	10.86 ± 0.003	9.85 ± 0.002	9.61 ± 0.002	0.01000
2.0	80.76 ± 0.23	106.31 ± 0.11	10.83 ± 0.003	9.82 ± 0.002	9.59 ± 0.002	0.00755
1.5	80.44 ± 0.54	106.47 ± 0.31	10.82 ± 0.002	9.83 ± 0.002	9.61 ± 0.002	0.00592
1.0	80.45 ± 1.03	106.05 ± 0.34	10.87 ± 0.004	9.83 ± 0.004	9.61 ± 0.004	0.00333

of a structure factor and the neglect of interparticle interactions at this concentration. Yet, the deviation is distinct at 5.0 mg mL^{-1} (roughly 0.5 wt %), which implies the contribution of structure factors and interparticle correlations at this dilute micelle concentration.

3.3.2 Molecular weight, number density, and aggregation number

The properties of individual micelles, including the molecular weight, aggregation number, and the water fraction in the core were further calculated. The micelle number density and mean intermicellar distance were also derived to illustrate the extent of dilution. The molecular weight of the micelles can be calculated using:

$$M_w = \frac{c}{NN_A} \tag{3.14}$$

$$N = \frac{\emptyset_{mic}}{v_{mic}} \tag{3.15}$$

$$d = N^{-1/3} \times 10^7 \tag{3.16}$$

where N is the number of micelles per unit volume, c is the polymer concentration in mg mL^{-1}, v_{mic} is the volume of a single micelle which equals to $4/3\pi R^3$ with R being the radius of a micelle, the value of $\emptyset_{mic}$ is the volume fraction of micelles, d is the mean distance between the micelles assuming they are evenly distributed in the solution, and N_A is the Avogadro

Table 3.2: The average distance, number density, molecular weight, and aggregation number of PEC micelles.

c (mg mL^{-1})	d (nm)	N ($\times 10^{14}$ mL^{-1})	M_w ($\times 10^{16}$ g mol^{-1})	N_{agg}
5.0	111.19	7.27	4.14	105
4.0	121.55	5.56	4.33	109
3.0	134.67	4.09	4.41	111
2.0	147.90	3.09	3.90	98
1.5	160.40	2.42	3.73	94
1.0	194.30	1.36	4.42	112

constant. The aggregation number of the polycation is calculated as well. The results are shown in Table 3.2. It is clearly seen that even at the highest polymer concentration the mean distance of the micelles is far larger than the micelle size.

3.3.3 Interparticle interactions among PEC micelles

The nature of the interparticle correlation in the dilute solutions of PEC micelles is further identified and investigated by extracting the structure factor, S(q), from the I(q) data. The extracted S(q) versus q are shown in Figure 3.2. The selected micelle solutions were at 2.5 and 5.0 mg mL^{-1}. It is evident that, in the q range from 0.003 to 0.01 $Å^{-1}$, (i) the values of the S(q)s at the low q region are slightly smaller than 1.0, indicating the repulsive forces that the micelles exert on their neighbors, and (ii) the primary peaks are more pronounced at the higher concentration, meaning that the intermicellar correlation strengthened with the increasing polymer concentration. These results are in excellent agreement with the model fits to the data. Moreover, the primary peaks remain around $q_{peak} = 0.02$ $Å^{-1}$, independent of the polymer concentration. This first peak of on the structure factor curves corresponds to an average interparticle distance. Higher-order peaks are undiscernible because of the limited signal to noise at the high-q region.

We further modeled the effective structure factors using two forms of potentials often encountered in colloidal interactions: the excluded volume repulsive interactions (hard-sphere potential) and the electrostatic repulsive interaction (Debye-Hückel screened Coulomb po-

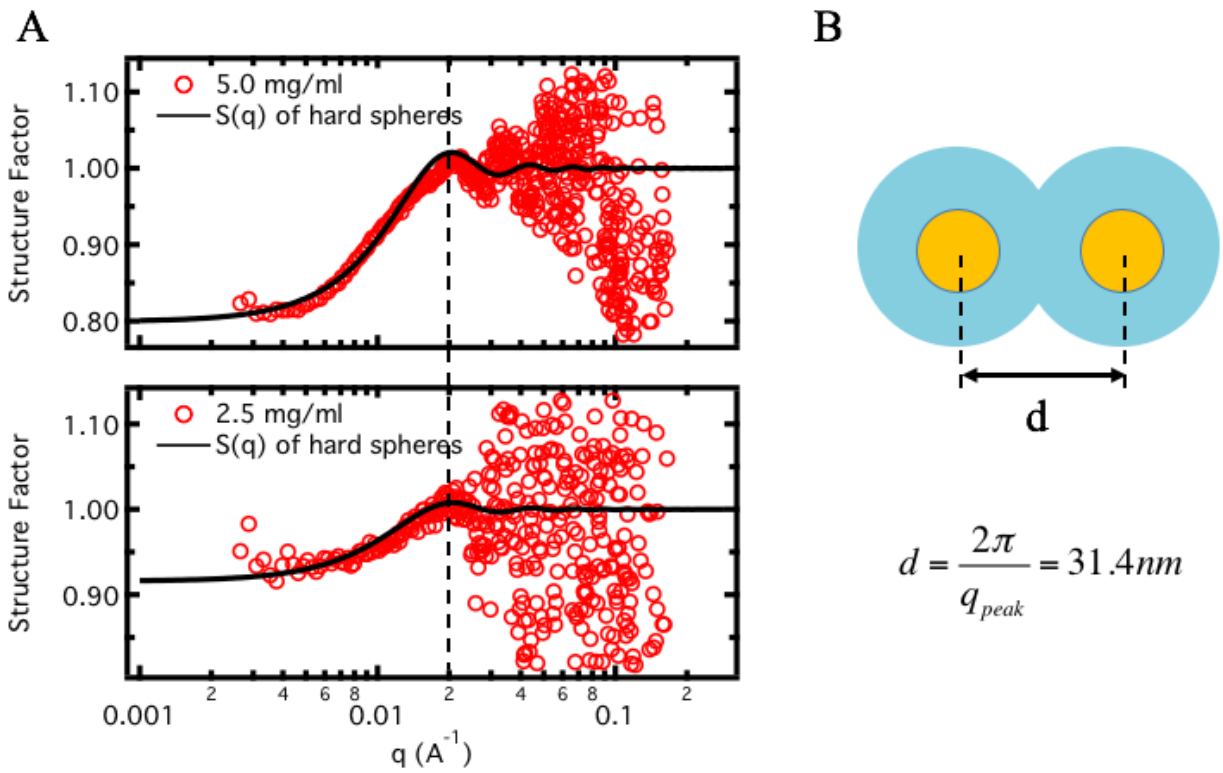

Figure 3.2: (A) Structure factors (red circles) and the fits of hard-sphere potential (black lines) of PEC micelles at polymer concentration of 5.0 and 2.5 mg mL^{-1}, respectively. (B) Schematic depiction of the determination of the effective micelle-micelle distance.

tential). The hard-sphere potential has been found to give reasonable description of the interparticle interactions of uncharged block copolymer micelles,[11, 12, 13] whereas the screened Coulomb potential is usually used to model the effective interactions in solutions of surfactant micelles,[14] macroions,[15, 16] and PECs.[17] PEC micelles made at stoichiometric conditions are theoretically believed to have cores with neutralized polyelectrolytes dispersing in a solution with free counterions. From the fit using the hard-sphere potential, we found that the hard-sphere interaction distance, d_{hs}, is about 29.6 nm, which is slightly smaller than the intermicellar distance when two micelles come into contact. From the SAXS fits aforementioned, the individual micelles have ca. 37.4 nm in diameter. But when two micelles come together, they are able to approach their centers within 29.6 nm, at which point a hard-sphere interaction takes over. This deviation is probably due to the compression of the neutral coronal layers. It is unclear whether the coronal chains are interpenetrating each other. Polymers tethered on flat surfaces tend not to interpenetrate one another when they approach,[18, 19] although evidence has shown that on spherical surfaces, tethered chains would be more penetrable than those on flat ones.[20] Corona deformation is expected at moderate concentrations in order to accommodate the micelles in the increasingly crowded volume, but to which extent PEC micelle coronas would compress at such a dilute concentration has never been determined. This is also in contrast to uncharged block co-polymer micelles where steric interactions between the coronas are anticipated to avoid micelle fusion/fission.[21] Moreover, we have investigated the influence of electrostatic interaction by fitting the structure factors into a repulsive screened Coulomb potential. Yet, no significant improvement with reasonable values of micelle surface charges were observed, denoting that the electrostatic force does not extend beyond the coronas.

3.3.4 Debye screening length and ζ-potential

The Debye screening length, κ^{-1}, is the scale over which solution counterions screen out electric fields in the polyelectrolyte solutions. The thickness of the double layer at a distance

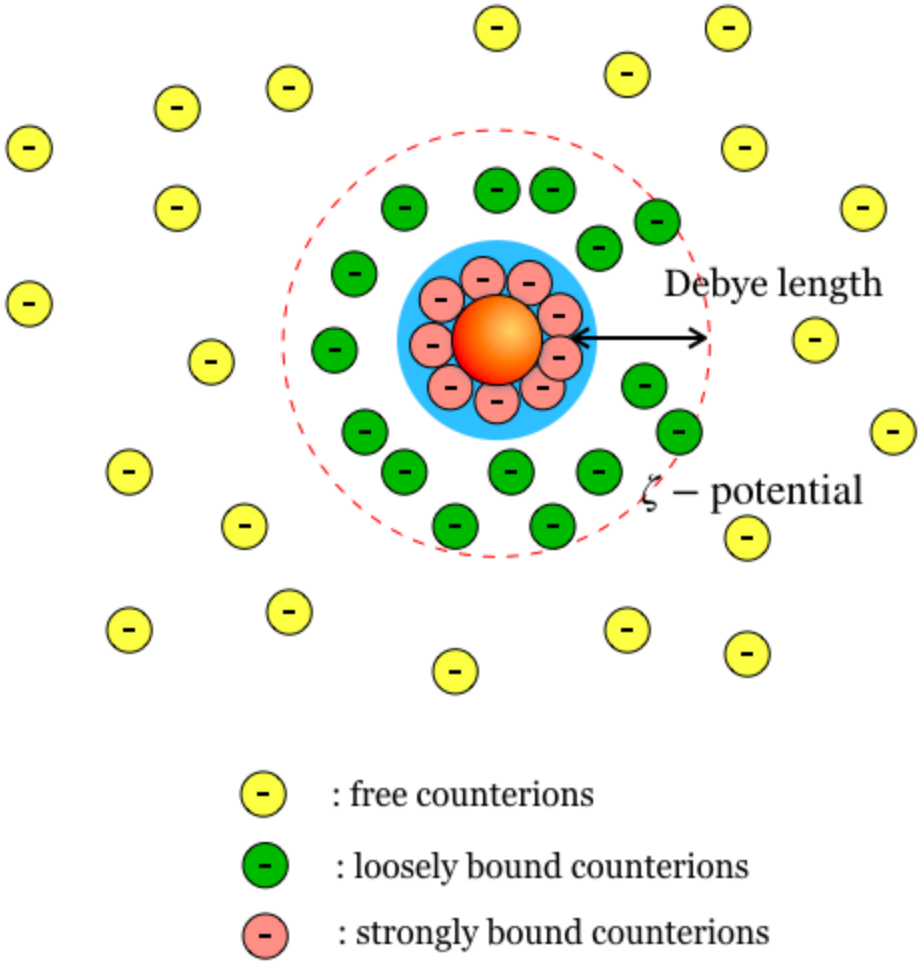

Figure 3.3: Scheme representation of the Debye screening length and ζ-potential.

where the surface potential is shielded from the bulk is called the Debye screening length. In other words, the Debye screening length represents the influence of the electric field generated by charged entities. As shown in Figure 3.3, consider presenting a core-shell micelle with a core containing positive charges into a solution with negative counterions, these counterions would evolve into three forms, i.e. free counterions, loosely bound counterions, strongly bound counterions, depending on their distances to the core surface and their diffusivity. The distance between the layer full of strongly bound counterions and the layer full of loosely bound counterions is called the Debye length. The electric potential generated by the absorbed counterions is referred to the ζ-potential.

From the discussion above, it is shown that the electrostatic force does not affect the interparticle interaction among PEC micelles. Two possibilities may cause this phenomenon. First, PEC micelles do not contain net charges, which means the micellar cores are electrostatically neutralized, which is premised by many reports. Second, the cores having polyelectrolyte complexes may have net charges but their influence is weak and influential distance is smaller than the closest distance that two micelles can approach. The influential distance of electrical field is determined by the Debye screening length, which can be calculated by the following way:

$$\kappa^{-1} = \frac{1}{\sqrt{8\pi\lambda_B N_A I}} \tag{3.17}$$

where λ_B is the Bjerrum length of the solvent, which is close to 0.7 nm for water at 25 ^{o}C. At room temperature, the above expression can be simplified to

$$\kappa^{-1}(nm) = \frac{0.304}{\sqrt{I(M)}} \tag{3.18}$$

where κ^{-1} is the Debye screening length in the unit of nm, and I(M) is the ionic strength in M or mol/L. The Debye screening lengths at different concentrations are accordingly calculated and are shown in Table 3.3. It is shown that they are all smaller than the thickness of the corona extracted from SAXS, which suggests that the electrostatic force, if there is any, does not extend beyond the corona. Further, we measured the ζ potential of the micelles and found that the ζ potential is almost zero (Figure 3.4). Although the absolute neutrality of micelle cores is unable to be drawn, the short Debye screening length and near-zero ζ potential suggest that it is unlikely that the core is markedly charge-unbalanced. This is different from the charged polyelectrolyte diblock copolymer micelles, where the charged corona chains are fully stretched and adopt a rod-like conformation.[22] Overall, these results suggest the absence of long-range Coulomb potential and indicate that the intermicellar repulsive interaction in dilute solutions of PEC micelles predominately arises from steric

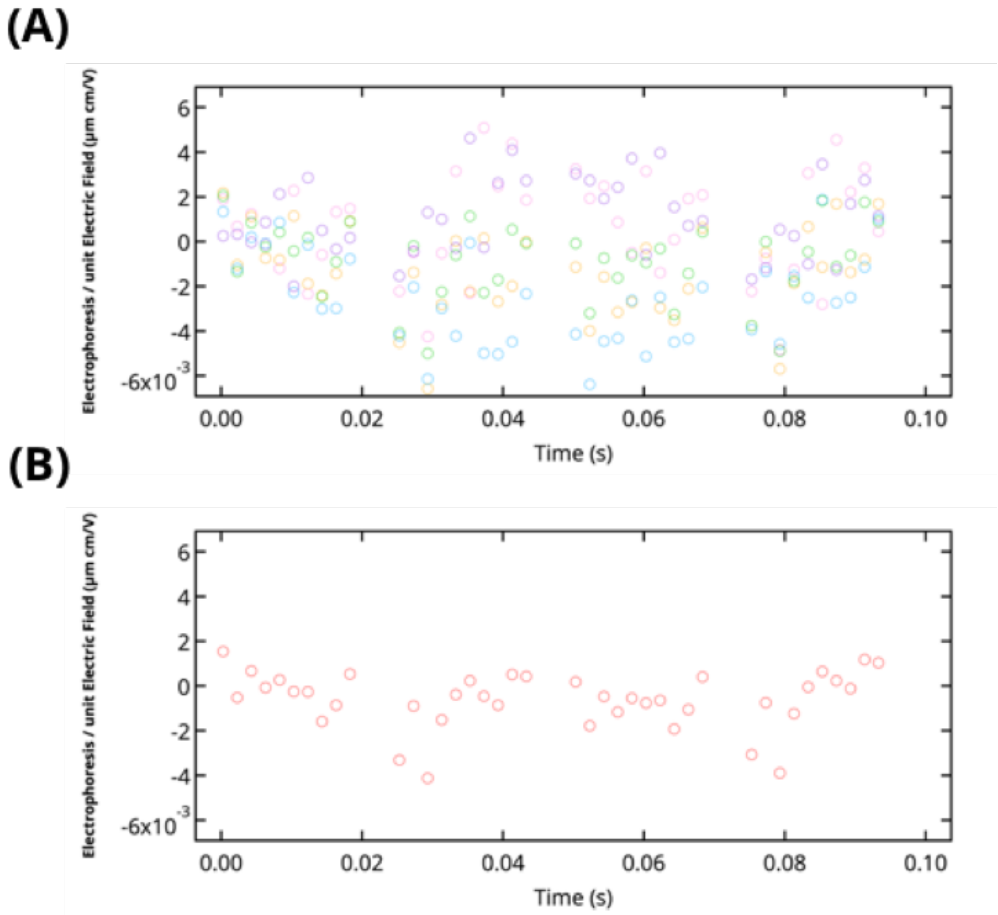

Figure 3.4: Mobility curves for a representative PEO-PVBTMA/PAA micelle showing the (A) raw data for 5 measurements and (B) average data for determining the ζ-potential.

hindrance.

3.3.5 Guinier approximation

The radius of gyration (R_g) of a scatterer is defined as the root mean square distance from the center of mass and is generally calculated by two methods. The first one is the Guinier approximation, where the low-q data points ($qR_g < 1.3$ for spherical objects) are linearly extrapolated to zero-angle scattering. The R_g is determined according to the linearized equation below:

$$I(q) \cong I(0) \exp\left(-q^2 R_g^2/3\right) \tag{3.19}$$

Table 3.3: The Debye screening lengths at various micelle concentrations.

Micelle concentration (mg mL^{-1})	Counterion concentration (mmol L^{-1})	Debye screening length (nm)
1.0	1.21	8.74
2.0	2.42	6.18
2.5	3.02	5.52
3.0	3.63	5.05
4.0	4.84	4.37
5.0	6.05	3.91

where I(q) the scattering intensity, I(0) is the forward scattering intensity which is proportional to the molecular weight M_w and concentration of the scatterers, and the scattering vector magnitude $q = (4\pi/\lambda)\sin(\theta/2)$ (θ is the scattering angle and λ the wavelength of the incident radiation). The low-q data was selected and fitted into the Guinier plot using the following equation:

$$\ln[I(q)] \cong \ln[I(0)] - \frac{R_g^2}{3}q^2 \tag{3.20}$$

We used two methods to extract the Guinier R_g values from a MATLAB code (shown in the Appendix) and the Primus package in ATSAS software.[23] These results are shown in Tables 3.4 and 3.5, respectively. The M_w of the scatterers can be determined from the zero-angle scattering intensity I(0), the partial specific volume v_{mic} and the micelle concentration is expressed as:

$$I(0) = \frac{CM_wV}{N_A}v_{mic}^2(\Delta\rho)^2 \tag{3.21}$$

Here, $C = NM_w/N_AV$ is the polymer concentration (w/v, i.e., in mg mL^{-1}).

The relationship between the polymer concentration and the zero-angle scattering intensity is fitted usign a quadratic function, which is written as:

$$I(0) = p_1c + p_2c^2 + p_3 \tag{3.22}$$

Table 3.4: The R_g and I(0) measurements by the Primus package in ATSAS software.

Concentration	Guinier R_g (Å)	I(0)	$q_{\max}R_g$ range	Fidelity	q range (points)[a]
5.0	136.60 ± 0.60	142.43 ± 0.17	[0.57, 1.27]	0.93	8-31
4.5	137.65 ± 0.85	131.12 ± 0.17	[0.43, 1.28]	0.98	3-31
4.0	137.91 ± 0.86	116.49 ± 0.14	[0.43, 1.28]	0.98	3-31
3.5	139.22 ± 0.34	104.75 ± 0.095	[0.43, 1.29]	0.98	3-31
3.0	138.54 ± 1.28	87.84 ± 0.15	[0.61, 1.28]	0.92	9-31
2.5	139.40 ± 0.70	80.51 ± 0.11	[0.43, 1.29]	0.98	3-31
2.0	139.59 ± 3.08	60.15 ± 0.11	[0.49, 1.29]	0.96	5-31
1.5	141.03 ± 1.08	43.01 ± 0.085	[0.44, 1.28]	0.98	3-30
1.0	142.08 ± 2.92	27.91 ± 0.085	[0.44, 1.29]	0.98	3-30

Table 3.5: The R_g and I(0) measurements by Guinier approximation using MATLAB code.

Concentration	Guinier R_g (Å)	I(0)	$q_{\max}R_g$ range	Resnorm	q range (points)[a]
5.0	136.53 ± 0.72	142.41	[0.60, 1.27]	0.00	8-30
4.5	137.17 ± 1.07	130.94	[0.42, 1.21]	0.00	3-30
4.0	137.35 ± 0.89	116.24	[0.42, 1.21]	0.00	3-30
3.5	139.14 ± 0.55	104.72	[0.42, 1.23]	0.00	3-30
3.0	138.13 ± 1.11	87.66	[0.61, 1.28]	0.00	9-31
2.5	139.50 ± 1.03	80.60	[0.46, 1.26]	0.00	3-30
2.0	139.58 ± 1.05	60.12	[0.49, 1.29]	0.00	9-31
1.5	141.44 ± 1.40	43.12	[0.44, 1.25]	0.00	3-30
1.0	142.49 ± 2.77	27.96	[0.47, 1.29]	0.00	3-30

where p_1, p_2, and p_3 are the variables and their estimates are 33.66, -0.84, and -5.02, respectively. The fit is shown in Figure 3.5, and the results are shown is Table 3.6. It is obvious that the dependency between the intensity at zero angle and the polymer concentration is not linear, which indicates that other factors rather than pure form factors are contributing to the intensity.

Table 3.6: The fit and errors of I(0) using the quadratic function.

Concentration	I(0)	Fit	Error
1.0	27.83	27.80	0.03
1.5	42.93	43.59	-0.66
2.0	60.10	58.96	1.14
3.0	87.73	88.43	-0.70
4.0	116.42	116.24	0.18
5.0	142.39	142.38	0.01

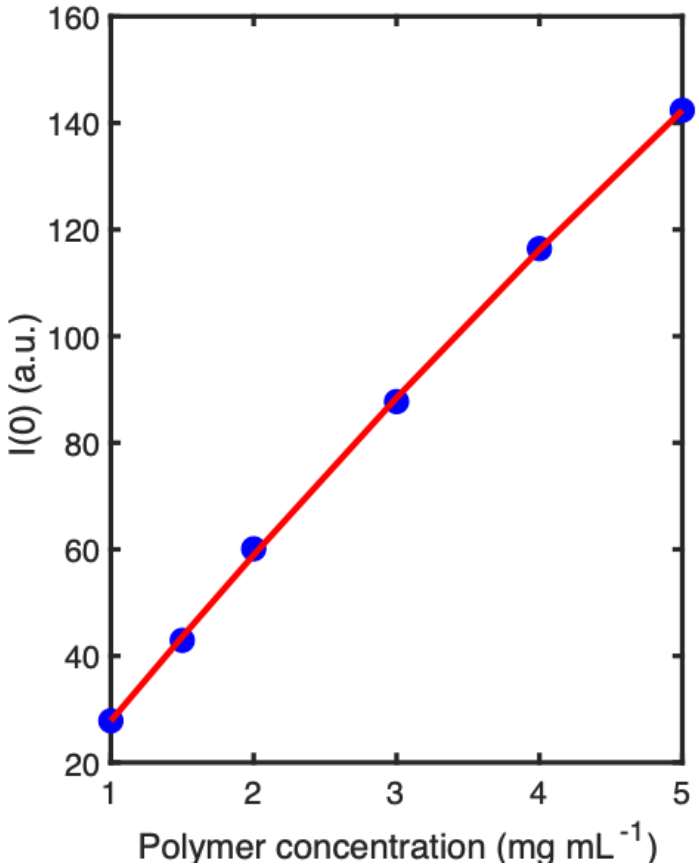

Figure 3.5: The quadratic fit between the polymer concentration and the zero-angle scattering intensity estimated by Guinier approximation. The blue circles represent the experimental data, and the dashed line denotes a linear regression to the data.

3.3.6 Real space R_g

The real space is directly derived from the pair distribution function of the entire SAXS curve and, thus, is much less sensitive to the low resolution data in the low q range. In principle, this formula provides a direct way to of calculating P(r). However, it is not practical in reality because the I(q) is only available at discrete points for limited q-range and is easily affected by experimental errors as well as possible instrumental distortions due to the beam-size and bandwidth. The Fourier transform of incomplete and noisy data is an ill-posed problem. A practical solution is to parameterize P(r) on the range of [0, D_{max}] by a linear combination of orthogonal functions using an indirect Fourier Transform technique.[24] Based on that, we processed the data using the GNOM package in ATSAS and replotted the P(r) vs. r curves using a MATLAB code (shown in the Appendix). The scattering at the origin is estimated as $I(0) = 4\pi \int_0^{D\,\max} P(r)dr$. The pair distribution functions of micelles at low concentrations are shown below in Figure 3.6. As expected, the resultant distributions appear to be identical, representing the independence of the real space R_g values as a function of polymer concentration. Fitting parameters are tabulated in Table 3.7. It is difficult to get error bars from P(r) as the math behind the determination of the real space R_g is rather complex. That is the reason why it is not reported in GNOM. The P(r)-distribution function is used to describe the paired-set of distances between all of the electrons within the macromolecular structure. Since the function histograms the set of all paired-distances within a structure, small changes in the relative positions of a few residues can be measured by changes in a P(r) distribution in a relatively accurate manner. Empirically, the accuracy of the R_g from the P(r) is around 0.5 to 1 Å; however, it is hard to proof as there are several different parameters that go into the calculation that are chosen by users.

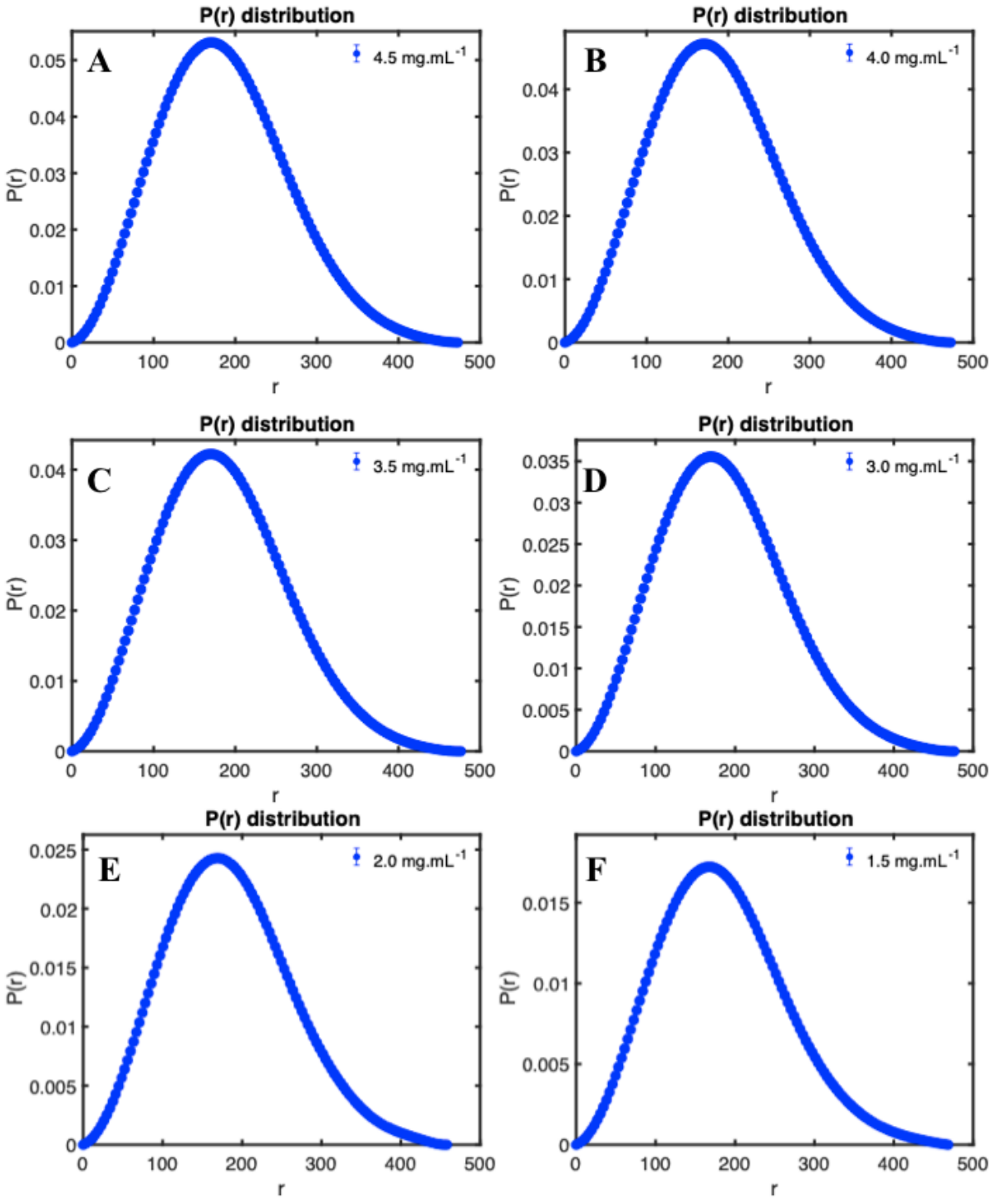

Figure 3.6: The pair distribution functions of the micelle samples at the polymer concentration of 4.5 (A), 4.0 (B), 3.5 (C), 3.0 (D), 2.0 (E), and 1.5 (F) mg mL^{-1} (D), respectively.

Table 3.7: The fitting parameters of the pair distribution function P(r).

Concentration	P(r)-derived R_g	Fit	Error
5.0	143.30	146.90	476.13
4.5	142.90	134.20	476.13
4.0	142.70	119.00	476.13
3.5	143.30	106.30	476.13
3.0	142.30	89.49	476.13
2.5	142.90	81.87	476.13
2.0	141.20	60.74	457.78
1.5	141.40	43.10	468.45
1.0	141.90	27.86	476.13

3.3.7 Comparison between Guinier R_g and real space R_g

As shown in Figure 3.7, we observed that the apparent Guinier R_g values monotonically decreases when the polymer concentration increases from 1.0 to 5.0 mg mL^{-1}. Meanwhile, the real space R_g determined from the pair distribution functions remained almost constant, with minimal fluctuations. At low concentrations, e.g. 1.0 mg mL^{-1}, the Guinier R_g and the real space R_g are in good agreement, which indicates the accuracy of the Guinier approximation under those concentrations. However, as concentration increases, the divergence between the Guinier R_g and the real space R_g expands. As stated above, the P(r)-derived real space R_g is more accurate because it is derived from the entire scattering curve and not just the lowest-resolution data that is used in approximating the Guinier R_g. This distinction between the real space R_g and the Guinier R_g implies the interference of structure factors, which further suggests the detection of interparticle interactions. From the aforementioned SAXS analysis, the S(q) is smaller than 1 at the low q range (0.003 $Å^{-1}$ < q < 0.01 $Å^{-1}$), which covers the Guinier approximation region. The Guinier plot can be rewritten as $I(q)/S(q) \cong \ln[I(0)] - R_g^2 q^2/3$. It is evident the apparent Guinier R_g determined from the low-resolution scattering is affected by the presence of a structure factor. When S(q) is smaller than a unity, the apparent Guinier R_g will be too small and will not represent the true values that would be measured under conditions where S(q) = 1. It is noteworthy that the error bars of the real space R_gs are omitted. Empirically, the accuracy of the R_g from

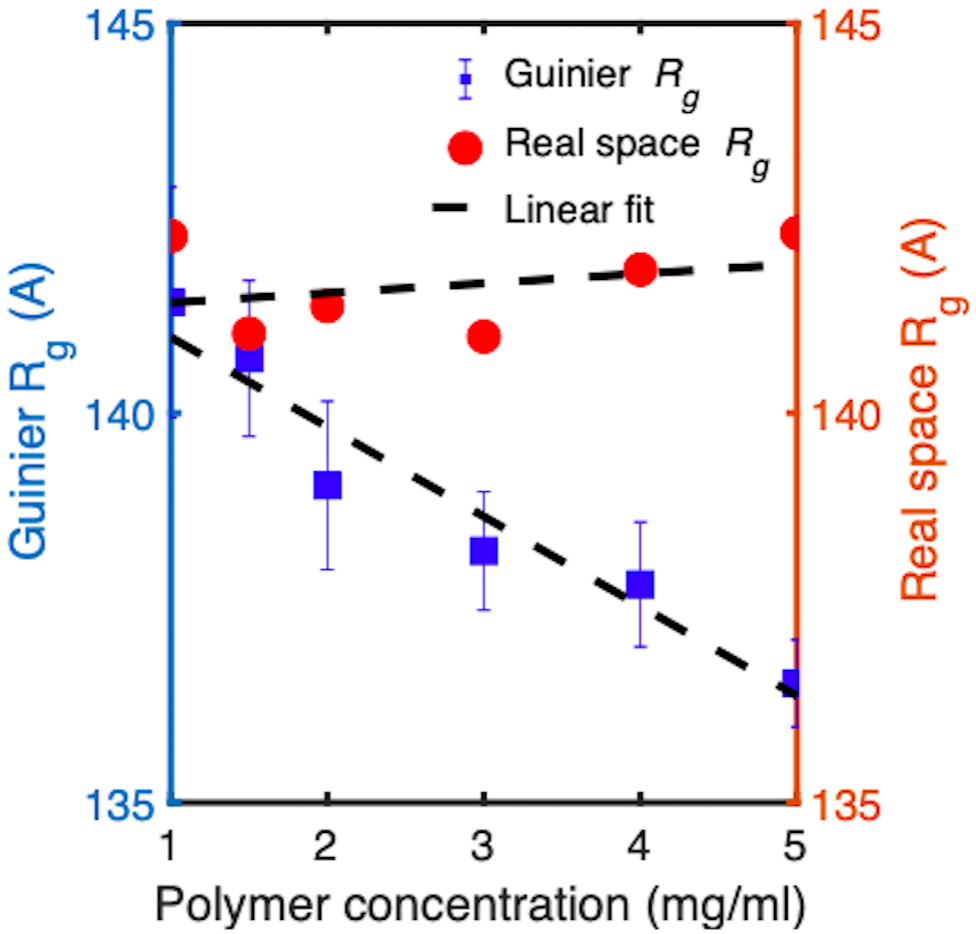

Figure 3.7: The decrease of the Guinier R_gs (blue squares) and the relatively consistent P(r)-derived real space R_gs (red dots) with the increase of the polymer concentration. Data points and error bars denote the average and standard deviation, respectively.

the P(r) is around 0.5 to 1 Å.

3.4 Concluding Remarks

In this Chapter, we report the measurement and determination of the repulsive micelle-micelle interaction in PEC micelles with polymer concentrations from 1.0 to 5.0 mg mL^{-1}. We have demonstrated that at such a dilute regime the interparticle interaction among PEC micelles is not as trivial as commonly treated. We found that the structure of PEC micelles can be depicted as hard spherical cores tethered with compressible Gaussian coronal chains.

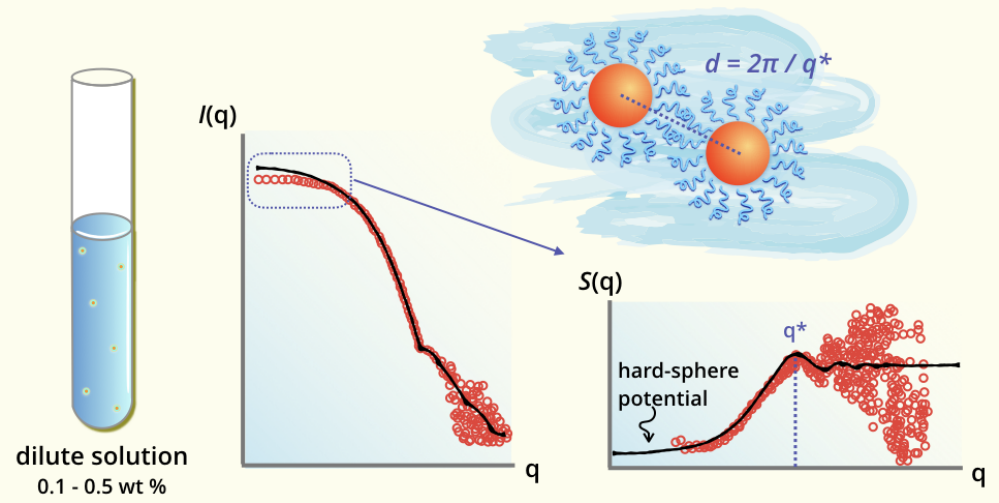

Figure 3.8: Schematic picture showing the structure factor on a SAXS curve due to the intramicellar repulsive correlation.

Moreover, long-range screened Coulomb potential is found to be absent, and the electrostatic force does not extend beyond micelle coronas. The repulsive intermicellar interaction is further evidenced by the disparities between the radii of gyration determined by Guinier approximation and pair distribution functions. We also point out that the nontriviality of the interparticle interaction among PEC micelles in dilute solutions renders the accuracy of the widely-implemented Guinier approximation to be subject to micelle concentration. These findings would pave ways to studying dynamics of PEC micelles, such as micelle fission/fusion kinetics, and might shed light on our under-standing of micelle behavior when intravenously injected into the bloodstream, through which the micelle concentration is significantly diluted.[25] The structure-property relationships of these self-assembling nanoparticles have been extensively studied and exploited as delivery vectors for DNA,[26, 27, 28] RNA,[29, 30] oligonucleotides,[31, 32] proteins,[33] and enzymes.[6] Moving such nanoparticle formulations forward as nanomedicine with control and precision over functionality will rely on these subtle yet important design considerations.

References

[1] Daniel V. Krogstad, Soo-hyung Choi, Nathaniel A Lynd, Debra J. Audus, Sarah L. Perry, D Gopez, Craig J. Hawker, Edward J. Kramer, and Matthew V Tirrell. Small Angle Neutron Scattering Study of Complex Coacervate Micelles and Hydrogels Formed from Ionic Diblock and Triblock Copolymers. *J. Phys. Chem. B*, 118:13011–13018, 2014.

[2] Daniel V.Krogstad, Nathaniel A.Lynd, Soo-Hyung Choi, Jason M.Spruell, Craig J.Hawker, Edward J. Kramer and Matthew V.Tirrell. Effects of Polymer and Salt Concentration on the Structure and Properties of Triblock Copolymer Coacervate Hydrogels. *Macromolecules*, 46:1512–1518, 2013.

[3] Samanvaya Srivastava, Marat Andreev, Adam E. Levi, David J. Goldfeld, Jun Mao, William T. Heller, Vivek M. Prabhu, Juan J. De Pablo, and Matthew V. Tirrell. Gel phase formation in dilute triblock copolyelectrolyte complexes. *Nat. Commun.*, 8:14131, 2017.

[4] Marc Lemmers, Ilja K. Voets, Martien a. Cohen Stuart, and Jasper Van der Gucht. Transient network topology of interconnected polyelectrolyte complex micelles. *Soft Matter*, 7:1378, 2011.

[5] Atsushi Harada and Kazunori Kataoka. Formation of Polyion Complex Micelles in an Aqueous Milieu from a Pair of Oppositely-Charged Block Copolymers with Poly(ethylene glycol) Segments. *Macromolecules*, 28:5294–5299, 1995.

[6] Atsushi Harada and Kazunori Kataoka. Switching by Pulse Electric Field of the Elevated Enzymatic Reaction in the Core of Polyion Complex Micelles. *J. Am. Chem. Soc.*, 125:15306–15307, 2003.

[7] Atsushi Harada and Kazunori Kataoka. Supramolecular assemblies of block copolymers in aqueous media as nanocontainers relevant to biological applications. *Prog. Polym. Sci.*, 31:949–982, 2006.

[8] Igor L. Smolsky, Ping Liu, Marc Niebuhr, Kazuki Ito, Thomas M. Weiss, and Hiro Tsuruta. Biological small-angle X-ray scattering facility at the Stanford Synchrotron Radiation Laboratory. *J. Appl. Crystallogr.*, 40:453–458, 2007.

[9] Steven R Kline. Reduction and analysis of SANS and USANS data using IGOR Pro. *J. Appl. Cryst.*, 39:895–900, 2006.

[10] B. Y. Otto Glatter. A new method for the evalutaion of small-angle scattering data, volume = 10, year = 1977. *J. Appl., Cryst.*, pages 415–421.

[11] Kell Mortensen and Jan Skov Pedersen. Structural Study on the Micelle Formation of Polyethylene Copolymer in Aqueous Solution. *Macromolecules*, 26:805–812, 1993.

[12] Jan Skov Pedersen and Carsten Svaneborg. Scattering from block copolymer micelles. *Curr. Opin. Colloid Interface Sci.*, 7:158–166, 2002.

[13] Jan Skov Pedersen, Carsten Svaneborg, Kristoffer Almdal, Ian W Hamley, and Ron N Young. A Small-Angle Neutron and X-ray Contrast Variation Scattering Study of the Structure of Block Copolymer Micelles: Corona Shape and Excluded Volume Interactions. *Macromolecules*, 36:416–433, 2003.

[14] Hirohito Hirata, Norikatsu Hattori, Makoto Ishida, Hirofumi Okabayashi, Michihiro Frusaka, and Raoul Zana. Small-Angle Neutron-Scattering Study of Bis(quaternary ammonium bromide) Surfactant Micelles in Water. Effect of the Spacer Chain Length on Micellar Structure. *J. Phys. Chem.*, 99:17778–17784, 1995.

[15] Zhuonan Liu, Tianbo Liu, and Mesfin Tsige. Elucidating the Origin of the Attractive Force among Hydrophilic Macroions. *Sci. Rep.*, 6:26595, 2016.

[16] Jean-pierre Hansen and John B Hayter. A rescaled MSA structure factor for dilute charged colloidal dispersions. *Mol. Phys.*, 8976:651–656, 2006.

[17] O. V. Borisov and E. B. Zhulina. Morphology of micelles formed by diblock copolymer with a polyelectrolyte block. *Macromolecules*, 36(26):10029–10036, 2003.

[18] A. Halperin, M. Tirrell, and T. P. Lodge. Tethered chains in polymer microstructures. *Macromol. Synth. Order Adv. Prop.*, 100:31–71, 1992.

[19] Sanjay Patel and Tirrell Matthew. Measurement of Forces Between Surfaces in Polymer Fluids. *Annu. Rev. Phys. Chem.*, 40:597–635, 1992.

[20] Edwin L. Thomas, David J. Kinning, David B. Alward, and Chris S. Henkee. Ordered Packing Arrangements of Spherical Micelles of Diblock Copolymers in Two and Three Dimensions. *Macromolecules*, 20(11):2934–2939, 1987.

[21] A. Halperin and S. Alexander. Polymeric Micelles: Their relaxation kinetics. *Macromolecules*, 22:2403–2412, 1989.

[22] F Muller, M Delsanti, L Auvray, J Yang, Y J Chen, J W Mays, and B Dem. Ordering of urchin-like charged copolymer micelles: Electrostatic, packing and polyelectrolyte correlations. *Eur. Phys. J. E.*, 53:45–53, 2000.

[23] D Franke, M V Petoukhov, P V Konarev, and A Panjkovich. computer programs ATSAS 2.8: a comprehensive data analysis suite for small-angle scattering from macromolecular solutions. *J. Appl. Cryst.*, 50:1212–1225, 2017.

[24] Anne Martel, Ping Liu, Thomas M. Weiss, Marc Niebuhr, and Hiro Tsuruta. An integrated high-throughput data acquisition system for biological solution X-ray scattering studies. *J. Synchrotron Radiat.*, 19(3):431–434, 2012.

[25] Elena E. Dormidontova. Micellization kinetics in block copolymer solutions: scaling model. *Macromolecules*, 32:7630–7644, 1999.

[26] Won Jong Kim, Yuichi Sato, Toshihiro Akaike, and Atsushi Maruyama. Cationic comb-type copolymers for DNA analysis. *Nat. Mat.*, 2:815–820, 2003.

[27] Won Jong Kim, Toshihiro Akaike, and Atsushi Maruyama. DNA Strand Exchange Stimulated by Spontaneous Complex Formation with Cationic Comb-Type Copolymer. pages 12676–12677, 2002.

[28] Tatiana K Bronich, Hong Khanh Nguyen, Adi Eisenberg, and Alexander V. Kabanov. Recognition of DNA Topology in Reactions between Plasmid DNA and Cationic Copolymers. *J. Am. Chem. Sci.*, 122:9338–8343, 2000.

[29] Rosemary Kanasty, Joseph Robert Dorkin, Arturo Vegas, and Daniel Anderson. Delivery materials for siRNA therapeutics. *Nature Materials*, 12:967–977, 2013.

[30] James C Kaczmarek, Piotr S Kowalski, and Daniel G Anderson. Advances in the delivery of RNA therapeutics: from concept to clinical reality. *Genome Med.*, 9:60, 2017.

[31] Michael Lueckheide, R Vieregg, Alex J Bologna, Lorraine Leon, and Matthew V Tirrell. Structure-Property Relationships of Oligonucleotide Polyelectrolyte Complex Micelles. *Nano Lett.*, 18:7111–7117, 2018.

[32] Ryszard Kole, Adrian R Krainer, and Sidney Altman. RNA therapeutics : beyond RNA interference and antisense oligonucleotides. *Nat. Rev. Drug. Discov.*, 11:125–140, 2012.

[33] Yan Lee, Shigeto Fukushima, Younsoo Bae, Shigehiro Hiki, and Takehiko Ishii. A Protein Nanocarrier from Charge-Conversion Polymer in Response to Endosomal pH. *J. Am. Chem. Soc.*, 129:5362–5363, 2007.

CHAPTER 4

NONEQUILIBRIUM SELF-ASSEMBLY KINETICS IN POLYELECTROLYTE COMPLEX MICELLES

4.1 Introduction

4.1.1 Formation kinetics in surfactant micelles

Back to 1970s, Aniansson and Wall proposed two possible mechanisms for the kinetics of dissociation (association) in surfactant micelles: (1) a step-wise single chain expulsion and insertion mechanism and (2) a collective micelle fission and fusion mechanism[1, 2, 3] Later, experimental observations using light scattering techniques have clearly confirmed that the kinetics of surfactant micelle dissociation-formation equilibrium can be characterized by two well-separated relaxation processes.

Individual micelles are found to be able to evolve into more complex structures, like vesicles.[4] There are typically two mechanisms that are used to explain the kinetic pathway of micelle-to-vesicle transition. The first one describes the micelle-to-vesicle transition as a multi-step process where spherical micelles fist coalesce to rodlike micelles, then rodlike micelles aggregate into bilayers, and finally bilayers bend and close up to form vesicles. This mechanism has been confirmed by computer simulations of different coarse grained and experimentally observed using in situ synchrotron X-ray scattering with millisecond time resolution.[5, 6, 7, 8] For example, using the MTR-SAXS facilities at ERSF, Weiss et al. first investigated the structural evolution and kinetic pathway of zwitterionic-anionic micelle to monodisperse unilamellar vesicle transition within a second.[8] The millisecond time resolution unveils the multiple kinetic steps in the micelle-vesicle transition, which includes the incipient formation of floppy micelles, the transformation to intermediate disklike micelles, and the evolution to unilamellar vesicles.

The other pathway was proposed by He and Schmid.[9] They claimed that intermediate structures like rodlike micelles and bilayers do not necessarily form; micelles grow by merging free polymers from the solution and then swell into vesicles when solvent molecules diffuse into the cores. Using a mesoscopic field-based simulation method, they built a phase diagram of final self-assembled structures, depending on the concentration and solvophilicity of the

polymers.

4.1.2 Formation kinetics in amphiphilic block copolymer micelles

Like surfactant molecules, amphiphilic block copolymers self assemble into various nanostructures in selective solvents.[10, 11, 12, 13, 14] Typically, micelles formed by amphiphilic block copolymers consist of a dense core containing solvophobic blocks and a relatively loose corona containing solvophilic blocks. Since the 1990s, studies on the micellization of synthetic amphiphilic block copolymers have been prevailing. Different from liquid molecules, amphiphilic block copolymers usually have longer block lengths and smaller solvophilic-solvophobic block ratios, which is desirable to achieve the goals of long circulation time and large loading capacity. Amphiphilic block copolymer micelles are often found to be kinetically trapped in polar solvents, such as water, and so their morphologies are subject to a variety of inherent or external parameters, e.g., block lengths, solvent-polymer interfacial tension, and preparation methods.[15, 10]

In theory, in the late 1980s, Halperin and Alexander proposed that the single-chain insertion mechanism is dominant and micelle-micelle fusion is prohibited due to the osmotic repulsion stemming from thick micellar coronas.[16] They claimed that micelle fission (or fusion) may be deactivated due to the high free energy penalty from coronal interactions, which scales as

$$U_{\text{fusion}} \simeq N_B^{2/3}(P_1/P_2^2) \tag{4.1}$$

where N_B is the length of the core-forming block, and P_1 and P_2 are the aggregation number of the *fusionable* aggregate and the initial micelle, respectively. The activation energy clearly minimizes when $P_1 = 1$, which favors the single chain insertion mechanism. It is noteworthy that the result is only valid for starlike micelles that undergo small deviations from equilibrium states. Results from a few experiments suggested that the single chain expulsion/insertion alone can not explain the phenomena well. For example, Esselink et

al. investigated the evolution of mixed diblock copolymer micelles formed by two polymers that have the same composition but different coronal block lengths, and pointed out that the redistribution of polymer chains among micelles proceeds mainly via micelle fusion.[17]. Dormidontova theoretically predicted that in the initial stage after unimer binding is completed, micelle fusion becomes a major pathway for micelle growth because it is more effective to reach the final states[18].

Experimentally, direct observation of the formation pathway and structural evolution of ABC micelles is a challenging task and has been little investigated. Such experiments require state-of-the-art facilities that are equipped with both nanoscale spatial resolution and millisecond temporal resolution. Using the MTR-SAXS facilities at ERSF, Lund and coworkers reported the micellization kinetics of a well-defined amphiphilic block copolymer micelles that consist of poly(ethylene-*alt*-propylene)-poly(ethylene oxide) (PEP-PEO) at a temporal resolution of 100 ms.[19] Through quantitative physical modeling, they demonstrated that the birth and formation of micelles can be viewed as a fast nucleation (within 10 ms) followed by a slow growth process where the elemental growth is via the single-chain insertion mechanism. This work presents solid evidence for the Aniansson-Wall theory and provides a promising way to predict the growth rate dependency on polymer properties. Yet, the PEP-PEO block copolymer used is largely asymmetric and the hydrophobic block PEP is small, i. e. 1 kg/mol, which is not common and not ideal for therapeutic encapsulation and delivery. It would provide more insights on biomedical applications if PEP-PEO block polymers with different block lengths have been used.

By employing Argonnes synchrotron X-ray Beamline equipped with a microfluidic device, Kalkowski et al. Investigated micellization kinetics of a biocompatible and biodegradable amphiphilic diblock copolymer, poly(ethylene glycol)-*block*-poly(caprolactone) (PEG_{114}-*b*-PCL_{32}), in a time resolution of 500 ms.[20] Subscripts represent the numbers of the repeat units. They distinguished three successive stages of the polymer self-assembly into micelles process, including nucleation, micelle fusion, and polymer insertion, which is evidenced by

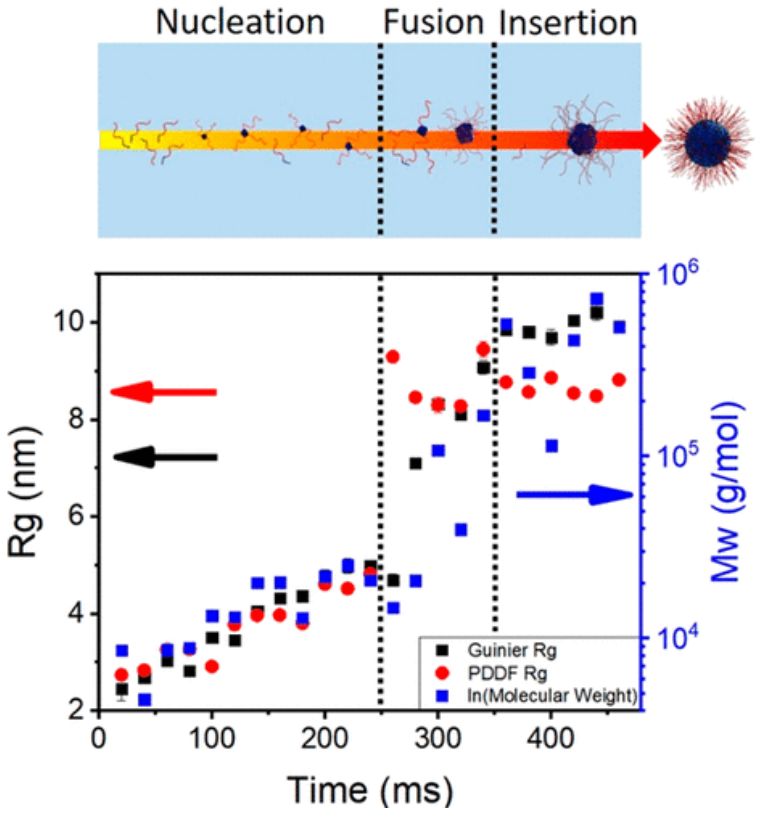

Figure 4.1: Three stages, i. e. nucleation, fusion, and insertion, during amphiphilic block copolymer micelle formation and their corresponding R_gs.

the temporal evolution of micelles radii of gyration, R_g. At the beginning of the micellization, the R_g increases steadily, which is likely to proceed through the coupling of free unimers into nuclei. After 250 ms, the size of R_g abruptly doubles, indicating that the nascent nuclei start to merge with each other, as shown in Figure 4.1. These phenomena are in stark contrast with the Halperin-Alexander unimer insertion mechanism and the experimental results of Lunds work; however, they are in good agreement with the micellization kinetics proposed by Dormidontova.[18]

Parent et al. utilized *in situ* liquid-cell transmission electron microscopy to directly observe the birth and growth of individual amphiphilic block copolymer micelles in real time with nanometer spatial resolution.[21] They clearly captured the snapshots of micelle-micelle collision and fusion events. The block copolymer they used was poly(phenyl)-*block*-poly(peptide-*co*-hydroxyl) and its formation happened at a temporal resolution of a few hundred seconds, which makes possible the direct observation of micelle evolution in an enclosed liquid-cell even without stopped-flow setups.

These studies indicated that the micellar structures and size distribution not only depend on molecular attributes, i.e., the chain length of the amphiphilic molecules, the hydrophilic-hydrophobic ratio, the molecular stiffness, and the intermolecular interactions, but also on system parameters such as the concentration, and on kinetic factors such as the diffusion ability of the amphiphilic molecules and the details of the manufacturing process.

Over the last two decades, it is becoming increasingly clear that the self-assembly of many block copolymer systems are nonergodic and morphological transitions among kinetically metastable nanostructures have evoked broad interest.[10] For example, in the cylinder-to-sphere micelle transition, in which kinetic pathway does the morphological transformation proceed and what intermediate non equilibrium structures are involved? Two kinetic pathways have been proposed: (1) the end budding mechanism where spherical micelles are pinched off one-by-one from the cylindrical ends; (2) the direct decomposition mechanism in which metastable cylinders with undulations split into discrete micelles driven by the

Rayleigh instability. The latter mechanism may be further distinguished between an all-or-none fashion and a random scission fashion.[22]

In 2001, the end budding mechanism was first reported by Burke and Eisenberg in their pioneering work about the rod-to-sphere transition occurring in polystyrene-*block*-poly(acrylic acid) (PS-*b*-PAA) aggregates.[23] They imaged the formation of the irregular pearl-necklace-like intermediate structures. Later, in their successive work, Discher and coworker visualized similar end cleavage phenomena in degradable poly(ethylene oxide)-*block*-polycaprolactone (PEO-*b*-PCL) worm micelles and pH-dependent poly(acrylic acid)-*block*-polybutadiene worm-like micelles.[24, 25, 26]

On the other hand, the direct decomposition kinetic pathway has also been observed. Taking advantage of time-resolved neutron and X-ray scattering integrated with stopped-flow technique, Lund and coworkers identified a two-step kinetic pathway during the cylinder-to-sphere transition in a model block copolymer micelle system with a millisecond temporal resolution.[19] They claimed that first, the metastable cylindrical micelles strongly fluctuate, and thus fragmentize into spherical micelles. No short rodlike structures were observed. These findings support the direct decomposition mechanism. Likewise, Wang et al. reported the direct visualization of the direct decomposition pathway of a spontaneous cylinder-to-sphere transition of amphiphilic poly(2-vinyl pyridine)-*block*-poly(ethlyene oxide) (P2VP-*b*-PEO) diblock copolymer micelles in water.[27] They, for the first time, observed the intermediate structures between spheres and cylinders, including cylinders with undulations and pearl-necklace-like structures, which presents strong evidence for the direct composition mechanism.

4.1.3 Formation kinetics in polyelectrolyte complex micelles

Polyelectrolyte complexation is an associative liquid-liquid phase separation process between oppositely charged polyelectrolytes. Cationic polymers conjugated with hydrophilic, uncharged blocks can electrostatically collapse negatively charged macromolecules into nanos-

tructure composed of a core of polyelectrolyte complexes and a corona of neutral polymer chains. Often, these electrostatic self-assemblies are termed as polyelectrolyte complex (PEC) micelles, coacervate complex core micelles (C3Ms), or polyion complex micelles (PICs). It is reasonable to infer that the formation kinetics of PEC micelles is related to the thermodynamics of polyelectrolyte complexation.

A few groups have taken endeavors to investigate the kinetics e formation of bulk polyelectrolyte complexes. Stopped-flow light scattering and fluorescence have been commonly used to monitor the evolution of fluorescent intensities over time upon complexation. In the early 1980s, Morawetz et al. studied the kinetics of complexation between dansyl-labeled poly(acrylic acid) (PAA) and poly(oxy-ethylene) (POE) through fluorescence experiments with a stopped-flow device. The temporal dependencies of fluorescence intensity are well fitted with double-exponential functions, and two rate constants are extracted.[28] Yet, no specific physical process has been proposed to match the two rate constants. Later, in the early 1990s, Kabanov and coworkers investigated the complexation kinetics in complexes consisting of oppositely charged linear polyelectrolytes, pyrene-labeled poly(sodium methacrylate) (PMANaPy) and poly(N-ethyl-4-vinyl pyridinium bromide) (PEVPB), by luminescence quenching and laser light scattering techniques.[29] They concluded that the complexation process consisted of a first rapid coupling of the oppositely charged polyions with the formation of a nonequilibrium inter-polyelectrolyte network, followed by a slow relaxation process, finally leading to the formation of the individual PICs.

Recently, through stopped-flow light scattering, Liu et al. studied the early stage kinetics of polyelectrolyte complexation between poly(acrylic acid) (PAA) and poly (diallyldimethylammonium chloride) (PDADMAC) at different mixing charge ratios. They revealed three distinct kinetic stages by monitoring the time-dependent light scattering intensity.[30] First, oppositely charged chains form soluble PECs within one second. Second, these soluble PECs aggregate into larger ones. Last, a neutral dense complex phase is formed via coalescence.

Besides, isothermal titration calorimetry (ITC) is a powerful technique to probe the

thermodynamic characteristics of intermolecular bindings.[31, 32, 33] In a typical ITC measurement, under a controlled isothermal condition, a small amount of polypeptide is added to a solution containing an oppositely charged polypeptide, and the heat flow between a sample cell and a reference cell is monitored. Quantitative values of the binding affinity (K_a), enthalpy changes (ΔH), and binding stoichiometry (n) of the polypeptide interaction can be determined using proper models. The Gibbs free energy changes (ΔG) and entropy changes (ΔS) can be further determined using the relationship:

$$\Delta G = -RT \ln K_a = \Delta H - T\Delta S \tag{4.2}$$

Profits et al. investigated the thermodynamics of polypeptide complex coacervation polypeptide complex coacervation using ITC and light scattering. By studying the thermodynamic characteristics of the coacervation process, they found two distinctive binding steps: the first step is called ion pairing, where two oppositely charged polypeptide pair with each other to form a soluble complex, and the second step is the complex coacervation process, in which the incipient soluble complexes aggregate into insoluble inter-polymer complexes.

Using a combination techniques of ITC, light scattering, and electrophoresis, Vitorazi and coworkers studied the thermodynamics of the complexation between poly (diallyldimethylammonium chloride) (PDADMAC) and poly (sodium acrylate) (PANa) and found a similar two-step process.[34] Further, they revealed the important role of the mixing order in coacervation. By adding PDADMAC to PAA or vice-versa, it is found that the phase separation exhibited an exothermic profile upon addition of PDADMAC to PAA but an endothermic profile for the reverse in terms of titration calorimetry response.

From the aforementioned work, we have made two observations regarding the kinetics of polyelectrolyte complexation. First, in thermodynamics, polyelectrolyte competition can be an endothermic or an exothermic process, depending on the mixing order. Second, the formation of polyelectrolyte complexes mainly comprise two distinct stages: a fast ion pair-

ing step where oppositely charged polymers form soluble complexes, and a slow growth step where complexes coalesce into a dense complex phase. These findings have made strides towards the fundamental understanding in the formation kinetics of polyelectrolyte complexes. However, due to the limitations on the instruments, monitoring the structural evolution evolution of the polyelectrolyte complexes in a real time still remains a challenge, specially in the first fast step.

Very recently, time-resolved small-angle X-ray scattering (TR-SAXS) equipped with stopped-flow devices has been demonstrated as a powerful tool to probe the structural transformation in soft matter systems with a millisecond time resolution. Takahashi and coworkers investigated the kinetic process of the polyelectrolyte complexes formed by two oppositely charged homo-polyelectrolytes, sodium polyacrylate (SPA) and polyallylamine hydrochrolide (PAH), in aqueous NaCl solution.[22] By employing time-resolved ultra-small-angle X-ray scattering (TR-USAXS) coupled with a stopped-flow device, they were able to reveal the evolution of the complexes size, structure, and molecular weight in a time range from 2.5 ms to 8733 ms. They found a similar three-step process: (i) a very rapid ($<$ 2.5 ms) step where oppositely charged chains pair by electrostatic interactions; and (ii) a complexation step where the ion pairs further coalesce into nearly neutral aggregates driven by van der Waals and hydrophobic interations; and (iii) a growth step where these aggregates grow into complexes. The growth rate of molar mass is similar to the Brownian-coagulation kinetics of spherical colloidal particles.

The formation kinetics of PEC micelles have been much less studied and understood compared to surfactant micelles, ABC micelles, or PECs. Despite the stark contrast of their driving forces, PEC micelles have been oftentimes understood in an analogous way to diblock copolymers micelles. It may be plausible with respect to the static micellar structures, which has been the focus so far. In Chapter 3, we point out that the long-range electrostatic interactions do not significantly affect micelle-micelle correlation, meaning that PEC micelles in dilute solutions behave in a similar way to their uncharged counterparts.

However, when it comes to micelle kinetics, distinctions emerge. First, block copolymer micelles is usually a ternary system that contains solvent, coronal chains, and core chains; PEC micelles in most cases is a multi-component system in which the interplay between positively-charged blocks, negatively-charged blocks, one or two coronal blocks, counterions, and solvent (normally water) complicates micellar dynamics. Second, unlike block copolymer micelles, the core chains in PEC micelles are hydrophilic and maintained a complex state via electrostatic interactions, which means the expulsion of a chain from micelle cores exposes no unfavorable chains in solvent but rather needs to counteract the Coulomb attraction between positive and negative charges. The breakup of the electrostatic bonds may retard the kinetics. Our results from time-resolved small-angle neutron scattering indicates that these micelles in equilibrium remain frozen up to 40 hours. Third, block copolymer micelles have solid-like cores, whereas PEC micelle cores contain a large amount of water (ca. 30 - 90 %), which is subject to environmental factors such as salt ion concentration and system temperature. All these features combined makes studies on the mechanism of PEC micelle dissociation or formation difficult.

Stuart et al. reported the kinetics of micelle formation with polyelectrolyte complex cores formed by PAA and poly(dimethyl amino ethyl methacrylate)-*b*-poly(glyceryl ethacrylate) (PDMA-*b*-PGMA) in aqueous solution at pH 7.[35] Upon mixing, they unexpectedly observed a non-monotonic phenomenon in which the scattering intensities have a rapid rise followed by a relatively slow decay. Such transient behaviors were speculated to be caused by two successive steps of micelle formation: (1) immediately after mixing, oppositely charged blocks tend to phase separate into large and dense complex droplets, which happens within a second, and (2) these droplets spontaneously rearrange themselves into smaller micellar structures due to the existence of the neutral blocks. This mechanism is partly evidenced by the fact that the addition of salt strongly expedited the rate of rearrangement by the factor of 10^4 from pure water to 0.3 M NaCl. However, this transient phenomenon has not been observed in other systems and is unlikely universal. We speculate this is related to the

chemical structure, composition, and charge density of the constituent polyelectrolytes.

Lindhoud and coworkers further compared the relaxation behaviors of two polyelectrolyte complex systems.[36] One is composed of two weakly charged polyelectrolytes, positively charged hompolymer PDEAMEAM and negative charged diblock copolymer PAA-PAAm, and the other consists of one weakly charged homopolymers PAA and one strongly charged diblock copolymer P2MVP-b-PEO. The found that the former system reached equilibrium while the latter one was kinetically trapped in non-equilibrium states over the period of at least of week.

Ting and coworkers reported similar observations in PEC systems that contain two oppositely charged styrenic cationic or anionic blocks coupled with poly(ethylene oxide), namely, poly(ethylene oxide)-*block*-poly(vinyl benzyl trimethylammonium chloride (PEO-*b*-PVBTMA) and poly(ethylene oxide)-*block*-poly(sodium 4-styrenesulfonate) (PEO-*b*-PSS), both of which are strong polyelectrolytes, can not form well-defined micelles but kinetically trapped PEC aggregates.[37] In contrast, PEO-*b*-PVBTMA and a weakly charged polyelectrolyte poly(acrylic acid) (PAA) can form uniform spherical micelles. In Chapter 2, we report the temporal evolution of the internal structures and relaxation behaviors of the kinetic products formed by PEO-*b*-PVBTMA and PEO-*b*-PSS. By designing two mixing methods, they pointed out that the strong electrostatic interactions between two strongly charged blocks led to the kinetic complex products and prohibited the rearrangement of the polymer chains into equilibrium states. The relaxation time was decreased when ionic interaction weakened by the addition of salt. Using PEO-*b*-PVBTMA as a cationic component, Marras et al. demonstrated that this styrenic cationic polyelectrolyte can condense DNA oligonucleotides into spheroidal or cylindrical morphologies, depending on the block length and DNA hybridization.[38] Single-stranded DNA and PEO-*b*-PVBTMA formed spheroidal micelles, while double-stranded DNA, with doubled charge density, and PEO-*b*-PVTBMA formed cylindrical micelles. Lueckheide et al. reported that when complexed with PEO-*b*-polylysine, single-stranded DNA formed spheroidal micelles whereas double-stranded DNA

formed cylindrical micelles.[39]

As stated above, the formation of PEC micelle is a rather complicated process which not only depends on molecular parameters such as polymer block lengths and charge density. Consequently, all of these factors play roles in the formation kinetics of PEC micelles. Previous studied reported by Eisenberg and Kabanov and their coworkers claimed that there are two possible stages during the formation of PEC micelle: a fast step that involves the pairing of oppositely charged polyelectrolytes and a slow step where the ionic pairs aggregate into complexes. Using stopped-flow light scattering, Zhang et al. first investigated the formation process of the PEC micelles consisting of anionic poly(ethylene oxide)-*block*-poly(sodium 4-styrene sulfonate) (PEO-*b*-PSSNa) and cationic poly(ethylene oxide)-*b*-poly(quaternized 2-dimethyl amino ethyl methacrylate) (PEO-*b*-PQDMA).[40] By fitting the time dependent intensity into a double-exponential model, they identified two distinct steps in micelle formation: a fast relaxation process that attributes to the initial formation of small complexes and a slow process where complexes reach final equilibrium states via micelle redistribution and rearrangement. The two steps happen within one second and are proceed via second-order reactions, which indicates that PEC micelles form through a micelle fusion-fission mechanism.

However, these early endeavors failed to address some critical challenges. First, none of these work has made direct observation of the first stage due to the limitations on the time resolution of the facilities. Second, the structural evolution of the polyelectrolyte complexes in a millisecond time resolution has never been obtained. Third, no quantitative physical model was proposed to describe the kinetic pathway of PEC micelle formation, which is probably due to the lack of good understanding of the polyelectrolyte complexation itself and the absence of a micelle scaling law.

Using the same facility at ESRF, Takahashi et al. further studied the kinetics of the morphological transitions between spherical and cylindrical micelles formed by an anionic-neutral diblock copolymer and a cationic-neutral diblock copolymer.[41] By changing the

Table 4.1: Samples for formation kinetic studies using the time-resolved small-angle X-ray scattering technique.

Sample	Polycation	Polyanion	Concentration
5K50158	PEO_{5K}-*b*-$PVBTMA_{50}$	PAA_{158}	2.5 mg mL^{-1}
10K100158	PEO_{10K}-*b*-$PVBTMA_{100}$	PAA_{158}	2.5 mg mL^{-1}
10K100158	PEO_{10K}-*b*-$PVBTMA_{100}$	PAA_{158}	3.75 mg mL^{-1}

molar ratio between the cationic and ionic blocks, the cylinder-to-sphere transition was triggered, and its kinetic pathway was found to follow the random scission process in which spherical micelles are generated along the cylindrical micelle contour.

However, little work has been reported about the structural evolution and kinetic pathway of the formation of polyelectrolyte complex micelles.

4.2 Experimental Details

4.2.1 Materials

The micelles are formed by PEO-*b*-PVBTMA and PAA as we discussed in the above chapters. Two block copolymers with different block lengths are studied, namely, PEO_{5K}-*b*-$PVBTMA_{50}$ and PEO_{10K}-*b*-$PVBTMA_{100}$. The samples are listed in Table 4.1.

4.2.2 Time-resolved small-angle X-ray scattering

All the time-resolved small-angle X-ray scattering experiments were carried out on the Biological Small Angle Scattering Beamline BL4-2 at the Stanford Synchrotron Radiation Lighthouse (SSRL), SLAC National Accelerator Laboratory. The TR-SAXS facility at BL4-2 equipped with stopped-flow mixer setup provides access to reaction kinetics on the millisecond time scale and above. It has customized Bio-Logic 4 syringe stopped-flow mixer (SFM400).

A typical TR-SAXS experiment is proceeded in the following way. First, aqueous solutions of positively charged polymers and and negatively charged polymers are loaded in two

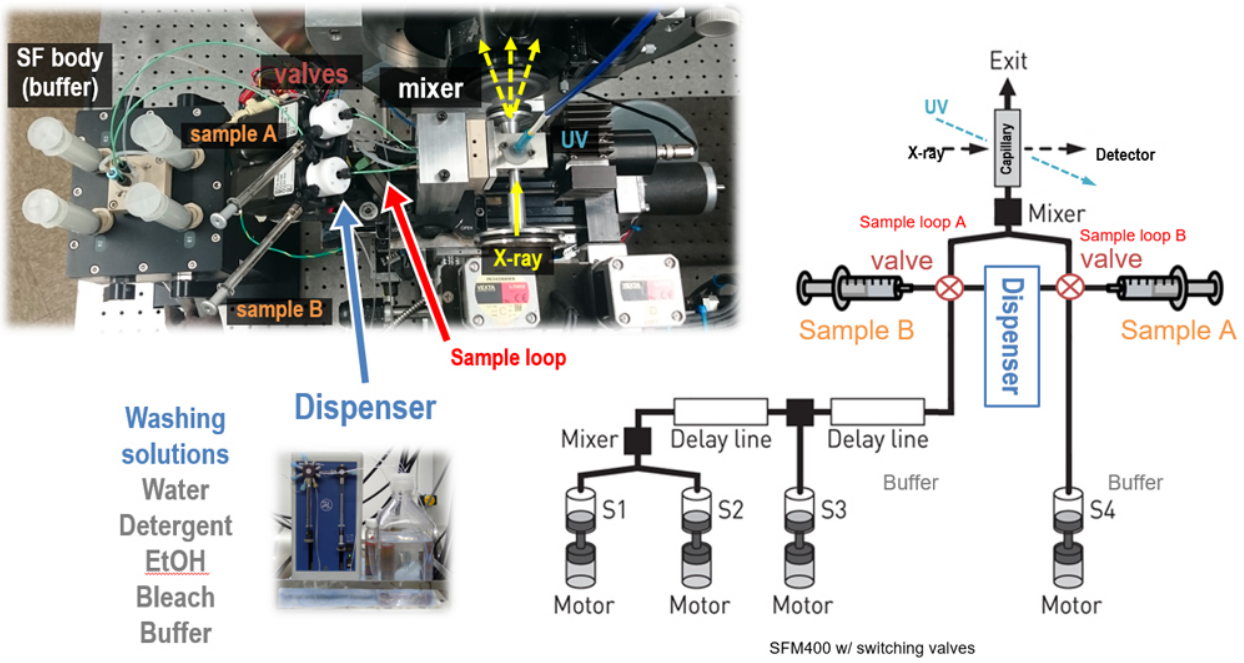

Figure 4.2: The stopped-flow setup at Beamline BL4-2 at the SLAC National Accelerator Laboratory.

separate syringes. Second, equal volumes of polycation and polyanion solutions are pumped int to the mixer by the motors, corresponding to the equimolar concentration of the cationic and anionic monomer units. The dead time is about 4 ms. Third, the mixed solution is further dispensed into the capillary cell where the incident X-ray radiates through. The sample solution is sealed by its buffer on the two ends of the capillary cell. The exposure time for each each measurement is 20 ms.

4.2.3 SAXS modeling

SAXS modeling was performed using the Macro package in Igor Pro provided by NIST and the ATSAS software.[42, 43] A polydisperse core-shell sphere model was used to fit the SAXS curves, as described in Chapter 2.

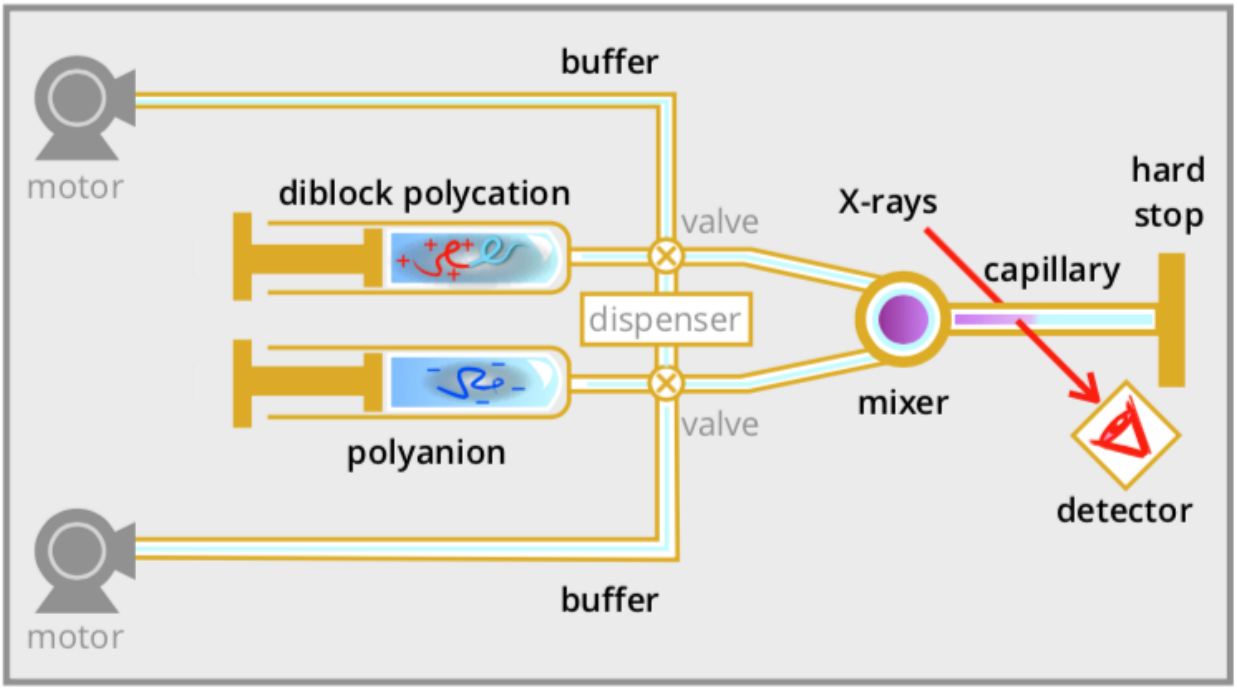

Figure 4.3: Schematic representation of a typical time-resolved small-angle X-ray scattering experiments with a stopped-flow device.

4.3 Results and Discussion

4.3.1 Structural evolution of PEC micelles

The time evolution of the X-ray scattering curves is presented in Figure. Three independent kinetic experiments were carried out from the 5K50158 sample, where the polycation is PEO_{5K}-*b*-$PVBTMA_{50}$, the polyanion is PAA_{158}, and the total polymer concentration is 1.0 mg mL^{-1}. In order to get a high time resolution, we used a very low exposure time of 20 ms, which may reduce the quality of the scattering curves due to noise. To avoid that, we repeated the same experiment for three times. It is shown that the scattering data is reliable and reproducible even under a very low exposure time of 20 ms. The effect of polymer concentration and block length on micelle formation kinetics in also investigated using the same polyanion but a longer polycation, PEO_{10K}-*b*-$PVBTMA_{100}$. The samples are named as 10K100158 and two concentrations are studied, i.e. 2.5 mg mL^{-1} and 3.75 mg mL^{-1}.

All of the curves are well fitted by the polydisperse core-shell sphere model described in

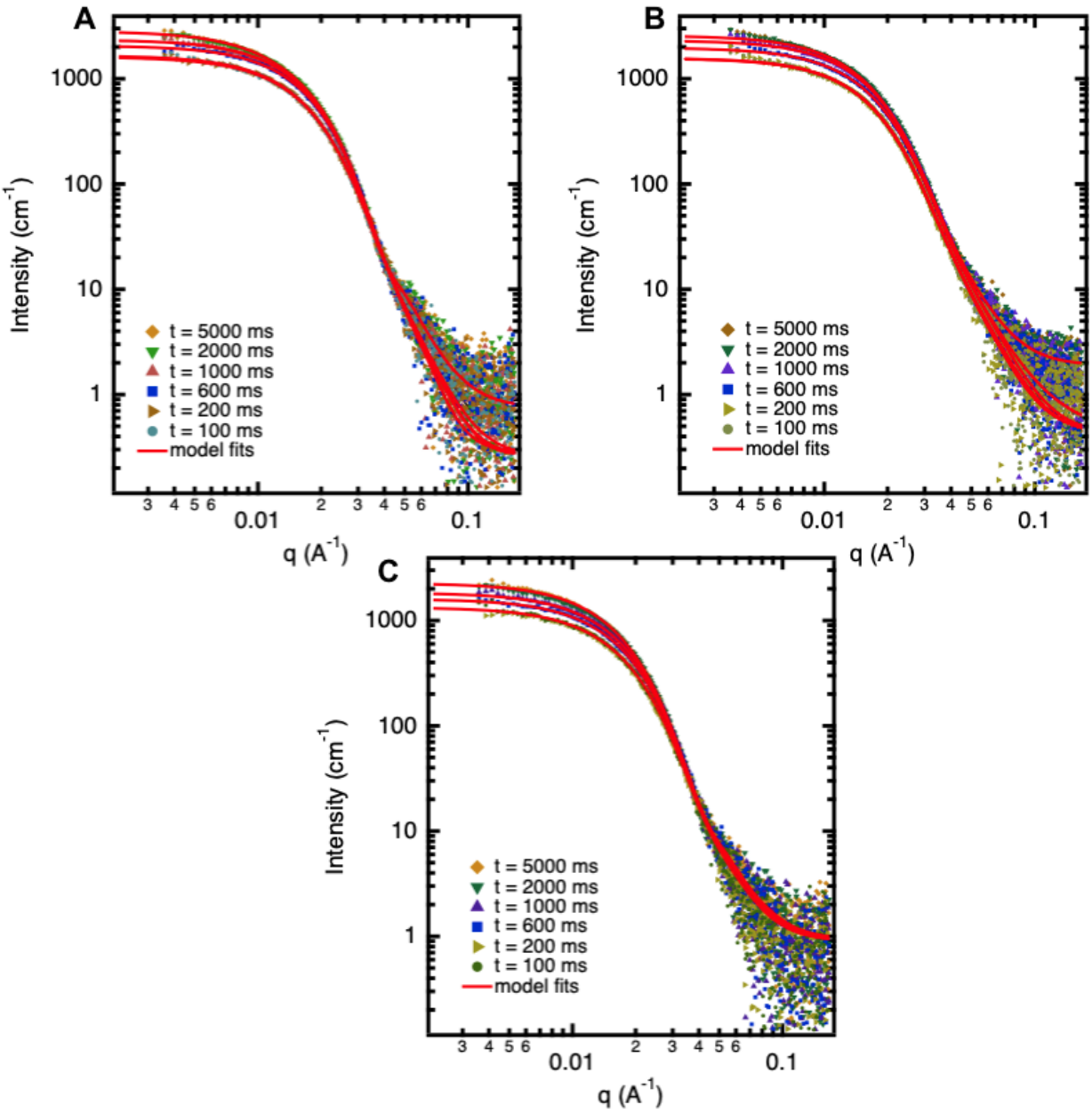

Figure 4.4: The SAXS curves of micelle samples 5K50158 at 2.5 mg mL^{-1}.

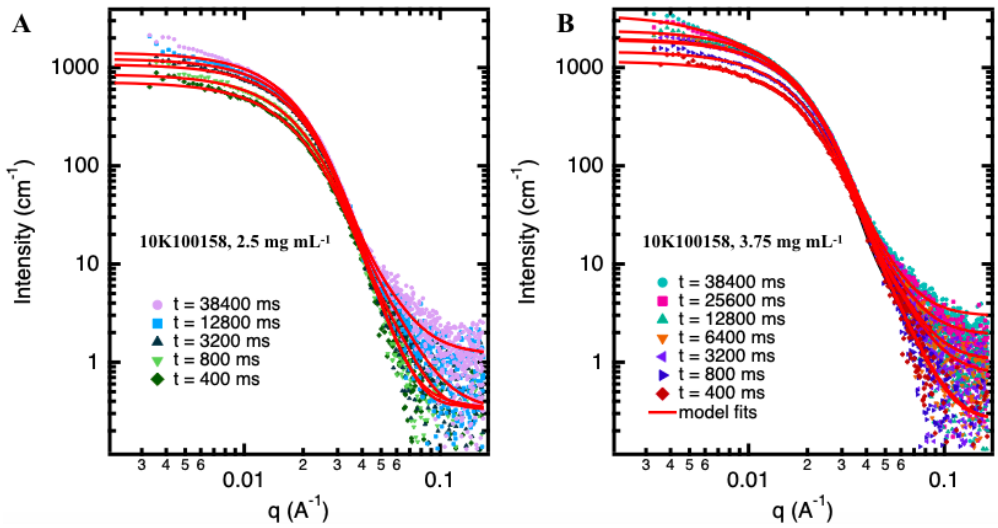

Figure 4.5: The SAXS curves of micelle samples 10K100158 at 2.5 mg mL^{-1} (A) and 3.75 mg mL^{-1}(B).

the experimental details. The increase in the scattering intensity reflects the micelle growth in real time. Due to the limitations of the setup, the low limit of the experimentally probed time period is 100 ms. We investigated the structural evolution of the polyelectrolyte self-assemblies in the time range from 100 ms to 5000 ms. Above 5000 ms, the changes of the scattering intensities are barely discernable, indicating that the micelle growth is very slow. At t = 100 ms, spherical micellar aggregates have already formed.

We also investigated the effects of block length and polymer concentration on the formation kinetics of PEC micelles, particularly on the growth rate. The structural evolution of PEC micelles formed by PEO_{10K}-*b*-$PVBTMA_{100}$ and PAA_{158} at total polymer concentrations of 2.5 and 3.75 mg/mL were monitored. The exposure time is set to be 80 ms in order to get a longer experimental time. The recorded time for 2.5 mg/mL and 3.75 mg/mL are 19200 seconds and 38400 seconds, respectively. It is observed that: (i) PEO_{10K}-*b*-$PVBTMA_{100}$ and PAA_{158} form a bigger micellar aggregates; (ii) they form micelles slower than 5K50; and (iii) high polymer concentration slows down the formation process.

4.3.2 Size evolution

The radii of gyration of the micellar aggregates at successive time moments are extracted via the Guinier approximation using the GNOM package. Three independent measurements were repeated for the micelle sample 5K50158 with a total concentration of 2.5 mg mL, and the time dependent evolution of Gunier R_g is plotted in Figure. All three sets of data show a similar profile. We observe that: first, micellar aggregates with a R_g of 10.5 nm have formed within the initial 100 ms, which is too fast to be captured by the instrument. Second, these micellar aggregates keep growing as their size increases steadily, starting from 10.5 nm at 100 ms to 12.0 nm at 5000 ms.

Similar phenomena have been found in the samples 10K100158 at two total concentrations, i.e. 2.5 and 3.75 mg mL^{-1}, shown in Figure 4.6. However, it is found that the formation process is much slower for the micelles with polycations containing longer block lengths. For example, for the micelle sample 5K50158, their R_gs tend to remain constant around t = 5000 ms, while for the 10K10158, the R_g increases from 11.0 nm at t = 5000 ms to 14.0 nm at t = 38400 ms. This slowdown is probably due to the increase of the activation energy and longer time of polymer rearrangement for longer chains. It is also found that the formation rate has no marked dependence on polymer concentration.

The exact kinetic pathway in the initial 100 ms cannot be addressed since it is beyond the measurement of the instruments. As aforementioned, there are two possible mechanisms for micelle formation: single-chain insertion or micelle fusion. In the time period from 100 to 5000 ms, it is unlikely that micelle fusion takes place. Otherwise, the size of the micellar aggregates would have shown an abrupt jump, as Kalkowski et al. have observed in amphiphilic block copolymer (ABC) micelles. Thus, the incremental growth of the micellar aggregates should be caused by a chain insertion mechanism. However, the classical single-chain insertion mechanism can be reasonably excluded. According to the theories of polyelectrolyte complexation, free individual polyelectrolytes tend to form complexes with their oppositely charged counterparts even at extremely low concentrations. Free cationic or anionic chains

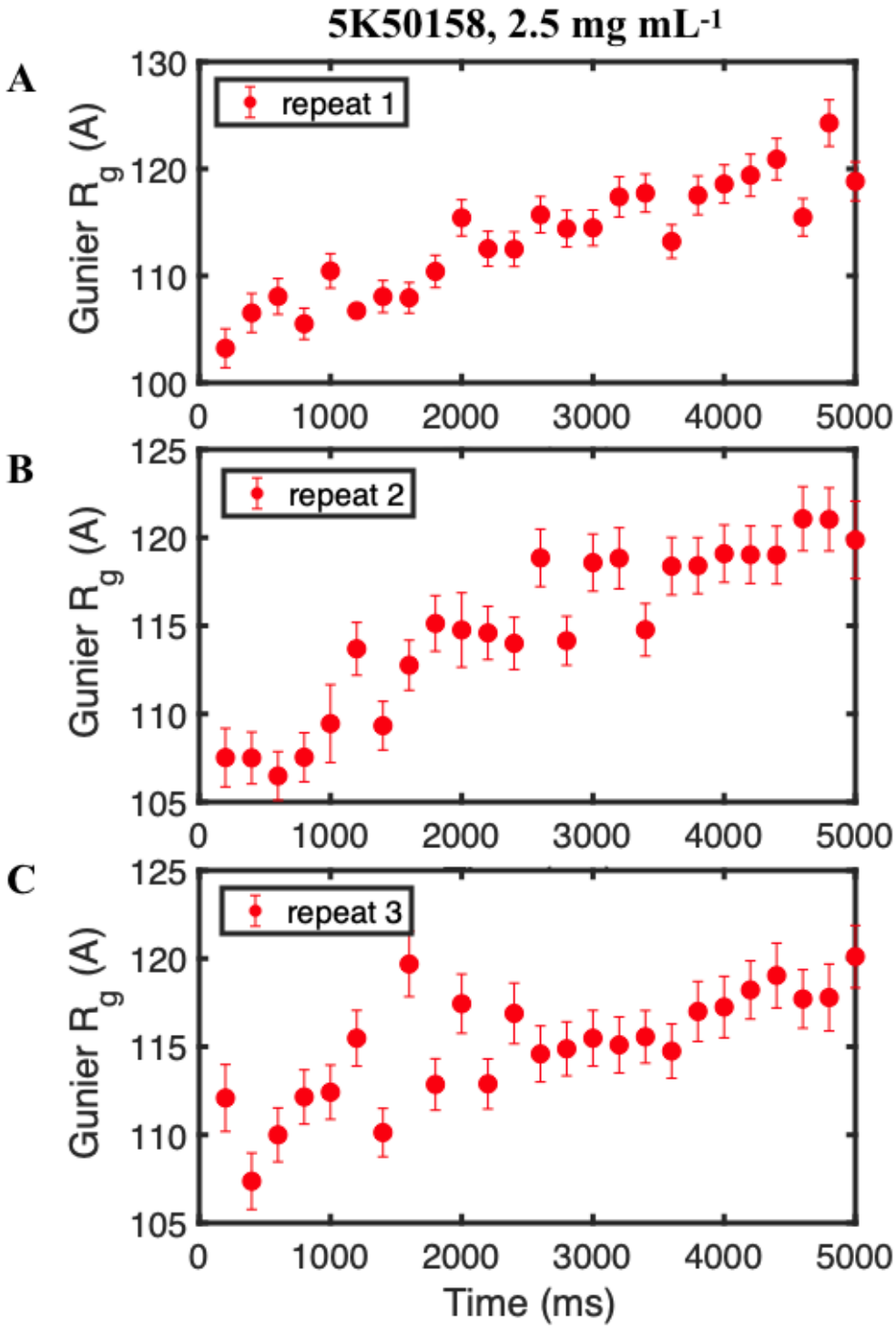

Figure 4.6: Fitted R_g via Guinier approximation of the three repeats of the sample 5K50158.

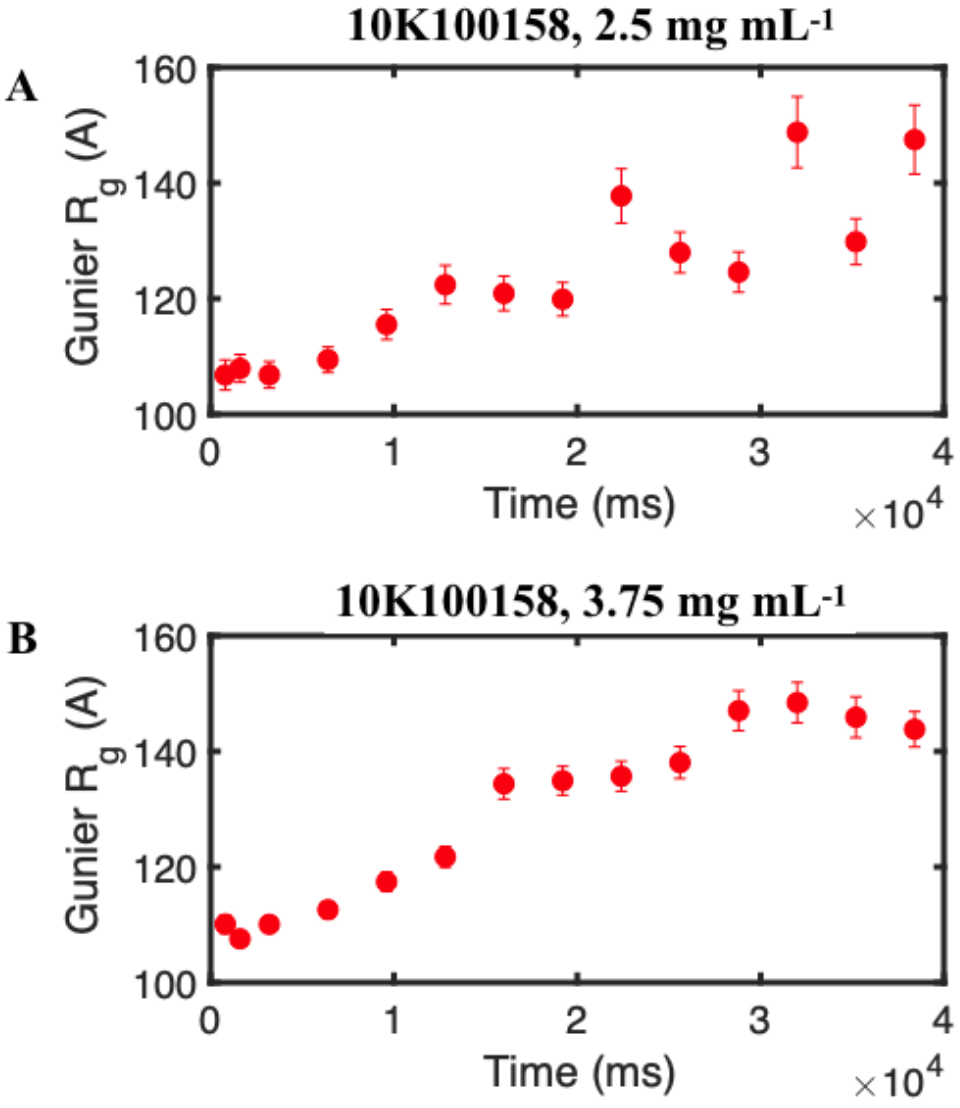

Figure 4.7: Fitted R_g via Guinier approximation of the sample 5K50158 at 2.5 mg mL^{-1}(A) and 3.75 mg mL^{-1}(B).

are unlikely to exist at a time moment when micellar aggregates with an R_g of 10 nm have already formed. Illustrated by the formation kinetics of bulk polyelectrolyte complexes, it is reasonable to infer that, immediately after mixing, oppositely charged blocks pair with each other to form neutral and soluble clusters within a few milliseconds. Then these incipient clusters start to aggregate into bigger micellar structures. The formation of interconnected mesoscopic structures is hindered in diblock copolymers due to the favorable stretch of the neutral blocks in the aqueous solvent and the lack of bridging chains among discrete micelles. In micelle systems where triblock copolymers are a constituent component, gel phases and macroscopic phase separation are found in dilute solutions as the triblock copolymers act as bridges among micelle cores.

4.3.3 Physical modeling

Thus, we speculate that in the probed experimental time periods, the growth pathway of PEC micelles is mainly through a cluster insertion mechanism. We consider that why micelle fusion or cluster fusion is not favored. When two micelles merge, one of the micelles has to penetrate the dense corona region of the other

$$F_{\text{interface}}^{P_i} \simeq 4\pi R_i^2 \gamma \tag{4.3}$$

$$\Delta F = 4\pi\gamma \left(R_3^2 - R_1^2 - R_2^2 \right) \tag{4.4}$$

$$R_3^3 = R_1^3 + R_2^3 \tag{4.5}$$

where $F_{interface}^{P_i}$ represents the free energy of the solvent-core interfaces, γ is the interfacial tension, and R_3, R_2, and R_1 are the core radius of micelle 1, micelle 2, and micelle 3, respectively.

Mathematically, ΔF is always negative and reaches its maximum absolute value when

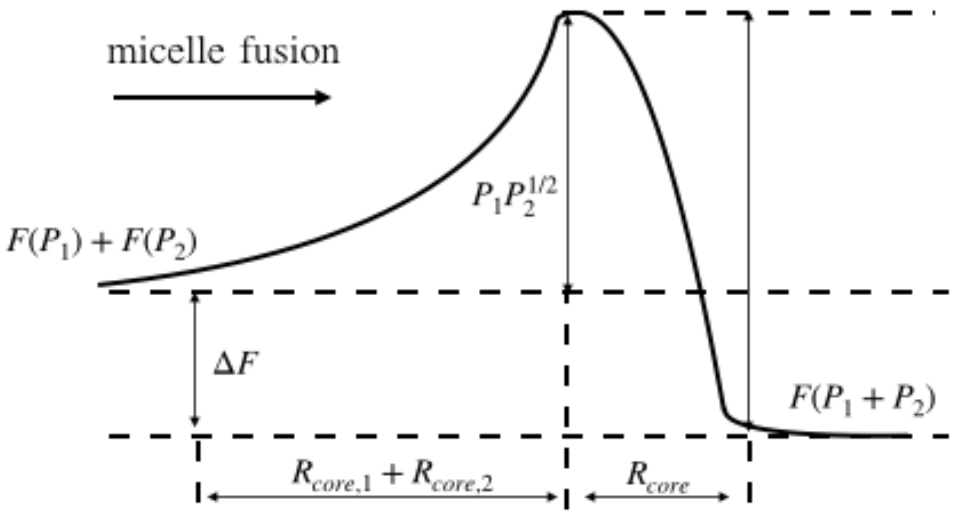

Figure 4.8: Schematic description of the potential barrier for micelle fusion in the framework of Kramer's rate theory.

$R_1 = R_2$. However, before the core fusion, the micelles have to overcome the energetic barrier mainly coming from the adoption of more extended conformations of the coronal chains as long as two micelles penetrate each other. When micelle 1 with P_1 chains penetrates micelle 2 with P_2 chains, each chain loses $P_2^{1/2}$ free energy, and the total energy, U_{fusion} can be given by:

$$U_{\text{fusion}} \simeq P_1 P_2^{1/2} \tag{4.6}$$

From the above expression, it is obvious to know that U_{fusion} is proportional to the aggregation numbers of the two merging micellar aggregates, and the energetic barrier of micelle-micelle fusion is higher than that of the cluster-micelle insertion. Thus, the cluster-micelle insertion mechanism is energetically favored over the micelle-micelle fusion mechanism. Yet, at the very beginning of micelle growth, when the aggregation numbers are small enough, micelle-micelle fusion may be possible. Only in the late stage where micelle coronas are too large and too dense to be penetrated, the cluster insertion becomes dominant, as we observed in Chapter 4. In Chapter 4, we observed that when two full-grown micelles approach, the coronas are compressed to some extent, but the depth of the compressed area is only half

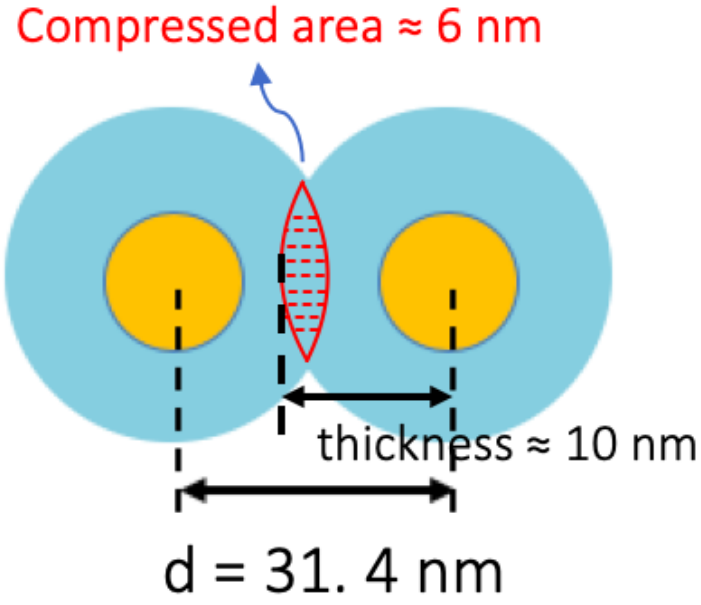

Figure 4.9: Schematic representation of micelle compression when two micelles collide.

of the corona thickness, as shown in Figure 4.9. The micelle cores are still unable to touch each other, which makes the micelle fusion unlikely. Similar argument has been made by theories.[16, 18] It is noteworthy that in the above analysis, the polyelectrolyte clusters and intermediate micelles are assumed to be electrostatically neutralized.

Therefore, we speculate that the kinetic pathway of PEC micelle formation can be described as a three-staged process, as illustrated by the Scheme. First, immediately upon mixing, oppositely charged polyelectrolytes form small and neutral clusters within a few milliseconds. Second, these incipient clusters aggregate into micellar aggregates via cluster insertion mechanism and micelle fusion. Third, as micelles grow bigger, cluster insertion becomes the main pathway.

4.4 Concluding Remarks

In this Chapter, first, I overview the literature regarding the kinetic pathways and morphological transformation in a range of polymeric self-assemblies, including surfactant micelles,

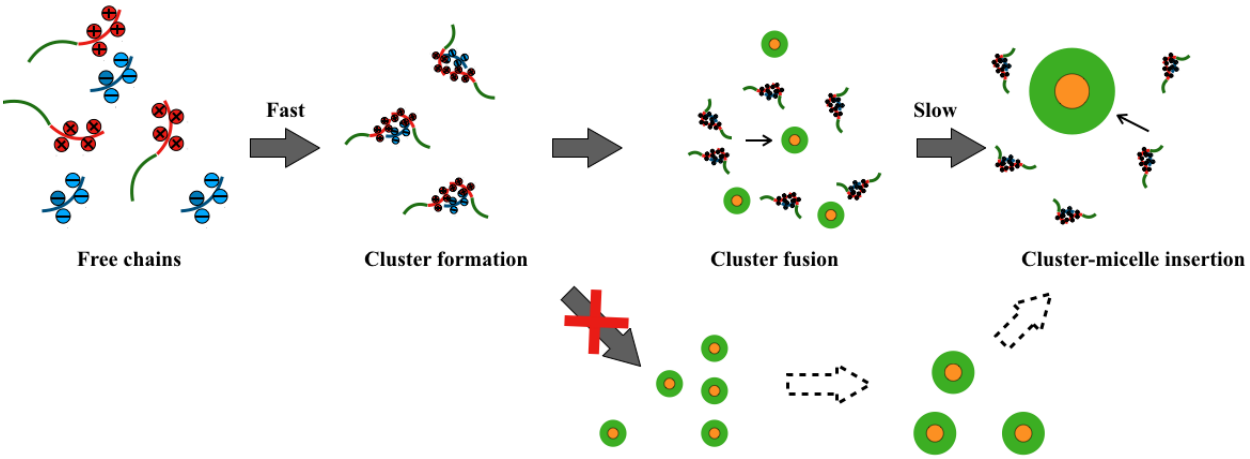

Figure 4.10: Schematic representation of the kinetic pathway in PEC micelle formation.

amphiphilic block copolymers, and polyelectrolyte complex micelles. Based on these studies, a few conclusions can be drawn. (i) The formation of surfactant micelles is driven by both the single chain insertion/expulsion mechanism and the micelle fusion/fission mechanism. (ii) For amphiphilic block copolymer micelles, both single chain insertion and micelle fusion have been observed but the latter takes place significantly slower than the former. (iii) The non equilibrium transition from cylinder to spheres amphiphilic block copolymer micelles is mainly proceeded via the direct composition mechanism, although contradicting results are observed.

Second, the vast differences between polyelectrolyte-based micelles and their uncharged counterparts are discussed. Progress on understanding the underlying mechanism and kinetic pathway of the formation of polyelectrolyte complexes is introduced. Evidence from a large volume of studies has shown that polyelectrolyte complexation is a two-step kinetic process: an ion pairing step followed by an aggregate coalescence step.

Third, by employing time-resolved small-angle X-ray scattering technique with millisecond time resolution, the structural evolution of polyelectrolyte complex micelles is investigated. It is shown that the formation of micelles with an average radius of 10 nm has been completed within the initial 100 ms. These micelles continue to grow in a steady manner to ca. 12 nm in radius after 5 seconds. By applying a quantitative physical model, it is

evidenced that neither the classical single chain insertion nor the micelle fusion mechanism stands. Instead, PEC micelle formation is likely to proceed via a cluster-micelle insertion mechanism. Immediately after mixing, driven by strong electrostatic interactions, oppositely charged polyelectrolytes pair with each other to form clusters. Then these nascent clusters start to merge into micellar aggregates. As micelle grows bigger, the cluster-micelle insertion pathway becomes increasingly dominant. In the late stage, micelle grows via cluster-micelle insertion only.

References

[1] E. A. G. Aniansson and S. N. Wall. Kinetics of step-wise micelle association. *J. Phys. Chem.*, 78:1024–1030, 1974.

[2] E. A. G. Aniansson and S. N. Wall. Kinetics of step-wise micelle association. Correction and improvement. *J. Phys. Chem.*, 79(8):857–858, 1975.

[3] E. A. G. Aniansson, S. N. Wall, M. Almgren, H. Hoffmann, I. Kielmann, W. Ulbricht, R. Zana, J. Lang, and C. Tondre. Theory of the kinetics of micellar equilibria and quantitative interpretation of chemical relaxation studies of micellar solutions of ionic surfactants. *J. Phys. Chem.*, 80:905–922, 1976.

[4] Irene C. Reynhout, Jeroen J.L.M. Cornelissen, and Roeland J.M. Nolte. Self-assembled architectures from biohybrid triblock copolymers. *J. Am. Chem. Soc.*, 129(8):2327–2332, 2007.

[5] S. U. Egelhaaf and P. Schurtenberger. Micelle-to-vesicle transition: A time-resolved structural study. *Phys. Rev. Lett.*, 82(13):2804–2807, 1999.

[6] Mu Ping Nieh, Velayudhan A. Raghunathan, Steve R. Kline, Thad A. Harroun, Chien Yueh Huang, Jeremy Pencer, and John Katsaras. Spontaneously formed unil-

amellar vesicles with path-dependent size distribution. *Langmuir*, 21(15):6656–6661, 2005.

[7] J. Leng, S. U. Egelhaaf, and M. E. Cates. Kinetic pathway of spontaneous vesicle formation. *Europhys. Lett.*, 59(2):311–317, 2002.

[8] T. M. Weiss, T. Narayanan, C. Wolf, M. Gradzielski, P. Panine, S. Finet, and W. I. Helsby. Dynamics of the self-assembly of unilamellar vesicles. *Phys. Rev. Lett.*, 94(3):1–4, 2005.

[9] Xuehao He and Friederike Schmid. Spontaneous Formation of Complex Micelles from a Homogeneous Solution. *Phys. Rev. Lett.*, 137802:137802, 2008.

[10] J R Sanes, J W Lichtman, T L Walunas, J A Bluestone, K Simons, W Halfter, S Kroger, G J Cole, F Rupp, M M Davis, E Freire, A B Heimberger, D Y Loh, S Lustig, D H Puznick, N Razi, A Varki, A Viola, S Schroeder, Y Sakakibara, A Lanzavecchia, M L Dustin, and A C Chan. On the Origins of Morphological Complexity in Block Copolymer Surfactants. *Cell*, 292(June):1686–1689, 2001.

[11] Stephen Mann. Self-assembly and transformation of hybrid nano-objects and nanostructures under equilibrium and non-equilibrium conditions. *Nat. Mater.*, 8:781–792, 2009.

[12] Darrin J. Pochan, Zhiyun Chen, Honggang Cui, Kelly Hales, Kai Qi, and Karen L. Wooley. Toroidal triblock copolymer assemblies. *Science*, 306(5693):94–97, 2004.

[13] D. J. Pochan, K. L. Wooley, H. Cui, S. Zhong, and Z. Chen. Block Copolymer Assembly via Kinetic Control. *Science*, 317(5838):647–650, 2007.

[14] Ian Wyman, Gabriel Njikang, and Guojun Liu. When emulsification meets self-assembly: The role of emulsification in directing block copolymer assembly. *Prog. Polym. Sci.*, 36(9):1152–1183, 2011.

[15] Yiyong Mai and Adi Eisenberg. Self-assembly of block copolymers. *Chem. Soc. Rev.*, 41(18):5969, 2012.

[16] A. Halperin and S. Alexander. Polymeric Micelles: Their relaxation kinetics. *Macromolecules*, 22:2403–2412, 1989.

[17] F. J. Esselink, E. Dormidontova, and G. Hadziioannou. Evolution of block copolymer micellar size and structure evidenced with cryo electron microscopy. *Macromolecules*, 31:2925–2932, 1998.

[18] Elena E. Dormidontova. Micellization kinetics in block copolymer solutions: scaling model. *Macromolecules*, 32:7630–7644, 1999.

[19] Reidar Lund, Lutz Willner, Dieter Richter, Peter Lindner, and Theyencheri Narayanan. Kinetic pathway of the cylinder-to-sphere transition in block copolymer micelles observed in situ by time-resolved neutron and synchrotron scattering. *ACS Macro Lett.*, 2(12):1082–1087, 2013.

[20] Joseph Kalkowski, Chang Liu, Paola Leon-Plata, Magdalena Szymusiak, Pin Zhang, Thomas Irving, Weifeng Shang, Osman Bilsel, and Ying Liu. In Situ Measurements of Polymer Micellization Kinetics with Millisecond Temporal Resolution. *Macromolecules*, 52:3151–3157, 2019.

[21] Lucas R. Parent, Evangelos Bakalis, Abelardo Ramírez-Hernández, Jacquelin K. Kammeyer, Chiwoo Park, Juan De Pablo, Francesco Zerbetto, Joseph P. Patterson, and Nathan C. Gianneschi. Directly Observing Micelle Fusion and Growth in Solution by Liquid-Cell Transmission Electron Microscopy. *J. Am. Chem. Soc.*, 139(47):17140–17151, 2017.

[22] Rintaro Takahashi, Theyencheri Narayanan, and Takahiro Sato. Growth Kinetics of Polyelectrolyte Complexes Formed from Oppositely-Charged Homopolymers Studied

by Time-Resolved Ultra-Small-Angle X-ray Scattering. *J. Phys. Chem. Lett.*, 8(4):737–741, 2017.

[23] Susan E. Burke and Adi Eisenberg. Kinetics and mechanisms of the sphere-to-rod and rod-to-sphere transitions in the ternary system PS310-b-PAA52/dioxane/water. *Langmuir*, 17(21):6705–6714, 2001.

[24] Yan Geng, Fariyal Ahmed, Nishant Bhasin, and Dennis E. Discher. Visualizing worm micelle dynamics and phase transitions of a charged diblock copolymer in water. *J. Phys. Chem. B*, 109(9):3772–3779, 2005.

[25] Yan Geng and Dennis E. Discher. Hydrolytic degradation of poly(ethylene oxide)-block-polycaprolactone worm micelles. *J. Am. Chem. Soc.*, 127(37):12780–12781, 2005.

[26] Sharon M. Loverde, Vanessa Ortiz, Randall D. Kamien, Michael L. Klein, and Dennis E. Discher. Curvature-driven molecular demixing in the budding and breakup of mixed component worm-like micelles. *Soft Matter*, 6(7):1419–1425, 2010.

[27] Lulu Wang, Haiying Huang, and Tianbai He. Rayleigh instability induced cylinder-to-sphere transition in block copolymer micelles: Direct visualization of the kinetic pathway. *ACS Macro Lett.*, 3(5):433–438, 2014.

[28] Bohumil Bedná, Herbert Morawetz, and Jules A. Shafer. Kinetics of the Cooperative Complex Formation and Dissociation of Poly(acrylic acid) and Poly(oxyethylene). *Macromolecules*, 17(8):1634–1636, 1984.

[29] Kirill N. Bakeev, Vladimir A. Izumrudov, Semeyon I. Kuchanov, Alexander B. Zezin, and Victor A. Kabanov. Kinetics and Mechanism of Interpolyelectrolyte Exchange and Addition Reactions. *Macromolecules*, 25(17):4249–4254, 1992.

[30] Zhuonan Liu, Tianbo Liu, and Mesfin Tsige. Elucidating the Origin of the Attractive Force among Hydrophilic Macroions. *Sci. Rep.*, 6:26595, 2016.

[31] Bas Hofs, Ilja K. Voets, Arie de Keizer, and Martien A. Cohen Stuart. Comparison of complex coacervate core micelles from two diblock copolymers or a single diblock copolymer with a polyelectrolyte. *Phys. Chem. Chem. Phys.*, 8(36):4242–4251, 2006.

[32] Dimitrios Priftis, Nicolas Laugel, and Matthew Tirrell. Thermodynamic characterization of polypeptide complex coacervation. *Langmuir*, 28:15947–15957, 2012.

[33] Jingcheng Fu, Hadi M. Fares, and Joseph B. Schlenoff. Ion-Pairing Strength in Polyelectrolyte Complexes. *Macromolecules*, 50(3):1066–1074, 2017.

[34] L. Vitorazi, N. Ould-Moussa, S. Sekar, J. Fresnais, W. Loh, J.-P. Chapel, and J.-F. Berret. Evidence of a two-step process and pathway dependency in the thermodynamics of poly(diallyldimethylammonium chloride)/poly(sodium acrylate) complexation. *Soft Matter*, 10:9496–9505, 2014.

[35] M A C Stuart, N A M Besseling, and R G Fokkink. Formation of micelles with complex coacervate cores. *Langmuir*, 14(24):6846–6849, 1998.

[36] Saskia Lindhoud, Willem Norde, and Martien A.Cohen Stuart. Reversibility and relaxation behavior of polyelectrolyte complex micelle formation. *J. Phys. Chem. B*, 113(16):5431–5439, 2009.

[37] Jeffrey M. Ting, Hao Wu, Abraham Herzog-Arbeitman, Samanvaya Srivastava, and Matthew V. Tirrell. Synthesis and Assembly of Designer Styrenic Diblock Polyelectrolytes. *ACS Macro Lett.*, 7(6):726–733, 2018.

[38] Alexander E Marras, Jeffrey R Vieregg, Jeffrey M Ting, Jack D Rubien, and Matthew V Tirrell. Polyelectrolyte Complexation of Oligonucleotides by Charged Hydrophobic Neutral Hydrophilic. *Polymers*, 11:83, 2019.

[39] Michael Lueckheide, R Vieregg, Alex J Bologna, Lorraine Leon, and Matthew V Tirrell.

Structure-Property Relationships of Oligonucleotide Polyelectrolyte Complex Micelles. *Nano Lett.*, 18:7111–7117, 2018.

[40] Jingyan Zhang, Jian Xu, and Shiyong Liu. Chain-length dependence of diblock copolymer micellization kinetics studied by stopped-flow pH-jump. *J. Phys. Chem. B*, 112(36):11284–11291, 2008.

[41] Rintaro Takahashi, Theyencheri Narayanan, Shin Ichi Yusa, and Takahiro Sato. Kinetics of Morphological Transition between Cylindrical and Spherical Micelles in a Mixture of Anionic-Neutral and Cationic-Neutral Block Copolymers Studied by Time-Resolved SAXS and USAXS. *Macromolecules*, 51(10):3654–3662, 2018.

[42] Steven R Kline. Reduction and analysis of SANS and USANS data using IGOR Pro. *J. Appl. Cryst.*, 39:895–900, 2006.

[43] D Franke, M V Petoukhov, P V Konarev, and A Panjkovich. computer programs ATSAS 2.8: a comprehensive data analysis suite for small-angle scattering from macromolecular solutions. *J. Appl. Cryst.*, 50:1212–1225, 2017.

CHAPTER 5

NEAR-EQUILIBRIUM CHAIN EXCHANGE KINETICS IN POLYELECTROLYTE COMPLEX MICELLES

5.1 Introduction

5.1.1 Theory

In their seminal paper published in 1989, Halperin and Alexander proposed a theoretical model to describe the chain exchange kinetics in polymeric micelles, based on a combination of the micelle scaling theory and Kramers rate theory for diffusion.[1] According to this theory, the chain exchange is dominated by single chain expulsion and follows a single exponential decay that is characterized by a unique chain expulsion activation energy barrier. For starlike micelles, where the size of the corona is much larger than that of the core, they claim that the extraction of a hydrophobic chain from a micelle core can be divided into two stages. First, a solvophoic polymer block is ejected out from the core into the corona/solvent mixture, collapsing into a spherical bud with a radius of r_{bud}, which consequently leads to an increase of the contacting area between the solvophobic blocks and the solvent, Second, the entire polymer chain, consisting of a collapsed solvophobic block and a solvophilic block, gradually travels through the micelle corona. The exposure of a solvophobic block in an unfavorable corona/solvent area generates an interfacial energy penalty that is viewed as the activation energy, E_a. It can be expressed by the relationship $E_a \propto r_{bud}^2 \gamma$, with γ being the interfacial tension. Overall, the model can be described by a combination of the following equations:

$$k \propto \exp\left(-\mathrm{E}_a / k_B T\right) f\left(N_A, N_B\right) \tag{5.1}$$

$$E_a \propto r_{bud}^2 \cdot \gamma = \gamma N_B^{2/3} l_B^2 \tag{5.2}$$

Where k is the expulsion constant rate, N_A and N_B are the number of the repeat unit of the solvophilic and the solvophobic block, respectively, l_B is the monomer length of the solvophobic block, $f(N_A, N_B)$ is a prefactor whose value dependents on whether the

micelle is a crew-cut ($N_A >> N_B$) type or a starlike ($N_A << N_B$) type. In the cases where polymeric micelles can be regarded as starlike micelles, the prefactor is written as $f(N_A, N_B) = N_B^{-2/25} N_A^{-9/5}$.[2] The complete derivation can be found in the original publication in reference 10. One can infer that the activation energy depends only on the degree of polymerization of the core-forming block. The corona block length also plays a role in the exchange rate constant, but not as significant as the core block, since it is not within the exponential form. In 2011, Halperin modified the activation energy term to resolve competing mechanism hypotheses in parallel experiments, which will be discussed in detail later.[3] It is noteworthy that this model is premised on that fact that the results are only valid for small perturbation from equilibrium states.

Besides the unimer expulsion and insertion mechanism, micelle fusion and fission also play an important role in the micelle equilibration and size redistribution, especially after an environmental perturbation. Micelle fusion starts from the deformation of the coronas of two micelles when they collide. An aggregate is formed when the coronas deform to a point where the core areas of two micelles come into contact and where a merge is thermodynamically favored. Micelle fission, in a reverse manner, entails the compartmentation of the core chains, which results in an increase of the total interfacial free energy. Dormidontova derived the expressions for the rate of micelle fusion and fission.[4] In the case where micelle 1 (with aggregation number Q_1) and micelle 2 (with aggregation number Q_2) are comparable in size, the micelle fusion rate and fission rate are written as:

$$k_{fus} \cong \exp\left(-Q_1 Q_2^{1/2}\right) / \tau_{mic} \tag{5.3}$$

$$k_{fis} \cong \exp\left[-Q_{eq}^{5/6}\left(Q_1^{2/3} + Q_2^{2/3} - Q^{2/3}\right)\right] / \tau_{mic} \tag{5.4}$$

where k_{fus} and k_{fis} are the rate constants of the fusion and fission process, respectively; Q_1, Q_2, Q, and Q_{eq} are the aggregation numbers of the two fusion-able micelle 1 and micelle

2 with comparable sizes, and the aggregated micelle from micelle 1 and micelle 2, and the equilibrium micelles of the system, respectively; τ_{mic} is the time to reach activated states, which is defined as an intermediate state from which point the possibilities of proceeding to the final state or withdrawing back to the initial state are equal.

In this model, fusion among small micelles is the dominant way to reaching the equilibrium state after the initial micellar nucleation; micelle fission is relatively slow but also thermodynamically favored in disturbed conditions, in which the size of micelles is much larger than the micellar size at the equilibrium state.

5.1.2 Molecular exchange in amphiphilic block copolymer micelles

Single-chain expulsion/insertion versus micelle fission/fusion. Both the single-chain expulsion/insertion and micelle fission/fusion are theoretically predicted and experimentally observed in surfactant micelles. Yet, in polymeric micelles, Halperin and Alexander claimed that micelle fission/fusion is energetically suppressed due to the steric repulsion between thick micelle coronas.[1] However, some experimental results suggested that the unimer exchange mechanism alone could not explain well the observations.[5, 6, 7, 8, 9] Dormidontova developed a framework where both micelle fusion/fission and unimer exchange take place in polymeric micelles, as discussed above. Experimentally, some effort has been taken to observe micelle fission/fusion.[4] In 2009, Fernandez et al. [10] studied the micellization kinetics of poly(ethylene oxide)-*b*-poly(propylene oxide)-*b*-poly(ethylene oxide) (PEO-PPO-PEO) triblock copolymer micelles and demonstrated the existence of micelle fragmentation and fusion. More recently, micelle fusion has been directly reported during the micellization process by in situ liquid-cell transmission electron microscope.[11] In 2012, using fluorescence probe, micelle fission/fusion in PEO-PPO-PEO micelles at equilibrium is experimentally observed and quantitatively demonstrated that the micelle fusion/fission rate is six orders of magnitude slower than the chain expulsion/insertion rate.[12] This result in part explains why micelle fission/fusion has never been observed in TR-SANS experiments in which most

experimental measurements range from minutes to hours (or days in the cases when micelles are frozen).

Single-chain expulsion/insertion: exponential versus logarithmic decay. In 2001, Willner et al. [13] first reported using the TR-SANS technique in the determination of the chain exchange kinetics in poly(ethylene propylene-ethylene oxide) PEP-PEO micelles in dimethylformamide (DMF). Interestingly, they found that the relaxation function could only be well fitted by a double exponential decay, rather than a single exponential decay. It was suggested that there were two independent processesthe fast mode could be attributed to the single chain expulsion/insertion process, but the relatively slow mode could not be matched a physically meaningful phenomenon. In 2006, Lund and coauthors re-investigated the chain exchange kinetics of PEP-PEO micelles in DMF/water mixture via TR-SANS.[14] They fitted the relaxation functions using the model derived from Halperin-Alexander theory, and unexpectedly, the relaxation behavior followed a logarithmic decay rather than a single exponential decay. This clear discrepancy was not addressed even after taking the core chain polydispersity into account. With the failure to quantitatively fit the experimental data, the authors claimed that such a broad logarithmic relaxation might result from the possible interchain correlations in the geometrically constrained core. This landmark study shed light on the understanding of chain exchange kinetics mechanisms in polymeric micelles for a series of follow-up investigations.

In 2010, Choi et al. [15] reported a similar logarithmic relaxation behaviour of chain exchange in poly(styrene-b-ethylene-*alt*-propylene) (PS-PEP) micelles in squalane. With a combination of Rouse dynamics and the time-temperature superposition principle, they developed a physical model that fits the relaxation behaviors quite well, demonstrating that the chain exchange rate is hypersensitive to the core block length and pinpointing that the core polydispersity drives a single exponential decay into a logarithmic decay. In this model, the authors correlated the time correlation relaxation function $R(t)$ to the instantaneous exchange of state $K(t, N)$ of the core chain by $R(t) \sim K(t, N) = \exp[-t/\tau(N)]]$, where the

$\tau(N)$ is the characteristic exchange time. The authors concluded that because the hydrophobic chains in the core are not entangled, the extraction of chains should behave according to Rouse dynamics. The Rouse relaxation time is given by $\tau_{\text{Rouse}} = \left(N^2 b^2 \zeta\right) / \left(6\pi^2 kT\right)$), where k, T, b, and ζ are the Boltzmann constant, temperature, statistical segment length, and the monomeric friction factor, respectively.[56] Furthermore, the extraction of a hydrophobic core chain N into the unfavorable corona/solvent would create an enthalpic penalty that is proportional to $\exp(-\alpha\chi N)$, where χ is the Flory-Huggins interaction parameter between the core block and the corona/solvent mixture, and α is a prefactor that reflects the chain conformation upon passing through the corona area. Thus, the time correlation relaxation function could be given by:

$$R(t) \sim K(t, N) = \exp\left[-\frac{t}{\tau_{\text{Rouse}}} \exp(-\alpha\chi N)\right] \tag{5.5}$$

The polydispersity of the core block was then considered in the final relaxation function:

$$R(t) = \int_0^\infty P(N) K(t, N) dN \tag{5.6}$$

where $P(N)$ is the Schulz-Zimm distribution function of core block chain lengths, a single function of core polydispersity (N_w/N_n). By subtly varying the core polydispersity parameter in a narrow range (1.0-1.04), the relaxation function dramatically transforms from an exponential decay to an approximately logarithmic form.

To summarize, the merits of this key study in overcoming previous challenges are two-fold. First, the use of squalane as the selective solvent enables the TR-SANS experiments to be conducted at a relatively broad temperature range. This allows the chain exchange rate to be measured over longer time scales using the time-temperature superposition principle. Second, the use of two diblock copolymers with different core block lengths clearly revealed the exponential-of-exponential dependence of $R(t)$ on the core block length. This design feature clearly established the relationship between core block polydispersity and the consequential

logarithmic relaxation behavior. Compared with the model proposed by Lund,[14] a few subtle distinctions are noteworthy. The first difference involves the value of the power law that represents the scaling of the activation energy with the core block length, i.e., $E_a \sim \exp\left(N_B^{\beta}\right)$. In the Choi-Lodge-Bates model, the expression for the activation energy is given by $E_a = \exp(-\alpha\chi N)$, where the scaling exponent β is assumed to be 1, indicating that the expelled core block remains swollen after traveling through the corona. In contrast, Lund et al. used a term $E_a = \alpha\gamma N_B^{2/3} l_B^2$, where β equals to 2/3, assuming that the B block collapses and forms a bud at the corona-core interface. This controversy was resolved theoretically by Halperin in 2011,[3] where a term that accounts for osmotic penalty and the change of micellar free energy is taken into consideration. Secondly, in their original modelling, Lund et al. simply set the prefactor α to be 1. If they assume the core block forms a spherical bud, this prefactor should have a value of $\alpha = (4\pi)^{1/3} \cdot 3^{2/3} \approx 4.8$. The hypersensitivity of any term in the activation energy function explains the unsuccessful fitting to the experimental relaxation function. Shortly after, Lund and coworkers reported successful fitting of their original data using the model proposed by Choi et al.[14] However, the determination of the exact value of α remained unclear.[16]

Despite this rather satisfactory outcome, the hypothesis in the Choi-Lodge-Bates model that the core dispersity induces the exponential-to-logarithmic transition needed to be experimentally proven. In 2012, Zinn et al. [17] showed that the relaxation function could indeed be well fitted into a first-order single exponential decay for n-alkyl-PEO (n = 18, 24 or 30) polymeric micelles, where the hydrophobic alkyl chains were regarded as strictly monodispersed. In the same year, Lodge and colleagues designed a delicate experiment to further confirm the dramatic sensitivity of chain expulsion rate on the core block length [59]. They introduced high core block dispersity in micelles by blending two relatively monodispersed PS-PEP copolymers, where the PS block differed by a factor of 1.6 in molar mass. The exchange rate of the short or long core chains was measured by matching out the other constituent using isotopic solvent. According to the Chois model, the relaxation function of

the binary micelles could be deconvoluted into contributions from two individual core block expulsion events, as given by: $R(t)_{binary} = \nu_1 R_1(t) + (1 - \nu_1) R_2(t)$, where ν_1 and $R_1(t)$ are the mole fraction and relaxation function, respectively, of copolymer 1. The experimental data of binary micelles coincided perfectly with the model predictions. Collectively, these two studies highlighted the hypersensitivity of core block size in chain exchange dynamicsthe relaxation function behaves as a single exponential decay in micelles with strictly monodispersed core block, while in the vastly dispersed case, it follows as a sum of two logarithmic relaxation decays.

Although these mechanistic discrepancies appeared to be fully resolved, in 2017, a computational work by Daza et al. using coarse-grained simulation reported that a logarithmic decay still exists in micelles that were formed by a strictly monodispersed chains.[18] In other words, they suggested that the logarithmic relaxation behavior is an intrinsic property of the chain exchange process and is not necessarily a result of the chain polydispersity. Using the so-called single-chain mean-field (SCMF) theory, they were able to investigate the exchange kinetics over 5 decades in time. It should be noted here that, due to the practical resolution limitations of SANS experiments, almost all the experimental data could span only about 3 decades, even with the employment of time-temperature superposition principle. They observed that in the central regime that spanned over two decades, the time dependence relaxation function followed a logarithmic decay even in micelles with strictly monodispersed core blocks. This peculiar phenomenon was qualitatively ascribed to the broad distribution of activation energy barriers when core chains leave the micelle assembly. This computational result contradicts key conclusions from the previous theoretical predictions and experimental data. Since many other simulation works reported single exponential kinetics in their systems where core polydispersity is eliminated, more evidence is needed to test and validate this phenomena.[19, 20, 21]

5.1.3 Design parameters

Interfacial tension. Micelles in aqueous environment are reported to be frozen due to the high amphiphilicity and interfacial tension in highly polar environment. In 2001, Willner et al. first reported that amphiphilic PEP-PEO micelles had no unimer exchanged in aqueous solutions, even at high temperatures or over days.[13] Similarly, Bates and co-workers also investigated the exchange dynamics of poly(ethylene oxide-butadiene) (PEO-PB) micelles using TR-SANS and found that these micelles were completely frozen, even at measurements over the course of 8 days.[22] Epps and coauthors further confirmed this lack of chain exchange of PEO-PB micelles in water, where the TR-SANS measurements were collected up to 10 days.[23] PEO-PB micelles were also revealed to be locked in the imidazolium-based ionic liquid with temperature up to 200 ^{o}C.[24] These results prompted researchers to unlock chain exchange by tuning the solvent quality, e.g., by adjusting temperature or including co-solvents such as dimethylformamide (DMF) or tetrahydrofuran (THF). For instance, after observing no unimer exchange in water, Willner et al. performed TR-SANS experiments on PEP-PEO micelles in pure DMF that selectively favors PEO blocks.[13] The time dependence of chain exchange was not significant until temperature was above 70 ^{o}C. In another example, varying the composition of water/DMF mixture led to the manipulation of the interfacial tension and, subsequently, the time scale of PEP-PEO chain exchange rate.[25] Li and Kidd and their coworkers built a coexistence phase diagram against solvent compositions for micelles that self-assemble from poly(ethylene oxide)-*b*-poly(caprolactone).[26, 27]

The quantitative relationship between the interfacial tension and the chain exchange rate was recently investigated.[28] Three isotopically substituted pairs of poly (methyl methacrylate) -*b*- poly(n-butyl methacryate) (PMMA-*b*-PnBMA) diblock copolymers were synthesized. PMMA is well soluble in ionic liquids, while the solubility of PnBMA is dependent on the solution temperature. Micelles formed by these polymers were prepared and their equilibrium chain exchange kinetics was measured in a mixture of ionic liquids. It is observed that a 10% increase in χ accelerated the chain expulsion rate by an order of magnitude,

which is in line with the hypersensitive dependence of exchange rate on . The dependence of activation energy on the interfacial tension is furthermore represented by an empirical expression, $E_a \propto \alpha f(\chi)N$, with the term $f(\chi)$ expressed by:

$$f(\chi) = \frac{\nu_2}{\nu_1}\left(\chi - \frac{\nu_2}{\nu_1}\right) + \frac{1}{a\chi^2 + b\chi + c} \tag{5.7}$$

where ν_1 and ν_2 are the molar volume of the solvent and the repeat unit of the core block, respectively. Using this modified expression, the authors found good agreement between the TR-SANS data and the Flory-Huggins theory. Further work is warranted to test the universality of this empirical function to other block copolymer micelles. Using the same system, Zhao et al. compared the exchange kinetics between micelles having the same polymers but different micelle core sizes.[29] A 30% larger of the core size led to 3 times slowdown of the chain exchange, which was attributed to the smaller interfacial area per chain in larger micelles.

Temperature and Core crystallization. As aforementioned, chain exchange kinetics is highly dominated by the nature of micelle cores. The thermodynamic and mobility of the core-forming chain in the nanoscale core are critical to understand the fundamental mechanism of the chain expulsion process for a system of interest. The frozen micelles are anticipated to have glassy cores and the lack of chain mobility leads to the absence of intermicellar chain exchange at the timescale up to months. But the melt state of the polymer core does not necessarily confer chain extraction. PS-PEO diblock copolymer micelles are found to be frozen even when heated to the glass transition temperature, T_g, of the polystyrene block.[30] PEO-PB (polybutadiene) micelles in water is also frozen in a time scale of 8 days even though the experimental temperature is much higher than the T_g of the hydrophobic block PB, i.e., -12 ^{o}C.[22] Similarly, micelles composed by amphiphilic charged diblock copolymers poly(butyl acrylate)-*b*-poly(acrylic acid), PBA-*b*-PAA, have been reported to show no unimer exchange over months, even though the T_g of the core-forming PBA block is only -54 ^{o}C.[31]

The decrease of the interfacial tension upon temperature increase cannot explain either because the dependence is linear and far from the critical point. Compared to bulk polymer melts, polymer chains in micelle cores are restricted from extra space-filling constraints due to the geometrical confinement. Polymer chains tend to adopt more structured conformations when they are limited in a nanoscale space, which is more obvious for molecules that tend to crystalize. Our group reported that DNA oligonucleotide formed parallel packing structures in electrostatic-driven self-assemblies.[32] Gilroy et al. reported the employment of crystallization to direct the self-assembly of monodisperse cylindrical micelles. The crystallization of the core-forming polymer chains has also been reported to induce the switching of the morphologies of PB-*b*-PEO micelles.[33] Yet, the chain exchange kinetics in micellar nanostructures containing crystalline polymer chains have been rarely studied. Generally, the extraction of a glassy or extended polymer chain from the micelle core involves three energetic contributions: (i) the entropic penalty of exposing the solvophobic chain in an unfavorable solvent, (ii) the entropic gain from the chain adopting conformations with more freedom, and (iii) the enthalpic gain of the chains undergoing a glass-to-liquid transition. The latter two were absent in the aforementioned formula of activation energy, $E_a \propto \gamma N_{\text{core}}^{\beta}$, where the state of core is understood in an analogous manner to polymer melts.

A previous work in our group has reported the marked difference of the activation energy of chain expulsion between micelles with a glassy and a liquid core.[34] Moreover, the chain expulsion rate in the glassy phase is significantly lower than that in the fluid phase. The core of the PEGylated phospholipid micelles undergoes a glass-liquid melting transition around 12.8 ^{o}C. Using fluorescence self-quenching technique, the authors have demonstrated that the activation energy for chain expulsion was 156 $\pm$ 7 kJ/mol for the glassy core micelles (5 ^{o}C $<$ T $<$ 15 ^{o}C) and 79 $\pm$ 5 kJ/mol for the liquid core micelles (15 ^{o}C $<$ T $<$ 30 ^{o}C). This elevation is speculated to arise from the enthalpic contribution of partially crystalline lipid chains melting upon exiting from the core to the surroundings. Taking advantage of TR-SANS, Lund et al. further examined the enthalpic and entropic contributions for chain

exchange during the melting transition. The examined micelles are formed by a series of amphiphilic n-alkyl-poly(ethylene oxide) (C_n-PEO). The n-alkyl chains partially crystallized upon confinement in micellar cores; when liberated, the chains lost crystallinity. These studies reveal the essential role that chain crystallization play in directing the size, shape, and long-term stability of polymer micelles. It is noteworthy that the interfacial tension also has a dependence on temperature, albeit quite weak.

Core density and thickness. Until recently the role of corona thickness has been little understood because the corona is believed to play a less important role compared to the core. Theories anticipate the travel of nascent buds through the bulk corona area, with which one can infer that the effect of micelle corona, if any, would be manifested as the buds pass through the corona cloud or as the corona-forming block releases from corona area to the solvent. Increasing the micelle concentration to a certain extent would lead to the overlapping of the micelle coronas and potentially, the increasing of the staying time of the core buds in the corona area. It is found that PS-PEP[35] or PEP-PS-PEP[36, 37] micelles with a body-centered cubic lattice structure has a chain exchange rate that is more than one order of magnitude slower than that micelles with a disorder structure. This retardation may have been caused by the increased corona concentration as another barrier for chain expulsion, but other confounding factors such as the increase of matrix viscosity may be involved. A similar hindrance was also reported when the corona density was further enhanced by adding PEP homopolymers to PS-PEP micelles. In the dilute condition, the corona chains could gain extra conformational entropy by adopting more stretched morphologies when they were released into the selective solvent; however, increasing micelle concentration led to the overlapping of neighboring coronal chains, which prevented the corona blocks from adopting extended conformation, and consequently retarded the chain expulsion.

The role of the corona chain length is nevertheless far away from unanimously agreed. Contradictory outcomes from theories, simulations, and experiments obscure the situation, in which a rigid dichotomy between the chain exchange retardation and chain exchange

acceleration can be drawn. In the retardation camp, Halperin and Alexander theory predicts that for micelles with thick coronas the passage of the chains through the corona area is a rate-limiting step and is proportional to the length of the corona chain with a power law of 9/5, due to the hindered chain diffusion through the micellar corona. A recent experimental work found that in amphiphilic diblock copolymers $C_{27}H_{55}$-PEO_x (x ranges from 4 to 36 kg/mol), the change exchange kinetics is in excellent agreement the theoretical prediction.[38] The scale is tipping the retardation camps favor when Prhashanna and coauthors found that the chain exchange rate decreased with longer corona chain length in BAB triblock micelles using dissipative particle dynamics.[20] The acceleration camp, however, has gained momentum starting off the simulation work done by Li and Dormidontova, in which they observed that a longer corona block length led to a faster chain exchange rate in A_4B_x micelles with 4 solvophobic beads and x solvophilic beads in a coarse grain model.[19] The acceleration is mainly contributed from the increase of the critical micelle concentration, the decrease of the aggregation number, and the increase of the unimer concentration. This phenomenon was echoed by a recent experimental observation in PS-PEP micelles in squalene, where the authors attributed the expedition of the chain exchange to the favorable entropy gain from the stretching of corona chains upon expulsion.[39]

Despite the stark contrast among these discoveries, it is reasonable to speculate that the effect of the corona chain length is probably exerted via the interplay between a couple of forces including the entropy gain from conformational transition, the impeded chain diffusivity, the change of aggregation number, and possible others. The combinatorial outcome may result in retardation in some cases or acceleration in other cases, depending on the characteristics of the chosen systems. It is worth noting that these studied micelle systems differ in many ways and have their own peculiar traits. For example, the $C_{27}H_{55}$-PEO_x micelles have a crystalline core; the PS-PEP micelles are dispersed in squalene rather than water.

Chain architecture. So far, we have focused on works involving diblock chain architec-

tures of amphiphilic systems, where chain conformation has been shown to play an important role in micelle formation and stability. Changing the arrangement of core-forming block(s) in higher order polymer architectures (e.g., triblock copolymers) can modulate the core compactness and hydrophobicity of equilibrium micelles due to selective chain-solvent interaction. A sharp distinction between hairy micelles and flower-like micelles formed by triblock copolymers should be drawn. Triblock copolymers can be represented in the architectural form of BAB or ABA, in which A is the core-forming block and B is the corona-forming block. Micelles formed by BAB polymers are called hairy micelles, while micelles formed by ABA polymers are called flower-like micelles. The architectural and topological influence on chain exchange kinetics between diblock copymer micelles, poly(styrene)-*b*-poly(butadiene) (PS-PB) and their counterpart flower-like micelles, PB-PS-PB, was first studied by Lund and coworkers.[40] TR-SANS results show the kinetics in diblock copolymer micelles are much faster than that in their corresponding flower-like micelles. They attributed the effect to the increased activation energy to pulling out two PB chains and the potential topological knots among the hydrophobic chains in micelle cores. Lu et al.[36] later revealed the profound effect of polymer architecture on molecular exchange in triblock copolymer micelles using TR-SANS in a more quantitative manner. The micelles were formed by symmetric PEP-PS-PEP or PS-PEP-PS triblock copolymers, and neutron contrast was obtained using normal and perdeuterated PS blocks. In a solvent that favors PEP, the PEP-PS-PEP system forms hairy micelles, whereas the PS-PEP-PS system forms flower-like micelles. Both of these macromolecular self-assemblies have cores containing the PS blocks.

The differences between the relaxation dynamics of PEP-PS-PEP triblock and PS-PEP diblock micelles were first compared. Both systems were approximately equivalent in molar mass and composition, but the triblock micelle coronas were denser than the diblock ones as a result of the chain architecture. A clear change in relaxation kinetics was found: the triblock chains moved out of micelles 2000 times faster than the diblock system. This finding contradicts the commonly-used model of the energy barrier of chain expulsion was ascribed

merely to the entropic penalty of increasing the contact interface between the core block and solvent/corona mixture. The corona confinement did play a significant role in determining the chain expulsion penalty, as the authors suggested and supported by a previous theoretical work. However, other factors, may also result in accelerated chain exchange. For example, the PEP-PS-PEP micelle core can be less compact than the PS-PEP core. The micelle formation from triblock copolymers entails the bending of the core chains, limiting chain-chain intertwining, and consequently decreasing the net energy barrier of expelling chains from the core. This idea was confirmed by a complementary computational work from Peters and Lodge.[41]

Interestingly, when two types of triblock copolymer micelles were compared, the hairy micelles exhibited a chain exchange dynamic that was 9 orders of magnitude higher than that of the flower-like ones. Though initially perplexing, the intrinsic relaxation mechanisms are actually explicable: the PEP-PS-PEP chain movement requires one PS block to be expelled, whereas the PS-PEP-PS requires the successful extraction of two PS blocks simultaneously. The expulsion of only one PS block is futile because it will be inserted back to the core within a millisecond time scale. Therefore, the chain exchange rate of PS-PEP-PS micelles should be much slower. A mechanism to describe this phenomenon is still lacking.

Recent advances in polymer synthesis has enabled a myriad of new chain architectures to be explored, such as cyclic,[42], tadpole,[43, 44, 45] and Y-shaped,[46] etc. The self-assembly behaviors of these polymers are inherently different from their linear counterparts. To date, very limited reports on these detailed micellization behaviors exist, so the chain exchange kinetics for equilibrium polymeric micelles is even less understood. It is not surprising because experimental quantitative investigation via SANS involves painstaking endeavors from a synthetic standpointthe synthesis of deuterated polymers with exotic building blocks with desired architectures requires strenuous effort. Computational simulation, however, is more viable and has been pursued. By dissipative particle dynamics, Dormidontova and coworkerschave investigated the thermodynamic and chain exchange kinetics in polymeric

micelles formed by tadpole-shaped diblock copolymers containing loop-shaped hydrophobic blocks.[21] In this work, tadpole diblock copolymer formed monodispersed spherical micelles with a smaller size and aggregation number, compared with the corresponding linear diblock copolymer. Moreover, the chain exchange process in the tadpole block copolymer micelles exhibited a first-order exponential decay $R(t) = \exp(-t/\tau)$ with a characteristic relaxation constant τ of 17.5×10^3, which is remarkably higher than that of its linear counterpart, i.e., 102×10^3. The authors argued that the looped structure of the hydrophobic blocks in the tadpole polymers decreased hydrophobicity by lowering the exposure of core chain into the solvent/corona mixture. Therefore, chain escape can be accelerated when the energy barrier is diminished. The argument was further confirmed by measuring the exchange kinetics in mixed micelles formed by tadpole and linear diblock copolymers.

Physical preparation protocols. One of the major challenges when applying amphiphilic block copolymer micelles for cargo encapsulation and delivery is to obtain reproducible and uniform nanostructures while sequestering payloads effectively. In many cases, the dynamics of the solvophobic blocks is hampered in selective solvents, which leads to the formation of kinetically trapped self-assemblies. Producing kinetic products in a repeatable manner has remained an elusive task and is highly case-dependent so far, although a few successful attempts have been reported on the self-assembly of non-equilibrium nanostructures via kinetic trapping.[47, 48, 49] Physical preparation protocols have been known to have important effects on the equilibrium micelle size and shape; however, less was known about the influence on chain exchange kinetics. It is well studied that micelle formation and morphologies have a remarkable dependence on the physical formation pathways. A rich variety of micelle morphologies have been reported resulting from the same amphiphic block copolymers but using different methods, including stepwise dialysis, thin-film, cosolvent addition, and solvent annealing. This is also an indication of the frozen state of the micelle core at least within the experimental timescale. Our earlier studies show that reversing the mixing order in charged polymeric self-assemblies completely led to different nanostructures

even using the same polymer compositions.[50] Understanding the unimer-micelle equilibrium under different proceeding conditions requires a fundamental investigation of the chain exchange dynamics.

TR-SANS experiments entail mixing protocols that blend micelles formed by paired deuterated and protonated polymer pairs into a homogeneous mixture in nanoscale. Choi et al. showed that using a commercial MiniMAX mixer, completely random mixture of deuterated and protonated micelles is achievable in concentrated polymer solutions.[35] The physical mixing process can also facilitate the intermicellar chain exchange. For example, PB-*b*-PEO micelle system has been proven to be kinetically frozen in pure water, however, Epps and co-workers demonstrated that rapid vortexing could unlock the chain exchange and the chain exchange process completed after 20 minutes.[51] A possible explanation of that is the creation of deformed air-water interface via rapid vortexing, and the polymer micelles were absorbed to the interface to exchange change with each other, even though the exact mechanism remains unknown. However, it is crystal clear that solvent agitation has a distinct impact on the chain exchange process, which emphasizes the importance of selecting an appropriate physical mixing protocol for chain exchange studies in designing a TR-SANS experiment. So far, not many works have reported their mixing protocols in detail. For future studies, we anticipate that more attention should be paid to the physical factors and the physical factors should be rationally separated from the thermal factors. Avoiding air-water interface generation with homogeneous mixing would be a suitable way to circumvent such issues and warrant more detailed investigations.

5.1.4 Chain exchange kinetics in polyelectrolyte complex micelles

The knowledge gaining from micelles of diblock and triblock neutral polymers can be extended to investigate the chain exchange kinetics in other nanoparticulate systems. We encourage more effort in the chain exchange kinetics in micelle systems of charged polymers, the most interesting one of which may be polyelectrolyte complex (PEC) micelles or complex

coacervate core micelles (C3Ms) where the core contains neutralized oppositely charged polyelectrolytes and the corona is consisted of hydrophilic polymer blocks like polyethylene glycol (PEG). The unique advantage of PEC micelles lies in their potency to encapsulating and delivering charged biological molecules via electrostatic interaction, including DNA, RNA, oligonucleotides, proteins, and enzymes, capabilities that are absent in amphiphlic block copolymer micelles. The past two decades have witnessed an enormous interest and a burst of publications, in which focus mainly is on their co-micellization with biomacromolecules, environmental stimuli-responsiveness, and in vitro and in vivo stability. To our best knowledge, not a single paper has reported on the chain exchange in PEC micelles. Compared to micelles formed by a single uncharged bock copolymer, PEC micelles are formed by two oppositely charged block copolymers with tunable charge density and solution salinity, possess many paradigms that create tremendous obstacles to the investigation of intermicellar chain exchange. First, obtaining well-defined, low-polydisperse polyelectrolyte complex micelles remains a challenge; reproducibility is still a goal to achieve. Second, synthesizing fully deuterated block polyelectrolytes with matched positively or negatively charged blocks entails sophisticated synthesizing facilities. Last but not least, unanticipatedly, we found that deuterated polyelectrolytes have different solubilities in D_2O or H_2O solutions compared to their protonated counterparts; moreover, polyelectrolytes having the exact chemical composition but differing only on deuterium or protonation form self-assemblies with different sizes and morphologies. Besides of experimental difficulties, the scaling law and the physical state of the core of PEC micelles are also less examined. Unlike amphiphilic block copolymer micelles, whose scaling law has been well developed for decades, the dependence of micelle size and morphology on polymer block lengths are largely unknown. The cores of PEC micelles can be solid-like or liquid-like, depending on the volume fraction of solvent. All of these hurdles combined renders the TR-SANS study on PEC micelles extremely challenging.

In this chapter, we investigate investigate the chain exchange in PEC micelles in water using TR-SANS.

5.2 Experimental Details

5.2.1 Materials and scattering length densities

All reagents were used as received without any further purification unless otherwise stated. Ethyl ether anhydrous, *n*-hexanes and magnesium sulfate anhydrous (Powder/Certified) were purchased from Fisher Scientific; Dichloromethane anhydrous was received from VWR; Chloromethyl methyl ether, potassium t-butoxide, aluminum chloride (anhydrous, powder, 99.999% trace metals basis), hydrogen bromide solution (33 wt. % in acetic acid) and t-butanol were obtained from Sigma-Aldrich; Styrene (d_8, 98%; Item number DLM-380-10) and trimethylamine (d_9, 98%; Item number DLM-603-5) were purchased from Cambridge Isotopes Laboratories, Inc.

^{1}H- and ^{13}C-Nuclear Magnetic Resonance (NMR) spectra were obtained on a Varian VN-MRS 500 NMR spectrometer and were recorded at 23 ^{o}C in CDCl3 (7.27 ppm 1H reference and 77.23 ppm ^{13}C reference) and methanol-d_4 (49.00 ppm ^{13}C reference). For ^{13}C-NMR, inverse-gated decoupling with a recycle delay of 25 seconds was employed.

Deuterated polymers were synthesized by aqueous reversible addition-fragmentation chain transfer (RAFT) polymerization using VA-044 thermal initiator, poly(ethylene oxide) macromolecular chain-transfer agent (PEO-CTA; M_n = 10,000 g mol^{-1}), and deuterated VBTMA monomer. As an example, deuterated PVBTMA (*d*-PVBTMA) was prepared at a molar ratio of [monomer: VA-044 : PEO-CTA] = [1000 : 1 : 10] in a 25 mL round bottom flask at 0.2 M monomer concentration in acetate buffer solution and ethanol mixture (3:1, *v/v*). The solution was sealed, degassed under dried nitrogen for 45 min, and heated at 50 ^{o}C under constant stirring for 24 h. To end the polymerization, the reaction was quenched to room temperature and opened to air. Polymers were then dialyzed against water and lyophilized to provide free flowing powder.

Table 5.1: The scattering length densities of the polymer blocks.

Polymer blocks	Density (g mol^{-1})	SLD (10^{-6} A^{-2})	Chemical structure
hPVBTMA	1.2	0.21	$C_8H_{18}NCl$
dPVBTMA	1.33	8.48	$C_8D1_{18}NCl$
hPSS	1.1	1.72	$C_8H_8SO_3$
dPSS	1.2	4.60	$C_8D_8SO_3$
hPLK	1.2	1.10	$C_6H_{12}N_2O$
PEO	1.2	0.89	$C_2H_4O_2$

5.2.2 Polymer synthesis

Deuterated polymers were synthesized by aqueous reversible addition-fragmentation chain transfer (RAFT) polymerization using VA-044 thermal initiator, poly(ethylene oxide) macromolecular chain-transfer agent (PEO-CTA; Mn = 10,000 g mol^{-1}), and deuterated VBTMA monomer prepared above. As an example, deuterated PVBTMA (*d*-PVBTMA) was prepared at a molar ratio of [monomer : VA-044 : PEO-CTA] = [1000 : 1: 10] in a 25 mL round bottom flask at 0.2 M monomer concentration in acetate buffer solution and ethanol mixture (3:1, *v/v*). The solution was sealed, degassed under dried nitrogen for 45 min, and heated at 50 C under constant stirring for 24 h. To end the polymerization, the reaction was quenched to room temperature and opened to air. Polymers were then dialyzed against water and lyophilized to provide free flowing powder.

5.2.3 Time-resolved small-angle neutron scattering

The data were corrected for background scattering, empty cell scattering, sample transmission, sample thickness, and detector sensitivity and were normalized to an absolute scale using a pre-calibrated secondary standard.

In dilute solution, the time dependent intensity of neutron scattering, I(q,t), is given by:

$$I(q,t) = nP(q)V^2 \left(\rho_{\text{particle}(t)} - \rho_{\text{sol}}\right)^2 \tag{5.8}$$

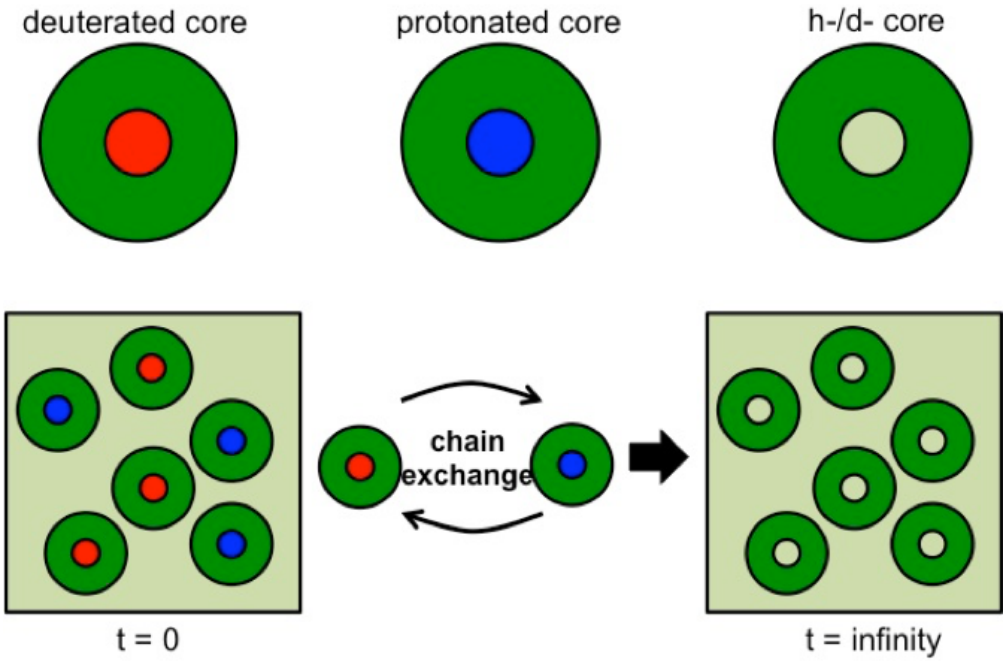

Figure 5.1: Schematic representation of the time-resolved SANS experiment design for the study of molecular exchange in polyelectrolyte complex micelles.

where n is the number density of the scatterers, P(q) is the micelle form factor, V is the volume of a single scatterer, $\rho_{particle}(t)$ and ρ_{sol} are the scattering length densities of the scatterers and the solvent, respectively.

Upon mixing, under the scenario where the deuterated and hydrogenated polymer chains would escape from and re-insert into the micelles, the scattering length density of the micelle is a function of time. It is assumed that the concentration and the morphology of the mixed micelles do not change over time.

Experimental design. We define *d-micelle* as the micelle where the core-forming chains is fully or partially deuterated, and **h-micelle** as the micelle where all the constituent polymer chains are fully hydrogenated. Both d- and h-micelle are prepared in pure D_2O. Under the scenario where polymer chains tend to exchange thoroughly over a long enough time, the micelle cores at equilibrium state are consisted of half number of deuterated chains and half number of hydrogenated chains. A schematic representation of the experiment can be seen in Figure 5.1

Table 5.2: Size of the core and corona of the deuterium-rich micelles and hydrogen-rich micelles.

Sample ID	Polycation		Polyanion		R_{core} (nm)	R_{corona} (nm)
	PEO (g mol^{-1})	PLK (DP)	hPSS (DP)	dPSS (DP)		
20K50145	20K	50	145	-		
20K50180	20K	50	-	180		
20K100145	20K	100	145	-	9.4	12.8
20K100180	20K	100	-	180	7.2	12.4

Data acquisition and reduction. Experiments were performed on the NG-7 30m SANS instrument at the National Institute of Standards and Technology, Center for Neutron Research. An incident wavelength of 6.0 Åwas used with sample-to-distances of 1, 4 and 13.5 m to cover q-range from 0.004 Å^{-1} $< q <$ Å^{-1}. Data reduction was performed using the Maccro package provided by NIST. Additional experiments were conducted on the Bio-SANS instrument at the High Flux Isotope Reactor (HFIR) and Spallation Neutron Source (SNS) at Oak Ridge National Laboratory (ORNL).

SANS modeling. All SANS curves were fitted using the polydisperse core-shell sphere model introduced in Chapter 2.

5.3 Results and Discussions

5.3.1 Micelle structure

The SAXS curves are fitted using the polydisperse core-shell model. It is seen in Figure 5.2, the two SAXS curves of the hydrogen-rich micelle 20K100145 and deuterium-rich micelle 20K100180. The power law of -1.67 at the high q range can be attributed to the scattering from the individual polymer chains. The results are shown in Table 5.2.

$$I_{equi} = nV^2[\left(\frac{1}{2}\rho_{dm} + \frac{1}{2}\rho_{hm} - \rho_{sol}\right)^2] \tag{5.9}$$

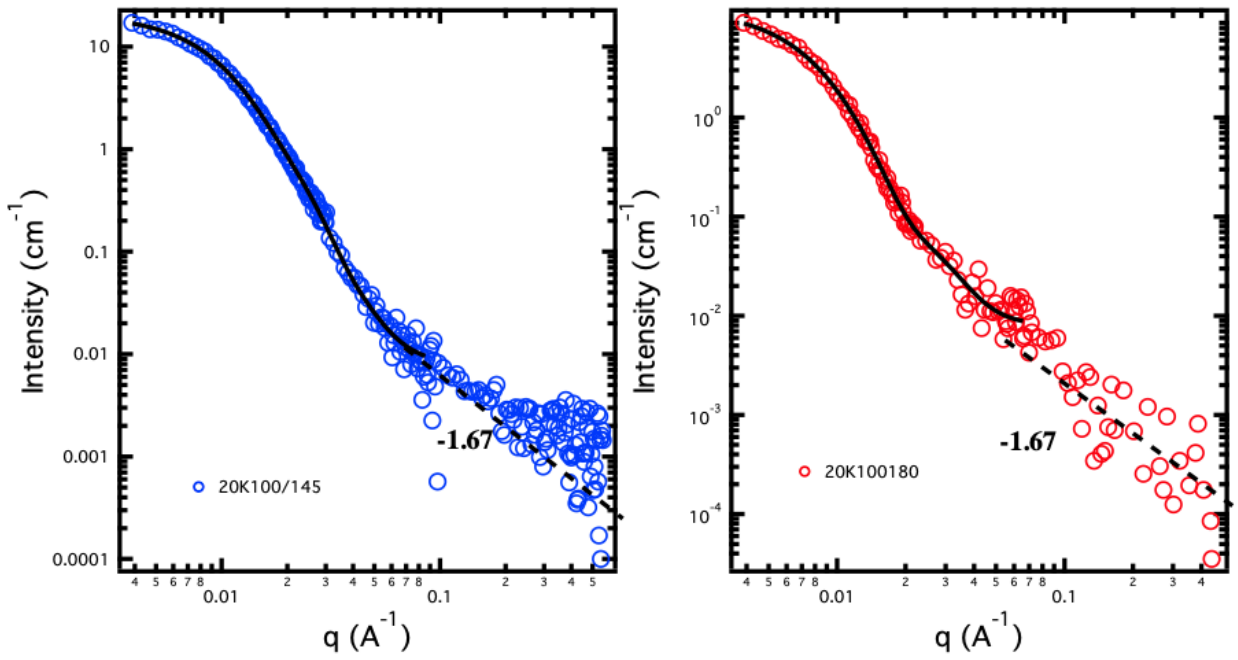

Figure 5.2: SAXS curves and fits of the hydrogen-rich micelle 20K100145 (A) and deuterium-rich micelle 20K100180 (B).

5.3.2 Chain exchange kinetics

According to SANS theories, the neutron scattering intensity from a solution of nanoparticles can be calculated as:

$$I(q) = nP(q)V^2 \left(\rho_{\text{particle}} - \rho_{\text{sol}}\right)^2 \tag{5.10}$$

where I(q) is the strength of intensity, n is the number density of the scatterers, P(q) is the form factor, V is the volume of a single scatterer, $\rho_{particle}$ and ρ_{sol} are the scattering length densities of the scatterers and the solvent, respectively.

Upon mixing, the postmixed micelles is composed of half number of deuterated micelles (d-micelles) and half number of hydrogenated micelles (h-micelles). The intensity of the postmixed micelles, I_{postm}, can be expressed as:

$$I_{\text{postm}} = nV^2[\frac{1}{2}\left(\rho_{dm} - \rho_{\text{sol}}\right)^2 + \frac{1}{2}\left(\rho_{hm} - \rho_{\text{sol}}\right)^2] \tag{5.11}$$

where ρ_{dm}, ρ_{hm} are the scattering length densities of the deuterated micelles and hydrogenated micelles, respectively. It should be noted that we simply take an arithmetic mean between the deuterium-rich micelles and hydrogen-rich micelles due to the fact that the structure factor has a negligible influence on the intensity distribution for the q range studied.

The equilibrium state is defined as a stage where the deuterated polymer chains and hydrogenated polymer chains have exchanged completely between the d- and h- micelles, meaning each micelle at equilibrium state is composed of half number of deuterated chains and half number of hydrogenated chains. Thus, the neutron scattering intensity can be written as:

We first investigated the size and structures of the invididual micelles. The SAXS curves of the micelle samples 20K100145 and 20K100180 are shown in Figure 5.2 and are well fitted using a Gaussian core-shell sphere model. The intensities at the high q regions exhibit a power law of -1.67 dependency on the q value, which is mainly from the blob scattering of individual polymer chains. Both of these two micelle samples can be viewed as equally-sized spheres, which is important for the implementation of the SANS model. Further, we also measured the intensity of the postmixed micelles containing half number of 20K100145 micelles and half number of 200K100180 micelles. Mathematically, when no polymer exchanges, the intensity of the postmixed micelle should sit right in the middle of the two individual micelles.

$$I_{equi} = nV^2 \left(\frac{1}{2}\rho_{dm} + \frac{1}{2}\rho_{hm} - \rho_{sol} \right)^2 \tag{5.12}$$

As shown in Figure 5.3, the neutron scattering curve of the postmixed micelles lies right between the curves of the deuterated micelles and hydrogenated micelles. This experimentally proves that the intensity of the postmixed micelles is the arithmetic average of the deuterium-rich micelle and hydrogen-rich micelle.

Then we monitored the time evolution of the scattering after mixing over a time period

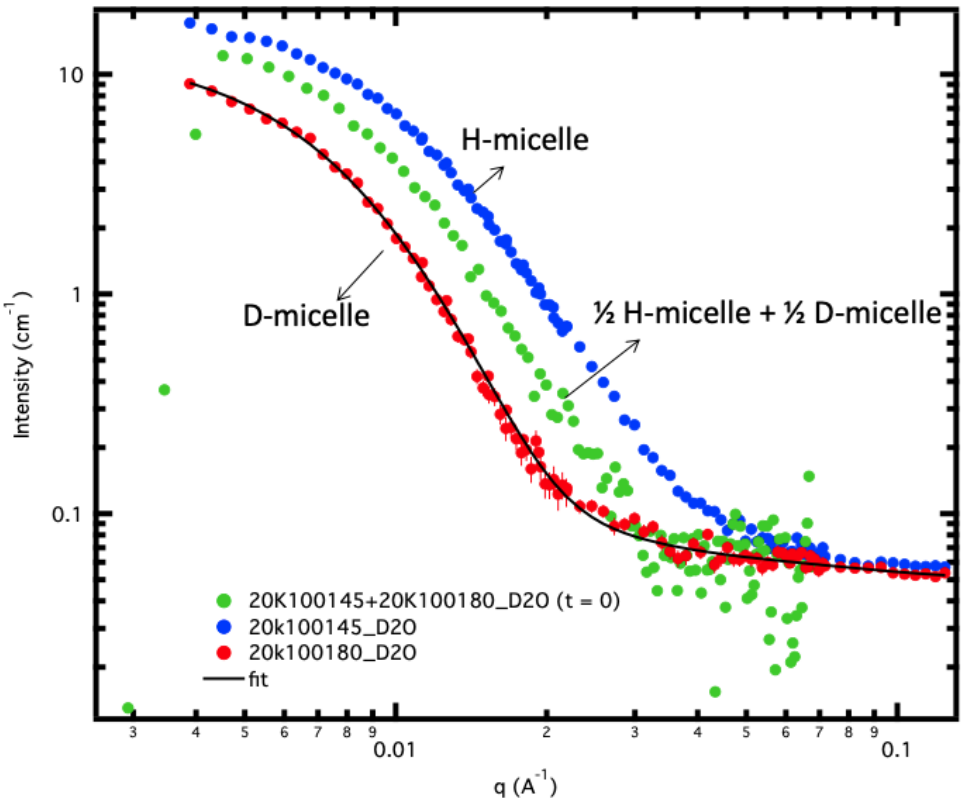

Figure 5.3: The scattering curves of deuterated micelles (read dots), hydrogenated micelles (blue dots), the postmixed micelles (green dots).

of 12 hours. However, as shown in Figure 5.4, the scattering curves at different measured time moments, i.e. 6 hours, 9 hours, and 12 hours, overlap with the initial scattering curve well, indicating that deuterated PSS chains and hydrogenated PSS chains do not exchange among micelles.

5.3.3 Effect of temperature and salt concentration

We speculate the molecular exchange might be unlocked by weakening the strength of the ionic interaction between the oppositely charged groups. Elevation of temperature and salinity are two common ways. As shown in Figure 5.5 and Figure 5.6, the sizes of the two pairs of samples at 70 ^{o}C are extracted using the polydisperse core-shell model, and the results are shown in Table 5.3 . The time-dependent evolution of intensity of the postmixed samples are shown in Figure 5.7. The neutron scattering measurements are performed up to 5 hours.

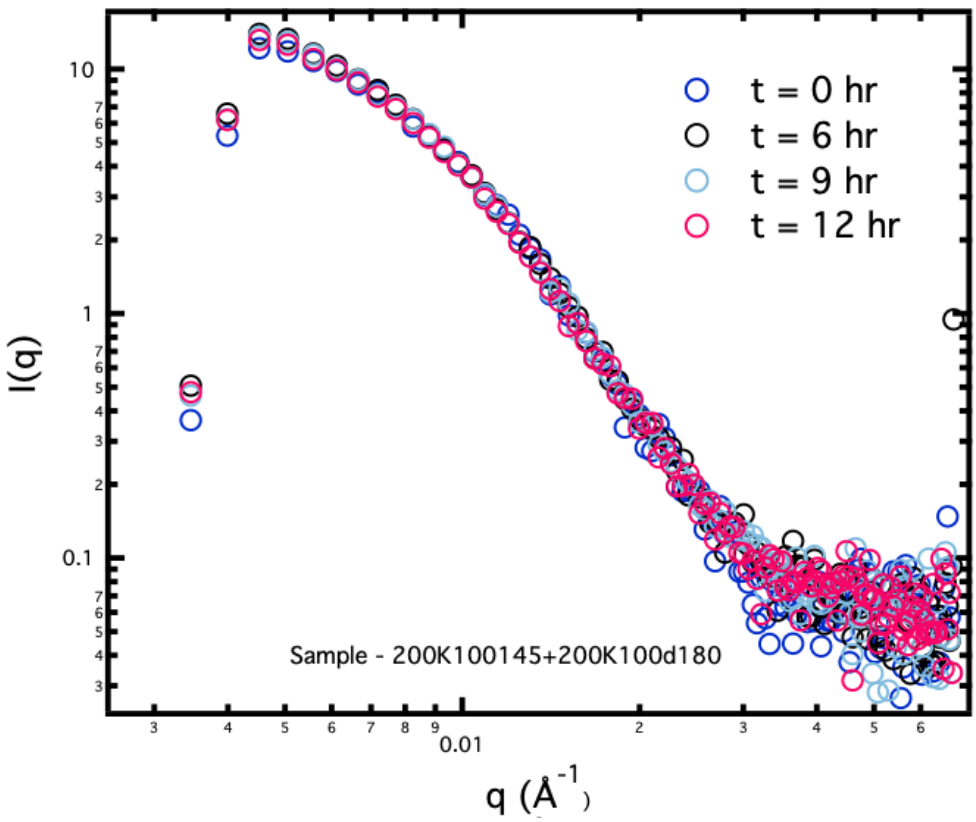

Figure 5.4: The time evolution of the scattering intensity of the postmixed micelles.

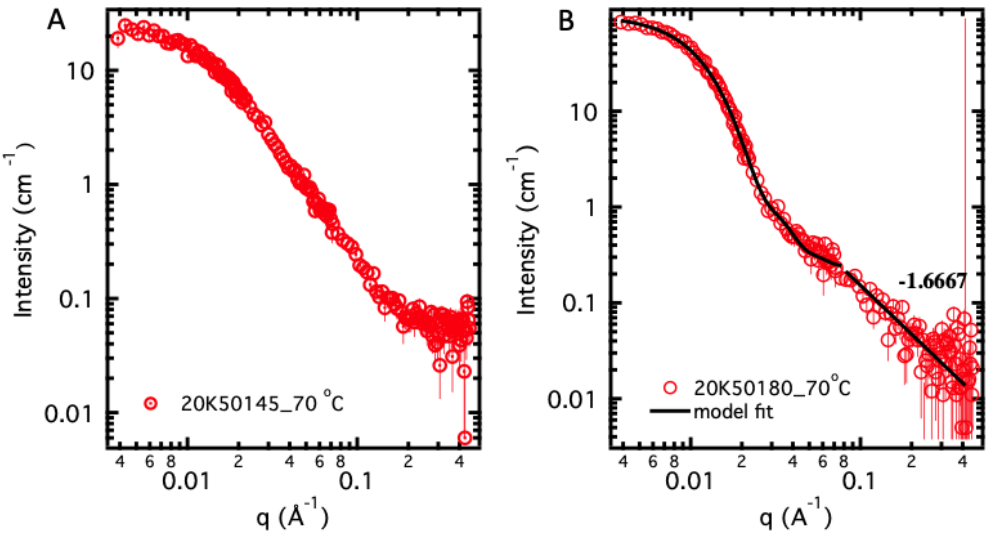

Figure 5.5: SAXS curves and fits of samples 20K5045 (A) and 20K50180 (B) at 70 °C.

Table 5.3: Size of the core and corona of the deuterium-rich micelles and hydrogen-rich micelles at 70 °C.

Sample (at 70 °C)	R_{core} (nm)	R_{corona} (nm)
20K50145	-	-
20K50180	8.6	11.5
20K100145	11.3	10.1
20K100180	10.3	12.4

Remarkably, we found that the intensities of the postmixed micelle measured at different time moments virtually overlap with each other. Similar results are found in micelle samples with 2 M KBr.

5.3.4 Modeling

As discussed above, the cores of PEC micelles contains polyelectrolyte complexes formed by two oppositely charged polyelectrolytes. Ionic bonds are formed between charged groups to maintain the phase. These ionic bonds act as sticky points that increase the effective friction of polymer chains, such that the motion of polymer chains are largely slowed down. A sticky Rouse model has been developed to describe the dynamics of the transient networks formed by unentangled polymers with many sticky points. In the case where polymer chains are

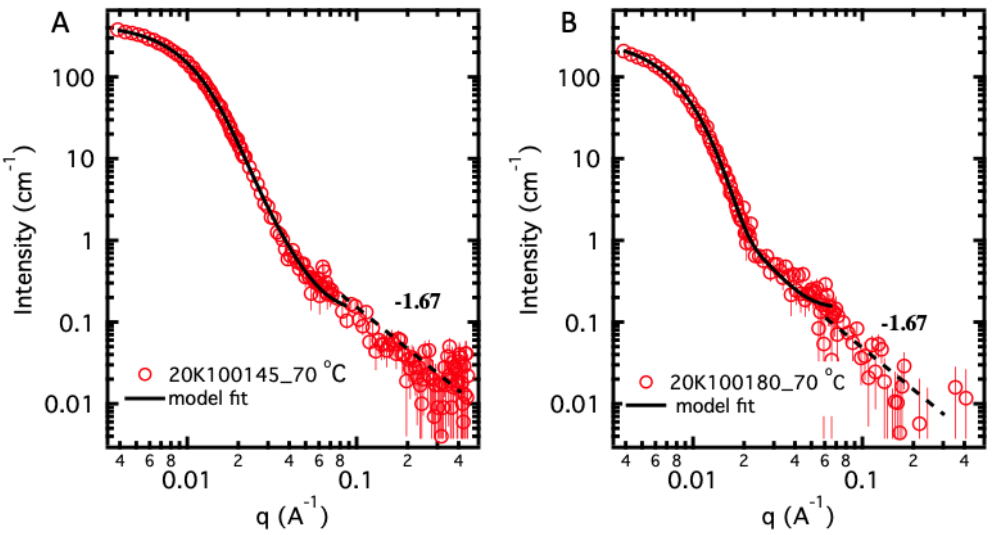

Figure 5.6: SAXS curves and fits of samples 20K10045 (A) and 20K100180 (B) at 70 ^{o}C.

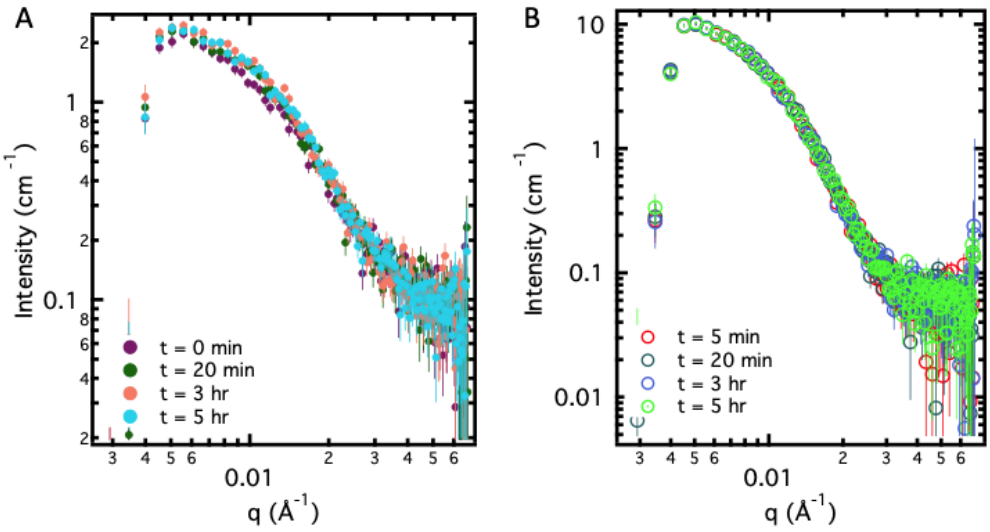

Figure 5.7: The intensities of the postmixed micelles comprised of 20K50145 and 20K50180 (A) and postmixed micelles of 20K100145 and 20K100180 (B) as the measurements are performed up to 5 hours.

entangled, a sticky reptation model can be applied, which is essentially a sticky Rouse model confined in a tube. For ionic bonds in polyelectrolyte complexes, breaking on associated sticky point into two separated ionic groups needs to overcome an activation energy barrier, E_a, which can be estimated as the energy difference between the electrical free energy of two separated ionic groups in an electrolyte medium, E_{corr}, and the Coulombic energy of a ion-ion pair in contact, E_{Coul}.

$$E_a \approx E_{\text{corr}} - E_{\text{Coul}} \tag{5.13}$$

$$E_{corr} \approx -\kappa e^2/4\pi\epsilon\epsilon_0 = \kappa l_B \propto \sqrt{c_{\text{salt}}} \tag{5.14}$$

$$E_{\text{Coul}} = -e^2/\pi\epsilon\epsilon_0 d = \frac{l_B}{d} \tag{5.15}$$

where κ is the inverse Debye length, l_B is the Bjerrum length, d is the distance between two ionic groups when they are bound, and c_{salt} is the solution salinity. It is seen that the activation energy barrier decreases with the increase of salt concentration. Thus, the lifetime of an ionic bond, τ_0,can be approximated as:

$$\tau_0\left(c_{\text{salt}}\right) = \frac{1}{\omega_0}\exp\left[\frac{E_a}{k_B T}\right] \tag{5.16}$$

where ω_0 is the dissociation rate in the absence of ionic bonds.

Scenario 1: single chain expulsion. Expulsion of a single polycation or polyanion chain entails the breaking of all the ionic bonds on the chain simultaneously, and no new bonds are formed before the complete removal of the chain out of the core domain. In mathematics,

$$E_{\text{a}}^{\text{expul}} = NfE_{\text{a}} \tag{5.17}$$

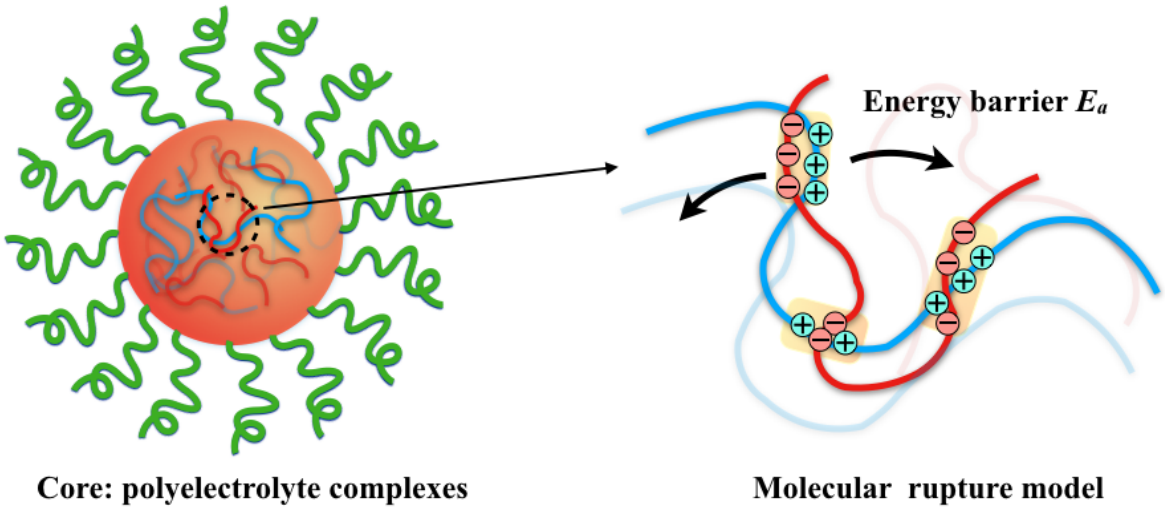

Figure 5.8: Schematic representation of the molecular rupture model for ionic binds in polyelectrolyte complex micelles.

$$\tau_{\text{expul}} < \tau_0 \tag{5.18}$$

where N is the degree of polymerization and f is the fraction of the paired charged groups.

At a high degree of pair-pair association, most charged groups are either involved in an interchain association or intrachain association, such that the concentration of unpaired charged groups are low. When a charged group breaks up with its partner, the number of available unpaired groups within its domain of freedom is very small. Thus, it is hard for it to form a bond with another uncharged group. It is likely that, after unsuccessfully searching for a new partner, it will re-form a bond with its old partner, which effectively prolongs the lifetime of a bond. It is reasonable to infer that these factors combined significantly increase the difficulty of expelling a single chain out of the complex phase and dramatically reduces the probability of the single chain expulsion scenario. It should be noted that the expulsion of a pair of associated polymers may need the breaking of less ionic bonds, given the possibility that many of the charged groups are paired between the two polymer chains. However, in reality, it is largely likely that the ionic groups form and re-form bonds with charged groups on other polymer chains. Moreover, the steric hindrance for the movement of a pair polyelectrolytes will be enhanced.

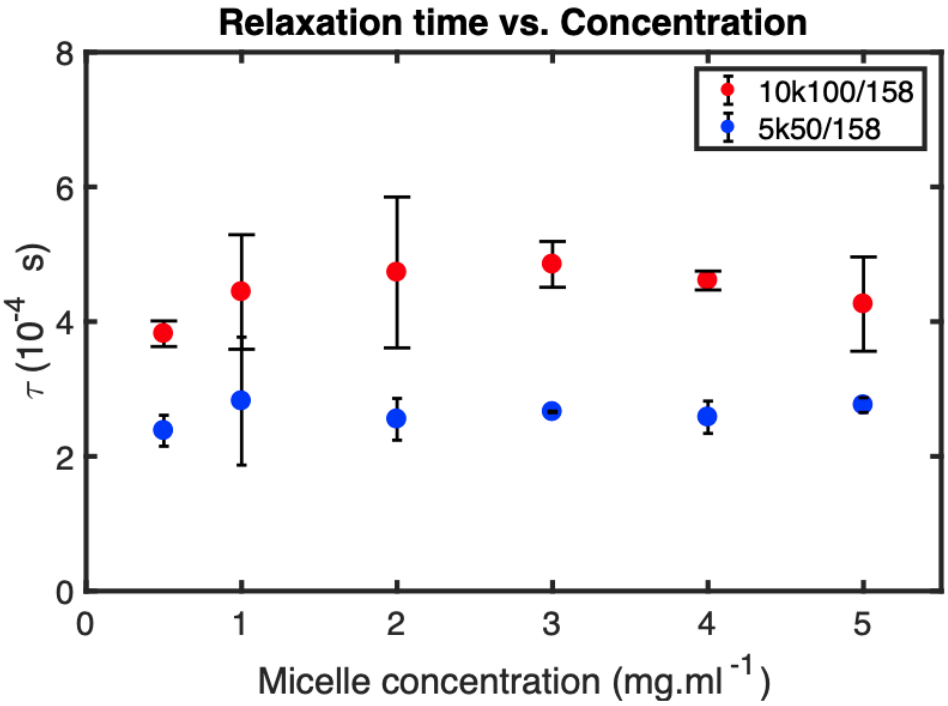

Figure 5.9: Concentration dependence of the relaxation time for the two samples with different polymer block lengths.

Scenario 2: micelle fission/fusion. In the case where micelles might split into two neutralized micelles, especially in solutions with high salt concentration. This split may be triggered by the collision and penetration among micelles due to the hydrodynamic force and thermal fluctuation. In Chapter 3, we demonstrate that, when two micelles collide, the extent of penetration is confined within the corona area, which limits the molecular exchange between the deuterium-rich micelles and hydrogen-rich micelles. In a micelle fusion/fission scenario, as pointed out by a few studies,[52, 7, 53, 24] the relaxation rate is dependent on the micelle concentration, since the collision between micelles is expected to yield second-order kinetics. Figure 5.9 demonstrates that the relaxation time of micelles is independent with the micelle concentration. Based on the discussion above, it is not unreasonable to infer that the molecular exchange via micelle fusion/fission mechanism is absent in polyelectrolyte complex micelles.

5.4 Concluding Remarks

In this chapter, time-resolved small-angle neutron scattering and deuterium labeling are employed to study the molecular exchange among PEC micelles near equilibrium states. Neutron contrast is achieved by mixing micelles formed by deuterium-rich polymers and micelles formed by hydrogen-rich polymers. It is shown that, when these two types of micelles are mixed, experimental measurements do not show obvious signal of molecular exchange up to tens of hours. The chain exchange can not be unlocked even at 70 ^{o}C and 2 M salt. It is speculated that the chain expulsion from the core of the PEC micelles is hindered by the large activation barrier energy among oppositely charged groups of the polyelectrolytes.

References

[1] A. Halperin and S. Alexander. Polymeric Micelles: Their relaxation kinetics. *Macromolecules*, 22:2403–2412, 1989.

[2] A. Halperin. Polymeric Micelles: A Star Model. *Macromolecules*, 20:2943–2946, 1987.

[3] A. Halperin. On micellar exchange: The role of the insertion penalty. *Macromolecules*, 44:5072–5074, 2011.

[4] Elena E. Dormidontova. Micellization kinetics in block copolymer solutions: scaling model. *Macromolecules*, 32:7630–7644, 1999.

[5] Minmin Tian, Anwei Qin, C Ramireddy, Stephen E Webber, Petr Munk, and Karel Proch. Hybridization of Block Copolymer Micelles. *Langmuir*, 9:1741–1748, 1993.

[6] Chikako Honda, Yuki Hasegawa, Rieko Hirunuma, and Takuhei Nose. Micellization Kinetics of Block Copolymers in Selective Solvent. *Macromolecules*, 27(26):7660–7668, 1994.

[7] Bernard Michels, Gilles Waton, and Raoul Zana. Dynamics of Micelles of Poly(ethylene oxide)-Poly(propylene oxide)-Poly(ethylene oxide) Block Copolymers in Aqueous Solutions. *Langmuir*, 13:3111–3118, 1997.

[8] Isabella Goldmints, Josef F. Holzwarth, Kenneth A. Smith, and T. Alan Hatton. Micellar Dynamics in Aqueous Solutions of PEO-PPO-PEO Block Copolymers. *Langmuir*, 13:6130–6134, 1997.

[9] Yongmei Wang, Charles M. Kausch, Moonseok Chun, Roderic P. Quirk, and Wayne L. Mattice. Exchange of Chains between Micelles of Labeled Polystyrene-block-poly(oxyethylene) As Monitored by Nonradiative Singlet Energy Transfer. *Macromolecules*, 28(4):904–911, 1995.

[10] V V A Fernandez, J F A Soltero, J E Puig, and Y Rharbi. Temporal Evolution of the Size Distribution during Exchange Kinetics of Pluronic P103 at Low Temperatures. pages 3015–3023, 2009.

[11] Lucas R. Parent, Evangelos Bakalis, Abelardo Ramírez-Hernández, Jacquelin K. Kammeyer, Chiwoo Park, Juan De Pablo, Francesco Zerbetto, Joseph P. Patterson, and Nathan C. Gianneschi. Directly Observing Micelle Fusion and Growth in Solution by Liquid-Cell Transmission Electron Microscopy. *J. Am. Chem. Soc.*, 139(47):17140–17151, 2017.

[12] Y. Rharbi. Fusion and fragmentation dynamics at equilibrium in triblock copolymer micelles. *Macromolecules*, 45:9823–9826, 2012.

[13] L Willner, A Poppe, J Allgaier, M Monkenbusch, and D Richter. Time-resolved SANS for the determination of unimer exchange kinetics in block copolymer micelles. *Europhys. Lett.*, 55(5):667–673, 2001.

[14] Reidar Lund, Lutz Willner, J??rg Stellbrink, Peter Lindner, and Dieter Richter. Loga-

rithmic chain-exchange kinetics of diblock copolymer micelles. *Phys. Rev. Lett.*, 96(6):1–4, 2006.

[15] Soo Hyung Choi, Timothy P. Lodge, and Frank S. Bates. Mechanism of molecular exchange in diblock copolymer micelles: Hypersensitivity to core chain length. *Phys. Rev. Lett.*, 104(4):1–4, 2010.

[16] Reidar Lund, Lutz Willner, Jörg Stellbrink, Peter Lindner, and Dieter Richter. Erratum: Logarithmic Chain-Exchange Kinetics of Diblock Copolymer Micelles [Phys. Rev. Lett. 96, 068302 (2006)]. *Phys. Rev. Lett.*, 104(4):049902, 2010.

[17] Thomas Zinn, Lutz Willner, Reidar Lund, Vitaliy Pipich, and Dieter Richter. Equilibrium exchange kinetics in n-alkylPEO polymeric micelles: single exponential relaxation and chain length dependence. *Soft Matter*, 8(3):623–626, 2012.

[18] Fabián A. García Daza, Josep Bonet Avalos, and Allan D. Mackie. Logarithmic Exchange Kinetics in Monodisperse Copolymeric Micelles. *Phys. Rev. Lett.*, 118(24):1–5, 2017.

[19] Zhenlong Li and Elena E. Dormidontova. Equilibrium chain exchange kinetics in block copolymer micelle solutions by dissipative particle dynamics simulations. *Soft Matter*, 7(9):4179, 2011.

[20] Ammu Prhashanna, Saif A. Khan, and Shing Bor Chen. Kinetics of Chain Exchange between Diblock Copolymer Micelles. *Macromol. Theory Simulations*, 25(4):383–391, 2016.

[21] Ammu Prhashanna and Elena E. Dormidontova. Tadpole and Mixed Linear/Tadpole Micelles of Diblock Copolymers: Thermodynamics and Chain Exchange Kinetics. *Macromolecules*, 50(4):1740–1748, 2017.

[22] You Yeon Won, H. Ted Davis, and Frank S. Bates. Molecular exchange in PEO-PB micelles in water. *Macromolecules*, 36(3):953–955, 2003.

[23] Elizabeth G. Kelley, Ryan P. Murphy, Jonathan E. Seppala, Thomas P. Smart, Sarah D. Hann, Millicent O. Sullivan, and Thomas H. Epps. Size evolution of highly amphiphilic macromolecular solution assemblies via a distinct bimodal pathway. *Nat. Commun.*, 5:3599, 2014.

[24] Luciana Meli, Jessica M. Santiago, and Timothy P. Lodge. Path-dependent morphology and relaxation kinetics of highly amphiphilic diblock copolymer micelles in ionic liquids. *Macromolecules*, 43:2018–2027, 2010.

[25] Reidar Lund, Lutz Willner, Dieter Richter, and Elena E. Dormidontova. Equilibrium chain exchange kinetics of diblock copolymer micelles: Tuning and logarithmic relaxation. *Macromolecules*, 39(13):4566–4575, 2006.

[26] Tyler J. Cooksey, Avantika Singh, Kim Mai Le, Shu Wang, Elizabeth G. Kelley, Lilin He, Sameer Vajjala Kesava, Enrique D. Gomez, Bryce E. Kidd, Louis A. Madsen, and Megan L. Robertson. Tuning Biocompatible Block Copolymer Micelles by Varying Solvent Composition: Core/Corona Structure and Solvent Uptake. *Macromolecules*, 50(11):4322–4334, 2017.

[27] Lu Li, Samanvaya Srivastava, Marat Andreev, Amanda B. Marciel, Juan J. de Pablo, and Matthew V. Tirrell. Phase Behavior and Salt Partitioning in Polyelectrolyte Complex Coacervates. *Macromolecules*, 51:2988–2995, 2018.

[28] Yuanchi Ma and Timothy P. Lodge. Chain Exchange Kinetics in Diblock Copolymer Micelles in Ionic Liquids: The Role of χ. *Macromolecules*, 49(24):9542–9552, 2016.

[29] Dan Zhao, Yuanchi Ma, and Timothy P. Lodge. Exchange Kinetics for a Single Block Copolymer in Micelles of Two Different Sizes. *Macromolecules*, 51(6):2312–2320, 2018.

[30] Guy Hurtrez, Philippe Dumas, and Gérard Riess. Polystyrene-Poly(ethylene oxide) diblock copolymers micelles in water. *Polym. Bull.*, 40(2-3):203–210, 1998.

[31] M. Jacquin, P. Muller, R. Talingting-Pabalan, H. Cottet, J. F. Berret, T. Futterer, and O. Théodoly. Chemical analysis and aqueous solution properties of charged amphiphilic block copolymers PBA-b-PAA synthesized by MADIX®. *J. Colloid Interface Sci.*, 316(2):897–911, 2007.

[32] Michael Lueckheide, R Vieregg, Alex J Bologna, Lorraine Leon, and Matthew V Tirrell. Structure-Property Relationships of Oligonucleotide Polyelectrolyte Complex Micelles. *Nano Lett.*, 18:7111–7117, 2018.

[33] Adriana M. Mihut, Arnaud Chiche, Markus Drechsler, Holger Schmalz, Emanuela Di Cola, Georg Krausch, and Matthias Ballauff. Crystallization-induced switching of the morphology of poly(ethylene oxide)-block-polybutadiene micelles. *Soft Matter*, 5(1):208–213, 2009.

[34] Mark Kastantin, Badriprasad Ananthanarayanan, Priya Karmali, Erkki Ruoslahti, and Matthew Tirrell. Effect of the lipid chain melting transition on the stability of DSPE-PEG (2000) micelles. *Langmuir*, 25(13):7279–7286, 2009.

[35] Soo Hyung Choi, Frank S. Bates, and Timothy P. Lodge. Molecular exchange in ordered diblock copolymer micelles. *Macromolecules*, 44(9):3594–3604, 2011.

[36] Jie Lu, Frank S. Bates, and Timothy P. Lodge. Remarkable effect of molecular architecture on chain exchange in triblock copolymer micelles. *Macromolecules*, 48(8):2667–2676, 2015.

[37] J. Lu, F. S. Bates, and T. P. Lodge. Addition of Corona Block Homopolymer Retards Chain Exchange in Solutions of Block Copolymer Micelles. *Macromolecules*, 49:1405–1413, 2016.

[38] Thomas Zinn, Lutz Willner, Vitaliy Pipich, Dieter Richter, and Reidar Lund. Molecular Exchange Kinetics of Micelles: Corona Chain Length Dependence. *ACS Macro Lett.*, 5(7):884–888, 2016.

[39] En Wang, Jie Lu, Frank S Bates, and Timothy P Lodge. Effect of Corona Block Length on the Structure and Chain Exchange Kinetics of Block Copolymer Micelles. *Macromolecules*, 51:3563–3571, 2018.

[40] Reidar Lund, Lutz Willner, Dieter Richter, Hermis Iatrou, Nikos Hadjichristidis, and Peter Lindner. Unraveling the equilibrium chain exchange kinetics of polymeric micelles using small-angle neutron scattering - Architectural and topological effects. *J. Appl. Crystallogr.*, 40:327–331, 2007.

[41] Andrew J. Peters and Timothy P. Lodge. Chain Exchange Kinetics of Asymmetric B_1AB_2 branched triblock copolymers. *Macromolecules*, pages 6303–6313.

[42] Dawanne M. Eugene and Scott M. Grayson. Efficient preparation of cyclic poly(methyl acrylate)-block-poly(styrene) by combination of atom transfer radical polymerization and click cyclization. *Macromolecules*, 41(14):5082–5084, 2008.

[43] Weikun Li, Chung Hao Kuo, Istvan Kanyo, Srinivas Thanneeru, and Jie He. Synthesis and self-assembly of amphiphilic hybrid nano building blocks via self-collapse of polymer single chains. *Macromolecules*, 47(17):5932–5941, 2014.

[44] Jianguo Wen, Liang Yuan, Yongfang Yang, Li Liu, and Hanying Zhao. Self-assembly of monotethered single-chain nanoparticle shape amphiphiles. *ACS Macro Lett.*, 2(2):100–106, 2013.

[45] Jianguo Wen, Jing Zhang, Yue Zhang, Yongfang Yang, and Hanying Zhao. Controlled self-assembly of amphiphilic monotailed single-chain nanoparticles. *Polym. Chem.*, 5(13):4032, 2014.

[46] Yuanli Cai, Yiqing Tang, and Steven P. Armes. Direct synthesis and stimulus-responsive micellization of Y-shaped hydrophilic block copolymers. *Macromolecules*, 37(26):9728–9737, 2004.

[47] Yun Yan, Jianbin Huang, and Ben Zhong Tang. Kinetic trapping-a strategy for directing the self-assembly of unique functional nanostructures. *Chem. Commun.*, 52(80):11870–11884, 2016.

[48] Mei Li and Stephen Mann. Emergent hybrid nanostructures based on non-equilibrium block copolymer self-assembly. *Angew. Chemie Int. Ed.*, 47:9476–9479, 2008.

[49] Antonia G. Denkova, Eduardo Mendes, and Marc-Olivier Coppens. Non-equilibrium dynamics of block copolymer micelles in solution: recent insights and open questions. *Soft Matter*, 6(11):2351, 2010.

[50] Hao Wu, Jeffrey M. Ting, Olivia Werba, Siqi Meng, and Matthew V. Tirrell. Non-equilibrium phenomena and kinetic pathways in self-assembled polyelectrolyte complexes. *J. Chem. Phys.*, 149:163330, 2018.

[51] Ryan P. Murphy, Elizabeth G. Kelley, Simon A. Rogers, Millicent O. Sullivan, and Thomas H. Epps. Unlocking chain exchange in highly amphiphilic block polymer micellar systems: Influence of agitation. *ACS Macro Lett.*, 3(11):1106–1111, 2014.

[52] Yanfeng Zhang, Tao Wu, and Shiyong Liu. Micellization kinetics of a novel multi-responsive double hydrophilic diblock copolymer studied by stopped-flow pH and temperature jump. *Macromol. Chem. Phys.*, 208:2492–2501, 2007.

[53] Jingyan Zhang, Jian Xu, and Shiyong Liu. Chain-length dependence of diblock copolymer micellization kinetics studied by stopped-flow pH-jump. *J. Phys. Chem. B*, 112(36):11284–11291, 2008.

CHAPTER 6

NONEQUILIBRIUM DISSOCIATION KINETICS IN POLYELECTROLYTE COMPLEX MICELLES

6.1 Introduction

Knowledge on the underlying mechanism that governs PEC micelle dissociation kinetics remains limited. The vast majority of the endeavors of the past two decades has remained on the static properties of PEC micelles, such as their stimuli-responsiveness, co-micellization with various biological macromolecules, and therapeutic applications[1]. The difficulties to studying micelle kinetics stem from a limited understanding of the polyelectrolyte complexes and a lack of a universal model to illustrate the micelle scaling law.

Direct endeavor to addressing the dissociation (or formation) kinetics in polyelectrolyte complex micelles has been rarely reported to date; yet, previous effort and progress on micelles formed by low weight surfactants and nonionic block copolymers may provide insights. In the 1960s, Aniansson and Wall proposed two possible mechanisms for the kinetics of dissociation in surfactant micelles: (1) a step-wise single chain expulsion and insertion mechanism and (2) a collective micelle fission and fusion mechanism[2]. Later, experimental observations using light scattering techniques have clearly confirmed that the kinetics of surfactant micelle dissociation-formation equilibrium can be characterized by two well-separated relaxation processes. Based on that, in the late 1980s, Halperin and Alexander developed a similar theory for amphiphilic block copolymer micelles[3]. They claimed that micelle fission (or fusion) may be deactivated due to the high free energy penalty it incurs owing to the coronal interaction , which scales as

$$U_{\text{fiss}} \simeq N_B^{2/3}(P_1/P^2) \tag{6.1}$$

where N_B is the length of the core-forming block, and P_1 and P are the aggregation number of the *fissionable* aggregate and the initial micelle, respectively. The fission activation energy clearly minimizes when $P_1 = 1$, which favors the single chain expulsion mechanism. It is noteworthy that the result is only valid for systems that undergo small deviations from equilibrium states. Results from a few experiments suggested that the single chain

expulsion/insertion alone can not explain the phenomena well. For example, Esselink et al. investigated the evolution of mixed ampphiphilic diblock copolymer micelles formed by two polymers that have the same composition but different coronal block lengths, and pointed out that the redistribution of polymer chains among micelles proceeds mainly via micelle fusion[4]. Dormidontova theoretically predicted that micelle fission is a slow process at dynamic equilibrium states but plays a major role when micelles re-equilibrate from a large perturbation (such as during T-jump experiments)[5]. Compared to unimer expulsion where the entropic penalty comes from the exposure of the solvophobic chains in selective solvent, micelle fission needs to overcome the free energy increase corresponding to the separation of micellar cores. The fission activation energy, U_{fiss} is given as:

$$U_{\text{fiss}} \simeq P_{\text{eq}}^{5/6} \left[P_1^{2/3} + P_2^{2/3} - (P_1 + P_2)^{2/3} \right] \tag{6.2}$$

where P_{eq}, P_1, and P_2 represent the aggregation numbers of the pre-fission micelles in equilibrium and post-fission micelle 1 and 2, respectively. It predicts that when a micelle system is far away from its equilibrium state, micelle fission or fusion becomes dominant. Recently, efforts from experiments have been taken to directly observe micelle fission. For example, Burke *et al.* observed that fragmentation of amphiphilic block copolymer micelles happened when micelles undergo morphological transitions from spherical micelles to rod-like aggregates[6]; Rharbi reported that, even at equilibrium states, micelle fission did take place in PEO-PPO-PEO micelles but with a rate 10^6 slower than that of chain expulsion and insertion[7].

However, experimental work devoted to revealing the dissociation kinetics of polyelectrolyte complex micelles is scarce. Despite the stark contrast of their driving forces, PEC micelles have been oftentimes understood in an analogous way to amphiphilic diblock copolymers micelles. It may be plausible with respect to the static micellar structures, which has been the focus so far. We recently pointed out that the long-range electrostatic interac-

tions do not significantly affect micelle-micelle correlation, meaning that PEC micelles in dilute solutions behave in a similar way to their uncharged counterparts[8]. However, when it comes to micelle kinetics, distinctions emerge. First, block copolymer micelles is usually a ternary system that contains solvent, coronal chains, and core chains; PEC micelles in most cases is a multi-component system in which the interplay between positively-charged blocks, negatively-charged blocks, one or two coronal blocks, counterions, and solvent (normally water) complicates micellar dynamics. Second, unlike amphiphilic block copolymer micelles, the core chains in PEC micelles are hydrophilic and maintained a complex state via electrostatic interactions, which means the expulsion of a chain from micelle cores exposes no unfavorable chains in solvent but depending on the ionic environment that needs to counteract the Coulomb attraction between positive and negative charges. The breakup of the electrostatic bonds may retard the kinetics. Our results from time-resolved small-angle neutron scattering indicates that these micelles in equilibrium remain frozen up to 40 hours[9]. Third, amphiphilic block copolymer micelles often have solid-like cores, whereas PEC micelle cores contain a large amount of water (ca. 30 - 90 %), which is subject to environmental factors such as salt ion concentration and system temperature. All these features combined makes studies on the mechanism of PEC micelle dissociation or formation different from either surfactant micelles or amphiphilic block copolymer micelles.

In this article, we aim to make strides forward toward the mechanism of dissociation kinetics in polyelectrolyte complex-based micelles. By combining knowledge of polyelectrolyte complexation and micelle scaling laws, we (1) develop a theoretical framework to describe the kinetic pathway of PEC micelle dissociation, (2) illustrate the rationale behind it, (3) derive an analytical expression of fission relaxation kinetics as a function of polyelectrolyte molecular weights, salt concentration and temperature, and (4) compare our experimental results with theoretical predictions. The model system we employ here consists of a positively charged diblock polyelectrolyte, poly(ethylene oxide)-*block*-poly(vinyl benzyl trimethylammonium chloride)(PEO_{225}-*b*-$PVBTMA_{100}$), and a negatively charged

homopolymer, poly(acrylic acid sodium) (PAA_{158})[10, 11]. (The subscripts indicate the numbers of repeat units.) The PVBTMA block has been demonstrated as an effective cationic polymer in DNA encapsulation and delivery, while the PAA block has been extensively studied as a proxy for weakly charged biomacromolecules[12, 13]. The physical properties of the micelles in equilibrium are characterized by a combination of techniques including dynamic light scattering, small-angle X-ray scattering, and cryogenic electron microscopy. The salt-dependent evolution of PEC micelles upon an abrupt salinity ascendance is investigated using time-resolved static light scattering. We have developed a quantitative model to predict the dependence of the dissociation rate on the ionic chain length, temperature and salt concentration, which approximately agree with our data and can be further examined.

6.2 Experimental Details

6.2.1 Materials

The materials used in this chapter are the diblock copolymers PEO-*b*-PVBTMA and homopolymers PAA.

6.2.2 Micelle preparation

Micelle preparation and characterization were performed according to the protocol established in our previous work.[11] Briefly, polymer stock solutions were prepared by dissolving polyelectrolytes in Milli-Q water at the total concentration of 5 mg mL^{-1} and filtering solutions through PVDF filters (average diameter $\approx$ 220 nm). Micellar assemblies were formed by directly mixing the polycation and polyanion solutions under stoichiometric conditions. The order of addition was checked and did not affect the assembly features. All the samples were set aside for at least 24 hours before any experiments.

6.2.3 Dynamic light scattering

Dynamic light scattering was carried out on a Brookhaven Instruments BI-200SM Research Goniometer System with a 637 nm incident laser. The scattering vector, q, is defined by $q = \frac{4\pi n}{\lambda}\sin(\frac{\theta}{2})$, where λ is the wavelength of the incident light, n is the refractive index of the solution, and θ is the angle between the incident and scattering laser. The fluctuation of the electric field generated by the ensemble collection of the solution particles under Brownian diffusion can be expressed using a field autocorrelation function: $\int_0^\infty E(t)E(t+\tau)d\tau = exp^{-Dq^2\tau}$, where E is the electric field, τ is the delay time, and D is the diffusion coefficient. The experimentally measured intensity correlation function, G_2, is equivalent to the actual electric field autocorrelation, G_1, through the Seigert relationship: $G_2(\tau) = 1 + \gamma G_1(\tau)$, where γ is a coherence factor indicating the efficiency of the photo collection system.

The hydrodynamic radii of scatters under Brownian diffusion can be calculated via Stokes-Einstein relationship: $R_h = (k_B T)/6D$, where k_B is the Boltzmann constant, T is the absolute temperature, and η is the viscosity of the solution, here as taken that of water. Diffusion coefficient and polydispersity index were extracted by fitting intensity correlation functions to a second order-expanded single exponential as below: $G_2 = A[1 + Bexp(-2\Gamma\tau + \mu_2\tau^2)]$, where A is the amplitude or intercept of the correlation function, B is the baseline, Γ is the decay rate, and μ_2 is proportional to the distribution width. The polydispersity index is expressed as: $PdI = \mu_2/2\Gamma = \sigma^2/(2R_h^2)$, where σ is the standard deviation of a hypothetical Gaussian distribution centered on R_h. The size distribution was obtained using the REPES algorithm.

Multi-angle measurement was conducted using a script that written by the *Cmm* scripting language. Correlation functions were typically collected at 12 scattering angles from 30^o to 140^o at 10^o increments, and running duration of each angle was at least 1 minute. The angular dependence of diffusion coefficient was acquired by plotting q^2 versus decay rate Γ. A linearity over a range of scattering angles is a good indication of isotropic scatters, *i.e.*, spheres when the radius is larger than $\lambda/20$ nm. The correlation function at each angle was

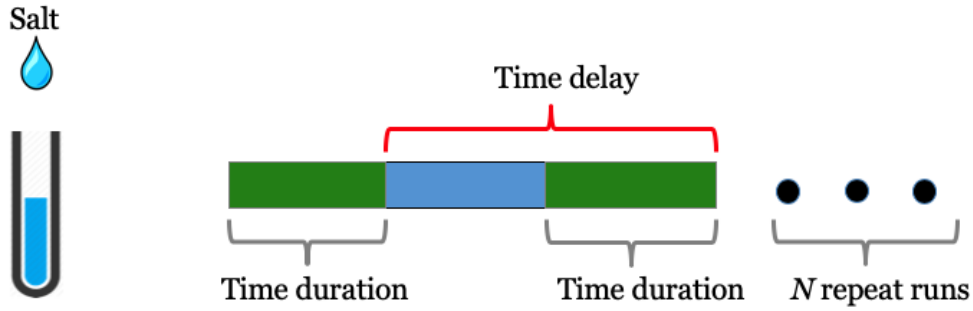

Figure 6.1: Schematic representation of the experimental setup of time-resolved static light scattering experiments.

fitted to a first-order single exponential relaxation function in MATLAB.

6.2.4 Time-resovled static light scattering

The time-resolved scattering experiments were carried out on a Brookhaven Instruments BI-200SM Research Goniometer System with a 637 nm incident laser. A *cmm* script is written to control the time-resolved measurements automatically, which is deadtime about 1 second. The acquisition time (usually 30 seconds) and a readout pause between two acquisitions are optimized according to different circumstance. All experiments were conducted at the angle of 90^{o}.

6.2.5 Small-angle X-ray scattering

All SAXS experiments were carried out on the Biological Small Angle Scattering Beam Line BL4-2 at the Stanford Synchrotron Radiation Lighthouse (SSRL), SLAC National Accelerator Laboratory. The sample-to-detector distance was set to 3.5 m and X-rays with the wavelength of $\lambda = 1.38$ Å (9 keV) were utilized for the measurements. Using a Pilatus3 X 1M detector (Dectris Ltd, Switzerland) the setup covered a range of momentum transfer q ≈ 0.0025 - 0.17 $Å^{-1}$ where q is the magnitude of the scattering vector. Aliquots of 30 μL of the polyelectrolyte micellar suspension were loaded onto the automated fluid sample loader at the beamline. Series of sixteen consecutive 1 second exposures were collected first from

Table 6.1: The calculated scattering length densities of polymers and water.

Chemical	Formula	Density (g cm^{-3})	SLD (10^{-6} $Å^{-1}$)
Water	H_2O	1.00	9.47
PEO	$CH_3(C_2H_4O)_n$	1.13	10.50
PAA	$(C_3H_3O_2Na)_n$	1.50	13.04
PVBTMA	$(C_{12}H_{18}NCl)_n$	1.20	12.00

the buffer blank (pure water) and followed by the micelle samples of different concentrations. Solutions were oscillated in a stationary quartz capillary cell during data collection to maximize the exposed sample volume and reduce the radiation dose per unit volume of sample. The collected data were radially integrated, analyzed for radiation damage, and buffer subtracted using the automated data reduction pipeline at the beam line. Only data that did not show any signs of the effects of radiation damage were included in the final average for each sample concentration. More details on the SAXS data collection are available in the literature[14]. The X-ray scattering length densities of the polymers are calculated using the SLD calculator provided by NIST and are shown in Table 6.1.

Micelle samples were fitted using a model that contains polydisperse core-shell sphere and a polydisperse Gaussian coil function, which has been reported by us previously[8]. The details of the model can be found in the Supporting Information.

6.2.6 Cryogenic electron microscope

FEI Tecnai^{TM} G2 Spirit BioTWIN TEM was used to image samples set at an accelerating voltage of 120 kV onto a LaB6 emitter at -178 ^{o}C. Samples vitrification was done on a FEI vitrobot system coupled with a Bal-Tec high-pressure freezer. A droplet of about 3.0 μL samples containing polyelectrolyte complex assemblies was pipetted onto a carbon/Formvar grid that is cleaned by a PELCO easiGlow glow discharge instrument. The grid was blotted for 3 seconds and was quenched rapidly in liquid ethane, and subsequently transferred to a single-tilt cryo holder for visualization on a Cryo-EM dedicated FEI Talos 2000kV FEG electron microscopy.

6.3 Results and Discussions

6.3.1 Characterization of PEC micelles

We characterize the morphology, size, internal structure of the PEC micelles by employing a combination of techniques including dynamic light scattering, small-angle X-ray scattering, and cryogenic electron microscopy. As the DLS result shows in Figure 6.2B, the PEC micelles have a monomodal size distribution, and the hydrodynamic radius is centered at 30 nm with a narrow distribution. SAXS is further employed to investigate the sizes of micelle core and corona. The SAXS profile exhibits a characteristic pattern of spherical objects: at low q values, the curve follows a quasi-plateau and transitions to a intensity drop that scales with q with a power law of -4 at the middle q region, as shown in Figure 6.2C. At the high q region, the intensity decreases along q with a power law of -2.3,[15, 16, 17] which is characteristic of the individual constituent polymers. Using a polydisperse core-shell model, we extract the radius of the core and the thickness of the corona, which are 10.3 nm and 6.8 nm, respectively. The morphology of the PEC mielles is further visualized by Cryo-TEM. Due to the light contrast between the coronas and the background, Cryo images only shows the micelle cores. As we can see in Figure 6.2D, the cores are generally spherical, and the average radius is around 13 nm. Results from DLS, SAXS, and Cryo-images are generally in line with one another.

6.3.2 Kinetics of salt-induced dissociation

A typical time-dependent light scattering experiment is schematized in Scheme 6.1 in the Experimental Section. The time evolution of light scattering was performed under two scenarios: (*i*) the temperature-dependence case where a micelle solution containing 1.0 mg mL^{-1} PEO_{225}-*b*-$PVBTMA_{100}$/PAA_{158} is measured, upon a salinity jump from 0 to 500 mM NaCl, at three different temperatures, i.e. 20, 37, and 57 ^{o}C, respectively, and (*ii*) the salt-dependence case where a micelle solution with 1.0 mg mL^{-1} PEO_{225}-*b*-$PVBTMA_{100}$/PAA_{158}

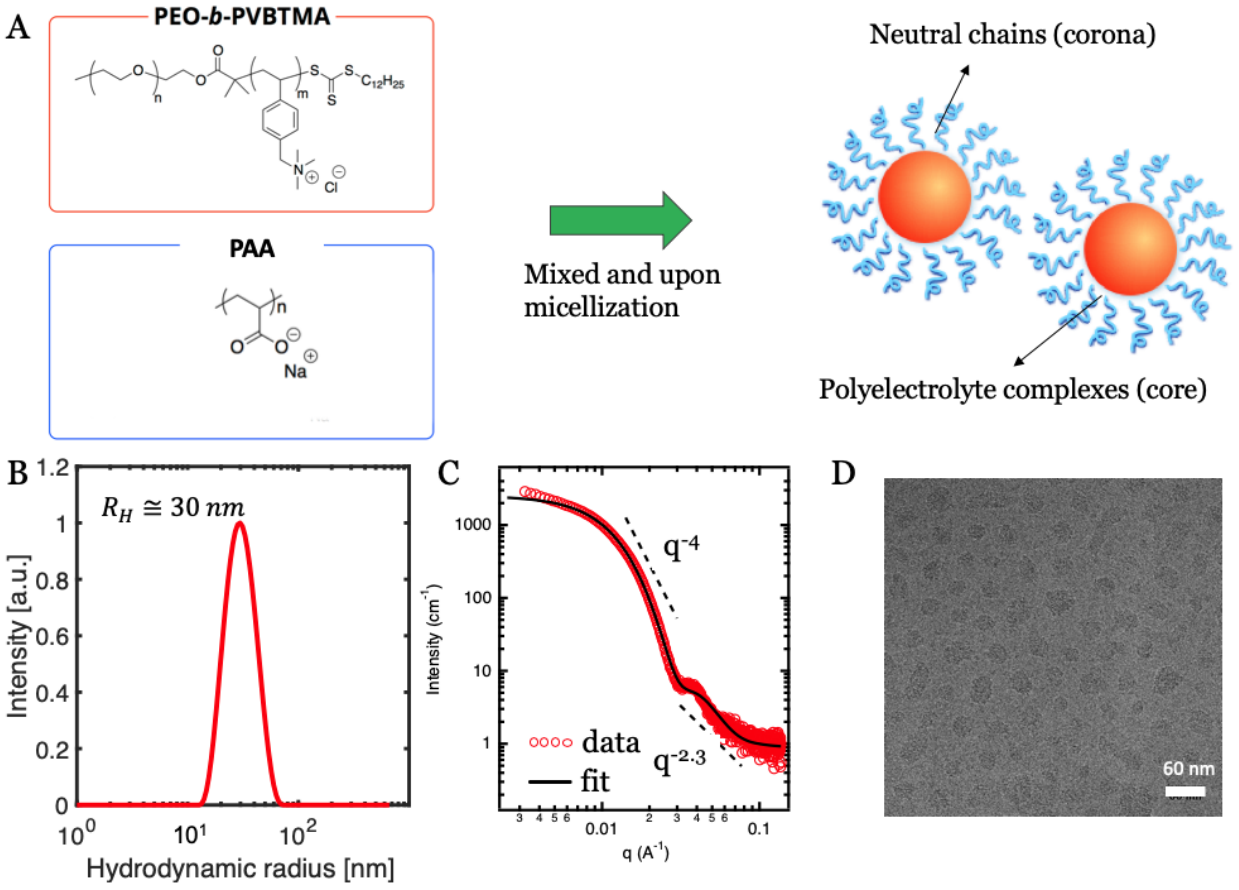

Figure 6.2: (A) Schematic representation of the core-corona strucure micelles formed upon the micellization of the oppositely charged polymers, i. e. PEO-*b*-PVBTMA and the poly(acrylic acid sodium) (PAA). Chemical structures are shown. (B) The size distribution and apparent hydrodynamic radius determined by DLS analysis using the REPES algorithm. The apparent hydrodynamic radis, R_H, is about 30 nm. (C) SAXS curve of the PEC micelles and the fitting using a polydisperse core-corona sphere model. (D) Representative cryo-TEM images to visualize the morphology of the PEC micelles. The average size of micellar cores is about 26 nm. The scale bar is 60 nm.

was measured when the solvent salt concentration jumps to 300 mM, 400 mM, 500 mM, and 600 mM, respectively. As illustrated by Figure 6.3 and 6.4, the induced disassembly causes strong decrease of the scattering intensities.

We take the structure factor as unity because the interparticle interaction is minimal at such a dilute polymer concentration, and also take the form factor as unity since $qR_{micelle} < 1$, where $R_{micelle}$ is the radius of the salt-free micelles, q is the scattering wave vector, λ_0 is the incident laser wavelength that equals to 637 nm, n is the solvent refractive index which is about 1.332 for H_2O at room temperature, and is the measuring angle which is 90^o. Therefore, the scattering intensity is written as[18]

$$I(t) \approx (\frac{dn}{dc})^2 (C - C_{CMC}) P_{mean}(t) M_w \tag{6.3}$$

where $\frac{dn}{dc}$ is the reflective index increment, C is the weight concentration of the polymers, C_{CMC} is the critical micelle concentration which is primarily a function of the solvent salt concentration, $P_{mean}(t)$ is the average aggregation number and is time dependent, and M_w is the molecular weight of a building block. A building block is defined as a neutralized group containing a diblock polyelectrolyte chain plus the amount of oppositely charged homopolymer needed to neutralize it. In this case, M_w approximately equals to 150 kg mol^{-1}. It is shown, for a given system, that the time evolution of the scattering intensity is only proportional to the average aggregation number. Equation (3) is therefore simplified to be

$$I(t) \approx P_{mean}(t) \tag{6.4}$$

Trial fits of a single exponential or a sum of two exponential functions do not give satisfactory results, which indicates the kinetic of the dissociation process is inherently broad. Similar results have been found and reported by us in kinetically trapped polyelectrolyte complexes.[11] Satisfactory fittings are only obtained when we fit the dissociation of the micelles with an Avrami-type model in the form of a compressed (or stretched) exponential,

Table 6.2: The relaxation rates and exponential exponents of micelle dissociation at three different temperatures.

Temp (K)	τ (min)	β
T = 293	61.54	2.0
T = 330	51.77	1.84
T = 350	38.57	1.66

which reads

$$P_{mean}(t) \approx exp[-(t/\tau)^{\beta}] \tag{6.5}$$

where τ is the relaxation rate and β is the exponential exponent that relates to the type of (de)nucleation and shrinking (or growth) geometry. The Avrami phenomenological model has been used to describe the relaxation kinetics in far-from-equilibrium systems, such as isothermal phase transformations.[19], crystallization kinetics in polymer blends.[20] aging dynamics in colloidal gels,[21] adsorption kinetics of polyelectrolytes on solution interfaces,[22] and morphological transitions in diblock copolymer micelles.[23] The exponential exponent, β, is assumed to range from 1 to 4 and is an indicator of the geometric dimension of the denucleation: Avrami exponent $\beta = 1.0$ denotes the one-dimensional rodlike denucleation and $\beta = 2.0$ indicates the two-dimensional disklike denucleation.[24, 25] In micelle dynamics, first-order kinetics ($\beta = 1.0$) corresponds to the single chain expulsion/insertion mechanism.[26, 3] Second-order kinetics ($\beta = 2.0$) has also been reported in diblock copolymer micelles. Meli et al. reported that the relaxation kinetics in poly(ethylene oxide)-*b*-poly(butadiene) micelles in ionic liquids over a broad range of temperature and concentrations can be well described by an Avrami-type relaxation function with an exponent 2. [27]. They attributed this temperature-dependence relaxation behavior to a micellar fission/fusion mechanism. Here, because the salinity jump renders micelle systems far way from equilibrium, we attempt to use the Avrami model to elucidate the relaxation behaviors in the PEC micelles.

The fitting results are shown in Table 6.2 and 6.3. It is observed that (*i*) the relaxation time decreases as temperature increases or salt concentration increases, (*ii*) all the exponential exponents are in the range of 1 and 2, and (*iii*) the exponent of the low temperature is in

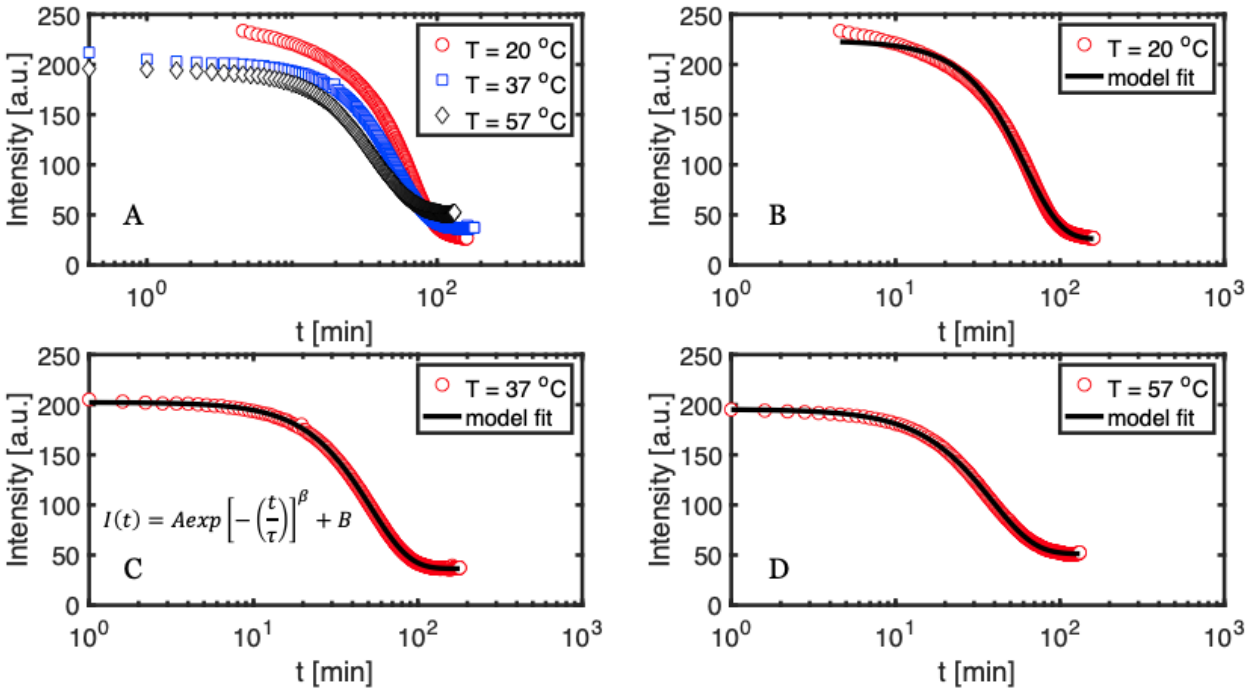

Figure 6.3: (A) The time evolution of light scattering intensity from three temperatures during the kinetics upon the salinity jumps to 500 mM NaCl in the 1.0 mg mL^{-1} PEO_{225}-*b*-$PVBTMA_{100}$ / PAA_{158} solution. The fits of the temperature-dependence dissociation profiles at (B) 20 °C, (C) 37 °C, and (D) 57 °C, respectively. The red lines are the experimental data and the black lines represent the fits.

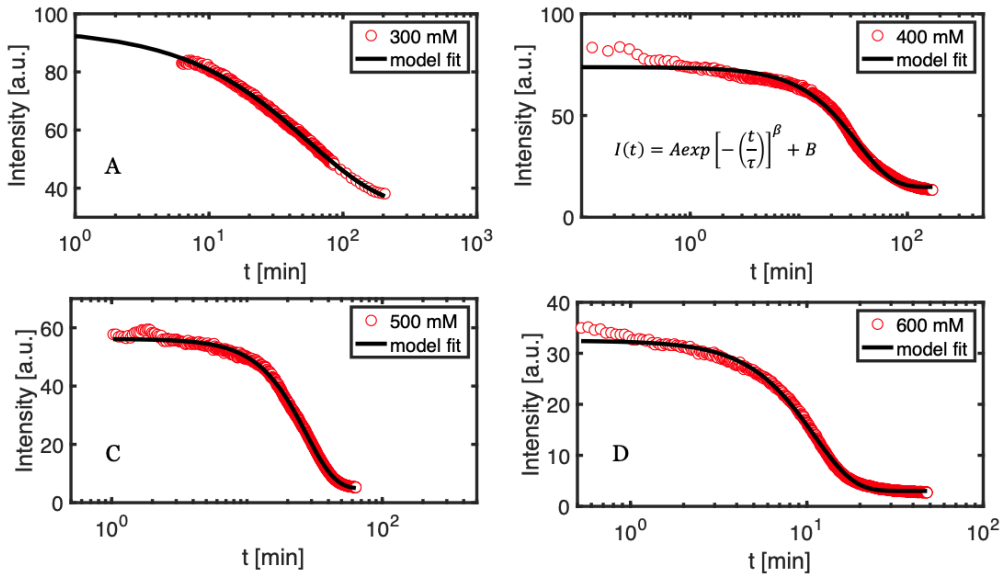

Figure 6.4: The salt-induced scattering intensity evolution of PEC micelles at four different salt concentrations: (A) 300 mM, (B) 400 mM, (C) 500 mM, and (D) 600 mM. Micelles are made of 1.0 mg mL^{-1} PEO_{225}-*b*-$PVBTMA_{100}$/PAA_{158} solution in aqueous solution at room temperature. The red lines are the experimental data and the black lines represent the fits.

Table 6.3: The relaxation rates and exponential exponents of micelle dissociation at three different temperatures.

C_s (mM)	τ (min)	β
300	51.87	0.82
400	35.15	1.43
500	27.37	2.03
600	10.88	1.94

proximity to 2 but decreases when the temperature increases. The acceleration of the micellar dissociation upon temperature increase is probably due to the thermally activated motion of the polymeric chains as well as the enhanced random forces from the solvent molecules. Almost all the values of exponent β is larger than 1 but smaller than 2. It seems like that the single chain expulsion/insertion is not the case here; neither is the fission-fusion scheme largely applicable, especially at high temperatures and low salt concentrations. However, in the following, by applying scaling law of conventional block copolymer micelles into PEC micelles and taking into consideration the salt and temperature dependence of the interfacial tension and ionic complex phase density, we demonstrate that the salt-induced dissociation of polyelectrolyte complex micelles can be well explained by a micelle fission model which separates the dissociation pathway into different stages. The mismatches between experimental data and the model fits at the onset of the dissociation will also be explained under the context of the micelle fission model.

6.3.3 Micelle fission model

Our model considers the micelle dissociation process involve three successive stages, as depicted in Figure 6.6. First, upon the addition of salt or the temperature increment, the initial micelle undergoes an instantaneous swelling or shrinkage with the changes of the interfacial tension and the complex density of the core, as denoted by $\gamma(C_s, T)$ and $\phi(C_s, T)$ respectively. This step is thought to be fast and cannot entirely be resolved experimentally, although some part is presence in the scattering data, which will be discussed later. Sec-

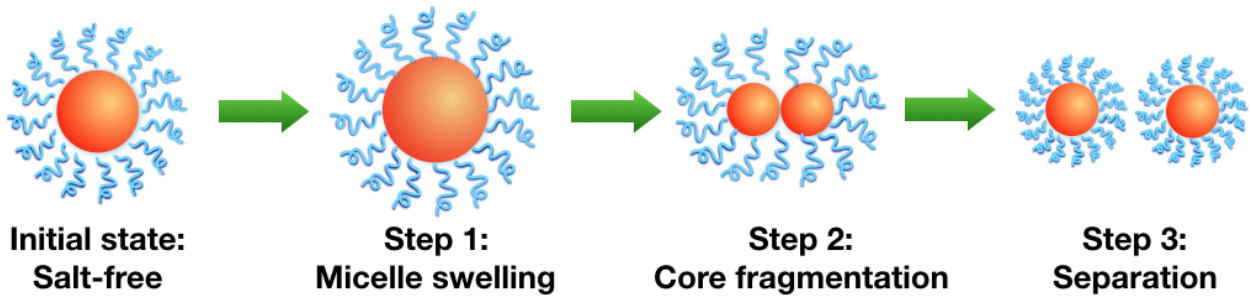

Figure 6.5: Schematic representation of the three-staged micelle dissociation model.

ond, this unstable and short-lived micelle tends to separate into two intermediate micellar aggregates, with the cores in contact and the corona areas overlapping. It is believed to be the rate-limiting step because it involves the compartmentation of the polymer chains in the core and redistribution of the corona-forming chains. Third, the nascent micellar aggregates drift into individual ones with the elimination of the corona crossing. The three-staged dissociation model is depicted in Figure 6.5.

Mathematically, the whole process can be represented as:

$$M_{init}(P_0, \gamma_0, \phi_0) \xrightarrow{\tau_1} M_{swell}(P_0, \gamma, \phi) \xrightarrow{\tau_2} M_{frag}(P_1, P_2, \gamma, \phi) \xrightarrow{\tau_3} M_{final}(P_1, P_2, \gamma, \phi) \tag{6.6}$$

where P_0, γ_0, and ϕ_0 are the aggregation number, interfacial tension, and core polymer density of the initial micelles, respectively. P_1 and P_2 are the aggregation number of the two intermediate micelles ($P_1 + P_2 = P_0$). It is assumed that changes of the interfacial tension and core density complete instantaneously upon the salinity or temperature jump and are kept the same onward, as denoted by the constant values of γ and ϕ. Also, the rate of each step are characterized by τ_1, τ_2, and τ_3, respectively.

6.3.4 PEC micelles at salt-free conditions

It is well known that the total free energy of a polymeric micelle in a salt-free solution, F, comes from three contributions: (1) F_{corona} that accounts for the stretching of the coronal blocks in the corona region, (2) F_{int} that represents the excess free energy of the corona-core

interface, and (3) F_{core} responsible for the extension of the core chains.[28, 29, 5, 30] Thus, it can be written as:

$$\begin{aligned} F &= F_{corona} + F_{int} + F_{core} \\ &= C_1 P^{3/2} + C_2 (\frac{N_{ionic}\nu}{\phi})^{2/3} P^{2/3} \gamma + C_3 (N_{ionic}\nu)^{-1/3} \phi^{-2/3} P^{5/3} \end{aligned} \tag{6.7}$$

where ν is the average volume per charged monomer unit, P is the aggregation number, and C_i are coefficients. $C_1 = ln[(R+H)/R]$, where R is the size of the core and H is the thickness of the corona. In our case, C_1 is close to 0.35, and C_2 is estimated to be $4\pi^{1/3}3^{2/3} = 4.84$. The first and the third terms are of the same order, but usually the third one is ignored in dilute micelle solutions. The minimization of the free energy with respect to P leading to the scaling law for PEC micelles in the absence of salt: the equilibrium properties of the PEC micelles are characterized by the aggregation number P_0, core radius R_0, core complex density ϕ_0, and core-solvent interfacial tension γ_0. Thus, the aggregation number, P_{eq}, and core radius, R_{eq}, of PEC micelles at equilibrium are given by:

$$R_{eq} \simeq \gamma^{2/5} (N_{ionic}\nu/\phi)^{3/5} \tag{6.8}$$

$$P_{eq} \simeq \gamma^{6/5} (N_{ionic}\nu/\phi)^{4/5} \tag{6.9}$$

6.3.5 Dissociation kinetics

Step 1: Micelle Swelling. As aforementioned, in sharp contrast to nonionic polymer micelles, PEC micelles possess a water-rich core where oppositely charged polymers are complexed via ionic interactions. The core-solvent interfacial tension and water fraction are subject to change with the surroundings. The addition of salt leads to the decrease of the Debye screening length, κ^{-1}, as $\kappa^{-1} = (8\pi l_B N_A I)^{-1/2}$, where l_B is the Bjerrum length, N_A is the Avogadro constant, and I is the ionic strength expressed in molar (M or mol L^{-1}). The salt-induced weakening of the long-range Coulomb interaction between opposite

charges results in the swelling of the polyelectrolyte complex phase in micelle cores, which consequently decreases the density of the core and the complex-solvent interfacial tension. This step is assumed to be fast due to the rapid diffusion of salt ions and characterized by a relaxation time τ_1. The aggregation number of the swelled micelles remain the same as that of the equilibrium micelles in salt-free solutions, $P = P_0$. Thus, the core radius of the swelled micelles, R, can be derived following the relationship, $P_0 N_{ionic} \nu = (3/4)\pi R^3 \phi = (3/4)\pi R_0^3 \phi_0$, and written as

$$R = R_0 (\frac{\phi_0}{\phi})^{1/3} \tag{6.10}$$

Step 2: Micelle Core Fragmentation. Upon the salt jump, the swelled micelles are in a metastable state and evolve into two charge-neutralized aggregates with aggregation numbers P_1 and P_2. The nascent aggregates continues to split until a final aggregate number is reached. We characterize the relaxation time for the chain reaction-like process with $\tau_{2,i}$. Unimer expulsion pathway is favored when P_1 or P_2 equals to 1. However, in the following, we are going to demonstrate that micelle fission is the more effective pathway to reach new equilibrium states with a significant decrease in the aggregation number. This first split reaction is characterized by the relaxation time $\tau_{2,1}$ and is assumed to be rate-limiting. The activation energy is given by:[3, 5]

$$\Delta F = F(P_1) + F(P_2) - F(P) \tag{6.11}$$

The free energy of a micelle can be rewritten as $F(P) = (3/2) P_{eq}^{5/6} P^{2/3} + P^{3/2}$, combing Equation (5) and (7). We define $\Omega \equiv P_1/P$, denoting the amount of the *fissionable* polymer chains. Then, the activation energy can be rewritten as:

$$\Delta F = \frac{3}{2} P_{eq}^{5/6} P^{2/3} [\Omega^{2/3} + (1-\Omega)^{2/3} - 1] + P^{3/2} [\Omega^{3/2} + (1-\Omega)^{3/2} - 1] \tag{6.12}$$

For $\Omega = 1/2$, the activation energy becomes negative when $P > 2P_{eq}$, meaning the micelle

fission is thermodynamically favorable. This may not stand for some cases in which a small perturbation is induced and the aggregation number does not change markedly. However, it certainly holds true in the irreversible salt-induced micelle dissociation experiments here, because P_{eq} is close to zero in most cases. In other words, the first term in Equation 6.12 is negligible, and the second term, which is always negative, reaches its minimum when $\Omega = 1/2$, meaning fission into two equal-sized aggregates is the most efficient way to decrease the free energy. It should be pointed out that, under this analysis, the unimer expulsion mechanism is not entirely excluded but is likely to play a minor role, as pointed out my theories.[5]

Further, in order to relate the fission activation energy with the micelle attributes, we rewrite the free energy into

$$F = C_1 P^{3/2} + 4\pi R^2 \gamma \tag{6.13}$$

Combing Equation 6.8, 6.9, and 6.11, we can get the expression of the fission activation energy, which reads

$$\begin{aligned} \Delta F &= \pi R^2 \gamma + C_1 (2^{-1/2} - 1) P^{3/2} \\ &= [\pi \frac{\gamma_0^{4/5}}{\phi_0^{8/15}} \frac{\gamma}{\phi^{2/3}} - \frac{3C_1}{10} \frac{\gamma_0^{9/5}}{\phi_0^{6/5}}] \nu^{6/5} N_{ionic}^{6/5} \end{aligned} \tag{6.14}$$

The second term in the bracket in negligible compared to the first term. In turn, the relaxation time of micelle core fragmentation can be estimated as

$$\tau_{2,1} \simeq exp(\Delta F) \tag{6.15}$$

Thus, the master equation for the micelle fission relaxation time reads

$$ln\tau_{2,1} \simeq \pi \frac{\gamma_0^{4/5}}{\phi_0^{8/15}} \frac{\gamma}{\phi^{2/3}} \nu^{6/5} N_{ionic}^{6/5} \tag{6.16}$$

The successive fission reactions proceed in an analogous way to the first fission, i.e., the

nascent aggregate splits into two equal-sized smaller aggregates. The interfacial tension coefficient, γ, and core density, ϕ, remain the same since the salt concentration is constant in this process. So, the total relaxation time for the micelle fragmentation is given as

$$ln\tau_2 = [\sum_{i=2}^{\infty} 2^{-i} + 1]\pi \frac{\gamma_0^{4/5}}{\phi_0^{8/15}} \frac{\gamma}{\phi^{2/3}} \nu^{6/5} N_{ionic}^{6/5} \tag{6.17}$$

From Equation 6.15, we can see that the further fission steps follow the same scaling law and their relaxation rates are in a geometric sequence with a common ratio of 1/2. If we consider the fission has infinite steps, the total relaxation time for the further steps, $\sum_{i=2}^{\infty}(1/2)^i \ln \tau_{2,1}$, is estimated to be $\frac{1}{2} \ln \tau_{2,1}$.

Step 3: Micelle Separation. The nascent aggregates from fission are initially in contact, but the coronal chains at the interface tend to stretch into the solvent, which renders the two aggregates drift apart. This process increases the system entropy and the relaxation time, τ_3, is considered negligible.

6.3.6 Effect of salt concentration

In the following, we aim to investigate the dependencies of the relaxation time on salt concentrations, solution temperature, and the length of the charged blocks, and compare our experimental data with theoretical predictions. From Equation 6.15, the scaling law between the relaxation time and salt concentration reads:

$$\ln \tau_2 \approx \frac{\gamma(C_s)}{\phi^{2/3}(C_s)} \tag{6.18}$$

where $\gamma(C_s)$ and $\phi(C_s)$ represent the dependencies of the interfacial tension and core density on the salt concentration, C_s, respectively.

The physics of the polymer complexes in micelle cores can be treated as bulk complexes, although the space-confinement is missing for the bulk. At stoichiometric conditions, the

polyelectrolyte complexes is a ternary system in which water, polyelectrolyte, and salt coexist. Previous efforts to illustrating the role of salt concentration on interfacial tension have been undertaken from experiments, theories, and simulation. For example, Qin et al. derived an analytical expression for the interfacial tension in near-critical regimes written as $\gamma \propto (1 - C_s/C_{cr})^{3/2}$[31]. Rumyantsev and coworkers theoretically predicted that for weakly charged polyelectrolytes, the interfacial tension should follow $\gamma \propto C_s^{-2}$[32]. Yet, a universal expression is still lacking. Here, we adopt the expression reported by Spruijt et al. because of the similarities between their polyelectrolytes and ours[33]. It reads as $\gamma \propto \left(\frac{1}{\sqrt{C_s}} - \frac{1}{\sqrt{C_{cr}}}\right)^{3/2}$. Further, the dependence of the complex density on the salt concentration is approximated to be $\phi \propto C_s^{-1}$ according to the data reported in experiment and computer simulations[34]. Thus, the relaxation time scales with salt concentration in a function of

$$\ln \tau_2 \propto C_s^{2/3}(\frac{1}{\sqrt{C_s}} - \frac{1}{\sqrt{C_{cr}}})^{3/2} \tag{6.19}$$

Using this relationship, we fit the micelle relaxation rates at 4 different salt concentrations, and the results are shown in Figure 6.6. The fit is reasonably well (with a squared residual of 0.06).

6.3.7 Effect of temperature

Solution temperature has influence on both the core-solvent interfacial tension and the core density. Although the term of temperature is absent in Equation 6.17, according to the Debye-Hückel theory, the interaction strength of oppositely charged blocks is a function of temperature. The interaction strength α is defined as $\alpha \equiv \left(16\pi^2/3\right)\left(l_B^3/v\right)^{1/2} \propto l_B^{3/2}$, where $l_B \equiv e^2/4\pi\varepsilon_0\varepsilon_r k_B T$ is the Bjerrum length. The interfacial tension scales with the interaction strength following a relationship of $\gamma \propto \alpha^{1/2} \propto l_B^{3/4} \propto T^{-3/4}$. The core density is viewed as constant in the temperature range studied here, which is supported by the evidence that the micelles remained the same size over the temperature range. Thus, we can derive the

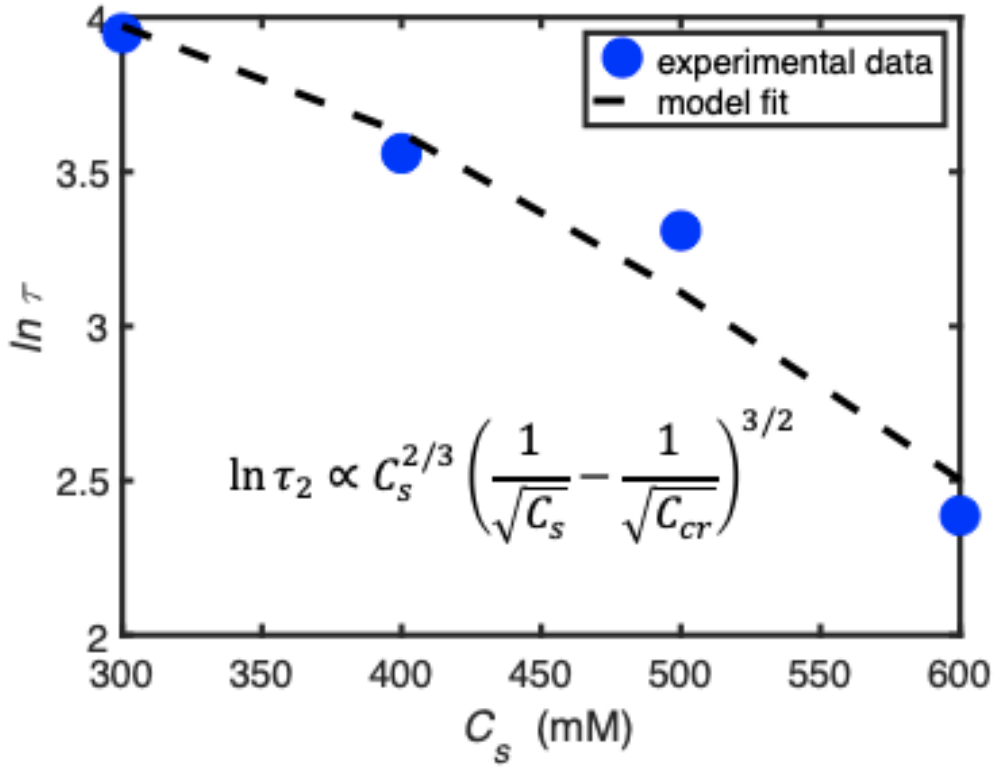

Figure 6.6: Micelle fission rate as a function of salt concentration. Blue circles corresponding to experimental data obtained from time-dependent light scattering. Black dash lines shows the theoretical predictions from the proposed model.

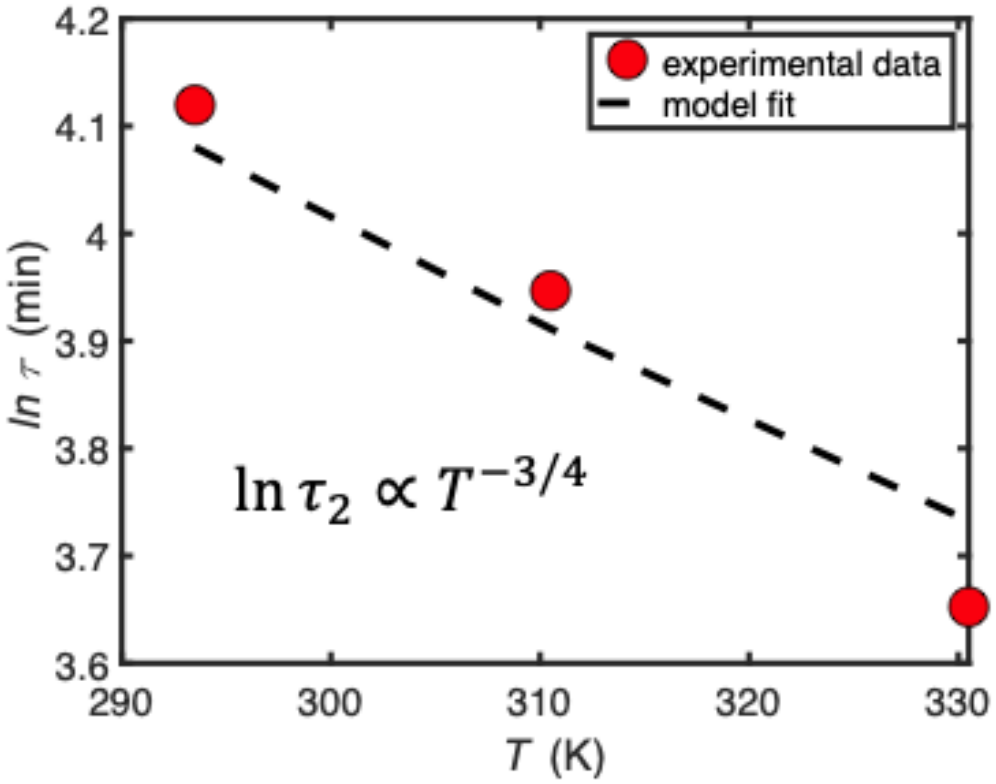

Figure 6.7: Micelle fission rate as a function of temperature. Red circles correspond to the experimental data from the time-dependent light scattering experiments. Black dashes shows the theoretical prediction.

temperature dependence of micelle fission rate as $\ln \tau_2 \propto T^{-3/4}$. The expression fits the experimental data well with a squared residual of 0.01, as shown in Figure 6.7.

The temperature dependence of micelle dissociation rates can be described by the Arrhenius equation. As shown in Figure 6.8, the natural logarithm of the micelle dissociation rates is plotted as a function of inverse absolute temperature. In such a plot, the slope of a best-fit line to the data is proportional to the activation energy required to reach the transition state from the ground state. Linear fit to the data points yields an activation energy E_a of 10.16 kJ mol^{-1}.

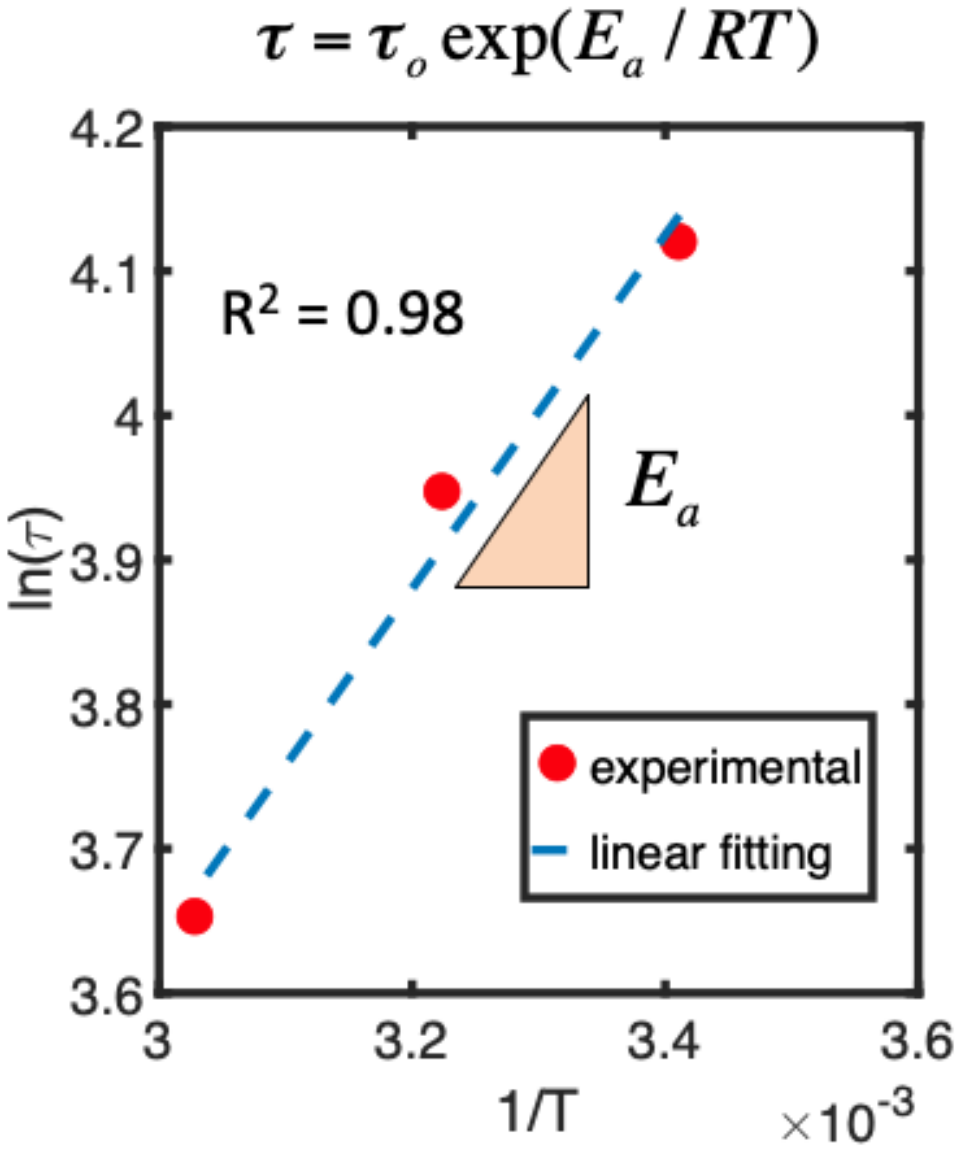

Figure 6.8: Arrhenius plot of the relaxation time τ for the dissociation of micelles.

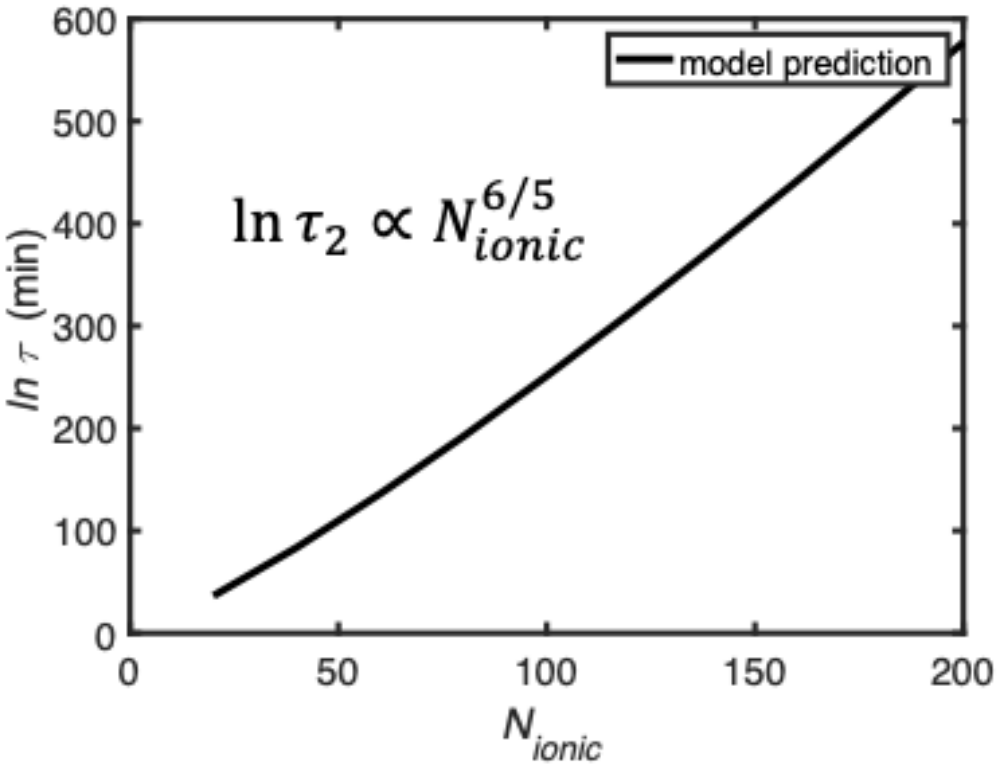

Figure 6.9: Theoretical prediction of the micelle fission rate as a function of ionic block length.

6.3.8 Effect of charged block length

From Equation 6.17, the dependence of the relaxation time on the length of ionic blocks reads

$$\ln \tau_2 \propto N_{ionic}^{6/5} \tag{6.20}$$

The dependence of micelle fission rate on ionic block length is drawn in Figure 6.9. We do not have experimental data to check this prediction so far. Such effort will be put in the future work.

6.4 Concluding Remarks

In this chapter, the mechanism of dissociation kinetics in polyelectrolyte complex micelles is demonstrated by a combination of light scattering experiments and theoretical modeling.

The theoretical frame for PEC micelle dissociation is built upon scaling law of PEC micelles, kinetic theories for amphiphilic block copolymers, and theories on polyelectrolyte complexes. Salt-induced micelle disassembly is characterized as a three-staged process. First, upon salt addition micelles immediately swell because of the weakening of the electrostatic interaction. Second, micelles undergo a successive chain reaction where micelle cores tend to fragment into two charge-balanced aggregates. Theoretical predictions show that splitting into two equal-sized aggregates is the most efficient way to reach new equilibrium states, which leads to the sharp drop of the scattering intensity, as we observe in the time-dependent light scattering experiments. Third, the nascent aggregates separate from each other.

Moreover, we illustrate the dependencies of micelle fission relaxation rates on salt concentration, temperature, and charged block length. By taking into account the recent advances about the relationship between interfacial tension and salt concentration/temperature in polyelectrolyte complexes, we derive an analytical expression for fission relaxation rates. The comparison of the predictions with our experimental data is in good agreement. We also make a prediction on the scaling law between the relaxation rate and the ionic block as $\ln \tau \propto N_{ionic}^{6/5}$, which can be further experimentally examined. We anticipate that these findings will provide insights on the fundamental understanding of micelle dissociation and encourage future effort on the kinetics of polyelectrolyte-based self-assemblies.[35]

References

[1] Ilja K Voets, Arie De Keizer, and Martien A Cohen Stuart. Complex coacervate core micelles. *Adv. Colloid Interface Sci.*, 147-148:300–318, 2009.

[2] E. A. G. Aniansson and S. N. Wall. Kinetics of step-wise micelle association. Correction and improvement. *J. Phys. Chem.*, 79(8):857–858, 1975.

[3] A. Halperin and S. Alexander. Polymeric Micelles: Their relaxation kinetics. *Macromolecules*, 22:2403–2412, 1989.

[4] F. J. Esselink, E. Dormidontova, and G. Hadziioannou. Evolution of block copolymer micellar size and structure evidenced with cryo electron microscopy. *Macromolecules*, 31:2925–2932, 1998.

[5] Elena E. Dormidontova. Micellization kinetics in block copolymer solutions: scaling model. *Macromolecules*, 32:7630–7644, 1999.

[6] Susan E. Burke and Adi Eisenberg. Kinetics and mechanisms of the sphere-to-rod and rod-to-sphere transitions in the ternary system PS310-b-PAA52/dioxane/water. *Langmuir*, 17:6705–6714, 2001.

[7] Y. Rharbi. Fusion and fragmentation dynamics at equilibrium in triblock copolymer micelles. *Macromolecules*, 45:9823–9826, 2012.

[8] Hao Wu, Jeffrey Ting, Thomas Weiss, Matthew Tirrell, Hao Wu, Jeffrey M Ting, Thomas M Weiss, and Matthew V Tirrell. Interparticle Interactions in Dilute Solutions of Polyelectrolyte Complex Micelles Interparticle Interactions in Dilute Solutions of Polyelectrolyte Complex Micelles. *ACS Macro Lett.*, 8:819–825, 2019.

[9] H Wu, Jeffrey M. Ting, and Tirrell V. Matthew. Mechanism of Chain Exchange in Polyelectrolyte Complex Micelles. .

[10] Jeffrey M. Ting, Hao Wu, Abraham Herzog-Arbeitman, Samanvaya Srivastava, and Matthew V. Tirrell. Synthesis and Assembly of Designer Styrenic Diblock Polyelectrolytes. *ACS Macro Lett.*, 7(6):726–733, 2018.

[11] Hao Wu, Jeffrey M. Ting, Olivia Werba, Siqi Meng, and Matthew V. Tirrell. Non-equilibrium phenomena and kinetic pathways in self-assembled polyelectrolyte complexes. *J. Chem. Phys.*, 149:163330, 2018.

[12] Emi Haladjova, Grigoris Mountrichas, Stergios Pispas, and Stanislav Rangelov.

Poly(vinyl benzyl trimethylammonium chloride) Homo and Block Copolymers Complexation with DNA. *J. Phys. Chem. B*, 120(9):2586–2595, 2016.

[13] Alexander E Marras, Jeffrey R Vieregg, Jeffrey M Ting, Jack D Rubien, and Matthew V Tirrell. Polyelectrolyte Complexation of Oligonucleotides by Charged Hydrophobic Neutral Hydrophilic. *Polymers*, 11:83, 2019.

[14] Igor L. Smolsky, Ping Liu, Marc Niebuhr, Kazuki Ito, Thomas M. Weiss, and Hiro Tsuruta. Biological small-angle X-ray scattering facility at the Stanford Synchrotron Radiation Laboratory. *J. Appl. Crystallogr.*, 40:453–458, 2007.

[15] Jan Skov Pedersen. Structure factors effects in small-angle scattering from block copolymer micelles and star polymers. *J. Phys. Chem.*, 114:2839–2846, 2001.

[16] Jan Skov Pedersen and Carsten Svaneborg. Scattering from block copolymer micelles. *Curr. Opin. Colloid Interface Sci.*, 7:158–166, 2002.

[17] Jan Skov Pedersen, Carsten Svaneborg, Kristoffer Almdal, Ian W Hamley, and Ron N Young. A Small-Angle Neutron and X-ray Contrast Variation Scattering Study of the Structure of Block Copolymer Micelles: Corona Shape and Excluded Volume Interactions. *Macromolecules*, 36:416–433, 2003.

[18] Marc Lemmers, Ilja K. Voets, Martien a. Cohen Stuart, and Jasper Van der Gucht. Transient network topology of interconnected polyelectrolyte complex micelles. *Soft Matter*, 7:1378, 2011.

[19] Melvin Avrami. Kinetics of phase change. II Transformation-time relations for random distribution of nuclei. *J. Chem. Phys.*, 8:212–224, 1940.

[20] Megan L. Ruegg, Amish J. Patel, Suresh Narayanan, Alec R. Sandy, Simon G.J. Mochrie, Hiroshi Watanabe, and Nitash P. Balsara. Condensed exponential correla-

tion functions in multicomponent polymer blends measured by x-ray photon correlation spectroscopy. *Macromolecules*, 39:8822–8831, 2006.

[21] Luca Cipelletti, S. Manley, R. C. Ball, and D. A. Weitz. Universal Aging Features in the Restructuring of Fractal Colloidal Gels. *Phys. Rev. Lett.*, 84:2275–2278, 2000.

[22] T. Abraham, S. Giasson, J. F. Gohy, R. Jérôme, B. Müller, and M. Stamm. Adsorption kinetics of a hydrophobic-hydrophilic diblock polyelectrolyte at the solid-aqueous solution interface: a slow birth and fast growth process. *Macromolecules*, 33(16):6051–6059, 2000.

[23] Adriana M. Mihut, Arnaud Chiche, Markus Drechsler, Holger Schmalz, Emanuela Di Cola, Georg Krausch, and Matthias Ballauff. Crystallization-induced switching of the morphology of poly(ethylene oxide)-block-polybutadiene micelles. *Soft Matter*, 5(1):208–213, 2009.

[24] Yueh Lin Loo, Richard A. Register, Anthony J. Ryan, and Gregory T. Dee. Polymer crystallization confined in one, two, or three dimensions. *Macromolecules*, 34:8968–8977, 2001.

[25] Jun Ting Xu, J. Patrick A. Fairclough, Shao Min Mai, Anthony J. Ryan, and Chiraporn Chaibundit. Isothermal crystallization kinetics and melting behavior of poly(oxyethylene)-b-poly(oxybutylene)/poly(oxybutylene) blends. *Macromolecules*, 35:6937–6945, 2002.

[26] Reidar Lund, Lutz Willner, J??rg Stellbrink, Peter Lindner, and Dieter Richter. Logarithmic chain-exchange kinetics of diblock copolymer micelles. *Phys. Rev. Lett.*, 96(6):1–4, 2006.

[27] Luciana Meli, Jessica M. Santiago, and Timothy P. Lodge. Path-dependent morphology and relaxation kinetics of highly amphiphilic diblock copolymer micelles in ionic liquids. *Macromolecules*, 43:2018–2027, 2010.

[28] T M Birshtein and E B Zhulina. Scaling theory of supermolecular structures in block copolymer-solvent systems: 1. Model of micellar structures. 30, 1989.

[29] A. Halperin. Polymeric Micelles: A Star Model. *Macromolecules*, 20:2943–2946, 1987.

[30] Artem M Rumyantsev, Ekaterina B Zhulina, and Oleg V Borisov. Scaling Theory of Complex Coacervate Core Micelles. *ACS Macro Letters*, 7:811–816, 2018.

[31] Jian Qin, Dimitrios Priftis, Robert Farina, Sarah L. Perry, Lorraine Leon, Jonathan Whitmer, Kyle Hoffmann, Matthew Tirrell, and Juan J. De Pablo. Interfacial tension of polyelectrolyte complex coacervate phases. *ACS Macro Lett.*, 3:565–568, 2014.

[32] Artem M. Rumyantsev, Ekaterina B. Zhulina, and Oleg V. Borisov. Complex Coacervate of Weakly Charged Polyelectrolytes: Diagram of States. *Macromolecules*, 51:3788–3801, 2018.

[33] Evan Spruijt, Joris Sprakel, Martien A. Cohen Stuart, and Jasper Van Der Gucht. Interfacial tension between a complex coacervate phase and its coexisting aqueous phase. *Soft Matter*, 6:172–178, 2009.

[34] Lu Li, Samanvaya Srivastava, Marat Andreev, Amanda B. Marciel, Juan J. de Pablo, and Matthew V. Tirrell. Phase Behavior and Salt Partitioning in Polyelectrolyte Complex Coacervates. *Macromolecules*, 51:2988–2995, 2018.

[35] Jingyan Zhang, Sangui Chen, Zhiyuan Zhu, and Shiyong Liu. Stopped-flow kinetic studies of the formation and disintegration of polyion complex micelles in aqueous solution. *Phys. Chem. Chem. Phys.*, 16:117–127, 2014.

CHAPTER 7

SUMMARY AND OUTLOOK

In summary, in this thesis, we explore the physics of polyelectrolyte complexes via synchrotron radiation, electron imaging, and modeling. We believe the contributions of this thesis come from the following aspects: (1) this thesis develops a new model system for polyelectrolyte complexes study; (2) this thesis comes up with a facile way to getting access to metastable structures in polyelectrolyte complexes at nonequlibrium states; (3) this thesis provides new paradigm in dynamics of polyelectrolyte complexes in nonequilibrium states; (4) this thesis build an analytical framework that can be used to demonstrate the particle-particle interactions in polyelectrolyte-based dilute solutions; (5) this thesis proposes a feasible way to probing the molecular exchange in polyelectrolyte complex micelles by employing time-resolved small-angle neutron scattering; and (6) this thesis comes up with a solution that can address challenges in the observation of superfast kinetic processes in multi-component systems.

In **Chapter 2** we focus mainly on polyelectrolyte complexes that are kinetically trapped at non-equilibrium states. A combination of time-resolved dynamic light scattering, small angle X-ray scattering (SAXS), and cryogenic transmission electron microscopy (Cryo-TEM) was employed here to investigate the internal structures and morphological evolution of non-equilibrium aggregates forming from a pair of two strong block polyelectrolytes over wide time and length scales. The role of formation pathways of electrostatically driven aggregates was assessed using two processing protocols: direct dissolution and salt annealing. The former led to thermodynamically stable products, while the latter resulted in kinetically trapped transient structures. After adding salt, the metastable structures gradually transformed into stable products. Cryo-TEM images showed the interconnected irregular morphologies of the aggregates, and SAXS data revealed the presence of fuzzy globular complexes with $R_g \propto$ 10 nm within them. A two-step process in the time-dependent structural transformation was found and characterized by a fast breakdown of interconnected transient aggregates followed by a slow redistribution of the incipient individual electrostatic assemblies. Furthermore, the prolonged aggregate disintegration process fitting to a stretched exponential

function unveiled the broad relaxation distribution and significant structural heterogeneity in these polyelectrolyte complex nanoaggregates. This findings brings new insight into the comprehension of non-equilibrium phenomena in self-assembled electrostatic assemblies and represents a first step toward constructing far-from-equilibrium polyelectrolyte complexes *de novo* for future applications.

In **Chapter 3** we investigate the interparticle interaction among PEC micelles in dilute solutions. Emphasis is given to a detailed characterization of PEC micelles in dilute solutions including their internal structures and the determination of the interparticle interactions. The polymer concentration ranges from 0.1 wt % to 0.5 wt %, a regime where micelle-micelle interactions are infrequent. We employ synchrotron small-angle X-ray scattering (SAXS) to simultaneously probe the morphology, internal structure, and radius of gyration (R_g) of the self-assemblies formed by charged diblock polyelectrolytes and homopolyelectrolytes. The emerging appearance of the structure factor in SAXS profiles with the increasing polymer concentration demonstrates the presence of the repulsive intermicellar correlations, which is further confirmed by the differences between the reciprocal R_g estimated by Guinier approximation and the real space R_g determined by pair distribution functions. We find that the soft corona chains tethered on the surface of phase-separated complex domains are compressed when micelles come close, at which point a hard-sphere interaction takes over. These findings contribute to the fundamental understanding of the structure and space-filling constraints in the complexation-driven self-assemblies and advance the rational design of cationic polymer-based non-viral gene delivery vectors.

Based on the analytical framework built in this study, we envision similar work can be implemented on other polyelectrolyte-based systems. On interesting domain is about the influence of electrostatic forces on strongly interacting polyelectrolyte micelles whose core is consisted of hydrophobic blocks and shell is constituted by positively or negatively charged polyelectrolytes. unlike PEC micelles where the oppositely charged groups are almost neutralized by each other, these polyelectrolyte-based micelles have net charges surrounding the

surface, creating an electrostatic field. When they approach, these micelles will encounter influence from both Coulombic interaction and steric hindrance, the interplay between which will create some unique characteristics. Another related direction is to study the ion distribution around polyelectrolyte-based self-assemblies. Heavy metal elements, e.g. yttrium, can be used to obtain electron contrast from carbon- and hydrogen-based light elements in polymers.

In **Chapter 4** we investigate the kinetic pathways of the formation of PEC micelles from oppositely charged polyelectrolytes. By employing time-resolved SAXS with a millisecond temporal resolution, we monitor the micelle creation and growth. The evolution of the R_gs of the polymer aggregates denotes that the micelle fusion mechanism plays a minimal role in PEC micelle formation, which is a major pathway in the formation of surfactant micelles and amphiphilic block copolymer micelles. By combing theoretical examination, it is suggested that the formation of PEC micelles proceeds via a three-step process: first, oppositely charged polyelectrolyte chains pair to form neutral culsters; second, these nascent clusters form larger micellar aggregates; and third, micelles continue to grow by merging clusters. This work has demonstrated the structural evolution and kinetic pathways in the process of PEC micelle formation, which provides useful insights for the design of ideal polyelectrolyte-based nanocarriers.

We believe that this work exemplifies a pioneering work in many related fields where fast formation stages are involved. Based on these results, we anticipate that many other studies can be further explored. First, the initial stage earlier than 100 ms can be reached by fine-tuning the instrumental setup. The early polyelectrolyte clustering and aggregation should happen in this time period. Monitoring the structural evolution will reveal the exact kinetic pathways of the initial formation of polyelectrolyte aggregates. Second, the dependency of the kinetic rate on many molecular attributes can be further investigated, including polymer block length, type of the charged groups, hydrophobicity of the polyelectrolyte backbones, and the ratio between the neutral block and the charged blocks. Other external parameters,

such as solution temperature and salt salinity, can also be studied. Last but not least, similar experiments should be done on polyelectrolyte complex micelles containing nucleic acids with bioactivities, such that the knowledge extracted from this research can be translated and extended directly to practical applications.

In **Chapter 5** we use time-resolved SANS to study the chain exchange kinetics in PEC micelles near equilibrium states. The effects of temperature, salinity, and ionic strength are investigated in two polyelectrolyte complex micelle systems. Results shown that, even at high temperature (70 ^{o}C) and high salt concentration (up to 2 M), no significant evidence of molecular exchange is observed. It is speculated that these micelles formed by strong ionic strength do not expel polyelectrolyte chains into solutions once they are in equilibrium states. This is in contrast to micelles of amphiphilic molecules. This work may reveal that polyelectrolyte-based micelles are super stable in aqueous solutions.

We believe that many challenges still remain in this field. First, better PEC micelle systems with more tunable features are needed. More deuterated diblock copolymer polyelectrolytes should be made to achieve better neutron contrast. Second, experimental methods that could unlock the molecular exchange of PEC micelles are unknown. Other salt types and salt concentration can be explored. Third, a satisfying physical model that can describe the dynamics of the complexes in PEC micelle cores are still lacking. This is partly owing to the incomplete understanding of the dynamics of bulk polyelectrolyte complexes. Last but not least, one can design proper experiemnts to demonstrate the affecting factors on the exchange rate, some of which should include polymer block length, charge density, and salt concentration.

In **Chapter 6** we study the mechanism of dissociation kinetics of PEC micelles. Using salt-jump time-dependent light scattering, the pathway of self-assembly dissociation is observed in polyelectrolyte complex micelles that have complex cores and neutral coronas. The micelle dissociation kinetics is considered as a three-staged fission process, which is in good agreement with the scattering data. By applying kinetic theories of amphiphilic block

copolymer micelles in polyelectrolyte complexation-driven micelles, we derive an analytical expression to illustrate fission relaxation rates as a function of solvent temperature, salt concentration, and the length of the charged polymer blocks. The theoretical predictions are in line with the experimental data from light scattering experiments. This Chapter experimentally demonstrates the relaxation kinetics of polyelectrolyte complex micelle dissociation and theoretically illustrates the underlying mechanism governing the dissociation kinetics. It is anticipated that these findings can be generalized to other electrostatic interaction-driven self-assemblies to better understand the relationship between the kinetics of dissociation, constituent polymer properties, and environmental parameters.

Further works in this field can come from a variety of aspects. First, structural evolution by small-angle X-ray or neutron scattering is feasible and desirable. By virtue of using stopped-flow devices, it is possible to capture the early stages of micelle dissociation, such as the fast micelle swelling step. The size evolution of different parts of the micelles may be revealed as well. Second, the dependency of dissociation rate on various parameters can be explored in a more comprehensive way. For example, polyelectrolytes with symmetric architectures and various block lengths can be synthesized and employed to form PEC micelles, such that the analytical relationship between the dissociation rate and block length can be experimentally examined.

APPENDIX A

APPENDIX

A.1 Synthesis of deuterated materials

The synthesis of deuterated monomers were led by our collaborators, T. Li and K. Hong, at Oak Ridge National Laboratory.

A.1.1 Synthesis of 1-(2-bromoethyl)-4-(chloromethyl)benzene-d_8

Anti-Markovnikov hydrobromination of styrene-d_8 was performed to yield 2-bromoethyl benzene-d_8. Into a round bottom flask, n-hexanes (250 mL) was added and purged with air for 1 hour. Then, styrene-d_8 (10.0 g, 89.1 mmol) and hydrogen bromide solution (32.0 g) were added. After stirring at 0 ^{o}C for 30 minutes, the solvent was removed, and the crude product was purified with column chromatography (hexanes) to give a colorless liquid as the product (13.7 g, 81% yield). ^{13}C $\{^{1}$H$\}$ NMR ($CDCl_3$): σ 138.83, 128.47 (t, J_{CD} =11.93 Hz), 128.20 (t, J_{CD} =12.34 Hz), 126.57 (t, J_{CD} =24.32 Hz), 39.28 (s, =CHD-, showed the added H from addition of HBr), 38.95 (t, J_{CD} =20.03 Hz, =CHD-), 32.58 (p, J_{CD} =23.37 Hz). See ^{13}C NMR spectrum in Figure A.1.

Then, 2-bromoethylbenzene-d_8 (10.0 g, 51.8 mmol) and chloromethyl methyl ether (16.7 g, 207.1 mmol) were dissolved in anhydrous dichloromethane (450 mL) under an inert atmosphere and cooled in an ice bath. To the stirred solution, aluminum chloride (5.45 g, 40.9 mmol) was added in small portions. The reaction was warmed to room temperature and monitored with TLC. After 2 hours, deionized water was added to quench the unreacted chloromethyl methyl ether (compared with 15% NaOH solution, quenching with deionized water needs longer time), followed by the extraction with dichloromethane (3 $\times$ 100 mL). Sequentially, The combined organic phases were dried over anhydrous $MgSO_4$, and the solvent was removed to afford a brown oil. Final purification was achieved by the column chromatography (hexanes) to yield a white solid as the pure monomer (3.36 g, 27% yield, with 72.5% *para*-CH_2-Cl and 5.9% *para*-CH_2-Br). ^{13}C$\{^{1}$H$\}$ NMR ($CDCl_3$): σ 139.42 (s, *meta*-product), 139.11 (s, *para*-product), 137.84 (s, *meta*-product), 136.46 (s, *ortho*-product), 136.17 (s,

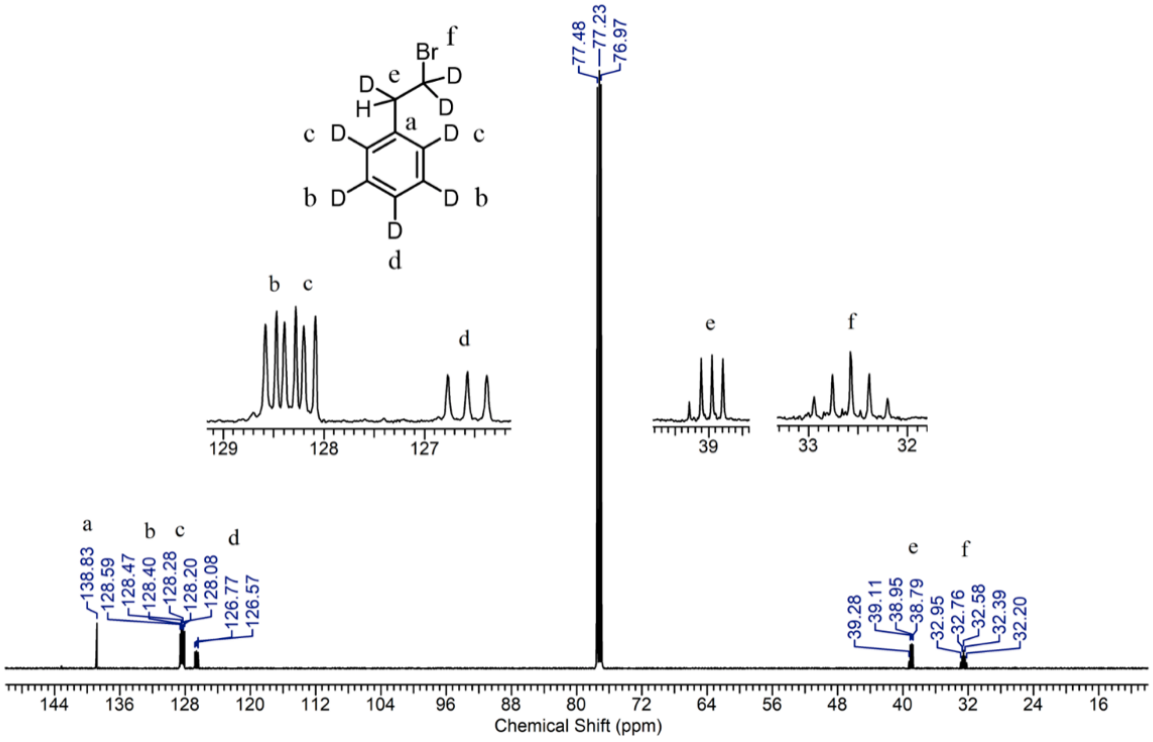

Figure A.1: ^{13}C NMR of (2-bromoethylbenzene)-d_8.

para-product), 135.70 (s, *ortho*-product), 128.65 (m, *para*- and *meta*-product), 126.93 (t, J_{CD} =24.32 Hz, *ortho*-product), 46.21 (s, *meta*-CH_2-Cl), 46.10 (s, *para*-CH_2-Cl), 44.22 (s, *ortho*-CH_2-Cl), 38.84 (s, =CHD-), 38.51 (t, J_{CD} =20.03 Hz, =CHD-), 33.45 (s, *meta*-CH_2-Br), 33.39 (s, *para*-CH_2-Br), 32.32 (p, J_{CD} =23.13 Hz). See ^{13}C NMR spectrum in Figure A.2.

A.1.2 Synthesis of 1-(chloromethyl)-4-vinylbenzene-d_7

An ethyl ether anhydrous suspension (220 mL) of potassium t-butoxide (1.8 g, 16.0 mmol) was prepared under an inert atmosphere. Into the suspension, *tert*-butanol (4.5 g, 60.7 mmol) was injected. After cooled in an ice bath, the solid of 1-(2-bromoethyl)-4-(chloromethyl) benzene-d_7 (3.0 g, 12.5 mmol) was added. Then, the reaction was stirred at room temperature for 5 hours and quenched with deionized water. The organic phase from the reaction mixture was collected, and the water layer was washed with ethyl ether (3 × 100 mL). The

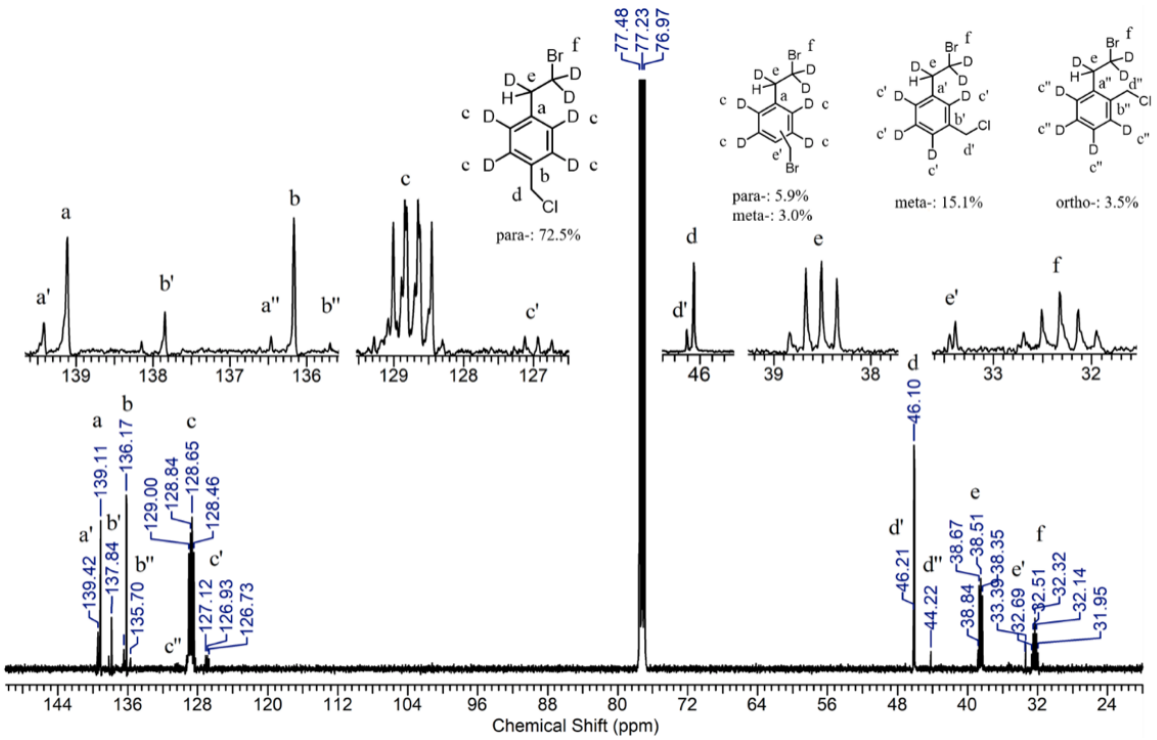

Figure A.2: ^{13}C1H NMR of 1-(2-bromoethyl)-4-(chloromethyl)benzene-d_7 (*para*-CH_2X: 78.4%).

combined ether was dried with anhydrous $MgSO_4$ and removed under vacuum to produce the crude product. The purification was performed with column chromatography (hexanes to DCM) to obtain a colorless liquid (1.5 g, 75% yield). 2,6-Di-*tert*-butyl-4-methylphenol (BHT) was added, and the product was kept in a freezer for the long-term storage. ^{13}C{^{1}H} NMR ($CDCl_3$): σ 151.71 (s, BHT), 137.70 (s, *para*-product), 136.90 (s, *para*-product), 136.13 (s, =CHD-), 135.99 (s, BHT), 125.72 (s, BHT), 135.80 (t, J_{CD} =23.37 Hz, =CHD-), 128.61 (t, J_{CD} =24.32 Hz), 126.29 (t, J_{CD} =24.32 Hz), 114.07 (t, J_{CD} =24.08 Hz), 46.27 (s, *meta*-CH_2-Cl), 46.18 (s, *para*-CH_2-Cl), 44.44 (s, *ortho*-CH_2-Cl), 34.43 (s, BHT), 30.52 (s, BHT), 21.40 (s, BHT). 13C NMR spectrum showed that the degree of deuteriation in =CHD- increased from statistical 50% in 1-(2-bromoethyl)-4-(chloromethyl)benzene-d_7 to 88% in 1-(chloromethyl)-4-vinylbenzene-d_7 during the reaction. See ^{13}C NMR spectrum in Figure A.3.

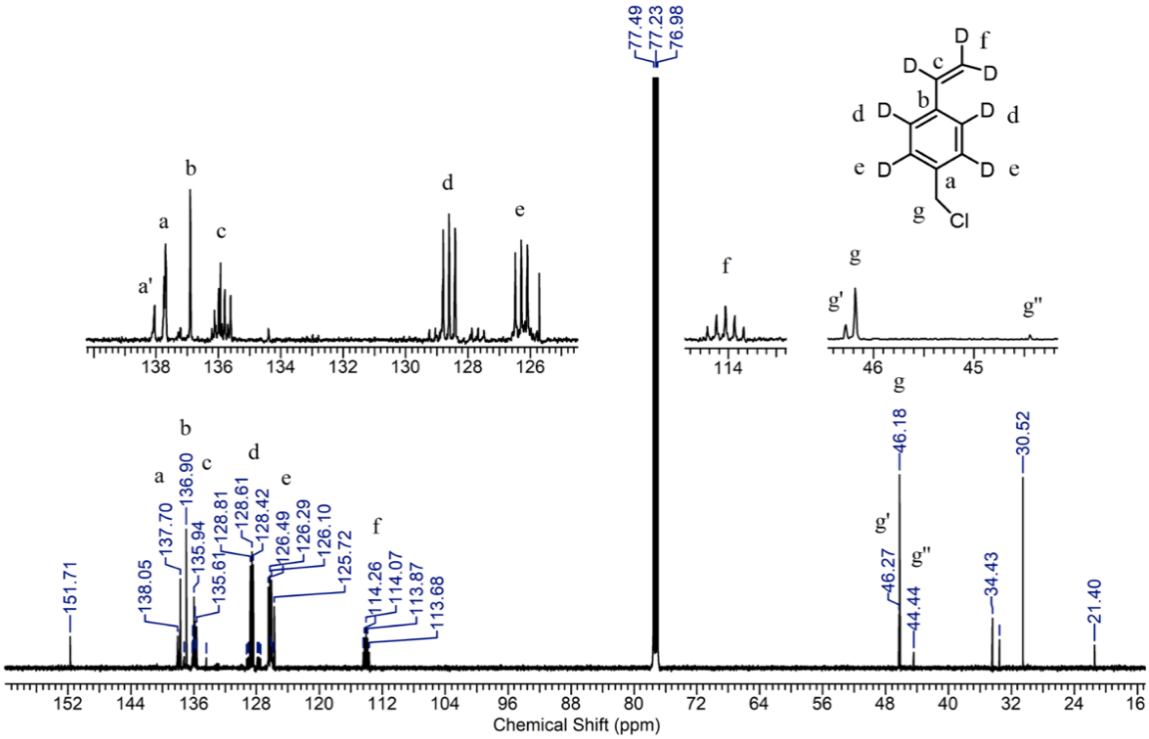

Figure A.3: $^{13}C\{1H\}$ NMR of 1-(chloromethyl)-4-vinylbenzene-d_7 (g: *para*-CH_2Cl; g:*meta*–CH_2Cl; g: *ortho*-CH_2Cl). Unlabeled peaks are signals from *meta*- and *ortho*-product (σ 144 to 104), and BHT.

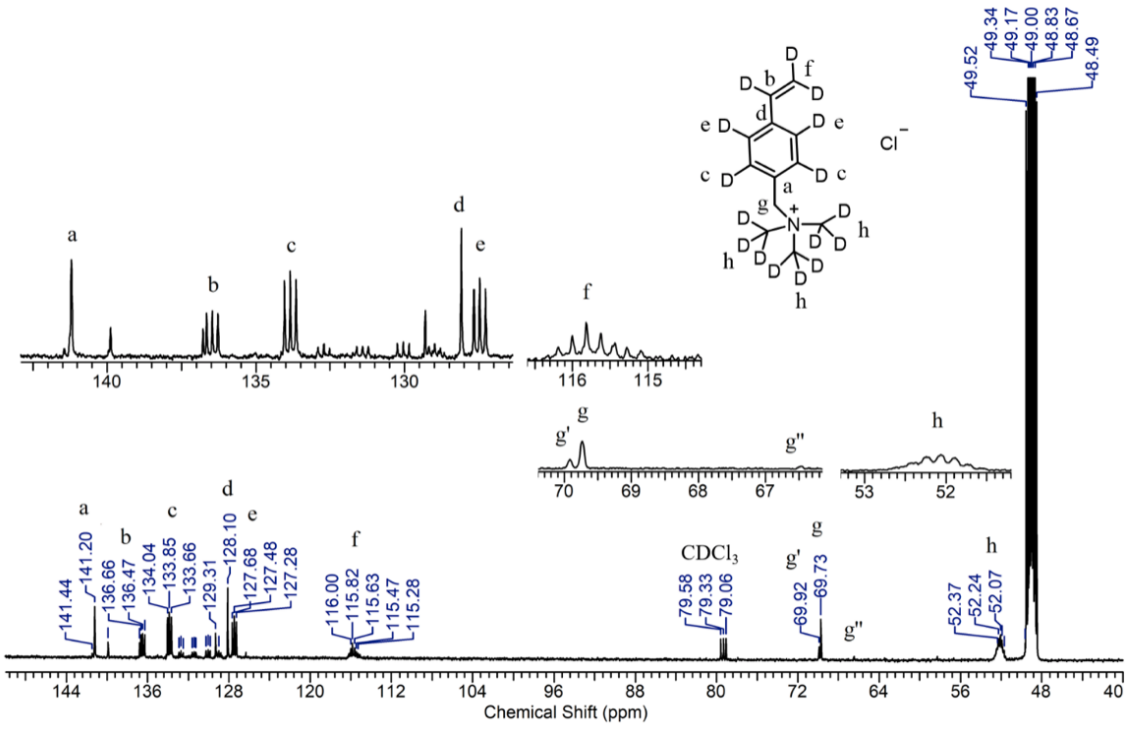

Figure A.4: ^{13}C NMR of (vinylbenzyl)trimethylammonium chloride-d_{16} (*para*-CH_2Cl: 78.4%). Unlabeled peaks are signals from *meta*- and *ortho*-product (σ 144 to 104).

A.1.3 Synthesis of (vinylbenzyl)trimethylammonium chloride-d_{16}

In a typical reaction, an excess amount of trimethylamine-d_9 (TMA-d_9) (2.0 g, 29.8 mmol) was dissolved in ethanol (200 mL). Then, 1-(chloromethyl)-4-vinylbenzene-d_7 (1.5 g, 9.4 mmol) was added in the above solution. After heated at 40 oC for 12 hours, the solvent and unreacted TMA-d_9 were removed under vacuum, and the product yielded a gel. The gel was then dissolved by dichloromethane and precipitated into cold ethyl ether to obtain a white solid as the product (1.4 g, 65% yield). ^{13}C{1H} NMR (methanol-d_4 and $CDCl_3$): σ 141.20 (s, *para*-product), 136.78 (s, =CHD-), 136.47 (t, J_{CD} =23.84 Hz, =CHD-), 133.85 (t, J_{CD} =24.32 Hz), 128.10 (s, *para*-product), 127.48 (t, J_{CD} =24.80 Hz), 115.82 (m), 69.92 (s, *meta*-CH_2-Cl), 69.73 (s, *para*-CH_2-Cl), 66.5 (s, *ortho*-CH_2-Cl), 52.07 (m, -$N^+(CD_3)_3$). See ^{13}C NMR spectrum in Figure A.4.

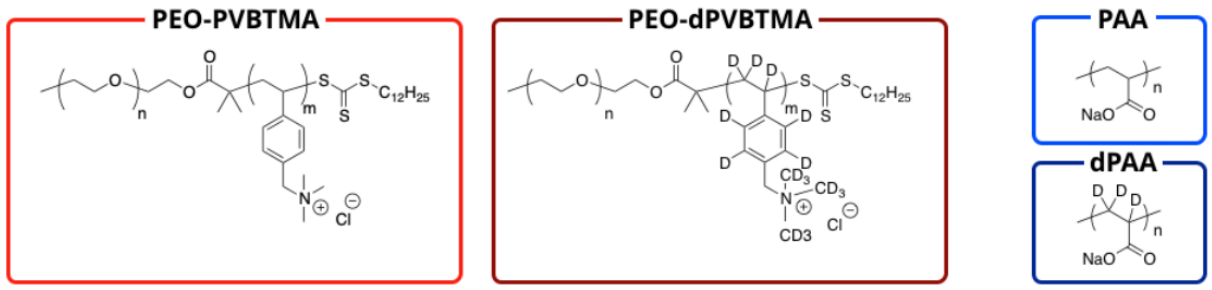

Figure X. Summary of hydrogenated and deuterated polymers in this study.

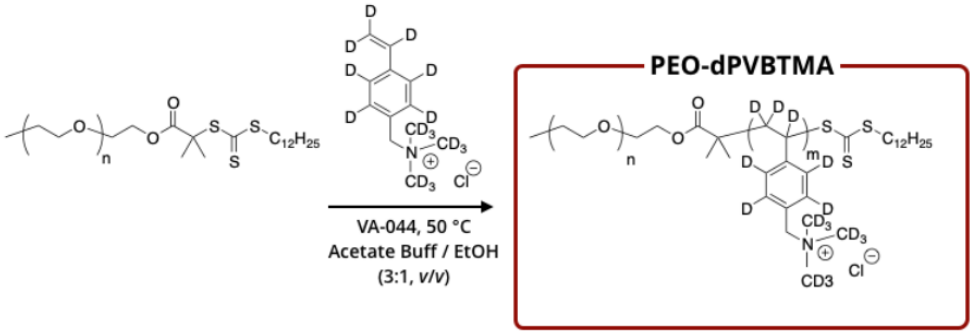

Figure A.5: Summary of hydrogenated and deuterated polymers in this study.

A.1.4 Synthesis of deuterated polyelectrolytes

Deuterated polymers were synthesized by aqueous reversible addition-fragmentation chain transfer (RAFT) polymerization using VA-044 thermal initiator, poly(ethylene oxide) macromolecular chain-transfer agent (PEO-CTA; M_n = 10,000 g mol^{-1}), and deuterated VBTMA monomer prepared above. As an example, deuterated PVBTMA (*d*-PVBTMA) was prepared at a molar ratio of [monomer : VA-044 : PEO-CTA] = [1000 : 1 : 10] in a 25 mL round bottom flask at 0.2 M monomer concentration in acetate buffer solution and ethanol mixture (3:1, *v*/*v*). The solution was sealed, degassed under dried nitrogen for 45 min, and heated at 50 ^{o}C under constant stirring for 24 h. To end the polymerization, the reaction was quenched to room temperature and opened to air. Polymers were then dialyzed against water and lyophilized to provide free flowing powder.

A.2 MATLAB codes for data fitting

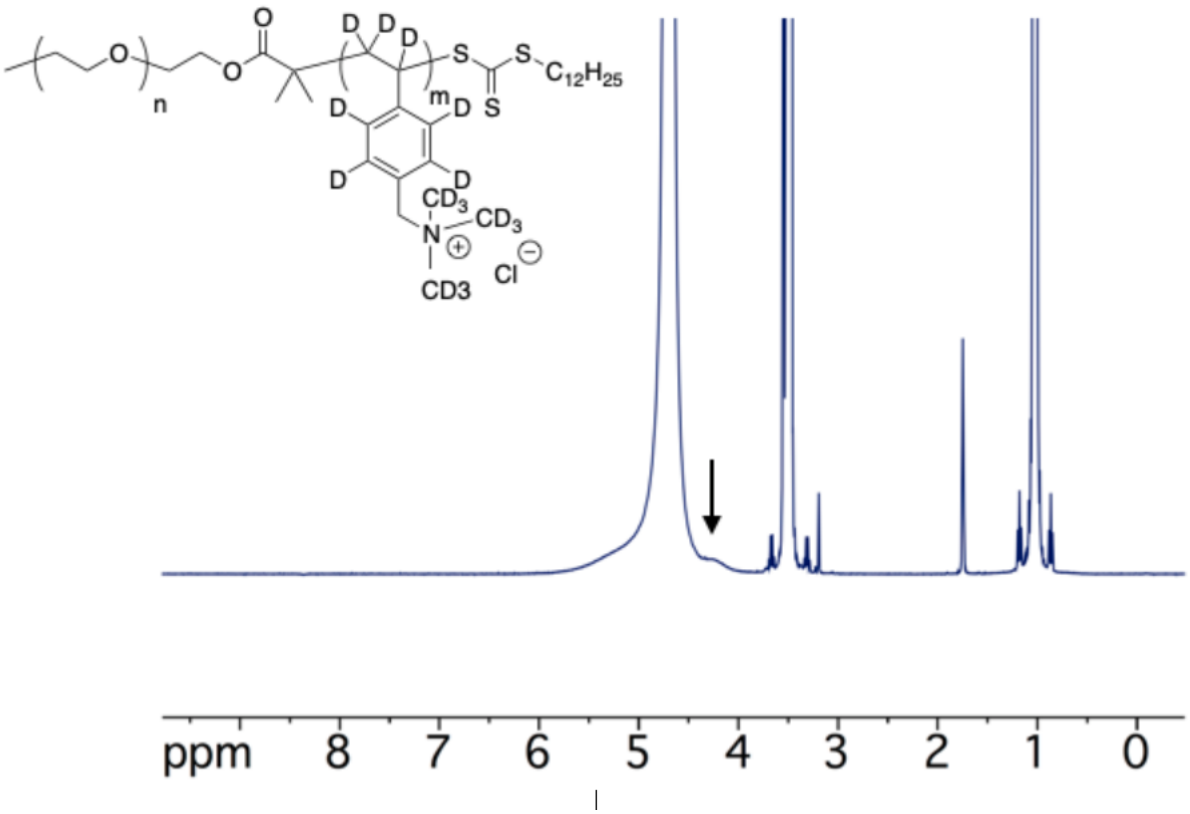

Figure A.6: 1H NMR of crude PEO-dPVBTMA polymerization after 18 h in D_2O. The arrow denotes the appearance of the non-deuterated protons at σ 4.1-4.6 ppm (2H, CH_2-N).

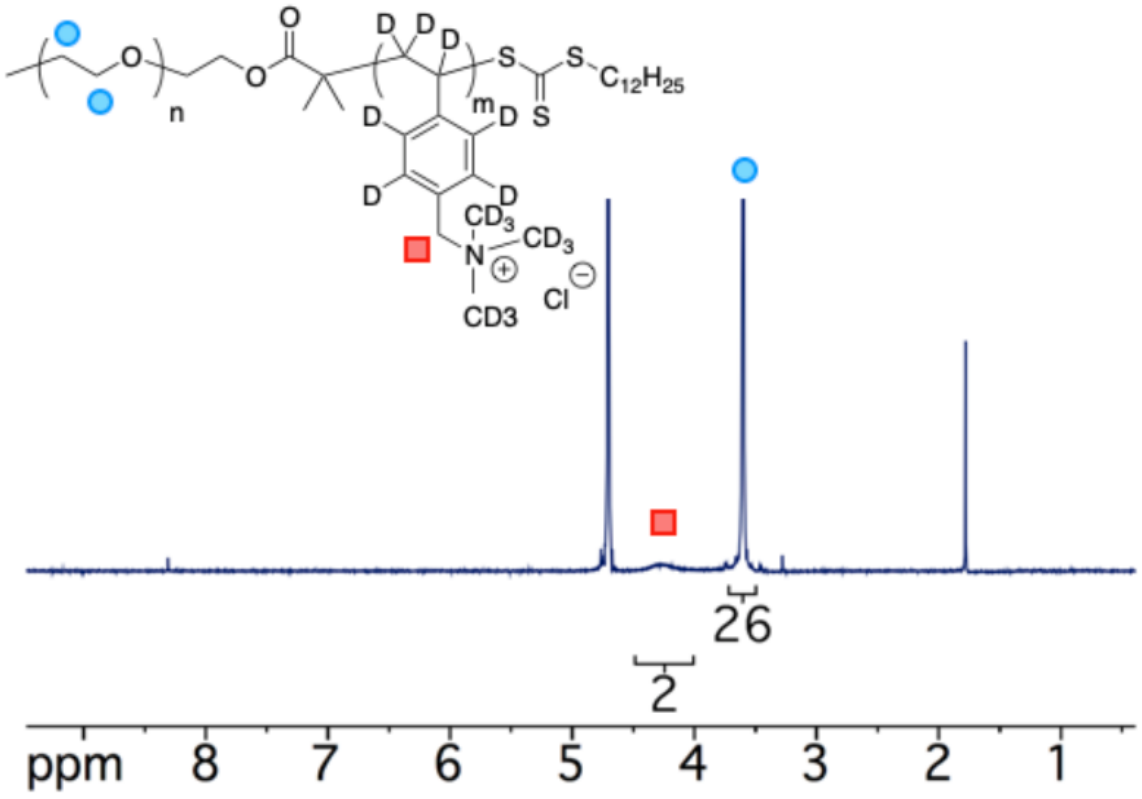

Figure A.7: ^{1}H NMR of purified PEO-dPVBTMA polymer in D_2O.

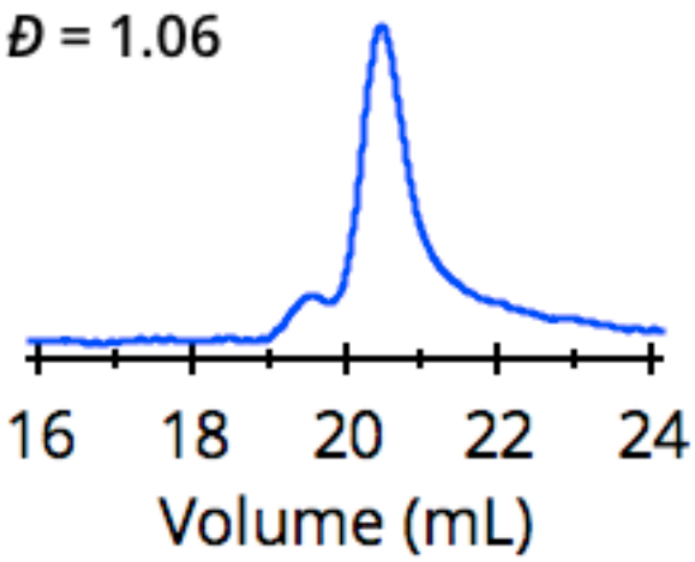

Figure A.8: SEC trace of the PEO-dPVBTMA polymer in a mixture of acetonitrile and water (40/60, %, *v/v*) with 0.1% trifluoroacetic acid was run as the mobile phase at 1.0 mL/min at 35 °C.

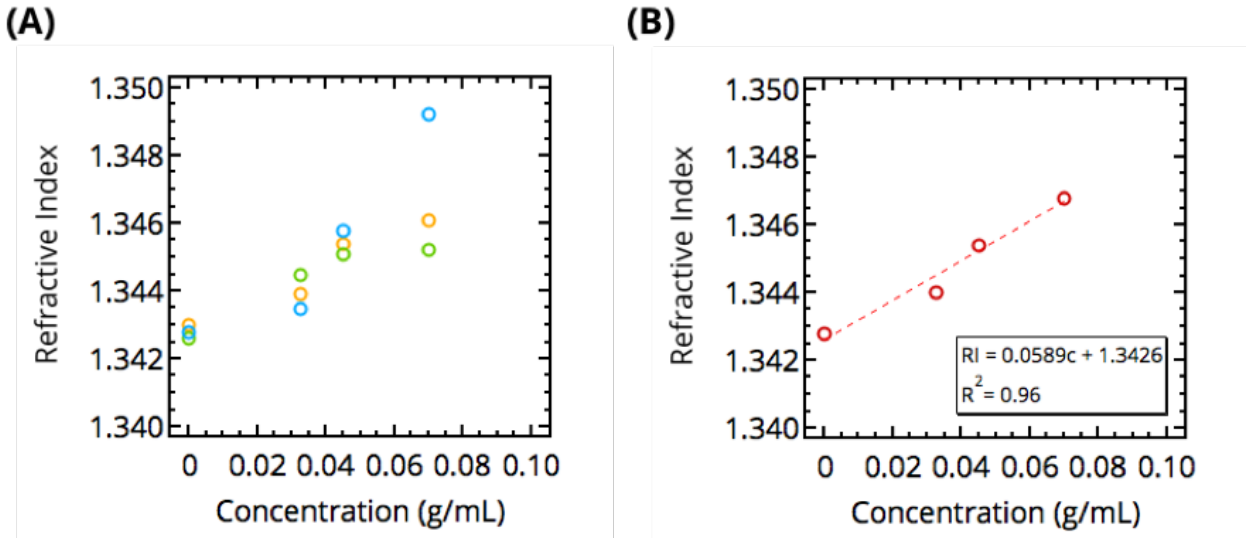

Figure A.9: Refractometry experiments to determine the *dn/dc* of PEO-dPVBTMA in the mixture of acetonitrile and water (40/60, %, *v/v*) with 0.1% trifluoroacetic acid, shown as (A) triplicate measurements by color and (B) the average (red circles) and linear regression (red dashed line).

```
%% data import
% read file, skip the 1st line
f =fopen('10k100158_01B_S029_4.5mgml.dat');
% 10k100158_01D_S026_1mgml
% 10k100158_01F_S033_2.0mgml
% 10k100158_01B_S024_5mgml
% 10k100158_01F_S033_2.0mgml
% 10k100158_01E_S032_3.0mgml
% 10k100158_01C_S030_4mgml
% 10k100158_01B_S029_4.5mgml
% 10k100158_01D_S031_3.5mgml
% 10k100158_01G_S034_1.5mgml

fgetl(f);
buffer = fread(f, [1,Inf],'*char');
fclose(f);

% get the file name
%[file, filepath] = unigetfile();
%S = uiimport(fullfile(filepath,file));


% eliminate 'injection' headers
buffer = regexprep(buffer, 'i.*?\n', '\n');

% convert to numeric type
data = textscan(buffer,'%f %f %f');

data = cell2mat(data); % convert to matrix from cell array

%% plot log(int) vs. log(q)

q = data(1:end,1);
int = data(1:end,2);

figure;

loglog(q, int, 'ro','MarkerSize', 10,'MarkerFaceColor', 'w');

ylim([0.005,200]);
xlim([0.002,0.15]);

ax = gca;
set(gcf,'position',[10,10,400,350]);
ax.FontSize = 20;
ax.LineWidth = 3;
ax = gca;
ax.FontSize = 20;
ax.LineWidth = 3;

%% plot Guinier region ln(int) vs. q^2

q_G = data(5:2:31,1);
int_G = data(5:2:31,2);
```

Figure A.10: MATLAB code of Guinier approximation (1/3).

```
figure;
%subplot(2,1,1);

plot(q_G.^2, log(int_G), 'ro','MarkerSize', 10,'MarkerFaceColor', 'r');


% fit the Guinier region

Guinier = @(param, t)(param(1)-(1/3)*param(2).^2.*t);

initial_param = [50, 100];
lb = [0 0];
ub = [inf inf];
options = optimoptions('lsqcurvefit', 'Algorithm', 'trust-region-
reflective');
[param, resnorm, residual, exitflag, output, lambda, jacobian] =
lsqcurvefit(Guinier, initial_param, q_G.^2, log(int_G), lb, ub, options);
hold on;

plot(q_G.^2, Guinier(param, q_G.^2), '--k','LineWidth', 4);

xlabel('q^2');
ylabel('log[I(q)]');
ang = char(197);
legend('4.5 mg mL^{-1}', 'R_{g} = 137.17 A');
legend('boxoff');
ax = gca;
set(gcf,'position',[10,10,400,350]);
%set(gca, 'Yticklabel', []);
ax.FontSize = 20;
ax.LineWidth = 3;
ax = gca;
ax.FontSize = 20;
ax.LineWidth = 3;

conf = nlparci(param,residual,'jacobian',jacobian);

Rg = param(2);
int_o = exp(param(1));
std = conf(2,2)-Rg;
fprintf('I(0) = %.2f \n', int_o);
fprintf('Rg = %.2f A\n', Rg);
fprintf('The resnorm is: %.2f\n', resnorm);
fprintf('The range of qRg is: %.2f  %.2f A\n', Rg.*q_G(1), Rg.*q_G(end));
fprintf('The standard error = %.2f\n', std);

%title(['Guinier Rg', num2str(Rg), ' A']);
dim1 = [.6 .75 .1 .1];
dim2 = [.6 .75 .1 .1];
dim3 = [.6 .7 .1 .1];
%str = sprintf('Rg: %.2f\n', num2str(Rg));
%annotation('textbox', dim1, 'String',
sprintf('R_{g}: %s\nI(0): %s\nq_{max}Rg: %s\n',
num2str(Rg),num2str(int_o),num2str(Rg.*q_G(end))), 'FitBoxToText', 'on');
%annotation('textbox', dim2, 'String', sprintf('I(0): %s\n',
num2str(int_o)));
```

Figure A.11: MATLAB code of Guinier approximation (2/3).

```
%annotation('textbox', dim3, 'String', sprintf('q_{max}Rg: %s\n',
num2str(Rg.*q_G(end))));


% plot Guinier peak analysis - q*I(q) vs. q^2

%subplot(2,1,2);
%plot(q_G.^2,q_G.*int_G, 'ko', 'MarkerSize', 10);

%xlabel('q^2');
%ylabel('q[I(q)]');
%ax = gca;
%ax.FontSize = 20;
%ax.LineWidth = 3;
%ax = gca;
%ax.FontSize = 20;
%ax.LineWidth = 3;
```

Figure A.12: MATLAB code of Guinier approximation (3/3).

```
clear all;
%% data immport


x_20 = xlsread('10k100_158_1mgml_500mM_20oC_kinetics.xlsx', 'A10:A263');
y_20 = xlsread('10k100_158_1mgml_500mM_20oC_kinetics.xlsx', 'B10:B263');

x_37 = xlsread('10k100_158_1mgml_500mM_37oC_kinetics.xlsx', 'A3:A302');
y_37 = xlsread('10k100_158_1mgml_500mM_37oC_kinetics.xlsx', 'B3:B302');

x_57 = xlsread('10k100_158_1mgml_500mM_57oC_kinetics.xlsx', 'A17:A236');
y_57 = xlsread('10k100_158_1mgml_500mM_57oC_kinetics.xlsx', 'B17:B236');

%% plot three original data
figure;
semilogx(x_20, y_20, 'ro','MarkerSize', 10,'MarkerFaceColor', 'w');
hold on;
semilogx(x_37, y_37, 'bs','MarkerSize', 10,'MarkerFaceColor', 'w');
hold on;
semilogx(x_57, y_57, 'kd','MarkerSize', 10,'MarkerFaceColor', 'w');
legend('T = 20 ^{o}C', 'T = 37 ^{o}C', 'T = 57 ^{o}C');
%title('PEO10k-PVBTMA100/PAA158 500mM');
xlabel('t [min]');
ylabel('Intensity [a.u.]');
xlim([0,1000]);

ax = gca;
set(gcf,'position',[10,10,500,280]);
ax.FontSize = 20;
ax.LineWidth = 3;
ax = gca;
ax.FontSize = 20;
ax.LineWidth = 3;

%% data fitting--single exponen
figure;
subplot(2,1,1);
%semilogx(x_all, y_count_all, 'ro','MarkerSize', 10,'MarkerFaceColor', 'r');
semilogx(x_37, y_37, 'ro','MarkerSize', 10,'MarkerFaceColor', 'r');
%ylim([0 1.1]);


SingleExp = @(param, t)(param(1)*exp(-param(2)*t)+param(3));

initial_param = [200 0.2 20];
lb = [100 -inf 0];
ub = [400 inf 50];
options = optimoptions('lsqcurvefit', 'Algorithm', 'trust-region-
reflective');

[param, resnorm, residual] = lsqcurvefit(SingleExp, initial_param, x_37,
y_37, lb, ub, options);

hold on;
```

Figure A.13: MATLAB code of Avrami fitting (1/5).

```
plot(x_37, SingleExp(param, x_37), '-k','LineWidth', 2);
%ylim([0 160]);
title('y = A * exp(-k*t) + B');
ylabel('I(t)');
xlabel('t (min)');
xlim([0.1 500]);

ax = gca;
ax.FontSize = 20;
ax.LineWidth = 3;
ax = gca;
ax.FontSize = 20;
ax.LineWidth = 3;


% plot residule
subplot(2,1,2);
plot(x_37, residual, 'ko','MarkerSize', 10);
%ylim([-0.1 0.1]);
title('Residual');
ylabel('Normalized percentage');
xlabel('time elapse (min)');
ax = gca;
ax.FontSize = 20;
ax.LineWidth = 3;
ax = gca;
ax.FontSize = 20;
ax.LineWidth = 3;

%display parameters
I0_1 = param(1);
tau_1 = 1/param(2);
bkg = param(3);
fprintf('I0_1 tau_1 bkg \n%.2f %.2f %.2f\n\n', I0_1, tau_1, bkg);
fprintf('The resnorm is: %.2f\n', resnorm);


% data fitting--single exponen & Avrami equation
figure;
%subplot(2,1,1);
semilogx(x_57, y_57, 'ro','MarkerSize', 10, 'LineWidth', 1,
'MarkerFaceColor', 'w');

SingleExp = @(param, t)(param(1)*exp(-(param(2)*t).^param(3))+param(4));


initial_param = [200 0.02 1.3 3];
lb = [10 0 -inf 0];
ub = [300 inf inf inf];
options = optimoptions('lsqcurvefit', 'Algorithm', 'trust-region-
reflective');

[param, resnorm, residual] = lsqcurvefit(SingleExp, initial_param, x_57,
y_57, lb, ub, options);
```

Figure A.14: MATLAB code of Avrami fitting (2/5).

```
hold on;

plot(x_57, SingleExp(param, x_57), '-k','LineWidth', 4);
%title('y = A * exp[(-k*t)^b] + B');
ylabel('Intensity [a.u.]');
xlabel('t [min]');
xlim([1 1000]);
ylim([0 250]);
legend('T = 57 ^{o}C','model fit');

ax = gca;
set(gcf,'position',[10,10,500,280]);
ax.FontSize = 20;
ax.LineWidth = 3;
ax = gca;
ax.FontSize = 20;
ax.LineWidth = 3;

% plot residule
%subplot(2,1,2);
%plot(x_20, residual, 'ko','MarkerSize', 10);
%ylim([-10 10]);
%title('Residual');
%ylabel('Normalized percentage');
%xlabel('time elapse (min)');
%ax = gca;
%ax.FontSize = 20;
%ax.LineWidth = 3;
%ax = gca;
%ax.FontSize = 20;
%ax.LineWidth = 3;

%display parameters
I0_1 = param(1);
tau_1 = 1/param(2);
beta = param(3);
bkg = param(4);
fprintf('I0_1 tau_1 beta bkg \n%.2f %.2f %.2f %.2f %.2f\n\n', I0_1, tau_1,
beta, bkg);
fprintf('The resnorm is: %.2f\n', resnorm);

%% plot Ea by ln tau vs. 1/T

figure;

T = [20+273.15 37+273.15 57+273.15];
t = 1./T;
Y = [log(61.54) log(51.77) log(38.57)];

p1 = polyfit(t, Y, 1);
yfit = polyval(p1,t);
disp(p1)

plot(t, Y,'ro', 'MarkerSize', 20,'MarkerFaceColor', 'r');
hold on;
plot(t, yfit, '--', 'Linewidth', 5);
```

Figure A.15: MATLAB code of Avrami fitting (3/5).

```
legend('experimental','linear fitting');
%title('ln(\tau)~Ea/T');
xlabel('1/T');
ylabel('ln(\tau)');
ax = gca;
ax.FontSize = 30;
ax.LineWidth = 5;
ax = gca;
ax.FontSize = 30;
ax.LineWidth = 5;

% computing R square
yresid = Y - yfit;
SSresid = sum(yresid.^2);
SStotal = (length(Y)-1)*var(Y);
rsq = 1 - SSresid/SStotal;
disp(rsq);




%%  data fitting--double-exponen

figure;

% plot data
subplot(2,1,1);

semilogx(x_37, y_37, 'ro','MarkerSize', 6,'MarkerFaceColor', 'r');
%ylim([0 1.1]);
% double expon fitting
DoubleExp = @(param, t)(param(1)*exp(-param(2).*t) + (y_37(1)-param(1))*exp(-
param(3).*t)+param(4));

initial_param = [200 0.01 0.01 20];
lb = [0 -inf -inf 0];
ub = [y_37(1) inf inf inf];

options = optimoptions('lsqcurvefit', 'Algorithm', 'trust-region-
reflective');
[param, resnorm, residual] = lsqcurvefit(DoubleExp, initial_param, x_37,
y_37, lb, ub, options);

hold on;

plot(x_37, DoubleExp(param, x_37), '-k','LineWidth', 2);
%ylim([0 1.1]);
%xlim([0.001 1000]);
title('y = A*exp(-k1*t) + B*exp(-k2*t) + C');
ylabel('Intensity (k.c.p.s)');
xlabel('time elapse (min)');
%legend('10k100 / 158 in 500mM NaCl','double exponential fit');
```

Figure A.16: MATLAB code of Avrami fitting (4/5).

```
ax = gca;
ax.FontSize = 20;
ax.LineWidth = 3;
ax = gca;
ax.FontSize = 20;
ax.LineWidth = 3;



subplot(2,1,2);
plot(x_37, residual, 'ko','MarkerSize', 6);
%ylim([-0.1 0.1]);
title('Residual');
ylabel('Normalized percentage');
xlabel('time elapse (min)');
ax = gca;
ax.FontSize = 20;
ax.LineWidth = 3;
ax = gca;
ax.FontSize = 20;
ax.LineWidth = 3;

%display parameters
I0_1 = param(1);
tau_1 = 1/param(2);
I0_2 = y_37(1)-param(1);
tau_2 = 1/param(3);
bkg = param(4);

fprintf('I0_1 = %.2f\n', I0_1);
fprintf('tau_1 = %.2f\n', tau_1);
fprintf('I0_2 = %.2f\n', I0_2);
fprintf('tau_2 = %.2f\n', tau_2);
fprintf('bkg = %.2f\n', bkg);
fprintf('The resnorm is: %.2f\n', resnorm);
```

Figure A.17: MATLAB code of Avrami fitting (5/5).